University of Adelaide

THE UNIVERSITY
of ADELAIDE

Doctoral Thesis

Development of an Integrated Stochastic Radiobiological Model for Electromagnetic Particle Interactions in a 4D Cellular Geometry

Michael John James Douglass

Supervisors: A/Prof. Eva Bezak & Dr. Scott Penfold

A thesis submitted in fulfilment of the requirements for the degree of Doctor of Philosophy

in the

School of Chemistry and Physics
University of Adelaide

May 2014

Declaration of Authorship

I, Michael John James Douglass, certify that this thesis titled, 'Development of an Integrated Stochastic Radiobiological Model for Electromagnetic Particle Interactions in a 4D Cellular Geometry' and the work presented in it are my own. I confirm that:

- This work contains no material which has been accepted for the award of any other degree or diploma in any university or other tertiary institution to Michael John James Douglass and, to the best of my knowledge and belief, contains no material previously published or written by another person, except where due reference has been made in the text.
- I give consent to this copy of my thesis, when deposited in the University Library, being made available for loan and photocopying, subject to the provisions of the Copyright Act 1968.
- The author acknowledges that copyright of published works contained within this thesis resides with the copyright holder(s) of those works.
- I also give permission for the digital version of my thesis to be made available on the internet, visa the University's digital research repository, the Library catalogue, the Australasian Digital Theses Program (ADTP) and also through web search engines, unless permission has been granted by the University to restrict access for a period of time.

Signed:

Date:

Peer Reviewed Publications

Published

1. Douglass M., Bezak E. and Penfold S., Development of a Randomised 3d Cell Model for Monte Carlo Microdosimetry Simulations. *Medical Physics*, 39:3502-3519, 2012.

2. Douglass M., Bezak E., Physical Modelling of Proton and Heavy Ion Radiation using Geant4, *EPJ Web of Conferences* 35, 2012.

3. Kempson I.M., Smith E., Douglass M., Thierry B., Liu T.Q., Howard D., DeJonge M. and Bezak E., Applications of Large Area XRF Mapping of Metals in Biology at the Australian Synchrotron *IAEA X-ray Fluorescence Newsletter*, 2012.

4. Douglass M., Bezak E. and Penfold S., Monte Carlo Investigation of the Increased Radiation Deposition due to Gold Nanoparticles using Kilo- and Mega-Voltage X-Rays in a 3D Randomized Cell Model", *Medical Physics*, 40, 2013.

Submitted for Publication

1. Douglass M., Bezak E. and Penfold S., An integrated radiobiological model for the prediction of the biological effects of protons and heavy ion radiation", *NASA Space Radiation*, 2014 (Submitted November 2013).

2. Douglass M., Bezak E. and Penfold S., Development and Calibration of a Simulation Toolkit for Cell Growth, Irradiation and Repair, Michael Douglass, *Medical Physics*, 2014 (Submitted March 2014).

Grants and Scholarships

- Co-recipient of a grant ($100K value) for x-ray fluoroscopy beam time at the Australian Synchrotron Centre. November 2012, Principal scientist, Dr. Ivan Kempson.
- Australian Postgraduate Award (APA) 2010 - 2013.
- ACPSEM EPSM 2012 Scholarship.

Conference Presentations and Awards

Local

- Douglass M., Bezak E., *Proton and Heavy Ion Radiotherapy*, ACPSEM (SA/NT) Student Paper Night, 2009, **1st Place (Physics Category)**.
- Douglass M., Bezak E. and Penfold S., *Proton and Heavy Ion Radiotherapy*, ACPSEM (SA/NT) Student Paper Night, 2010, **2nd Place (Physics Category)**.
- Douglass M., Bezak E. and Penfold S., *Heavy Ion Microdosimetry*, Postgraduate Poster Seminar - University of Adelaide, 2010, **"Prize for best first year physics research poster".**
- Douglass M., Bezak E. and Penfold S., *Development of a 3D randomised cell model*, Three minute thesis competition, 2010.
- Douglass M., Bezak E. and Penfold S., *Cellular Microdosimetry*, Three minute thesis competition, 2011.
- Douglass M., Bezak E. and Penfold S., *Development of a Randomized 3D Cell model for microscopic level radiation cell damages*, ACPSEM (SA/NT) Student Paper Night, 2011, **1st Place (Physics Category)**.
- Douglass M., Bezak E. and Penfold S., *Development, Testing and Application of a Complete Cell Growth, Irradiation, Repair and Death Model*, ACPSEM – SA/NT Student Paper Night, 2013, **1st Place**.
- Douglass M., Bezak E. and Penfold S., *Development, Testing and Application of a Complete Cell Growth, Irradiation, Repair and Death Model*, Adelaide University School of Chemistry and Physics Postgraduate Research Seminar, 2013, **Recipient of "Bob Crompton Award" for physics**.

National

- Douglass M., Bezak E. and Penfold S., *Development of Monte Carlo Input Code for Proton, Alpha and Heavy Ion Microdosimetric Track Structure Simulations*, EPSM, 2010. Melbourne, Australia

- Douglass M., Bezak E. and Penfold S., *Development of Monte Carlo Input Code for Proton, Alpha and Heavy Ion Microdosimetric Track Structure Simulations*, EPSM-ABEC, 2011, Darwin, Australia **"Prize for best student radiobiology presentation"**.
- Douglass M., Bezak E. and Penfold S., *Application of a Novel Cellular Microdosimetry model to investigate the impact of Gold Nanoparticles on the dose to cells*, EPSM-ABEC, 2012, Gold Coast, Australia.
- Douglass M., Bezak E. and Penfold S., *Physical Modelling of Proton and Heavy Ion Radiation Using Geant4*, Heavy Ion Accelerator Symposium, 2012, Australian National University ACT, Australia, **Prize for "Best student oral presentation**.
- Douglass M., Bezak E. and Penfold S., *Investigation of the dose enhancement effect of gold nano particles using a 3D randomized cell model*, Modelling of Tumours Meeting (MOT), 2012, Adelaide, Australia.
- Douglass M., Bezak E. and Penfold S., *Application of a Novel Cellular Microdosimetry model to investigate the impact of Gold Nanoparticles on the dose to cells*, MMND (Micro- Mini and Nanodosimetry conference), 2012, University of Wollongong, Australia.
- Douglass M., Bezak E. and Penfold S., *Development, Testing and Application of a Complete Cell Growth, Irradiation, Repair and Death Model*, 2nd Geant4 and Monte Carlo Workshop, 2013 University of Wollongong, NSW, Australia.

International

- Douglass M., Bezak E. and Penfold S., *Development of Monte Carlo Input Code for Proton, Alpha and Heavy Ion Microdosimetric Track Structure Simulations*, First Geant4 School and Users Workshop, 2010, University of Wollongong, NSW, Australia.
- Douglass M., Bezak E. and Penfold S., *Development of a Randomised 3d Cell Model for Microscopic Level Radiation Damages*, International Conference on Biological Physics, 2011, University of San Diego, CA, USA
- Douglass M., Bezak E. and Penfold S., *Investigation of the dose enhancement effect of gold nano particles using a 3D randomized cell model*, Medical Physics World Congress, 2012, Beijing, China.

- Douglass M., Bezak E. and Penfold S., *Development, Testing and Application of a Complete Cell Growth, Irradiation, Repair and Death Model*, Radiation Research Meeting 2013, New Orleans, LA, USA

"The fact that we live at the bottom of a deep gravity well, on the surface of a gas covered planet going around a nuclear fireball 90 million miles away and think this to be normal is obviously some indication of how skewed our perspective tends to be."

Douglas Adams

Abstract

An integrated radiobiological model has been developed in this thesis using the Monte Carlo toolkit "Geant4" to produce a radiobiological modelling software package. The result is a simulation capable of: (a) growing a simulated 3D cell structure (i.e. tumour or mammalian tissue) composed of individual cells (with accurate chemical composition and geometry), (b) irradiating the cells and recording the microdosimetric track structure in each cell, (c) clustering spatially correlated ionisation events into DNA double strand breaks and then (d) predicting the likelihood that any given cell will survive. The novelty of this model is its ability to predict both the microscopic and macroscopic outcome of radiobiology experiments while varying input parameters such as cell line, radiation type, tumour geometry, dose etc. Previous research in this area has been limited to simple water volumes as representations of cells and none have been combined into an integrated radiobiological model.

Model Development

Cellular Growth Model

The cellular growth model consists of two parts. The first part is a geometrical and chemical description of a single cell. The second is a cellular growth model describing the growth kinetics of a group of cells. When combined, they form a simulated macroscopic cell mass composed of individual microscopic cells.

A template was first designed within Geant4 for a single cell containing properties such as cell size, nucleus dimensions, and cytoplasm composition. Cellular dimensions and composition were obtained from previous publications.

The cellular growth model is a mathematical model which attempts to replicate the growth characteristics of either regular or cancerous cells. The code populates a volume of specified dimension and shape with cells of random dimension, rotation and position governed by the characteristics of a given cell line. A general requirement for Geant4 simulations is a non-overlapping geometry. A custom algorithm was developed in the current work to ensure that the cells in the tumour geometry did not overlap before importing into Geant4.

The time required to "grow" a tumour using this code is proportional to the number of cells in the volume. The time to produce a tumour containing approximately 10^5 cells is typically less than 1 hour. However, the time required to complete the irradiation stage of the code is strongly dependant on the number of cells in the tumour. To produce results in a reasonable amount of time, we were limited to using tumours containing less than 10^4 cells.

The position, rotation and size of each tumour were then exported to a file in a format which could be imported by our custom Geant4 simulation.

Cellular Irradiation

A method called parameterisation was used inside Geant4 to combine the single cell structure and the spatial properties of the cells (generated by the cellular growth model) to produce a cellular mass which can be irradiated virtually. To our knowledge, Geant4 has not been used to simulate particle interactions in such a large number of complex volumes. This achievement is the result of the efficiency of the unique parameterisation code developed in this thesis. The Geant4 particle tracking tool kit enables the cells to be irradiated with different types of radiation (such as protons, electrons, photons) and records the positions of the ionisation damage in each cell. For high LET radiation (such as heavy ions), the primary cell damage mechanism is direct ionisation damage. By recording the position and energy deposited in each ionisation event, the probability of a cell surviving or dying can be calculated.

The first two stages of the code were tested by predicting and quantifying the radiosensitisation effect of cells by gold nanoparticles. Gold nanoparticles were introduced into the cellular geometries and the frequency of ionisation effects within the cells was measured. It was determined that the radiosensitisation effect of gold nanoparticles is proportional to the concentration of gold within the cell, inversely proportional to the energy of the incident photon and strongly dependant on position within the cell. When the cells were irradiated with 80 kVp x-rays, the damage to the cells was determined to be approximately 10 times that of cells irradiated without gold nanoparticles. When a typical 6 MV linear accelerator x-ray beam was used to irradiate the cells, the damage to the cells was only 1.2 times higher that measured without gold nanoparticles. These results suggest that the primary dose enhancement effect is the result of the increase in photoelectric cross section caused by the local increase in the effective atomic number within the cell.

Ionisation Clustering

In order to predict the biological damage to the cells, the ionisation damage calculated in the previous two stages of the code needed to be clustered into DNA strand breakages. To cluster the ionisation events into double strand breaks, a hierarchical clustering algorithm was developed. Ionisation events are clustered into a DSB if the Euclidean distance from the centre of the DSB centroid ("centre of mass" of the cluster) is less than 3.4 nm (length of 10 base pairs in DNA). A DSB is defined to be "simple" if the cluster contains two ionisation events. A DSB is "complex" if it contains three or more ionisation events. In typical radiotherapy treatments, several grays of radiation dose are delivered. Microscopically, this corresponds to billions or trillions of individual ionisation events. When simulated computationally, this has obvious storage and processing issues. The effects of this problem were minimised by considering only a small volume of cells ($< 10^3$ cells). Even with such a small number of cells, the total number of ionisation events to process was in excess of 10^7. In terms of computational time, this section of the code is highly efficient but at the expense of system resources. The large system RAM requirements mean that the code can only be executed on a 64 bit processor in its current form.

DNA Repair Model

The basis for the DNA repair model in the current work is the two lesion kinetics (TLK) model. In the current work we have expanded on the TLK model and implemented it as a method of describing the repair of the ionisation damages produced in Geant4. The most notable improvement lies in implementing the model on a cell by cell basis instead of modelling the repair kinetics as an average of all cells in the volume (e.g. a tumour).

The DNA repair model was calibrated and tested using experimental data for V79 Chinese hamster cells irradiated with 0.76 and 1.9 MeV proton radiation. Once calibrated, the experimental and calculated values for cell survival were in good agreement ($< 7\%$ difference).

Cross Section Verification

The validity and accuracy of the Geant4 cross sectional data was tested by comparing simulated and experimental data.

Geant4 has been shown to be able to simulate radiation interactions of very low energy particles (to approximately ~ 1 eV (debated)). However, our investigation (and previous publications) has shown differences of up to $\pm 30\%$ (between simulated and experimental data) in the differential cross section of electrons and protons at energies below 100 eV. Our investigation also revealed a similar discrepancy with other comparable Monte Carlo packages including PARTRAC and RITRACKS. However, within the energy range we have investigated throughout this research, there is good agreement between both experimental data and data predicted by other MC packages.

Effect of Indirect Radiation Damages on Cellular Survival

To investigate the contribution from indirect damages in our previous studies, a MC software package called RITRACKS was used which is capable of simulating the production yields of free radical species due to the physical interactions of ionising radiation in water.

Utilising the clustering algorithm and DNA repair model from our previous Geant4 investigation, we attempted to quantify the cellular lethality of direct and indirect radiation damages. Our study has shown that for particles with LET ~ 1000 keV/µm (50 MeV/amu ^{56}Fe ions, the contribution to DNA damage from indirect damages is still approximately 50%.

Conclusion

A comprehensive radiobiological simulation has been developed capable of predicting the complex ionisation track structure of ionising radiation (e.g. photons, protons and carbon ions) through individual cells. Subsequently, predicting the biological outcome within

individual cells by tracking the formation and repair of DNA strand breaks. The capabilities of the software have been demonstrated for use in novel radiotherapy treatment techniques.

Acknowledgements

I would first like to thanks my Mum, Dad and brother who helped me through the difficult times and to reach my full potential. I'm not sure where I would be today if it were not for them. Thanks Dad for helping me with my coding issues and Mum for proof reading my publications.

Special thanks to my co-supervisor Dr. Scott Penfold. Your knowledge, skills and our combined interests helped to make the challenges we faced through this project a little less daunting. Thank you for the endless hours you spent proof reading my thesis. I hope we can work together on other projects in the future.

Thanks to the researchers from the centre for medial physics research at the University of Wollongong, in particular Susanna Guatelli for providing me with solutions to my coding issues and inviting me to speak at the numerous conferences in Wollongong.

Thank you to Dr. Ivan Kempson for inviting me to participate in the gold nanoparticle experiments at the Australian Synchrotron Centre in October 2012. It was a true highlight of my PhD and was a welcomed distraction from all the coding work.

Thank you to the ACPSEM for selecting me for the scholarship to attend the EPSM 2012 conference on the Gold Coast.

Thanks to Dr. Tibor Kibédi from the Australian National University for helping me to attend the Heavy Ion Accelerator Symposium, held in Canberra, 2012.

Thank you to Sébastien Incerti for inviting me to join the Geant4-DNA collaboration.

Thank you to Ianik Plante from NASA's Division of Life Sciences for giving me access to the RITRACKS software and your guidance in using it.

I would like to acknowledge the support from the staff at the University of Adelaide, School of Chemistry and Physics for arranging travel to conferences, signing forms and all the other administration jobs.

Thank you to Dr. Raghu Gowda of the Royal Adelaide Hospital for introducing me to the field of medical physics. You helped me to find an area of physics that I love and can make a positive contribution to. I am eternally grateful for your guidance and friendship.

Thank you to all the staff in the Medical Physics department at the Royal Adelaide Hospital. I love working with all of you. All of you have helped me at some point either

with my research or TEAP training. It was great to spend time outside of work as well. I couldn't have asked for a better group of people to work with. Special thanks to Christine Robinson who organises the medical physics department so well. Your cheery mood helps to brighten everyone's day.

Thanks to Joshua Moorrees and Siva Sarasanandarajah for organising the ACPSEM student paper night each year. The student paper night was an event I looked forward to every year.

Thanks to all the PhD and Masters students from the medical physics department. I enjoyed collaborating on problems and learning about other interesting areas of medical physics. Thanks to Leila Moghaddasi for cooking lots of wonderful snacks to keep me going during my thesis writing.

A very big thanks to Alexandre Santos, a fellow PhD student and friend right from the beginning of this medical physics journey. It was great to have someone to talk to and solve problems relating to my PhD.

And most importantly, to my supervisor A/Prof. Eva Bezak, You are the greatest mentor a person could have. Your knowledge, diverse skill set, creativity and dedication helped me through a wonderful PhD. What I appreciate most though is your kindness and understanding. I am eternally grateful for the support you gave me during the most challenging part of my life. I am honoured to call you a friend as well as a mentor. Few people could comprehend the time and effort you put in to the department to make it what it is today. I look forward to working with you in the future on new and ground-breaking research....

Contents

List of Figures

List of Tables

Abbreviations

AC	**A**lternating **C**urrent
AE	**A**uger **E**lectron
ATP	**A**denosine **Tri**p**h**osphate
CHO	**C**hinese **H**amster **O**vary
CPU	**C**entral **P**rocessing **U**nit
CSG	**C**onstructed **S**olid **G**eometry
CT	**C**omputer **T**omography
DEF	**D**ose **E**nhancement **F**actor
DER	**D**ose **E**nhancement **R**atio
DNA	**D**eoxyribo**n**ucleic **A**cid
DSB	**D**ouble **S**trand **B**reak
EBRT	**E**xternal **B**eam **R**adio**t**herapy
GBP	**G**iga **B**ase **P**airs
GEANT	**Ge**ometry **an**d **T**racking
GNP	**G**old **N**ano **P**article
GPU	**G**raphics **P**rocessing **U**nit
IGRT	**I**ntensity **G**ated **R**adio**t**herapy
IMAT	**I**ntensity **M**odulated **A**rc **t**herapy
IMRT	**I**ntensity **M**odulated **R**adio**t**herapy
LET	**L**inear **E**nergy **T**ransfer
LPL	**L**ethal **P**otentially **L**ethal
LQ	**L**inear **Q**uadratic
MC	**M**onte **C**arlo
MCDS	**M**onte **C**arlo **D**amage **S**imulation

MRI	**M**angetic **R**essonance **I**maging
PC	**P**ersonal **C**omputer
PDF	**P**robability **D**ensity **F**unctions
PET	**P**ositron **E**mission **T**omography
RAM	**R**andom **A**ccess **M**emory
RBE	**R**elative **B**iological **E**ffectiveness
RMR	**R**epair **M**is**r**epair
RNA	**R**ibo**n**ucleic **A**cid
TLK	**T**wo **L**esion **K**inetic
XFM	**X**ray **F**luorescence **M**icroscopy

Physical Constants

Speed of Light	c	=	$2.997\ 924\ 58 \times 10^{8}$ ms^{-1}
Gravitational Constant	G	=	$6.673\ 84 \times 10^{-11}$ m^{3} kg^{-1} s^{-2}
Plank's Constant	h	=	$6.626\ 069\ 57 \times 10^{-34}$ m^{2} kg s^{-1}
Fine Structure Constant	α	=	$7.297\ 352 \times 10^{-3}$
Electron Rest Mass Energy	m_e	=	510.99 keV
Proton Rest Mass Energy	m_p	=	938.27 MeV
Neutron Rest Mass Energy	m_n	=	939.56 MeV
Alpha Particle Rest Mass Energy	m_α	=	3727.37 MeV
Charge of an Electron	e	=	1.6021×10^{-19} C
Classical Electron Radius	r_e	=	$2.817\ 940 \times 10^{-15}$ m
Bohr Radius	a_0	=	0.529177×10^{-10} m
Compton Wavelength	λ_C	=	2.426×10^{-12} m
Stefan-Boltzmann Constant	σ	=	$5.670\ 373 \times 10^{-8}$ W m^{-2} K^{-4}
Boltzmann Constant	k	=	$1.380\ 658 \times 10^{-23}$ J K^{-1}
Rydberg Constant	$\mathfrak{R}$	=	$10\ 973\ 731.568 \times 10^{-1}$ m^{-1}
Avogadro's constant	N_A	=	6.0221×10^{23} mol^{-1}
Permittivity of Free Space	ϵ_0	=	8.8541×10^{-12} F m^{-1}
Permeability of Free Space	μ_0	=	$12.566\ 370 \times 10^{-7}$ N A^{-2}
Gas Constant	R	=	8.3144 J K^{-1} mol^{-1}

Symbols

D	Absorbed radiation dose	Gy
P	Power	Watts
S	Survival fraction	(dimensionless)
E	Particle energy	MeV
σ	Interaction cross section	cm^{-1}
Z	Atomic number	(dimensionless)
T	Kinetic energy	MeV
B	Binding energy	eV

Dedicated to those who inspired me to study science:
Carl Sagan and Amanda Tapping...

Chapter 1

Introduction

Cancer is estimated to affect one in three and one in four Australian men and women respectively by the age of 75 [1]. Various methods of treatment are available including surgery, chemotherapy, radiotherapy, immunotherapy and targeted therapies, many of which are often used in conjunction with each other.

Since the discovery of x-rays in the late 1800s [2], radiation has been applied in the treatment of various ailments including cancer. In the mid 1900s, clinical radiotherapy made several large advances including the use of ^{60}Co sources for the treatment of deep seated tumours and the development of linear accelerators for medical use. These advances have made radiation an effective tool for the treatment of cancer.

1.1 Radiation Therapy

Radiation dose is delivered to a cancer patient using a variety of methods including external beam radiotherapy (EBRT), brachytherapy and targeted therapy depending on the specific characteristics of the disease [3]. The primary objective of any radiation treatment is to maximise the dose to the tumour volume while minimising exposure to the healthy tissue surrounding it. This is to achieve the highest probability of curing the patient while reducing the severity of side effects and to reduce the probability of second primary cancers developing. External beam radiotherapy and brachytherapy are the

two most common radiotherapy treatment modalities at present due to several factors including: highly effective treatment outcomes, low cost of treatment per patient (c.f. chemotherapy), short treatment times per fraction and the knowledge and experience of decades of cancer treatment and research using these modalities. Many advances in the field of external beam radiotherapy have been made in the last fifty years. Some key advances include: use of megavoltage x-rays to treat deep seated tumours, linear accelerator (figure 1.1) development, implementation of multi-leaf collimators for better radiation field conformality, intensity modulated radiotherapy [4, 5] and image guided radiotherapy. These technologies have been made practical for external beam radiotherapy by the corresponding development of 3D treatment planning systems, CT simulators and PET imaging. These key advances have helped x-ray based external beam radiotherapy remain the treatment of choice for cancer and will remain so for many years to come.

Whilst megavoltage x-rays are effective in the treatment of many forms of cancer, recent scientific and technological advances have enabled other treatment modalities to be developed. One of the most important of these advances is proton and heavy ion radiotherapy [6, 7] due to the development of a new generation of medical cyclotrons/synchrotrons (figure 1.2) [8].

Protons and heavy ions have many physical and biological advantages over x-rays when used in radiotherapy. The primary advantage is the superior dose distribution (figure 1.3). Protons and heavy ions deposit very little energy in matter until coming to a complete stop. This physical behaviour gives rise to the so called "Bragg Peak". By precisely modulating the energy of the protons, the radiation dose can be precisely and conformally deposited in the tumour volume. The magnitude of the radiation damage caused by an individual proton is inversely proportional to its energy. As a result, the biological effectiveness of the radiation is up to 60% higher in the Bragg peak region. Both of these properties result in better treatment outcomes for the patient as a result of lower integrated radiation doses required to obtain the same tumour control and reduced radiation dose to normal tissue surrounding the tumour.

Whilst heavy ions are slowly being adopted in hospitals and treatment centres around the world, the high set-up costs still make this new treatment modality widely unaffordable.

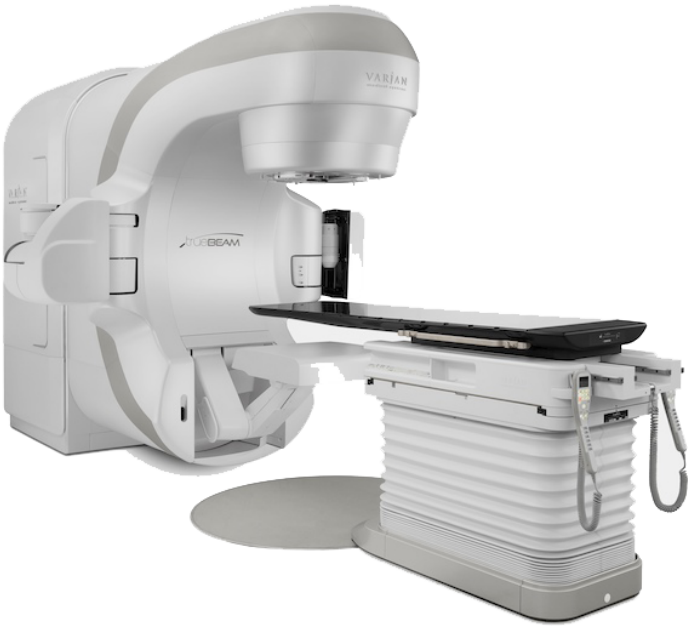

FIGURE 1.1: A Varian True Beam™ linear accelerator used in x-ray external beam radiotherapy. Courtesy of Varian Pty. Ltd.

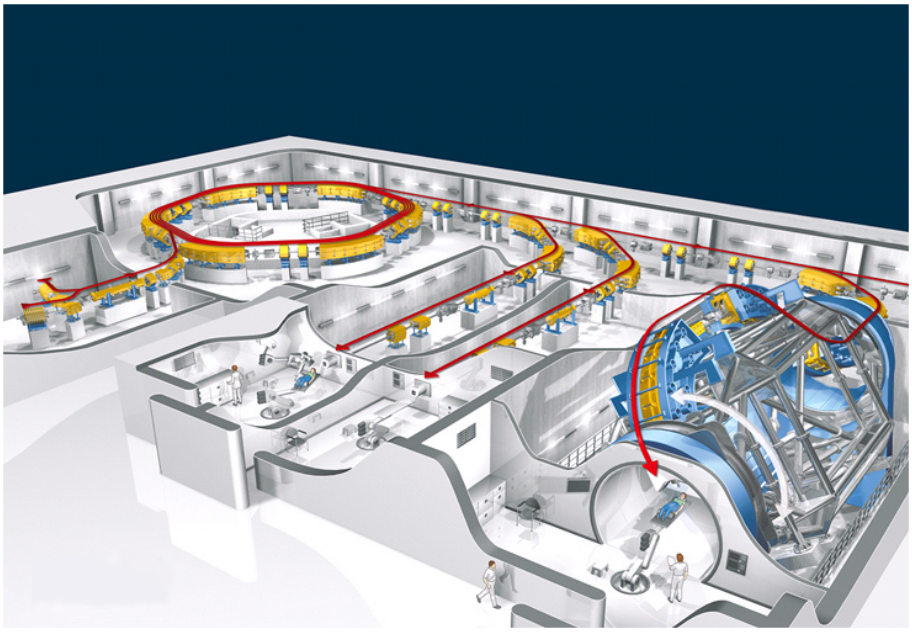

FIGURE 1.2: A synchrotron accelerator used in proton and heavy ion radiotherapy. Courtesy of Stern, Gruner+Jahr AG & Co. KG, Germany.

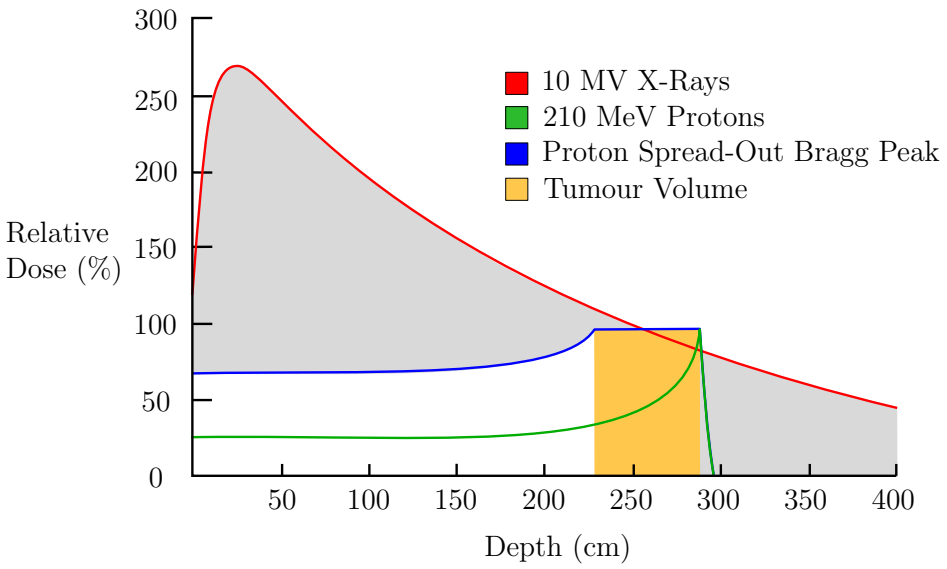

FIGURE 1.3: The percentage depth dose curves for 10 MV photons, 210 MeV protons and a proton spread-out Bragg peak. The benefits of proton radiotherapy are evident from the shape of the depth dose curve. The majority of the proton radiation is delivered to the tumour volume with reduced dose to the normal tissue surrounding it.

Proton and carbon ion facilities generally cost more than ten times as much to set-up compared with a traditional linear accelerator [9]. There are additional challenges associated with setting up and running a heavy ion facility such as modification of existing shielding in hospitals, new infrastructure and training of existing medical physicists, radiation oncologists and radiotherapist to properly operate, maintain the equipment and take advantage of the benefits of heavy ion radiation. Due to these issues, photon EBRT and brachytherapy will remain the dominant treatment modalities for the next decade [10].

1.2 Targeted and Adjunct Therapies

Conventional EBRT and brachytherapy treatments are designed to deliver the highest radiation dose to the tumour volume while sparing normal tissue. Whilst both of these methods are effective in treating localised tumours they both have several major disadvantages. EBRT treatments, while non-invasive can cause significant radiation damage to normal tissue surrounding the tumour volume. Brachytherapy is more effective than EBRT in delivering a localised dose to the tumour volume but can be highly invasive.

Both types of treatment require the tumour to be localised to a single volume and large enough to appear either on CT, MRI, PET or other imaging devices for detection and treatment planning. There are very few therapies currently available which are designed to target micrometastatic tumour cells after the treatment of the primary cancer. These cells can lead to the formation of second cancers if not destroyed and as a result targeted therapies are needed.

1.2.1 Targeted Alpha Therapy

One form of targeted therapy currently undergoing clinical trials is "targeted alpha therapy"[11]. An alpha emitting radioisotope (e.g. ^{213}Bi) is labelled with a monoclonal antibody (figure 1.4) or protein which targets the antigens expressed by cancer cells. The radioisotopes emit low energy (short range <80 µm) alpha particles which are highly detrimental to the targeted cells due to their high LET. Because the antibody binds preferentially to the tumour cells, the radiation dose from the alpha particles is delivered largely to the cancer cells and tumour blood vessel cells [11].

1.2.2 Gold Nanoparticles

Another proposed method of increasing radiotherapy treatment outcomes is through radiosensitisation of cancer cells. The use of gold nanoparticles is one proposed method. By introducing a solution of gold particles of nanometre dimensions to a region in close proximity to the cancer cells, the effective atomic number in the region of the tumour will be increased. The interaction cross section for low energy x-rays is strongly dependant on the atomic number of the material (i.e. $\sigma \propto Z^{3.8}$ for the photoelectric effect). The result is an increased probability of photoelectrons being produced in the tumour cells and therefore increased localised radiation damage [3].

It has been proposed that gold nanoparticles could also be used to benefit image guided radiotherapy [12]. By injecting a hydrogel/gold nanoparticle solution directly into the tumour, the gold nanoparticles would also act as markers (in addition to a sensitising agent) for IGRT. Upon injection of the hydrogel solution, the solution will solidify and

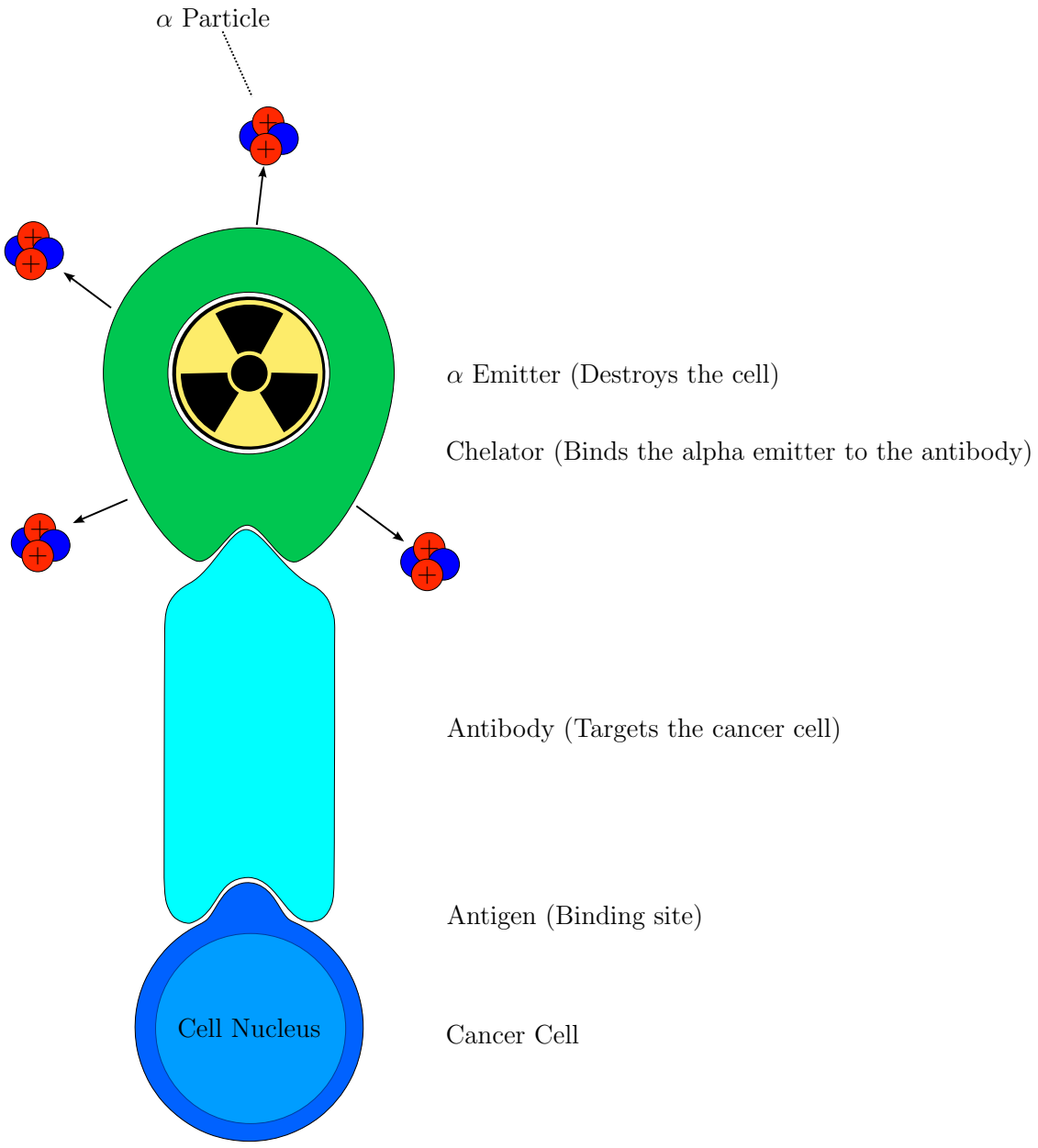

FIGURE 1.4: The alpha emitter is attached to the antibody by a chelator (binds metallic and organic materials). The antibody then binds to the cancer cell antigen. The short range α particles then damage the cancer cell.

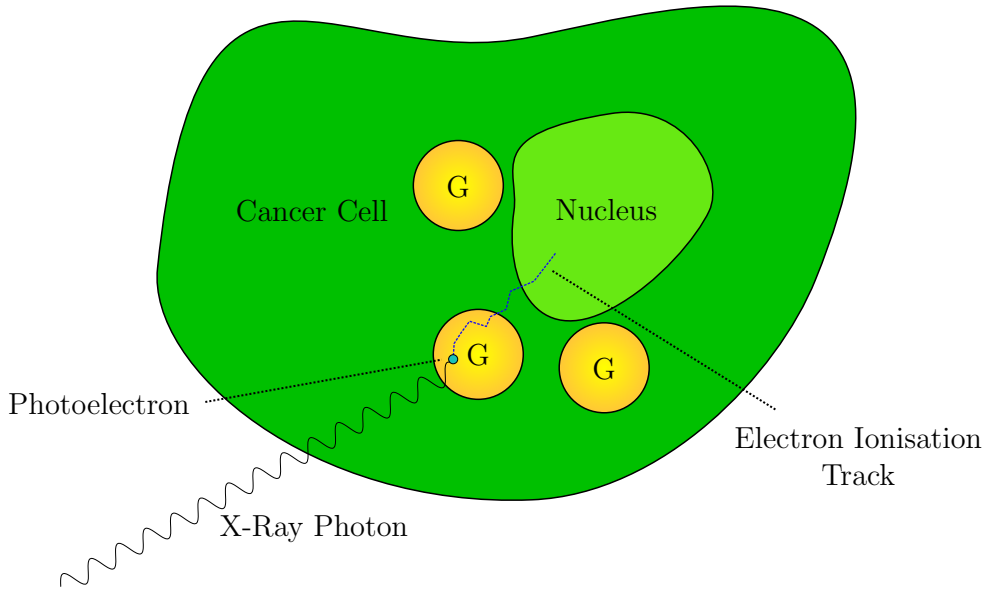

FIGURE 1.5: By introducing gold particles into the cell, the probability of photoelectrons being produced by x-rays is higher, increasing the probability of radiation damage to the cell.

remain at the site of injection for up to 6 weeks. Thereby improving the accuracy as well as effectiveness of radiation treatment [12].

1.3 Direction of Modern Radiotherapy

Newer technologies such as IMRT (intensity modulated radiotherapy), IGRT (image guided radiotherapy), gating and IMAT (intensity modulated arc therapy) have all been developed to increase the precision with which dose is delivered and to maximise the tissue sparing effect. It has been proposed that the hardware and software is quickly approaching the limits of what is possible with x-ray linear accelerators.

The implementation of heavy ion radiotherapy represents a change in direction from hardware/software development and a movement towards utilising alternative physical processes. Undoubtedly, as proton and heavy ion therapy becomes widely adopted, medical cyclotron and synchrotron technology will undergo a similar refinement process to linear accelerators. Another method of improving treatment outcomes is to refine our understanding of the radiobiology of radiotherapy treatments. Ideally, both the cancerous

and healthy cells of a patient should be assayed prior to treatment to provide information such as tumour oxygenation and the tolerance of normal tissue to radiation.

Mathematical radiobiological models have been developed since the mid 1950s [13] in order to understand the underlying physio-biological processes of radiation induced cell death. Analytical models are inherently inaccurate in predicting small scale behaviour in any physical system due to the stochastic nature of particle interactions. The underlying behaviour is typically hidden in the parameters of the model resulting in a lack of robustness.

Computer models have been demonstrated to be an invaluable tool in all areas of scientific research. Monte Carlo simulations have become particularly useful for modelling stochastic systems governed by probability density functions. The large scale behaviour of a physical system is modelled by simulating multiple small scale behaviours. This type of modelling is more accurate than analytical modelling but significantly slower due to the number of interactions that need to be simulated.

There are several computer models currently available for simulating the various radiobiological processes associated with radiotherapy. These models have been specifically designed for modelling processes such as: tumour growth properties, Monte Carlo (MC) particle track structure (e.g. Geant4) and DNA DSB repair. To our knowledge, there is currently no realistic radiobiological model in the literature capable of simulating stochastic radiobiological processes in 3D or 4D. There is a need for a robust stochastic model which unifies all of the essential processes of radiation induced cell death including: tumour growth, irradiation and DNA repair.

1.4 Aims of the Current Work

The aim of the current work was to develop a stochastic radiobiological model capable of simulating all the primary physical, chemical and biological effects associated with radiation induced cell death. The Monte Carlo model consists of three stages:

1. Cell growth.

2. Cell irradiation.

3. Cell repair and death.

This has been achieved using a combination of existing software toolkits and custom algorithms developed in this work.

The first component is a simulation for growing a tumour composed of individual cells of realistic dimensions and elemental composition.

An input code has been developed in this thesis using the MC toolkit Geant4 [14] to enable the simulation of various forms of radiation including x-rays and protons, providing detailed track structure of each particle as it passes through the tumour. The positions of each ionisation and excitation event in the target was extracted. The physical geometry of a typical cancerous growth was used as the target volume so that the positions of the individual ionisation events could be accurately be mapped onto the tumour.

The ionisation damage simulated by Geant4 inside each cell was used to predict the biological damage to the tumour. The model was developed to simulate the repair characteristics of each cell so that the biological outcome could be predicted.

It is believed that the limited correlation between the results of many of the previous models and experimental results is due to the over simplified model for the structure of the cell. A large fraction of the previous models developed to simulate the response of cells to radiation have not modelled the shape or size of the cells themselves thus limiting the various channels of cell death due to radiation exposure. It is believed that different components of the cell are more radiosensitive than others (i.e. nucleus – DNA damages, membrane – electrolyte imbalance). Different methods of cellular apoptosis and necrosis are also possible for different parts of the cells.

These are relevant processes leading to cell death which cannot be modelled by a single pixel representation of a cell. The importance of modelling the individual components of the cell is therefore emphasised. Exotic cell processes such as the radiation induced bystander effect (cell communication) should also be modelled to accurately predict the

probability of cell death. The few input parameters that are required for the simulation will be obtained from experimental results published in the literature. Using this information the resultant damage to the tumour volume will be assessed from a physically fundamental level enabling optimisation of treatment delivery methods for maximal treatment effectiveness.

Whilst performing this research, It is hoped that an understanding of the significance of fundamental radiation cell death processes will be developed and this information can be used to optimise existing and develop new methods of cancer treatment using photon and heavy ion radiation.

1.5 Thesis Outline

Chapter 2 is a review of previous and current mathematical and computational radiobiological models with an emphasis on key historical achievements. The major limitations of each model and potential additions for the current model are listed in the conclusion.

Chapter 3 begins with a mathematical description of radiation target theory used to calculate the probability of a cell surviving a given dose of radiation. The mathematical models are the basis for a large number of current published models and the model to be developed in the current work. The chapter continues with a description of the critical radiation physical processes which contribute to radiation induced cell death.

Chapter 4 includes a brief discussion of the Monte Carlo method for simulating stochastic physical processes and the structure of the Geant4 particle tracking toolkit.

Chapter 5 describes the development of the first stage of the new radiobiological model developed in the current work. It describes the development of a mathematical algorithm for growing randomised ellipsoidal cells in a 3D tumour volume and importing the tumour into Geant4.

Chapter 6 demonstrates the application of the radiobiological model to investigate the feasibility of the adjunct radiation therapy called gold nanoparticle therapy. The physical

processes associated with this therapy are modelled and the effects of modifying physical parameters on nanometre scales are investigated. Gold nanoparticles are investigated experimentally in chapter 7 by measuring the internal distribution of gold within EMT6 cells at the Australian Synchrotron Centre.

The outlined radiological model is completed in chapter 8 with the inclusion of a spatial and temporal description of the repair of radiation induced DNA double strand breaks. The functionality of the entire model is tested by comparing predicted biological outcomes to experimental data.

Chapter 9 tests the quality of the physical models used to develop the model in the current work by comparing interaction cross sections used in Geant4 with published data. Geant4 is also compared with the MC software RITRACKS for use in chapter 10.

A preliminary investigation is performed in chapter 10 to study the contribution from indirect (chemical) DNA damage using the MC software RITRACKS.

Chapter 11 concludes the thesis with a summary of the development and the major achievements of the model. The plans for extending the model in the future is discussed.

Chapter 2

A Review of Analytical and Stochastic Radiobiological Models

Mathematical and computational models have been used since the early 1960s in an attempt to understand the complex biophysical processes associated with radiation induced cell death [13, 15–22]. Mathematical models have always formed the basis of radiobiological computational simulations. This chapter will review the radiobiological models most relevant to the current work.

2.1 Analytical Models

Analytical models consist of one or more mathematical equations relating the properties of a system to other variables in the same system.

Chadwick first presented a mathematical formula which accurately fit experimental data of cell survival as a function of absorbed dose [15]. This model was derived from the concepts of radiation target theory for cell lines developed and investigated by Lea in 1956 [13]. The primary assumptions of the model are [15]:

1. The ability of a cell to reproduce is determined by the integrity of the DNA double helix.

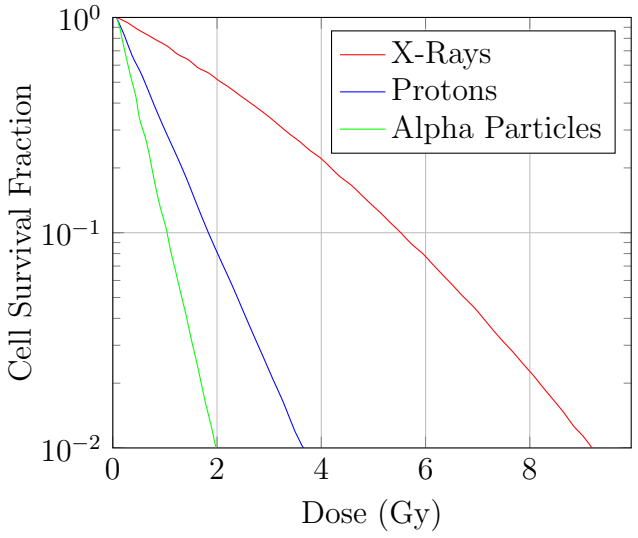

FIGURE 2.1: Cell survival curve showing the relative biological effectiveness of x-rays, protons and alpha particles.

2. Loss of integrity of the DNA double helix occurs through radiation induced ionisation events on one or both sides of the helix. These ionisation events cause molecular bond breaks in the DNA strands.

3. The repair of DNA is assumed to occur through physical recombination, chemical restitution and biochemical enzymatic repair processes.

Chadwick's was the first model to consolidate the then current theories of macroscopic dose deposition and micro/nanoscopic damages caused by ionising radiation leading to physical and biochemical changes in the cell. In [15], the first instance of the familiar linear-quadratic formula was presented:

$$S = e^{-\alpha D - \beta D^2} \tag{2.1}$$

Where S is the cell survival fraction for cells exposed to a dose of ionising radiation D. The α and β parameters represent the linear non-repairable component of the cell survival curve and the repairable component of the cell damage respectively.

This formulation of radiation induced cell death remains the most commonly used in modern radiobiology due to its simplicity and accuracy in predicting cell survival for a

given absorbed dose. For a more detailed description of the LQ model, see chapter 2. An example of the linear quadratic curve for the prediction of cell survival for x-rays, protons and alpha particles is shown in figure 2.1.

In later years, efforts were made to improve upon the linear-quadratic model by developing a more realistic model of the processes of radiation induced DNA damage. Tobias, developed the so called repair-misrepair (RMR) model in 1985 [16]. It was developed to model the physiochemical energy transfer involved in the formation of lesions in mammalian cells and the resultant molecular and biological events [16, 17]. In this model, DNA lesions are assumed to be caused by single electrons or delta rays (i.e. high energy secondary electrons). The kinematics of DNA repair are the foundation for the RMR model. It is assumed that a cell damaged by radiation has the ability to detect and repair this damage using an enzymatic repair process. The ability to repair this damage depends on the availability of the specific repair enzymes. Radiation has the ability to interfere with the repair mechanism (i.e. misrepair) by inactivating repair enzymes or conversely, may trigger the formation of additional enzymes. Radiation damage in a single cell is assumed to be cumulative until all previous lesions have been repaired. This implies that subsequent damage to an already damaged cell reduces its probability of survival. This assumption leads to non-linear cell survival kinematics. The mathematical formalism of this model is a single differential equation representing the time rate of lesion repair using linear self-repair and quadratic misrepair processes.

In 1986, Curtis published the "lethal potentially-lethal model"(LPL) which applied the then current knowledge of radiation induced cell death [18]. It included concepts such as DNA lesions formed by ionisation events, lesion fixation processes, lesion repair and binary misrepair processes. In this model, two different lesion types are considered, lethal and potentially lethal lesions which describe DNA damage of different severity. It was stated that "the parameters of a successful (radiobiological) model should depend on physical, chemical and biological variables in the environment". The LPL model consists of two differential equations (equations 2.2 and 2.3) for the rate of change in the number of lethal and potentially lethal lesions. These differential equations can be solved analytically under several conditions, yielding the survival fraction as a function of total dose and dose

rate. At low doses, the LPL model is reduced to the linear-quadratic model. The LPL model successfully reproduced cell survival data from experimental measurements:

$$\frac{dn_{PL}(t)}{dt} = \eta_{PL}\dot{D} - \epsilon_{PL}\eta_{PL}(t) - \epsilon_{2PL}n_{PL}^2(t) \tag{2.2}$$

$$\frac{dn_{L}(t)}{dt} = \eta_{L}\dot{D} + \epsilon_{2PL}n_{PL}^2(t) \tag{2.3}$$

Where ϵ_{PL} and ϵ_{2PL} are the repair rate of potentially lethal lesions and the interaction rate of potentially lethal lesions respectively. η_{PL} and η_L are the rates of production per unit dose of potentially lethal and lethal lesions for a given dose rate $\dot{D}$.

Ostashevsky [23] published a similar model which related the survival fraction of irradiated cells to unrepaired DNA DSBs. The assumptions of this model are: (a) fragments of DNA produced by DNA DSB have the ability to move out of the parent chromosome and "become lost" with a probability proportional to the size of the DNA fragment and (b) the cell will undergo apoptosis if there are any unrepaired DSB after irradiation. This model was an attempt to link both DSB formation and chromosomal aberrations to cell survival.

The formation of DSB is assumed to be described by a discrete stochastic process with a constant probability of $1/D_{dsb}$ where D_{dsb} is the average dose required to produce 1 DSB per DNA molecule. This leads to a Poisson distribution solution for f_k (f_k is the fraction of DNA molecules with k DSBs).

$$f_k(0) = \exp(-D/D_{dsb})\frac{(D/D_{dsb})^k}{k!} \tag{2.4}$$

The repair of DSB is assumed to occur at a constant rate $\lambda = 1/\tau_{dsb}$ which is independent of the number of DSB k and proportional to the number of available repair molecules. In this model, two repair mechanisms are assumed: cooperative and non-cooperative. The non-cooperative repair mechanism repairs DSB independently of all other DSB on a DNA molecule. Cooperative repair mechanism assumes that DNA molecules with DSBs

already being repaired are more likely to be repaired. This is because the binding of repair enzymes to the DNA molecule is easier if an enzyme is already attached.

The probability that all k DSB will be repaired on a given DNA molecule is:

$$P(x) = \begin{cases} 1 & : k = 0 \\ (1 - e^{-x})^k & : k > 0 \text{ (Non-Cooperative)} \\ (1 - e^{-x}) & : k > 0 \text{ (Cooperative)} \end{cases} \tag{2.5}$$

where:

$$x = t/\tau_{dsb} \tag{2.6}$$

The total number of unrepaired DSB per cell (equation 2.7) at x is the sum of $f_k(x)$ times k.

$$B(x) = Ne^y \sum_{k=1}^{\infty} (y^k/k!)k(1 - \mu + \mu e^{-x}) \tag{2.7}$$

where $\mu = k_1^{-\gamma}$, $k_1 = k+1$ for linear DNA and $k_1 = k$ for circular DNA, γ is an exponent which depends on the polymer characteristic of DNA and N is the number of DNA molecules per cell.

Table 2.1 shows the DNA concentration for various cell lines and the calculated number of DNA molecules in each cell [23]. These values were calculated by dividing the DNA content of the cell line by the molecular weight. The results indicated that there must be several DNA molecules in each chromosome because the number of molecules exceeds the number of chromosomes for the given cell line (46 for human and 22 for V79 Chinese hamster cells).

An assumption used in this model (and many other radiobiological models) is that there is a period of time after irradiation in which the cell can repair the DSBs (defined to be T_{rep} in [23]). If any DSBs remain after this time the cell is assumed to undergo apoptosis.

TABLE 2.1: DNA Content of various cell lines in the G_1 phase. [23].

Cell Line	DNA Content (Da)	# Molecules	DSB Yield/100 eV
NF	3.5×10^{12}	88 - 175	0.074
AT	3.5×10^{12}	88 - 175	0.074
EATC	3.5×10^{12}	88 - 175	0.112
V79	4.8×10^{12}	120 - 240	0.089
LY	4.6×10^{12}	115 - 230	0.089
Yeast	1.8×10^{10}	34	0.065
EC	2.7×10^{9}	1	0.119
T4	1.2×10^{8}	1	0.15

TABLE 2.2: Parameters for different cell lines for the model used described in [23].

Cell Line	τ_{dsb}	D_0 (Gy)	T_m	$T_{rep}(h)$
NF	2.3	4.4	4.79 - 5.30	11.0 - 12.2
AT	2.3	0.6	2.80 - 3.31	12.9 - 14.1
EATC	3	5.0	4.92 - 5.43	14.8 - 16.3
V79	1.5	8.0	5.70 - 6.21	8.6 - 9.3
LY-R	1.5	2.4	4.46 - 4.97	6.7 - 7.5
LY-S	1.5	0.6	3.07 - 3.58	4.6 - 5.4

An elegant equation for the survival probability of a given cell line was obtained with the assumption that the time required to irradiate the cells is much less than T_{rep} (i.e. high dose rate):

$$S = \left[e^{-y} \sum_{k=0}^{\infty} (y^k/k!) \mu^{k_1 - 1} P(T) \right]^N \tag{2.8}$$

where $T = T_{rep}/\tau_{dsb}$

and the equation for low dose rates:

$$S = \left[e^{-y} \sum_{k=0}^{\infty} (y^k/k!)(1 - e^{-T})^k) \right]^N \tag{2.9}$$

The model was demonstrated to be able to accurately reproduce the following experimental data:

- The values for T_{rep} for AT cells and normal fibroblasts.

- ΔT, the delayed plating time.
- The total number of chromosomal aberrations calculated for AT cells.

In 1994, Fertil [20] investigated and compared a selection of radiobiological models including the LQ, LPL, RMR and two models of similar mathematical basis called: the multi-target with initial slope model and the cybernetic model. These models were tested for their ability to accurately reproduce cell survival curves for human cells. The ability of a model to accurately reproduce and fit experimental data was found to depend strongly on the number of free parameters in the model. The LQ and RMR models were demonstrated to reproduce experimental data with the least accuracy of all the models tested. This was the result of using only two free biological parameters. The LQ model was reported to overestimate the effect at low and high doses of radiation. While the other models showed greater agreement with experimental data, the LQ model was commended for its ability to reproduce data using only two biological parameters directly related to the intrinsic radiosensitivity of a specific cell line.

In 2001, Stewart expanded on the LPL and RMR models by developing the "two-lesion kinetic model" (TLK) [21]. It aimed to more accurately model radiation induced cell death by relating cell death to the formation, repair and misrepair of DNA DSBs. The primary cause of radiation induced cell death is widely accepted to be clustered ionisation damage to the nucleus of the cell. In the TLK model, two types of radiation induced DNA damage are considered: simple and complex DSBs. Simple and complex DSBs have their own independent repair characteristics. A simple DSB is assumed to be a section of the DNA that contains a break in each strand of the DNA within a distance of 20 base pairs (bp). A complex DSB is a simple DSB surrounded by additional damages within the same region of DNA. The model uses a pair of differential equations to model the rate of repair of simple and complex DSBs. The model contains biological parameters such as repair rates of DSBs and other parameters that account for the physiochemical fixation of DSB. This model was originally calibrated and tested using data obtained for the survival of Chinese hamster ovary (CHO) cells when exposed to single dose and fractionated doses of radiation. The biological parameters for the TLK model were determined using a

parameter fitting method until the cell survival data produced by the model coincided with the experimental data. This model is the primary focus of chapter 8.

Hawkins developed an analytical model for the description of radiation induced cell killing in 2003 [24]. The model was called the microdosimetric kinetic (MK) model. The purpose of this model was to find a mathematical relationship between the relative biological effectiveness of radiation and the LET of the particle.

In the MK model, the nucleus of a cell is divided into p sub-units each with mass m. When the cells are exposed to a macroscopic quantity of radiation D each sub-unit will receive a random dose z such that the average over all sub-units $\langle z \rangle$ is equal to D. Similarly to [18], two types of lesions are assumed to exist. Type I lesions are assumed to be lethal and irreparable. Type II lesions can undergo four possible reactions including (1) conversion into a lethal lesion, (2) undergo a pairwise combination with another type II lesion and become lethal, (3) it may repair itself or (4) it will persist for a time t_r at which point it becomes lethal.

The important improvement made in [24] was the inclusion of a subdivided nucleus. Instead of the cell being treated as a single volume, the subdivision process enabled the spatial dependence of radiation damage to be accounted for.

2.2 Stochastic Models

Analytical models typically use differential equations to predict the large scale behaviour of a group of cells as a whole whereas stochastic Monte Carlo models attempt to describe the large scale behaviour by simulating small scale interactions of individual cells. In some cases a combination of both methods are used.

Since the early age of computing, models have been developed to simulate cell proliferation with increasing levels of complexity as the technology has become available. One of the earliest attempts to simulate cell death due to radiation damage was performed by Duchting [25]. The simulation modelled a regular array of cells ($40 \times 40 \times 40$ cells) each represented by a single cubic element of the lattice. The biological processes that each cell

could undergo were limited to division and cell phase cycling. Experimental validation was not performed due to the difficulty of performing *in vitro* and *in vivo* experiments at the time.

With computer facilities becoming readily available for public use in the early 1990s large strides were made towards developing an accurate simulation for inter/intra-cellular behaviour. In most cases, each model was capable of simulating limited responses of a single cell line under specific circumstances. With few models available for simulation of radiation track structure and the limitations of computational processing power at the time, models such as those described in Curtis [18] could not be accurately tested.

After the turn of the new millennium, interest in Monte Carlo modelling was increasing, being utilised in almost all areas of science including, astrophysics, high energy theoretical physics and chemistry. As described in chapter 3, Monte Carlo modelling provided medical physicists with the tools to calculate dose distributions in a wide range of materials and geometries. This also enabled physicists to calculate the resultant biological damage (in conjunction with experimental measurements). In [26], the Monte Carlo package "PARTRAC" was used to simulate DNA damage due to both high and low LET radiation. The simulation made several assumptions about the process in which radiation damages DNA including: DNA breakages occurring when ionisation events are within a distance of ten base pairs.

The model allowed several conclusions about heavy ion radiation to be made. It was concluded that exposure to higher LET radiation resulted in more single strand and double strand DNA breaks however correlation between simulated and experimental results was difficult due to the challenges associated with developing suitable microdosimetric detectors.

The Monte Carlo damage simulation (MCDS) software developed by Semenenko [22] in 2004 was the first step to develop a complete biological model of radiation induced cell death caused by ionisation damage to the DNA of the cell. MCDS used four adjustable physical and biological parameters; the number of strand breaks and the number of base damages per Gy of radiation per cell, DNA segment length and the minimum separation between isolated damages to be considered as two separate lesions. MCDS calculates the

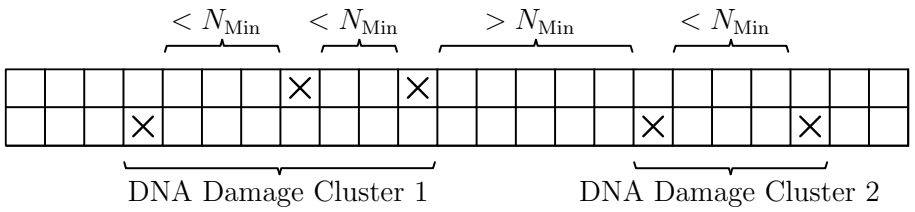

FIGURE 2.2: MCDS Clustering Algorithm - DNA base damages are clustered into double strand breaks if they are located within N_{min} bases of a subsequent base damage.

initial average number of simple and complex DSBs in the cells. This model utilises a 1D clustering algorithm to predict DSB formation in mammalian cells (figure 2.2). MCDS was integrated with the TLK model [22] to simulate the spectrum of DNA damage using Monte Carlo methods and accurately predict the resultant survival data for the cells. Prediction of DNA damage yields in mammalian cells by electrons, protons and alpha particles by the MCDS algorithm were in good agreement with experimental data.

Scholz [27] made significant progress towards integrating biological response of cells into treatment planning for ^{12}C radiotherapy. Microdosimetric treatment planning was used for individual patients in conjunction with existing treatment planning software to optimise treatments. The model was called the Local Effect Model which assumed that the biological effect on the sub volume of a cell nucleus is entirely dependent on the expectation value of energy deposition in that sub volume and is independent of the particular radiation type leading to that energy deposition. Based on this work several recommendations were made for the next generation of cellular models. The most significant of which was the use of mechanistic cell models. In such a model the individual forces on each cell are calculated and cells are no longer localised to discrete points in space. It was also reported that the repair and misrepair of cells are the most important processes in a cellular/radiation model.

Partridge [28] was able to reproduce many extra behavioural characteristics of several types of cells by introducing more interaction processes and developed a new geometry for simulating cells. It was reported that the use of single pixel representations of cells produces computational artefacts in the model. To this end, an alternative geometric representation for cells was utilised. Voronoi polygons were used to model the shape

of the cell. This allowed for a distribution of cell sizes and shapes to more realistically represent the structure of the cell.

In 2009 Incerti [29] modelled a single voxellised cell with a realistic geometrical and chemical description of a human keratinocyte cell. This model focuses on the estimation of delivered dose to the cytoplasm and nucleus using the Monte Carlo toolkit Geant4. This model expands on previous models by utilising realistic chemical compositions and a geometric cell morphology which was based on direct observation by confocal microscopy of real cells. The CENBG microbeam facility was modelled in its entirety enabling single cell irradiation by 3 MeV alpha particles. Every component in the experiment was modelled including beam switching magnets and circular object collimators [29]. The impact of realistic cellular chemical composition on the mean specific energy deposition in the nucleus was investigated. It was reported that while the assumption that the main components of the cell are primarily water for dosimetry purposes is valid, there was evidence to suggest that the mean specific energy deposition in the nucleus was affected by small variations in chemical composition.

Harriss-Phillips [30] developed a temporal Monte Carlo model of tumour growth and the effects of radiation called HYP-RT. This model was developed to simulate the influence of hypoxia in head and neck tumours. The model was capable of simulating the division of up to 10^8 individual cells and the radiobiological effects of each cell including: accelerated re-population and re-oxygenation. The model was designed and calibrated to simulate the biology of epithelial HNSCC tumours. To model the effects of hypoxia, each cell in the distribution is allocated an oxygen concentration.

The results of the model were compared with a modified version of the LQ model which included corrections for accelerated re-population and oxygen enhancement ratio (equation 2.10). The results of the simulation of an oxic tumour in HYP-RT showed good agreement with the modified LQ model:

$$S = \exp(-[\alpha d/q + \beta d^2/q^2 - \ln 2(t - T_k)/T_{pot}]) \tag{2.10}$$

The model was demonstrated to be an efficient tool for studying the effect of accelerated re-population and tumour hypoxia/re-oxygenation and their impact on cell killing during fractionated radiotherapy [30].

While the last four models greatly improved simulation accuracy, all previous works still lacked differentiation between individual cellular components such as nucleus, membrane and cytoplasm. In addition, none of these models simulate the quantities of cells needed to estimate macroscopic quantities such as cell survival fraction and relative biological effectiveness (RBE). Damage in any one of these regions may result in cell death through a variety of different processes which have yet to be modelled for radiation damage.

In recent years, the focus of radiation induced cell death models has moved to micro-dosimetry models as computer hardware improves and new experimental data becomes available.

Several key points can be drawn from the aforementioned papers. In order to accurately simulate the response of cells to radiation damage:

- A combination of stochastic and analytical based modelling approaches should be used when designing a model.
- Accurate spatial distribution of ionisation damage is essential.
- Regular geometries should be avoided to minimise computational artefacts.
- Next generation models should use a mechanistic approach (cellular forces, non-discrete localisation of cells).
- A complex cell structure needs to be modelled.
- Models with physically and biologically meaningful input parameters generate more accurate results.
- Verification of the model with experimentation is needed.

Cell death from radiation damage is a complex biophysical process which to date is not completely understood. Various models have been developed to simulate these processes.

These models have allowed a very specific group of cells and cell processes to be simulated. With each new generation of models, our understanding of radiation based cell death increases. The current theory of radiation induced cell death has been explored but has not been completely implemented into a working Monte Carlo model.

The work presented in this thesis aims to further our understanding of stochastic radiobiological processes by developing a comprehensive stochastic radiobiological model.

Chapter 3

Background Physics and Biology

3.1 Biology of Cancer Treatment

Radiation is classified as either directly ionising (electrons, protons and heavy ions) or indirectly ionising (photons and neutron radiation). In each case, radiation dose is deposited in a material when the primary or secondary particle's energy is absorbed in the medium.

Production of electrons and free radicals in the medium results in the breakage of covalent bonds of the DNA double helix resulting in cell death [31]. In the traditional view of radiotherapy, large enough doses of radiation are prescribed such that the probability that no cells remain (Poisson statistics – equation 3.1) after irradiation (probability of cure) is acceptably high [32].

$$P_N = \frac{a^n e^{-a}}{N!} \tag{3.1}$$

The physical, chemical and biological processes resulting from radiation damage occur on very different time scales. Physical interactions (e.g. ionisation and excitation events) occur on time scales of the order of 10^{-16} seconds. The next stage of radiation damage to occur is the physiochemical stage. When charged ions are produced due to the ionisation of the medium, these ions react chemically with various compounds to produce highly

reactive "free radicals". The production of free radicals results in chemical damage to the cells and occurs on time scales of the order of several seconds. The final stage of radiation damage is due to biological processes which occur between minutes and years after initial irradiation. Such processes include: inability of cell to proliferate, cell death and permanent genetic mutations which are passed onto daughter cells.

It is generally accepted that the primary mechanism of radiation induced cell death occurs when double strand breaks (DSB) are formed in the DNA double helix [21]. Double strand breaks are formed when ionising radiation damages two or more base pairs on opposite sides of the DNA. Photons will liberate secondary electrons through photoelectric and Compton scattering processes which ionise the cell and more importantly, in the cell nucleus where the DNA is located. Electrons will produce a low density ionisation track which will produce more single strand breaks than DSBs. A similar energy proton (high LET) will produce a much dense ionisation track leading to a greater fraction of DNA DSBs. Thus protons and other high LET particles are more biologically damaging than low LET radiation.

These damages are repaired by the cell through various enzymatic repair processes [33], depending on their complexity. Simple base damages are easily repaired because nucleobases in the DNA double helix come in pairs: Adenine with Thymine and Guanine with Cytosine. If the Adenine nucleobase is damaged, the repair enzyme "knows" to replace the missing base pair with the opposite nucleobase to what is present on the opposite side of the DNA double helix.

The complexity of repairing a DNA DSB is much greater and therefore it is much less probable that it will be repaired. Damages on opposite sides of the DNA double helix will cause the DNA to become detached forming two open/broken ends. A different enzymatic process will attempt to re-combine the corresponding open ends of the DNA. If two or more DSBs occur in close proximity, there is a chance that two different breakage ends may recombine in what is referred to as binary (or pair wise) misrepair. In this case, there are several possible outcomes for the cell. Before the mitotic (cell division) phase of the cell, various DNA integrity checks are performed. If the cell detects the defect in the DNA helix caused by binary mis-repair the cell may undergo apoptosis (programmed

cell death). Another possible, although far less likely outcome is that the DNA mutation is duplicated which may lead to undesirable cell behaviour including uncontrolled cell growth leading to radiation induced cancer.

Under certain conditions, the enzymatic repair processes which fix the damaged DNA, may become saturated [34]. Saturation occurs when the number of enzymes available for repair of DNA is exceeded by the total number of DSBs in the cell. In this case, the amount of time required to repair all damages increases and hence the probability of complete repair before the start of the next cell cycle is greatly reduced. This is more likely to occur when high LET particles such as protons and heavy ions irradiate the cells because the density of ionisation events is significantly higher.

While DNA DSB damage is accepted to be the primary channel of radiation induced cell death, there are several other mechanisms in which radiation can inactivate a cell. Other cellular targets include the membrane and cytoplasm [35–38]. A significant dose to the cell membrane may cause the membrane to become more porous allowing foreign molecules and minerals to enter the cell. This may lead to an electrolyte imbalance occurring in the cell. More generally, the radiation may cause the structural integrity of the cell to be weakened to the point where the cell simply disintegrates. The cytoplasm of the cell contains many sub volumes (defined as cell organelles) which may be affected by radiation. One of the cytoplasm's most important functional units is the mitochondria. Mitochondria are the energy production centres of the cell and are responsible for generating the majority of the cells Adenosine Triphosphate (ATP) energy supply. The mitochondria is an independent cellular sub-unit containing its own phospholipids bilayer (similar to cell membrane) and its own DNA [39]. The radiosensitivity of the cell due to the mitochondria is highly dependent on the cell line being irradiated. This is due partly to the fact that the number of mitochondria in a given cell is highly dependent on the cell type. A cell of a given type may contain anywhere from one to several thousand mitochondria and therefore a cell may have better redundancy if its mitochondria are damaged. Irradiation of mitochondria has been shown to produce loss in mitochondrial membrane potential, increased membrane permeability and the release of several proteins leading to apoptosis [40].

There are many other organelles in the cell which can be damaged but their importance in the radiation induced death pathway appear to be less significant than the pathways mentioned previously. The specific physical, chemical and biological mechanisms involved in radiation induced cell death, repair, mutation and communication are still not fully understood.

3.2 Radiation Target Theory

Various mathematical and computational models have been developed over the last several decades in an attempt to quantitatively predict the response of cells to radiation. Many of these models stem from the principles of radiation target theory [13] which postulates the existence of one or more radiation sensitive targets in the cell. The response of a cell to radiation is a stochastic process and the probability that a cell will be damaged is directly proportional to the dose that is received.

The most fundamental version of target theory is the 'single hit, single target' model which assumes that the cell contains a single radiation sensitive target. Cells are assumed to be constantly irradiated for a period of time t. The resultant damage to the cells is governed by Poisson statistics [32].

Let δt be the time interval which is small enough such that only one hit in the sensitive target is recorded. Let k be probability per unit time of the sensitive target being hit. $k\delta t$ is the probability that a target is hit during time δt. Given a large number of cells N_0, the probability p that one cell is hit is $p = \kappa N_0 \delta t$ where $k = \kappa N_0$, κ is the probability of a target being hit and therefore the probability that no targets are hit is $q = 1 - \kappa N_0 \delta t$.

To calculate the survival probability (number of cells which are likely to survive after time t), the probability that there will be zero hits during that time period needs to be calculated. This value is $q^{\frac{\delta t}{T}}$ where $\frac{\delta t}{T}$ represents the number of time intervals and T is the irradiation time.

If the limit is taken as the number of time intervals approaches infinity:

$$P(0) = \lim_{s\to\infty} q^s \tag{3.2}$$

$$P(0) = \lim_{s\to\infty} \left(1 - \frac{\lambda}{s}\right)^s = e^{-\lambda} \tag{3.3}$$

$$\text{where } \lambda = \kappa N_0 T$$

A more detailed analysis and derivation can be performed for the case when each base in the DNA of a cell is considered the target. In this case we have the 'single hit, multiple target' theory. In this theory, one hit to the target will still damage the target but multiple hits are needed for the cell to be damaged.

Suppose that there are n biological targets inside the cell which can be hit by radiation. The probability that one cell will be hit is $1 - e^{-\lambda}$. The probability that n targets will be hit is therefore $(1 - e^{-\lambda})^n$. The probability that the cell will survive is therefore $1 - (1 - e^{-\lambda})^n$ which can be expressed as [41]:

$$S = 1 - (1 - e^{-D/D_0})^n \tag{3.4}$$

3.2.1 Linear Quadratic Model

The linear quadratic model was first introduced by Douglass and Fowler in the mid-1970s [42] in an attempt to combine "single hit, single target"theory and "double hit, single target theories". This combination can be expressed mathematically by the identity $S = S_1 S_2$ which leads to the equation:

$$S = e^{-\alpha D - \beta D^2} \tag{3.5}$$

where S_1 and S_2 are the survival probabilities predicted by "single hit, single target"theory and "double hit, single target theories"respectively.

This equation can be modified to account for additional parameters. Equation 3.6 is a modification of the LQ model to account for tumour re-population in fractionated radiotherapy. The total dose $D = nd$ is delivered in n fractions of d grays per fraction.

$$S = e^{-n(\alpha d + \beta d^2)} \tag{3.6}$$

Various other correction factors for the LQ model have been proposed (e.g. correction for rapidly proliferating tumours).

This mathematical formalism is still the most commonly used model in radiobiology due to its simplicity and relative accuracy in predicting radiobiological outcomes. However, there is an increasing need for accurate micro/nano scale models of radiation interactions in order to gain a better understanding of the fundamental mechanisms of radiation induced cell death.

3.3 Ionising Radiation Interactions

3.3.1 Photons

For photons with energy in the clinical range (i.e. $\sim$ 10 keV to 25 MeV), there are several important physical processes which take place during interactions with matter. Unlike electrons and other ions, photons do not have charge, and therefore do not steadily lose energy via Coulombic interactions with atomic electrons. Photons therefore have the ability to traverse considerable distances before undergoing an interaction which would lead to the partial or total energy transfer from the photon to the medium. As a result, photons are a highly penetrating form of radiation. The three primary interactions with which photons lose energy (in the range of 10 keV to 25 MeV) are: photoelectric effect, Compton scattering and pair production [3].

3.3.1.1 Bulk Behaviour

Interactions of photons with matter can be considered either in terms of individual interactions or the bulk behaviour of photons in an absorber. For the purposes of radiation shielding and x-ray attenuation calculations, it is convenient to use the bulk behaviour model. The linear attenuation coefficient μ is defined to be the probability of interaction per unit distance travelled in the absorbing medium. It has dimensions of inverse length. The Lambert-Beer law [43, 44] describes the rate of change of the number of photons per unit length through an absorbing medium:

$$\frac{dN}{dx} = -\mu N_0 e^{-\mu x} \tag{3.7}$$

$$N = N_0 e^{-\mu x} \tag{3.8}$$

where N is the number of photons remaining from the primary fluence of the beam, x is the distance from the surface to a point within the absorbing medium and N_0 is the initial number of photons in the beam at the surface of the absorber. The linear attenuation coefficient μ depends on both the photon energy and the material being traversed. The linear attenuation coefficient is the sum of three possible photon interaction coefficients (above 10 keV):

$$\mu = \tau + \sigma + \kappa \tag{3.9}$$

Where τ is the photoelectric effect interaction probability, σ is the Compton scattering interaction probability and κ is the pair production interaction probability [3].

Not all of the energy of the incoming photons that interacts in the material is absorbed. Some of the energy is lost to the absorber due to fluorescence or bremsstrahlung.

A photon interaction will in general, result in the transfer of energy to a short range particle (mostly electrons). The energy transferred to the electron may be absorbed within

the material or leave the region of interest. Each of the energy transfer mechanisms has an energy transfer attenuation coefficient and an energy absorption attenuation coefficient. The coefficients each depend differently on the photon energy and the atomic number of the absorber.

3.3.1.2 Photoelectric Processes

In the photoelectric process, a photon is absorbed by an atomic electron in one of the bound shells of the atom [3]. For photons of sufficient energy, photoelectrons found in the most tightly bound shells (K-shell) are the most probable to be liberated. The photoelectron is liberated with energy given by:

$$E_e = h\nu - E_b \tag{3.10}$$

where E_b is the binding energy of the electron in the atom. Electrons in higher energy states may decay to fill the hole left by the photoelectron. Characteristic x-rays will be produced in such processes. The photoelectric process is the predominant photon interaction at low photon energies (keV range) and in materials with high atomic number. The interaction probability of photoelectric absorption, τ, is approximately proportional to:

$$\tau \propto \frac{Z^n}{(h\nu)^3} \tag{3.11}$$

where n varies with gamma ray energy (approximately 3 to 4) in the energy range of interest.

The strong dependence of photoelectric interaction on the atomic number is useful in both radiation shielding and radiation imaging. Materials with a high atomic number (such as lead) are an effective shield for gamma radiation as there is a very high probability of interaction in the material, thus greatly reducing the primary beam fluence. The strong dependence on the atomic number also results in excellent image contrast between two

materials of different atomic number. The photoelectric interaction is most likely to occur if the energy of the incident photon is approximately equal (must be at least equal to E_b) to the binding energy of the electron with which it interacts.

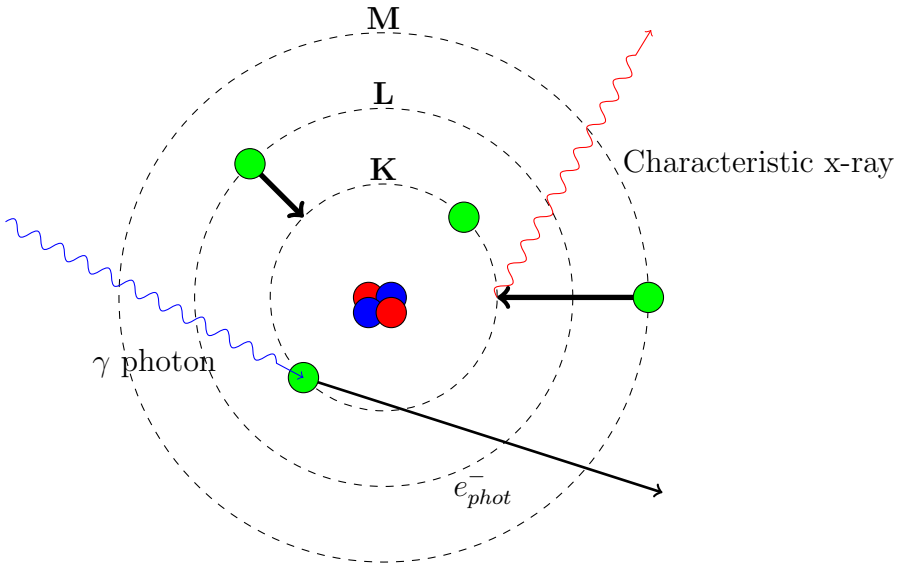

FIGURE 3.1: Photoelectric effect.

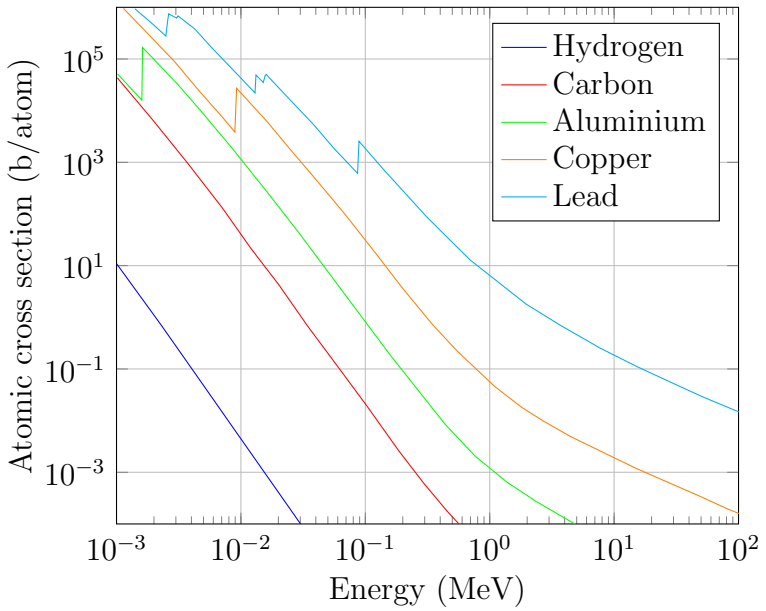

FIGURE 3.2: Photoelectric atomic cross sections for hydrogen, carbon, aluminium, copper and lead.

3.3.1.3 Compton Scattering

Compton scattering is an inelastic scattering process between an incident gamma ray photon and an electron (free or atomically bound). It is the predominant interaction of photons between a few hundred keV and several MeV. It is the dominant interaction in tissue for MeV photon radiotherapy [3].

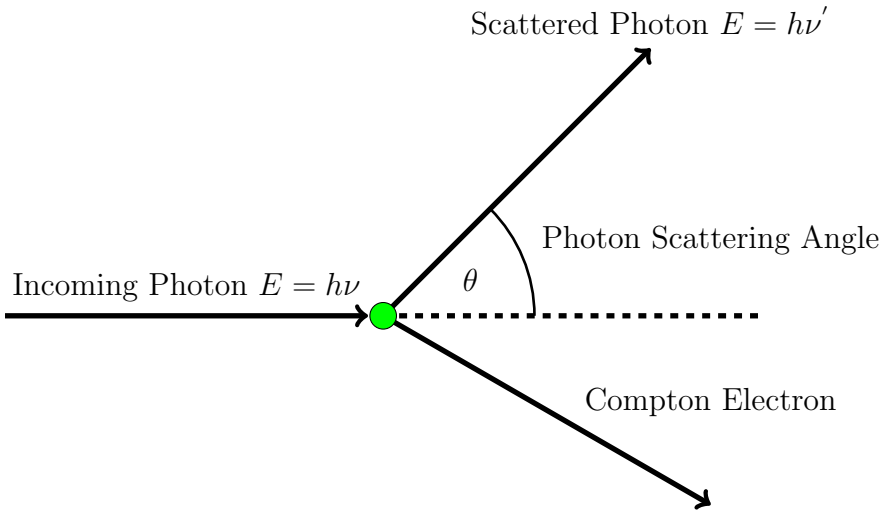

FIGURE 3.3: Compton scattering.

In Compton scattering, the incoming photon is deflected by an angle θ with respect to its incident angle [45]. The photon transfers a proportion of its energy to the target electron which is known as the recoil electron (or Compton electron). The photon will be scattered by an angle and the recoil electron can receive anywhere from zero to a large fraction of the photons initial energy. The Compton scattering interaction probability is given by (σ). The interaction probability is proportional to the ratio of the atomic number of the material to its mass number [46]. σ decreases as the photon energy increases.

The energies of the scattered photon and the Compton electron are given by:

$$h\nu' = h\nu \frac{1}{1 + \alpha(1 - \cos(\theta))} \tag{3.12}$$

$$E_e = h\nu \frac{\alpha(1 - \cos(\theta))}{1 + \alpha(1 - cos(\theta))} \tag{3.13}$$

where α is equal to:

$$\alpha = \frac{h\nu}{m_0 c^2} \tag{3.14}$$

and m_0c^2 is the rest energy of the electron (0.511 MeV) and $h\nu$ is the incoming photon energy.

Maximum energy transfer from the photon to the Compton electron occurs when the photon is scattered straight back ($\theta = 180°$). Under these conditions equation 3.12 and 3.13 simplify to:

$$h\nu'_{min} = h\nu \frac{1}{1+2\alpha} \tag{3.15}$$

$$E_{e\ max} = h\nu \frac{2\alpha}{1+2\alpha} \tag{3.16}$$

The transferred energy is proportional to the incoming photon energy. For example, photons with an initial energy of 5 keV, the maximum energy transferable to a Compton electron is 0.10 keV (2%). For photons with an initial energy of 5 MeV, the maximum energy which can be transferred to the electron is 4.8 MeV (95%). Energy transfer by Compton scattering processes does not become significant until the incident photon energy is in excess of 100 keV.

3.3.1.4 Pair Production

Providing a photon has energy in excess of 1.022 MeV (twice the rest mass of an electron), it may interact by a process called pair production. When a photon passes in close proximity to a nucleus of an atom, it is subjected to strong field effects from the nucleus and may be converted from a photon to an electron and positron pair [47].

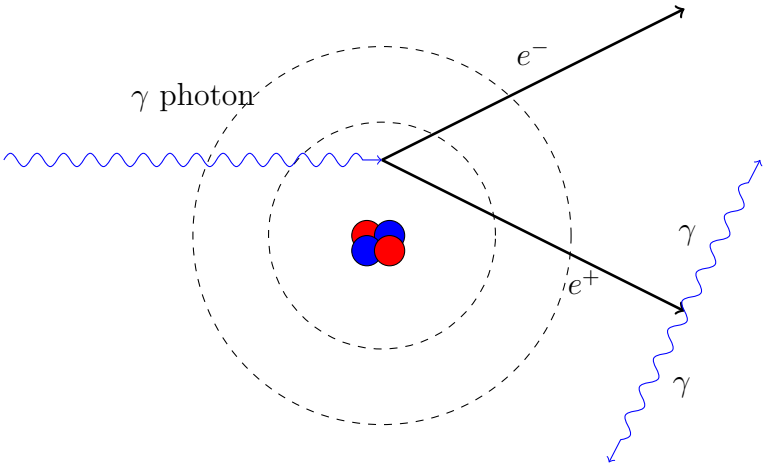

FIGURE 3.4: Pair production.

The kinetic energy of the electron and positron produced will be the difference between the energy of the incoming photon and the total rest mass of the electron and positron (2×511 keV):

$$E_{e^+} + E_{e^-} = h\nu - 2m_e c^2 \tag{3.17}$$

The interaction probability for pair production is denoted κ. The interaction probability increases with increasing photon energy and increases with the atomic number of the interacting materials as Z^2 [3].

3.3.2 Electrons

All forms of ionising radiation eventually result in a distribution of low energy electrons. The interactions of electrons with biological materials are of key importance in radiation biology. The primary difference between the interactions of beta particles (electrons and positrons) and heavy ions arises due to the large difference in mass. Beta particles lose their energy through two mechanisms: collisional and radiative loses.

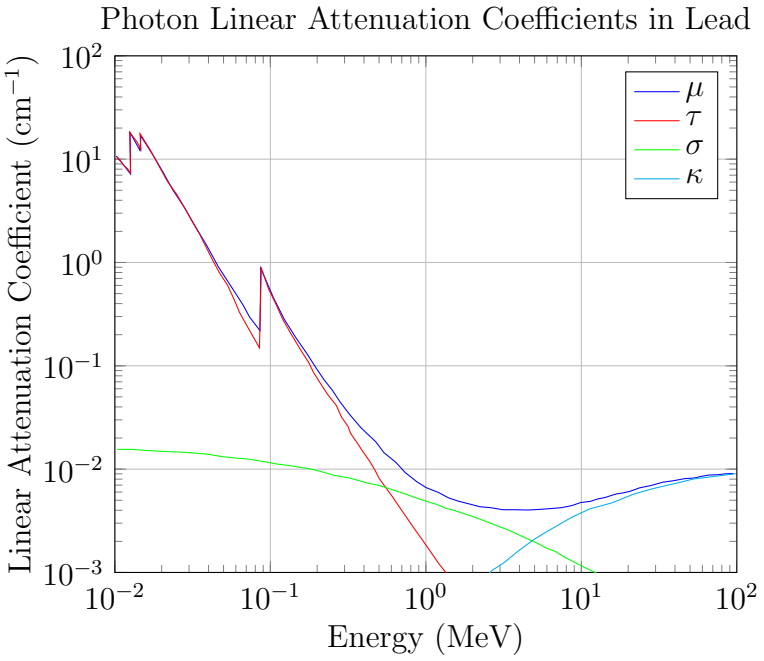

FIGURE 3.5: Photon linear attenuation coefficients in lead - μ - total, τ - photoelectric, σ - Compton scattering, κ - pair production.

3.3.2.1 Collisional Loses

Electrons are able to lose energy via interactions with orbital electrons in the interaction medium. These interactions lead to either excitation or ionisation of nearby atoms. This type of energy loss is called a collisional loss. The classical interpretation of a collision between two massive bodies taking into account momentum and energy conservation states that the maximum energy transfer in a collision is:

$$Q_{max} = \frac{4mME}{(M+m)^2} \tag{3.18}$$

where E is the kinetic energy of the incident particle. In the case of a "head-on" collision between two electrons, $M = m$ and therefore $Q_{max} = E$. Since the projectile (the incident electron) and the target (the orbital electron) have identical mass, the range of possible scattering angles is large. This results in a particle track with a torturous path instead of the more linear path of a heavy charged particle.

3.3.2.2 Radiative Loses - Bremsstrahlung

The second dominant electron interaction in the clinically significant energy range is Bremsstrahlung (braking radiation) radiative process [48]. This process is only significant in the case of electrons compared with protons and heavy ions due to the significant difference in masses. When an energetic electron is in proximity to an atomic nucleus, it is subject to Coulombic forces. The electron is attracted to the nucleus resulting in an change in momentum and energy. To conserve these quantities, electromagnetic radiation is produced. This radiation is called Bremsstrahlung (braking) radiation. For electrons, the Bremsstrahlung photons have a continuous energy distribution with a maximum energy equal to the kinetic energy of the incoming electron. The efficiency of Bremsstrahlung varies with the square of the atomic number of the material in which the particle is propagating.

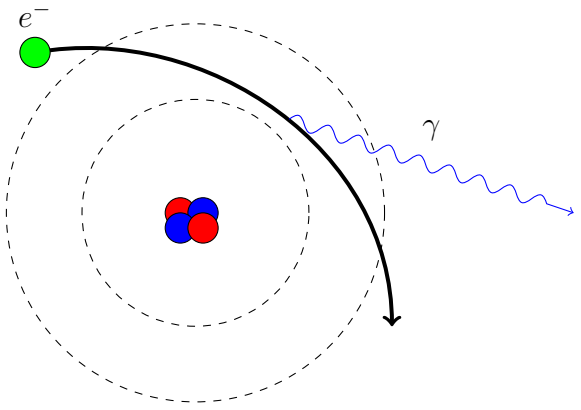

FIGURE 3.6: Bremsstrahlung Radiation.

3.3.2.3 Stopping Power

The stopping power of a charged particle is defined as the linear rate of energy loss due to electronic excitations and ionisations (the rate of energy loss due to collisional interactions). The Bethe formula for the linear rate of energy loss (also known as the linear energy transfer) of a charged particle in matter is:

$$\frac{dE}{dx} = -\frac{4\pi}{m_e c^2}\frac{nz^2}{\beta^2}\left(\frac{e^2}{4\pi\epsilon_0}\right)^2\left[\ln\left(\frac{2m_e c^2\beta^2}{I(1-\beta^2)}\right) - \beta^2\right] \tag{3.19}$$

where:

$$n = \frac{N_A Z \rho}{A} \tag{3.20}$$

Where ρ is the density of the material, Z is the atomic number of the material, N_A is Avogadro's number and A is the atomic weight of the material.

For low energies, the Bethe formula reduces to:

$$\frac{dE}{dx} = -\frac{4\pi n z^2}{m_e v^2}\left(\frac{e^2}{4\pi\epsilon_0}\right)^2\left[\ln\left(\frac{2m_e v^2}{I}\right)\right] \tag{3.21}$$

Where I is the mean ionisation potential for the medium.

The stopping power is therefore proportional to the electron density of the material being traversed and inversely proportional to the particle energy. The total stopping power for light charged particles is equal to the sum of the collisional and radiative stopping powers:

$$\frac{dE}{dx}_{total} = \frac{dE}{dx}_{collisional} + \frac{dE}{dx}_{radiative} \tag{3.22}$$

Collisional energy losses are dominant at low energies and radiative loses are dominant at high energies. The radiation yield Y is defined as the average fraction of a beta particle's energy that is radiated as Bremsstrahlung while approaching thermalisation energies. Radiation yield increases with electron energy and increases with the atomic number of the material.

The radiation yield is given approximately by:

$$Y = \frac{6 \times 10^{-4} ZT}{1 + 6 \times 10^{-4} ZT} \tag{3.23}$$

At very high energies, the dominance of Bremsstrahlung over collisional energy losses gives rise to photon/electron cascade showers. High energy electrons will produce high energy photons through Bremsstrahlung interactions. These photons will then produce Compton

electrons and electron/positron pairs which will then produce additional Bremsstrahlung photons.

3.3.3 Positrons

3.3.3.1 Annihilation

The physical interactions of positrons are virtually identical to that of electrons. The positive charge of the positron compared with the negative charge of an electron results in a deflection which is opposite in direction. The physics of collisional and radiative energy loses is identical for both particles.

One additional process that needs to be considered when discussing positron interactions is positron/electron annihilation [49]. At or near the end of the positron ionisation track (where the energy approaches thermalisation with the medium), the positron and nearby electron can annihilate producing a pair of photons. These photons will have total energy equal to the sum of the rest mass and kinetic energies of the positron and electron.

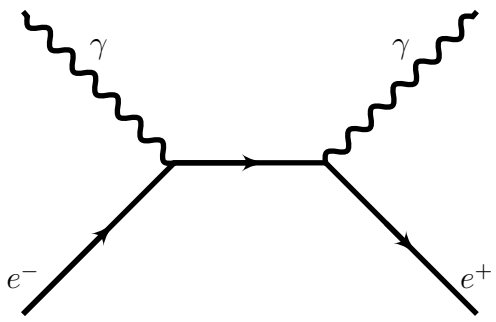

FIGURE 3.7: Feynman diagram of positron annihilation.

3.3.4 Protons and Heavy Ions

Protons, alpha particles and other heavy ions have been determined to be highly suitable for external beam radiotherapy due to the almost ideal dose distribution. As heavy ions propagate through a medium, they lose their energy primarily through the ionisation of nearby atoms [50]. As the ion loses energy, the interaction cross section increases. As a

result the energy deposited at the end of the ion track is significantly higher than at the entrance to the medium. This peak in dose is known as the Bragg peak. The resultant dose distribution of these ions means that a patient's tissue receives a lower dose in the regions of health tissue while the tumour region receives the same or larger dose compared to that delivered by x-rays. This advantage of protons and heavy ions means that patients will have fewer radiation induced side effects during treatment and improved treatment outcomes. [51]

The physics of heavy ion interactions in matter at energies below several GeV are very similar to that of electrons. The primary energy loss mechanism is ionisation and excitation of the medium in which they are propagating. The larger mass of these particles results in reduced scattering angles resulting in a more linear trajectory through the material. The emission rate of bremsstrahlung radiative losses is inversely proportional to the square of the mass of the particle. The energy loss of protons compared to electrons through radiative loses is orders of magnitude less as a result and no longer significant at clinical energies. Heavy ions also have higher atomic numbers than electrons which results in a greater linear energy transfer to the medium (i.e. heavy ions loses energy at a greater rate per unit distance than electrons) and are therefore less penetrating than electrons at the same energy.

For protons and heavy ions to be practical for external beam radiotherapy (sufficiently high penetration in tissue), the kinetic energy needs to be substantially higher than that used for x-rays and electrons (energy required increases with the square of the atomic number of the ion). For example, 150 MeV protons will have an average stopping distance of 15.8 cm. For alpha particles to reach the same depth, the particles require an energy of 600 MeV. For carbon ions, the energy required is 3500 MeV [52].

At these energies, inelastic nuclear interactions contribute significantly to the total dose deposited in tissue [52]. Protons at clinical energies ($\sim$100-200 MeV) have sufficient energy to undergo nuclear interactions with the nuclei in the target material. The protons can liberate a variety of secondary nuclei such as neutrons, deuterons, tritons and secondary protons. The primary proton can transfer a significant proportion of its energy to the secondary nuclei which can also ionise and excite the medium. However, figure 3.8

illustrates that less than 1% of the total dose to the patient being treated with protons is due to the secondary nuclei. The target nuclei are often transmutated into other elements or isotopes, some of which are radioactive. Positron emitting isotopes produced in these reactions can provide a useful method for externally determining dose localisation within a patient using the same technology as PET (positron emission tomography) scanners.

As heavier ions are used in radiotherapy (such as carbon, oxygen), the required kinetic energy increases. As a result the probability of inelastic nuclear interactions increases. Collisions between heavy ions and target nuclei are commonly referred to as nuclear fragmentation. These violent interactions may contribute as much as 17% of the total dose in a patient (figure 3.9). This percentage is as high as 25% for carbon ions if they travel through a higher density material such as bone.

Potentially of greater concern is the high energy neutrons produced in these reactions [52]. For carbon ions with an energy of 3500 MeV propagating through a tissue medium, neutrons are produced with a mean energy of 200 MeV [52]. Since neutrons have no charge, they are a highly penetrating form of radiation. The lack of charge also means that they are not affected by the Coulomb potential in nuclear interactions and therefore readily undergo inelastic nuclear reactions even at low energies. Secondary neutron radiation presents a hazard for the patient being treated, the staff and members of the public. Radiotherapy treatment bunkers must be designed to shield the effects of high energy neutron flux. This is typically achieved using boron shielding due to the high interaction cross section.

The physical interactions of radiation with matter discussed in this chapter are the dominant physical processes in the energy range applicable to x-ray and charged particle radiotherapy. Using Monte Carlo simulations, these interactions were modelled inside a realistic tumour geometry to predict the biological effects of ionising radiation. The methods in which these interactions are implemented computationally are discussed in chapter 3.

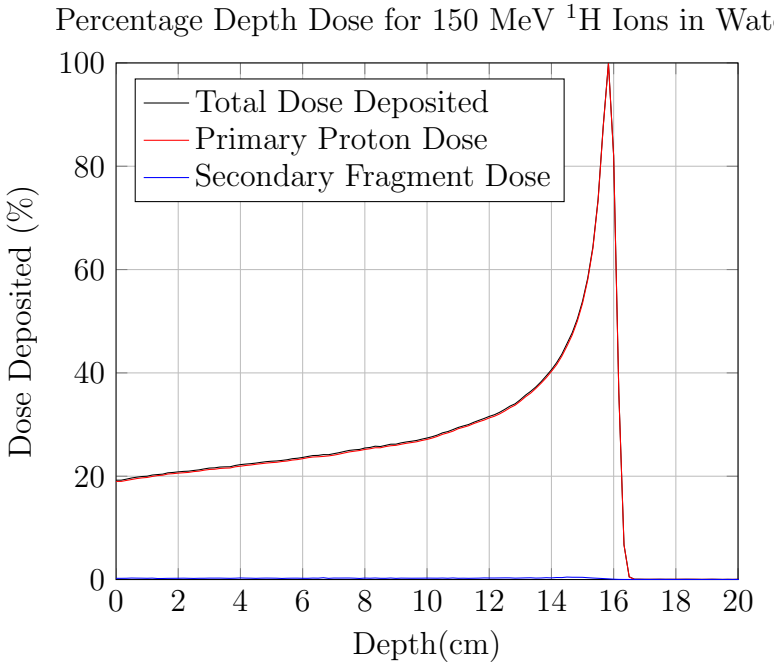

FIGURE 3.8: Dose deposited (Gy) vs depth in water (cm) for a mono-energetic 150 MeV proton ion beam [52].

TABLE 3.1: Summary of Physical Interactions of Ionising Radiation at Clinical Energies.

Photons	Electrons	Positrons	Protons and Heavy Ions
Photoelectric	Ionisation	Ionisation	Ionisation
Compton scattering	Atomic excitation	Atomic excitation	Atomic excitation
Pair production	Bremsstrahlung	Bremsstrahlung	Elastic nuclear
Photonuclear	Columbic scattering	Annihilation	Inelastic nuclear
		Columbic scattering	

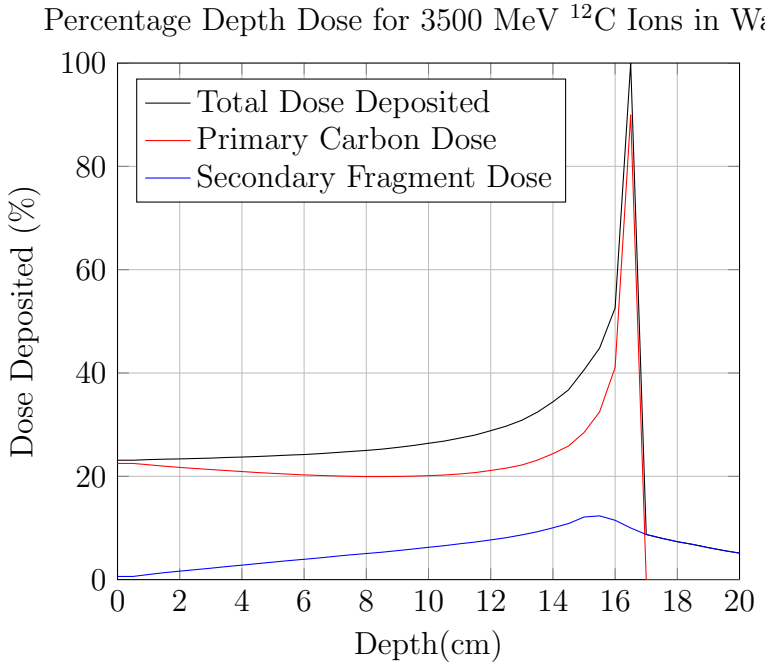

FIGURE 3.9: Dose deposited (Gy) vs depth in water (cm) for a mono-energetic 3500 MeV carbon ion beam [52].

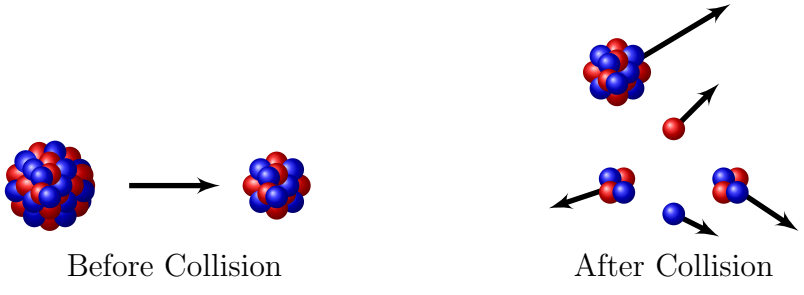

FIGURE 3.10: Ion Fragmentation. Inelastic collision between heavy ion and target nucleus produces various types of secondary fragments.

Chapter 4

Monte Carlo Particle Simulations

Monte Carlo simulations are a type of computer simulation which can model physical, chemical or biological characteristics using a stochastic mathematical method. Unlike other mathematical models such as those which use differential equations (e.g. analytical models), the stochastic nature of Monte Carlo simulations results in a unique solution set each time it is run. The solutions are based on probability density functions (PDFs) calculated at each of a long series of time (or position) increments. As a result of the random nature of the Monte Carlo method, a unique set of values in the simulation are generated each time but still conform to a likely set of outcomes based on the initial PDFs.

4.1 History of Monte Carlo

Computer simulations have been demonstrated to be an effective tool for simulating complex physical, chemical and biological processes. Computer simulations are an accurate and cost effective method of predicting or confirming scientific data. Once a simulation has been correctly calibrated or verified against experimental and/or theoretical data it has the capacity to predict data that would otherwise be difficult or impossible to measure experimentally (e.g. microdosimetric track structure formed by heavy ions on nanometre scales).

One of the earliest examples of a Monte Carlo solution to a practical problem was developed by Laplace in 1886 (based on Buffon's needle problem of 1777 [53]). This method was used to calculate an approximate value for π. This is the simplest example of a Monte Carlo method for solving a mathematical problem. The Buffon-Laplace model can be implemented computationally in the following way.

Consider a circle of radius 1 unit co-located inside a square with side length 2 units centred at (0,0) (figure 4.1). The area of the square is: $A_s = 4$ units^2. The area of the circle is: $A_c = 1$ unit^2. If a point is randomly placed with coordinates (x, y) such that $x \in [-1, 1]$ and $y \in [-1, 1]$, the probability that a point is located inside the circle is:

$$p = \frac{A_c}{A_s} = \frac{\pi}{4} \tag{4.1}$$

If N points are randomly placed within the square, the number of points that will lie inside the circle N_c is:

$$N_c = N \times p = \frac{N\pi}{4} \tag{4.2}$$

$$\Rightarrow \pi = \frac{4N_c}{N} \tag{4.3}$$

Figure 4.2 shows the results of this model when implemented in Matlab™. The figure shows the value of π predicted by the MC model as a function of the total number of points placed in the square. As the number of points increases, the value of π converges on the true value. Figure 4.3 shows the difference (%) between the computed and true value of π as a function of the number of points placed. Each of these curves is described by a power law relationship of the form:

$$\text{Uncertainty in MC Prediction} \propto \frac{1}{\sqrt{N}} \tag{4.4}$$

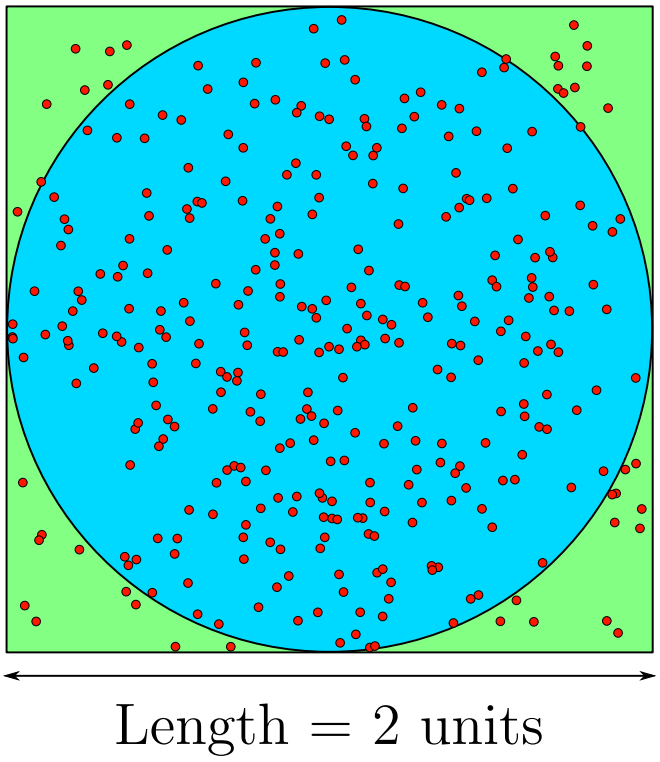

FIGURE 4.1: Monte carlo example - Calculation of π. N_c and N are the number of points in the circle and the total number of points respectively.

Where N is the number of points placed. Hence, the accuracy of the prediction increases with the number of points placed.

The first Monte Carlo computer simulations were performed in the 1940s during the development of the first nuclear weapons. John von Neumann consulted with the American military due to his expertise in mathematical modelling of explosions. Explosions are a difficult process to model analytically. Von Neumann and Stanislaw Ulam developed the first Monte Carlo simulations of the hydrodynamics of nuclear weapons and were the first to coin the term "Monte Carlo".

In 1963, Berger developed the first coupled electron/photon transport code which later became known as ETRAN [54]. ETRAN was designed to simulate the passage of photons and electrons through a plane parallel target of finite thickness in the direction of propagation of the incident particle and unbound in the other two dimensions.

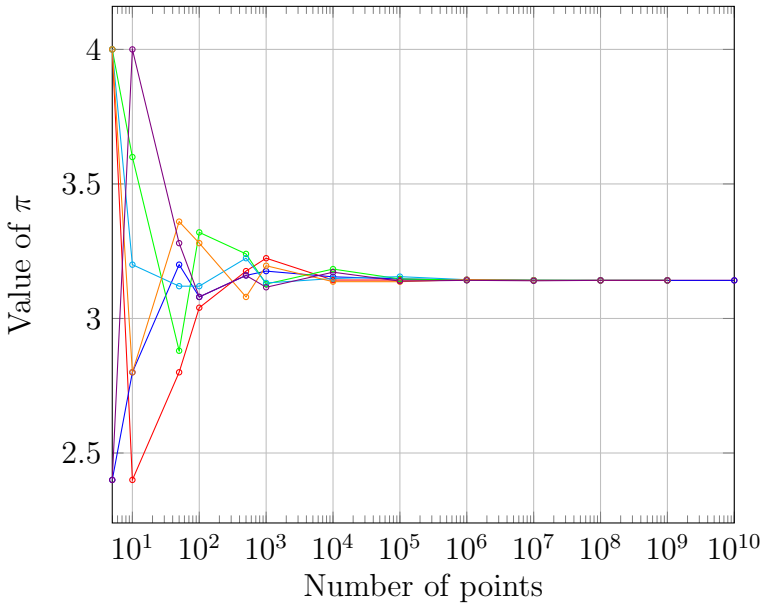

FIGURE 4.2: Monte carlo calculation of π - calculated value vs. number of points.

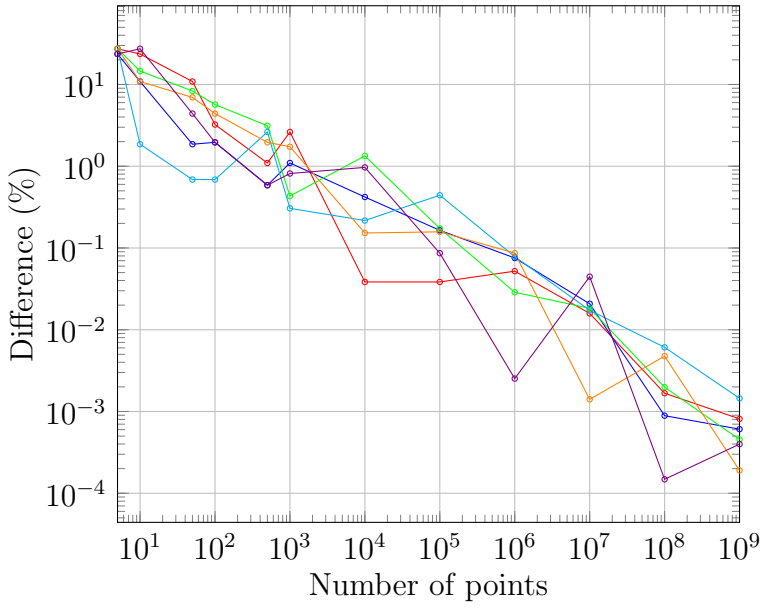

FIGURE 4.3: Difference between the calculated value π and the true value of π as a function of the number of points placed in simulation.

4.2 The Monte Carlo Method

The Monte Carlo method is a stochastic method for numerical integration [55]. If N points $\vec{x_i}$ are randomly generated in the problem space. To determine a quantity of interest $f_i = f(\vec{x_i})$ (e.g. particle flux, dose) the expectation value of f_i is calculated:

$$\langle f \rangle = \frac{1}{N} \sum_{i=1}^{N} f_i \tag{4.5}$$

$$\langle f^2 \rangle = \frac{1}{N} \sum_{i=1}^{N} f_i^2 \tag{4.6}$$

The central limit theorem states that for large N the expectation value of f will approach the true value $\overline{f}$.

The probability of observing $\langle f \rangle$ is given by:

$$p(\langle f \rangle) = \frac{\exp[-(\langle f \rangle - \overline{f})^2 / 2\sigma^2]}{\sqrt{2\pi}\sigma} \tag{4.7}$$

where the standard deviation σ is given by:

$$\sigma^2 = \frac{\langle f^2 \rangle - \langle f \rangle^2}{N - 1} \tag{4.8}$$

In any Monte Carlo (MC) simulation, the outcome is the result of a series of statistical processes. In a MC particle simulation, at any time, the permissible physical processes and relative probability for each to occur is known, either by experimentation or determined from theoretical models. At each iteration in the simulation, a random number generator is used to choose one of the allowed processes for the particle based on each relative probability. This process is repeated many times enabling the entire history of the particle as it moves through the medium to be recorded.

Monte Carlo particle simulations are generally considered the "gold standard" for dose calculations in medical physics due to the high accuracy of the results as confirmed by

experimental data. Such simulations can be used to predict the individual track histories of each primary particle enabling the dose in a patient to be calculated by integrating the energy losses of each particle along their tracks.

Every MC particle tracking simulation requires five components [55]:

1. A Random number generator.
2. A method of sampling random quantities from a probability density function (e.g. the rejection method).
3. A method of storing the histories of each particle and the quantity of interest (e.g. the absorbed dose in the material).
4. A method of describing the geometry in which the particle is propagating (e.g. material and dimensions).
5. A way of calculating the cross sections for every interaction being simulated in the MC simulation. This could be a list of cross section values for interpolation, semi-empirical formulas or theoretical models.

   In Monte Carlo particle tracking simulations there are typically two types of transport algorithms used: photon transport and charged particle transport (i.e. condensed history technique).

4.3 Monte Carlo Particle Transport Simulations

4.3.1 Photon Transport Technique

When a photon of energy E is incident on the surface of a homogeneous medium, the probability of interaction $p(s)$ after propagating a depth s into the medium is (Lambert-Beer law) [56]:

$$p(s)ds = \mu(E)e^{-\mu(E)s}ds \tag{4.9}$$

where $\mu(E)$ is the linear attenuation coefficient for a photon of energy E in the medium in which it is propagating. The mean free path length $\langle s \rangle$ of the photon can be calculated by solving for the expectation value of s:

$$\langle s \rangle = \int_0^\infty s \; p(s) ds = \mu(E) \int_0^\infty s \; e^{-\mu(E)} ds = \frac{1}{\mu(E)} \tag{4.10}$$

The number of mean free path lengths λ before the point of first interaction is defined as:

$$\lambda = \frac{s}{\langle s \rangle} = \mu(E) s \tag{4.11}$$

and therefore (from equation 4.9):

$$p(\lambda) d\lambda = e^{-\lambda} d\lambda \tag{4.12}$$

In Monte Carlo photon transport calculations, the photon tracing formula is:

$$\lambda = \sum_{i=1}^{P} \mu_i(E) s_i \tag{4.13}$$

This formula enables the length of a photon's straight line trajectory to be calculated through a series of heterogeneous media where: i defines the medium in which the photon is propagating (e.g. photon starts in air $i = 1$ and then passes into a water medium $i = 2$), μ_i is the linear attenuation coefficient for medium i and s_i is the path length of the photon in medium i. This algorithm is essential for radiation therapy Monte Carlo simulations [56].

Using equation 4.12, the probability of a photon traversing a distance $\lambda \langle s \rangle$ to the first interaction site can be calculated:

$$P(\lambda) = \int_0^\lambda p(\lambda') d\lambda' = \int_0^\lambda e^{-\lambda'} d\lambda' = 1 - e^{-\lambda} \tag{4.14}$$

The distance to the first point of interaction of the photon can be calculated by sampling the distribution in equation 4.14. Consider a random number ϵ_1 such that $\epsilon_1 \in [0, 1)$ and $P(\lambda) = \epsilon_1$, then from equation 4.14 [56]:

$$\epsilon_1 = 1 - e^{-\lambda_1} \Rightarrow \lambda_1 = -\ln(1 - \epsilon_1) \tag{4.15}$$

The photon is traced a distance $\lambda_1\langle s\rangle$ into the medium where it undergoes an interaction (figure 4.5). In chapter 2, the primary photon interactions in the energy range relevant to radiation therapy were listed as: photoelectric interactions, Compton scattering and pair production. The corresponding linear attenuation coefficients were defined to be:

$$\mu = \tau + \sigma + \kappa \tag{4.16}$$

where μ, τ, σ, κ are the total, photoelectric, Compton and pair production linear attenuation coefficients respectively. At the point of interaction in the medium, the type of photon interaction is sampled such that:

$$\begin{array}{lcl} [P_0, P_1] & : & \text{Photoelectric} \\ [P_1, P_2] & : & \text{Compton} \\ [P_2, P_3] & : & \text{Pair Production} \end{array}$$

where:

$$P_0 = 0,\ P_1 = P_0 + \frac{\tau}{\mu},\ P_2 = P_1 + \frac{\sigma}{\mu},\ P_3 = 1 \tag{4.17}$$

At the point of interaction, properties such as energy and scattering angles of the secondary particles are calculated by sampling corresponding differential cross sections.

The process described above repeats until: (a) the photon energy falls below a predefined value or (b) the photon leaves the region of interest. Throughout the simulation, properties of interest such as energy deposition per voxel are stored to calculate the integral dose in a radiotherapy simulation.

Secondary particles from photons of clinical energies are typically either electrons or positrons. Charged particles are conventionally tracked using a alternative algorithm called the condensed history technique.

4.3.2 Charged Particle Transport

Unlike neutral particles such as photons and neutrons, charged particles (e.g. electrons and protons) undergo a large number of interactions when propagating through a medium. Several MC packages (e.g. Geant4-DNA and RITRACKS) have been designed to simulate every particle interaction on nano-metre scales. Charged particle track structure requires significant processing time due to the large number of interactions. In practice, the processing time is too large to efficiently use this method for dose calculations in radiotherapy simulations.

When propagating through a medium, charged particles undergo two types of interactions: elastic and inelastic. Inelastic interactions (including ionisation and excitation processes) are the cause of radiobiologicaly significant damage to cells. However, some of the interactions are elastic or semielastic scattering processes which result in a change in trajectory. The particle may also experience a change in energy which depends on the total energy (rest mass energy and kinetic) of the particle and the atomic number of the medium of propagation. The changes in angle of the particle's trajectory are typically very small and can therefore be condensed into a single deflection angle. This method of particle transport in MC simulations is called condensed history transport.

The combination of multiple small angle elastic scattering processes for electrons can be simulated by sampling the scattering angle from a distribution calculated using multiple scattering theory. The theory of multiple scattering was developed by Fermi and Eyges [57] in 1948. The theory predicts the condensed scattering angle of an electron after multiple small scattering processes:

$$p(\theta,\varphi)d\theta d\varphi = \frac{\theta}{\pi\theta^2(s)}\exp\left(-\frac{\theta^2}{\overline{\theta^2}(s)}\right)d\theta d\varphi \tag{4.18}$$

where θ is the azimuthal multiple scattering angle, φ is the polar multiple scattering angle and $\overline{\theta^2}(s)$ is the mean square deflection angle after step length s.

Equation 4.18 can be integrated to calculate two separate angular distribution functions [56]:

$$P_\theta(\theta) = 1 - \exp\left(-\frac{\theta^2}{\overline{\theta^2}(s)}\right) \tag{4.19}$$

$$P_\varphi(\varphi) = \frac{\varphi}{2\pi} \tag{4.20}$$

The multiple scattering angles can be sampled using random numbers $\epsilon_\theta \in [0, 1)$ and $\epsilon_\varphi \in [0, 1]$ such that:

$$\theta = \sqrt{-\overline{\theta^2}(s)\ln(1 - \epsilon_\theta)} \tag{4.21}$$

$$\varphi = 2\pi\epsilon_\varphi \tag{4.22}$$

If $\theta > \pi$, θ must be rejected and re-sampled due to the rotational symmetry and $\varphi \in [0, 2\pi]$.

This method enables the continuous angular deflections of charged particles between inelastic interactions to be approximated by a single multiple scattering angle (figure 4.4).

4.4 Interaction Cross Sections

During the simulation of photon transport through a material, the distance between subsequent interactions is determined from the linear attenuation coefficient $\mu(E)$. In general, $\mu(E)$ is tabulated in MC packages for individual elements rather than compounds.

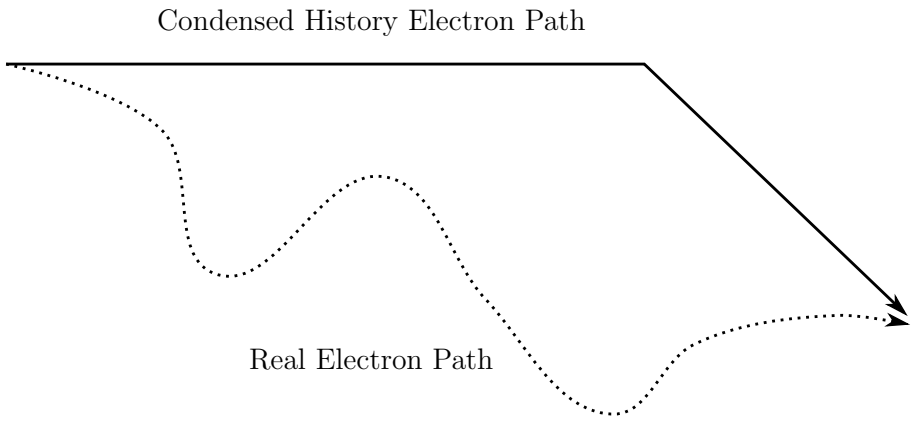

FIGURE 4.4: The path of an electron which undergoes continuous deflection through a medium and the condensed history transport path of a simulated electron.

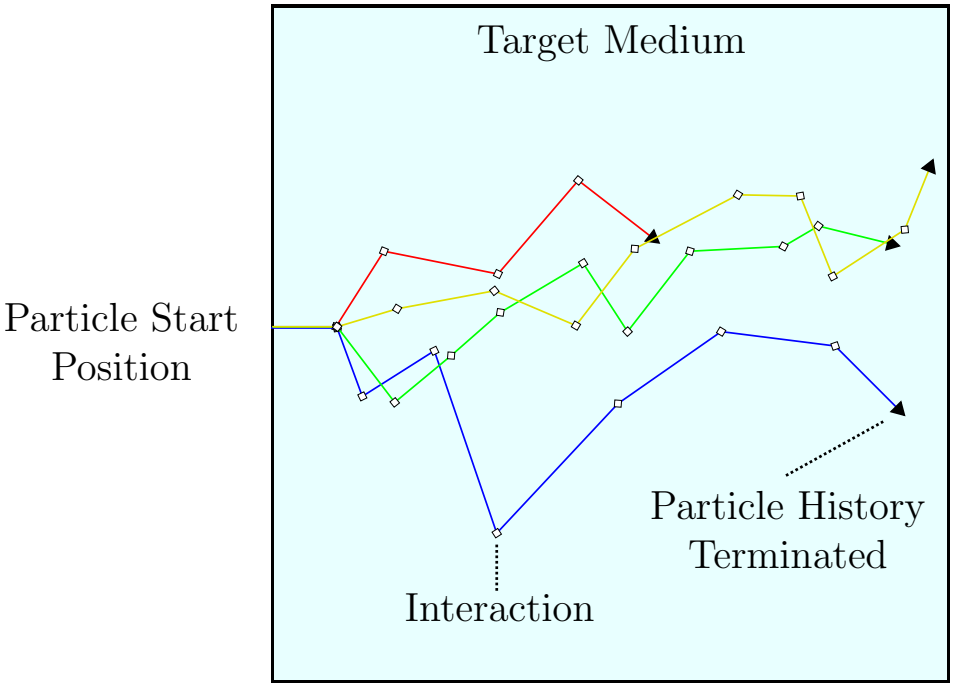

FIGURE 4.5: Example of condensed history particle transport. Vertices of coloured lines represent points where an interaction has occurred. The random number generator results in randomised trajectories for each particle.

In most MC simulations, compounds are needed to specify the geometry of a simulation (e.g. a water phantom). The resultant linear attenuation coefficient for a photon in a compound material is given by [56]:

$$\mu(E) = \sum_i N_i(\vec{r})\mu_i(E) \tag{4.23}$$

where $N_i(\vec{r})$ is the number of atoms of element i per unit volume at $\vec{r}$ and is calculated by:

$$N_i(\vec{r}) = \frac{\rho(\vec{r})N_A w_i(\vec{r})}{M_i(\vec{r})} \tag{4.24}$$

where $\rho(\vec{r})$ is the mass density at $\vec{r}$, $w_i(\vec{r})$ is the mass fraction of element i at point $\vec{r}$ and $M_i(\vec{r})$ is the molar mass of i$^{\text{th}}$ element at point $\vec{r}$ and N_A is the Avogadro constant.

The total linear attenuation coefficient $\mu_i(E)$ is given by:

$$\mu_i(E) = \tau_i(E) + \sigma_i(E) + \kappa_i(E) \tag{4.25}$$

4.5 Geant4 Monte Carlo Particle Tracking Toolkit

Geant4 is a freely available software toolkit for performing "Monte Carlo" simulations of the interactions of energetic particles in matter [14]. Geant is an acronym for "Geometry ANd Tracking". The toolkit was originally developed by CERN for the purpose of simulating the interactions of high energy particles in large accelerators. The first version of Geant was released in 1974 and was written in the scientific computer language FORTRAN. The Geant toolkits (in particular Geant4) have a wide variety of applications ranging from high-energy theoretical physics, nuclear and accelerator physics to medical physics and astrophysics. Collaboration from a diverse group of research areas means that software error fixes and enhancements developed on a regular basis which expands the toolkit further.

From 1994 to 1998, development of the most recent release of Geant known as Geant4 was underway. In this large update, the entire Geant code was translated and re-written from FORTRAN code to the object orientated language C++. In December 1998, Geant4 was released for public use with new releases being published twice a year [14]. This major update to the object orientated language C++ means that parameters within a simulation are treated as real objects with definable parameters enabling the experimental set-up to be configured easily and quickly. Whereas FORTRAN, while being a more familiar language, defines the properties of a simulation from a low level perspective using functions rather than objects (i.e. GEANT3). The advantage of Geant4 over the previous version is the use of objects which have already been defined by the developers of the Geant software, thus minimising the amount of coding required by the user. Geant4 was chosen for use in this project due to the large degree of user customisability and the large number of available physical models including electromagnetic processes with sub-nanometre accuracy and precision, which many other Monte Carlo toolkits do not include (e.g. SRIM which includes only electron ionisation and Rutherford scattering). Geant4 has also been used extensively in the field of medical physics with many tens of papers published each year.

4.5.1 Structure of Geant4

The Geant4 toolkit consists of C++ code structured into classes which can be utilised by the user of the toolkit. These classes are used as the building blocks for the development of a simulated experimental set-up including particle sources, geometry and detectors. At a fundamental level, class files exist which contain the instructions for building "objects"necessary for simulating the transportation of particles.

Geant4 simulations consist of several key processes [14]:

1. Geometry and Materials
2. Particle Interactions
3. Event and Track Management

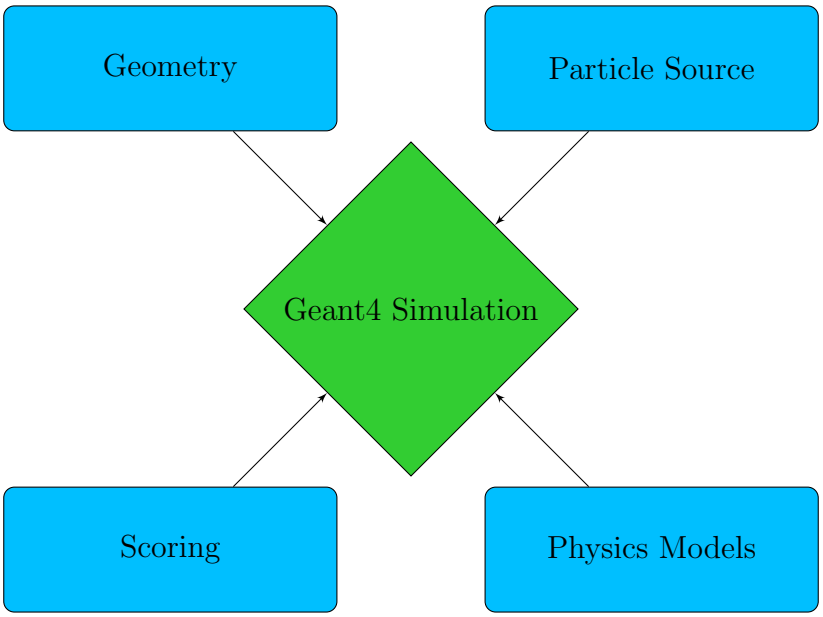

FIGURE 4.6: User defined classes for a Geant4 simulation.

4. Visualisation

5. User Interface.

The user must define four essential classes to perform the most basic of simulations (figure 4.6). These classes are inherited from parent classes in the Geant4 toolkit. The four essential classes are: the geometry (detector construction), the primary particle source (primary generator action),the physical processes (physics list) and a scoring class. The contents of these files form the basis of a functional simulation.

Beginning from a higher-level perspective of the code, the detector construction class consists of the details of the experimental set-up. In this file, information about the laboratory frame (the world volume) and all materials within the lab frame are defined. Objects within the world volume must be defined by position, rotation, size and composition as well as other characteristics including whether or not particles can interact with such a volume. All materials are defined within this class and can be re-used for each object. Materials are defined in terms of elemental composition and physical density. A material may contain a single element, a mixture of elements or a mixture of isotopes.

Materials can be defined by calling them from the default Geant4 materials list (NIST database) which includes a large assortment of elements and compounds. New materials can be created by the user by specifying the elemental composition and other characteristics such as density, molar mass, atomic number and ionisation potentials. These characteristics define how a particular form of radiation will interact with an object.

The primary generator action describes the properties of the primary particle source which will be used for the simulations. These properties include: particle start position, initial energy and particle type (e.g. proton, electron, heavy ions). Geant4 includes two main particle sources that can be utilised by the user. These are the primary generator action and the general particle source (GPS). The GPS system gives greater customisation ability to the user in terms of being able to define a greater number of particle properties including energy spectra, angular distribution and custom particle types.

Arguably the most important component of any Geant simulation is the Physics List. This class is written by the user and inherits the properties of the Geant4 toolkit. In this file, details about the allowed physical processes and particle types are defined. The first section of this file gives details about the particles which are to be used in the simulation. For example; a category of allowed particles may include a section for leptons, which may in turn only include electrons. This tells the simulation that only electrons should be included in the simulation and no other leptons should ever be created or tracked. Once the list of allowed particle types is defined, the physical processes associated with each of the particle types must be defined. A large selection of modular physics lists are available with the toolkit which have been tested and verified against experimental data. These physics list can simply be called by the users application saving a significant amount of time and effort. Physics list are available for many applications and cover a wide range of particle energies.

This physics list also includes details about the cut-off energies of the particles. In Monte Carlo simulations a particle cannot be tracked indefinitely as it progresses through a material. Such a simulation would take large amounts of time and in most cases has an insignificant effect on the final results. To save processing time, the user may define an energy cut-off (actually a minimum distance or time of flight), which prevents a secondary

particle from being created below this energy. When a secondary particle would be created with an energy below this cut-off value, the energy is instead deposited locally. This value must be chosen carefully as it may strongly influence the final dose distribution if the energy cut-off value is set too high.

In most cases, these few classes will not be sufficient to perform a suitable physics simulation. Additional features must be included such as; the ability to make measurements of the energy deposited within a particular material and the ability to visualise the simulation.

4.6 Conclusions

The development and availability of personal computers has enabled Monte Carlo based simulations to be utilised in a diverse range of mathematical and scientific fields. MC simulations are the method of choice for processes governed by probability density functions or for processes that cannot be predicted analytically.

While MC models have been shown to predict parameters of interest with a high degree of accuracy, the complex repetitive nature of the method results in high computation times compared with other numerical and analytical time models.

The Geant4 MC toolkit is now widely adopted for research and commercial applications around the world in organisations such as CERN and NASA. Geant4 is developed by a worldwide collaboration of scientists and software engineers with the goal of developing and maintaining the Geant4 toolkit. Sharing of experimental data, mathematical models and software throughout the collaboration helps to benefit all users and helps to make new scientific discoveries in the field of particle physics.

Chapter 5

Development of a Randomised 3D Cell Distribution

In this chapter, the development of the first stage of the radiobiological model is described; the tumour growth model. The development of the tumour growth model consists of the following stages:

- A geometric and elemental description of a single cell.
- Growth of a tumour composed of many cells with randomised size, position and rotation.
- Optimisation and testing of the algorithms and code.

5.1 Introduction

The first task was to develop a single cell model in Geant4 with realistic physical shape, appropriate dimensions and a realistic elemental composition. This single cell model must then be replicated to form a macroscopic tumour which can then be irradiated in Geant4.

A single cell geometry was modelled in Geant4 containing the critical structures which would become targets for ionising radiation. An ellipsoid was chosen to represent the

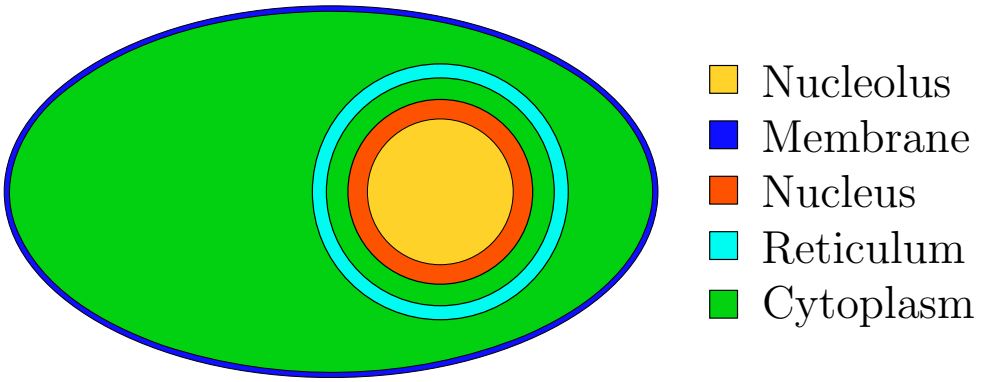

FIGURE 5.1: Single cell geometry.

cellular shape. Contained within the ellipsoid were several critical cell structures: the membrane, cytoplasm, endoplasmic reticulum, nucleus and nucleolus. The dimensions of the cellular constituents were based on the outer major axes of the ellipsoid. Each cell had dimensions ranging from 9 - 13 µm, consistent with average human keratinocyte cells [29]. At the present time, differentiation between cancer cells and non-malignant cells has not been included in the Geant4 cell model.

The cytoplasm was defined to be a concentric ellipsoid such that the outer membrane was 10 nm thick. The nucleus, nucleolus and endoplasmic reticulum were spheres with dimensions, positions and rotations randomised within the cytoplasm (figure 5.1). Mitochondria are also planned to be modelled in future versions of this Geant4 code. Due to the relatively large number of mitochondria in a single cell, their small size and randomised positions it is difficult to model these organelles at the current stage. However, damage to the mitochondria potentially inhibits the production of ATP (Adenosine Triphosphate) in the cell leading to cell death due to insufficient energy making these organelles of interest for future work.

Quasi-realistic chemical compositions were then added to each of the cellular components. The chemical compositions were obtained from [29] and are shown in table 5.1. The internal structure and dimensions in the model are preliminary and adjustable. The objective of this research was to develop a flexible cell model with the ability to modify and add structures in the future.

TABLE 5.1: The chemical composition and density (g/cm^3) of the cell membrane, nucleus, nucleolus, reticulum and cytoplasm used in the Geant4 Monte Carlo simulations. Data from [29].

Cell Region	Hydrogen	Oxygen	Carbon	Nitrogen	Phosphorus	Density
Membrane	44.4%	22.2%	11.2%	22.2%	$\sim 0\%$	1.1
Cytoplasm	59.0%	24.2%	11.1%	4.0%	1.0%	1.0
Reticulum	44.4%	22.2%	11.2%	22.2%	$\sim 0\%$	1.1
Nucleus	35.4%	15.1%	29.1%	18.9%	1.26%	1.0
Nucleolus	32.3%	12.6%	32.3%	21.1%	1.4%	1.0

TABLE 5.2: The cell component dimensions, shape and location of the cell organelles. All cells are permitted to be rotated by an arbitrary angle (e.g. $\theta, \phi, \psi \in [0, 2\pi)$).

Cell Region	Size (µm)	Position	Shape
Membrane	10^{-2}	Forms Cell Boundry	Hollow Ellipsoid
Cytoplasm	9 - 13	Centered within Membrane	Ellipsoid
Reticulum	6	Centered around Nucleus	Hollow Sphere
Nucleus	3	Centered within Cytoplasm	Sphere
Nucleolus	2	Centered in Nucleus	Sphere

5.2 Macroscopic Tumour Model: Randomisation of Cellular Properties and Placement

To produce a macroscopic tumour in Geant4, a Matlab™ script was written to generate a coordinate system for 10^9 cells with randomised individual cellular parameters of size, shape, rotation and position. The code first randomly places the desired number of cells within a volume of specified size. Each cell is allocated a random size in the range of values specified in table 5.2. The Matlab™ script then checks whether any of the cells overlap. If overlapping cells were detected, one of the intersecting cells was deleted. The result of this code was an output file containing the individual spatial cellular properties mentioned. This file was then used as input to Geant4, where the contents of the cells were populated with organelles with realistic elemental composition. The process is described in more detail below.

Initially, the Matlab™ code generated the geometrical properties of the macroscopic "tumour" by randomising the geometrical properties of 10^9 cells. The code generates a $m \times 9$ matrix where m is the number of cells in the distribution. The nine columns of this matrix

represent: the cartesian position the cell (x, y and z), the size of the ellipsoid representing the cell (a, b and c) and the rotation of the cell (θ, ϕ and ψ). Each of the $m \times 9$ elements were randomised (within the range of allowed values - shown in table 5.2) using a random number generator A general requirement of Geant4 is that geometric volumes cannot overlap. To ensure that no cells were overlapping, the following procedure was followed:

The cell positions were sorted by their coordinate in 1 arbitrary axis and the volume was sub-divided into n equal slices along this axis with a width of 100 µm. Each cell in each slice was compared against every other cell (minus the cells that preceded it). Two cells are defined to be separated if the distance between the centres of the cells is greater than the sum of their largest semi-major axis. If the cell centres are separated by less than this distance then an algorithm is used to determine if these cells overlap. If an overlapping cell is detected, one of the two cells is deleted.

The overlap algorithm is based on the mathematical proof presented in [58]. The algorithm can be used to determine if two quadratic surfaces intersect. This was translated into a Matlab™ script that can be summarised as follows. The equation of an ellipsoid centred at the origin with axis lengths of a, b and c in the x, y and z directions respectively is given by:

$$\frac{1}{a^2}x^2 + \frac{1}{b^2}y^2 + \frac{1}{c^2}z^2 = 1 \tag{5.1}$$

This can be written in matrix form as:

$$XMX^{'} = 0 \tag{5.2}$$

where:

$$M = \begin{bmatrix} \frac{1}{a^2} & 0 & 0 & 0 \\ 0 & \frac{1}{b^2} & 0 & 0 \\ 0 & 0 & \frac{1}{c^2} & 0 \\ 0 & 0 & 0 & -1 \end{bmatrix} \tag{5.3}$$

and:

$$X = [x\ y\ z\ 1] \tag{5.4}$$

Rotations about the x, y and z axes by angles α , β and γ respectively are then performed with the following matrices:

$$R_x = \begin{bmatrix} 1 & 0 & 0 & 0 \\ 0 & \cos\alpha & -\sin\alpha & 0 \\ 0 & \sin\alpha & \cos\alpha & 0 \\ 0 & 0 & 0 & 1 \end{bmatrix} \tag{5.5}$$

$$R_y = \begin{bmatrix} \cos\beta & 0 & \sin\beta & 0 \\ 0 & 1 & 0 & 0 \\ -\sin\beta & 0 & \cos\beta & 0 \\ 0 & 0 & 0 & 1 \end{bmatrix} \tag{5.6}$$

$$R_z = \begin{bmatrix} \cos\gamma & -\sin\gamma & 0 & 0 \\ \sin\gamma & \cos\gamma & 0 & 0 \\ 0 & 0 & 1 & 0 \\ 0 & 0 & 0 & 1 \end{bmatrix} \tag{5.7}$$

The ellipsoid can be translated from the origin with the following matrix.

$$T = \begin{bmatrix} 1 & 0 & 0 & x_0 \\ 0 & 1 & 0 & y_0 \\ 0 & 0 & 1 & z_0 \\ 0 & 0 & 0 & 1 \end{bmatrix} \tag{5.8}$$

By combining all of these transformations, the matrices A and B representing cell 1 and cell 2 with different spatial properties are given by:

$$A = T_1 R_{z_1} R_{y_1} R_{x_1} M_1 R'_{x_1} R'_{y_1} R'_{z_1} T'_1 \tag{5.9}$$

$$B = T_2 R_{z_2} R_{y_2} R_{x_2} M_2 R'_{x_2} R'_{y_2} R'_{z_2} T'_2 \tag{5.10}$$

Note the order in which the translation and rotation matrices are applied. The ellipsoid of specified dimensions is first rotated at the origin and then translated.

Incorporating equations 5.9 and 5.10 into 5.2, we have

$$XAX' = 0 \tag{5.11}$$

$$XBX' = 0 \tag{5.12}$$

We wish to solve equations 5.11 and 5.12 simultaneously to determine if an overlap of the quadratic surfaces exist. To achieve this, we apply a scalar constant λ to equation 5.11 without loss of generality since $XAX' = 0$ then $\lambda XAX' = 0$ must also equal zero.

$$X\lambda AX' = 0 \tag{5.13}$$

Subtracting equation 5.12 from 5.13, we obtain:

$$X(\lambda A - B)X' = 0 \tag{5.14}$$

$$XA(\lambda - A^{-1}B)X^{'} = 0 \tag{5.15}$$

This equation is then solved for the eigenvalues (λ_1 ,λ_2 ,λ_3 and λ_4) and eigenvectors of $A^{-1}B$ through calculation of the determinant:

$$det(\lambda - A^{-1}B) = 0 \tag{5.16}$$

It was reported by [58] that eigenvectors which contain a zero in their last component are considered non-physical because this formulation has been structured in a four-dimensional space with the last dimension fixed. There are always two eigenvectors with a zero in the fourth element which we treat as non-physical. This leaves two remaining eigenvectors whose corresponding eigenvalues determine the intersection status of the ellipsoids. The ellipsoids are not touching if the two eigenvalues are real and not equal. Ellipsoids are touching if the eigenvalues are real and equal. Ellipsoids are overlapping if the two eigenvalues are complex. The three possibilities are illustrated in figure 5.2. A flow chart summarizing the Matlab™ script is presented in figure 5.3.

5.3 Verification Method

In order to verify the functionality of the primary algorithm, a second independent algorithm was developed to measure the shortest distance between elliptical cells. While this algorithm is mathematically less complex than the eigenvalue approach, this formulation is up to two orders of magnitude computationally slower than the previous approach. To that end, the second algorithm was used in the preliminary stages of the study to ensure that the primary algorithm worked as expected. Equation 5.17 represents the polar form of an ellipsoid displaced from the origin by (x_0, y_0, z_0):

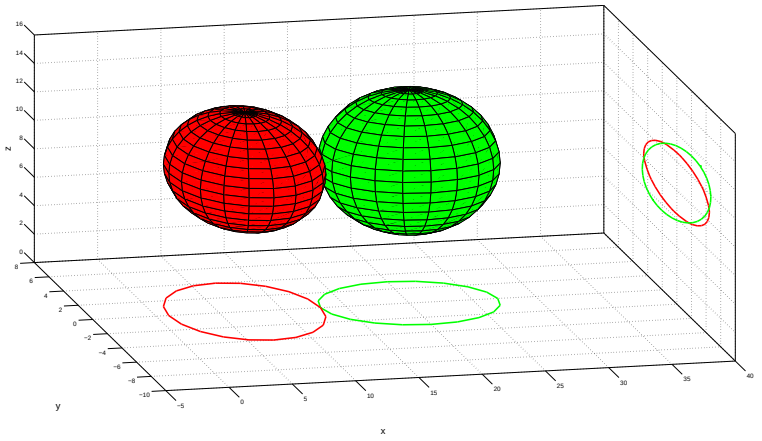

(a) Cells are touching at a single point - two equal real eigenvalues.

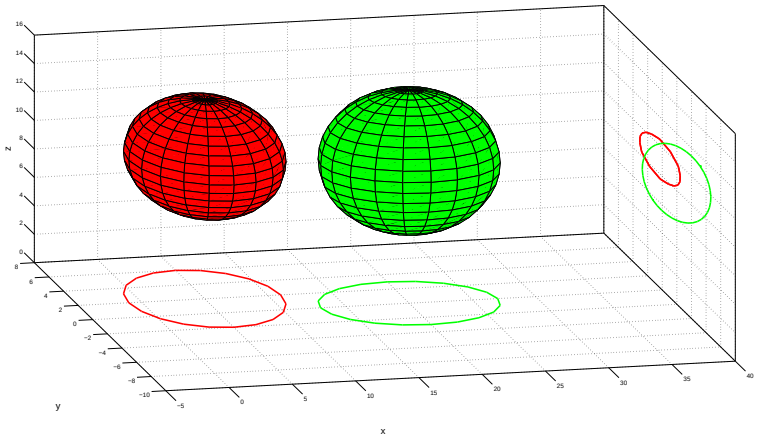

(b) Cells are separated - two distinct real eigenvalues.

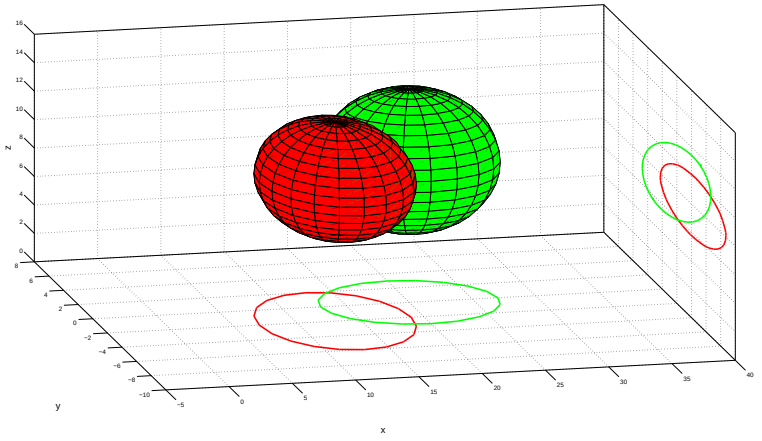

(c) Cells are overlapping - two distinct complex eigenvalues.

FIGURE 5.2: Possible cases for the ellipsoid overlap algorithm.

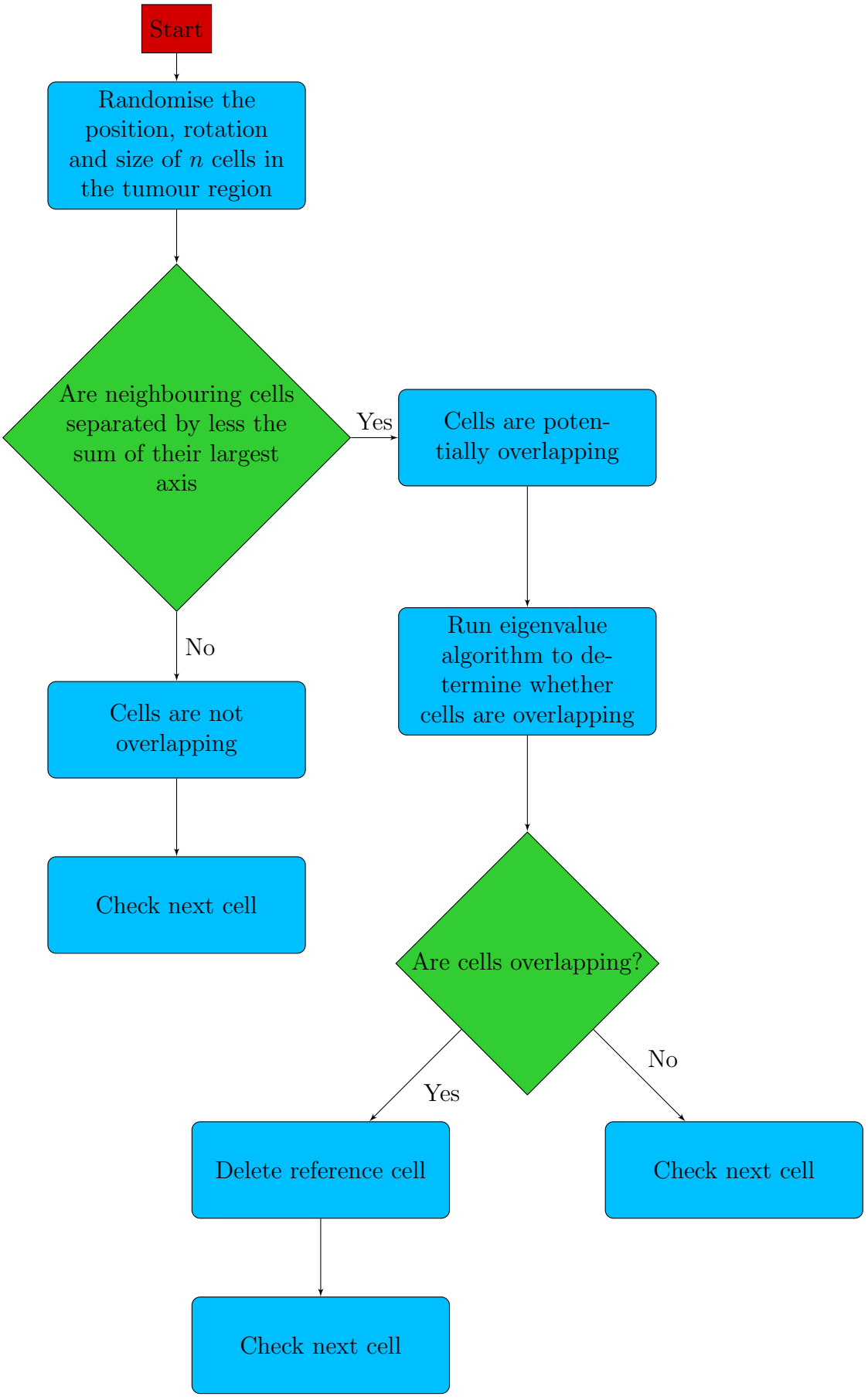

FIGURE 5.3: Flowchart showing the structure of the Matlab™ algorithm used to generate the geometrical properties of the individual cells in a macroscopic tumour.

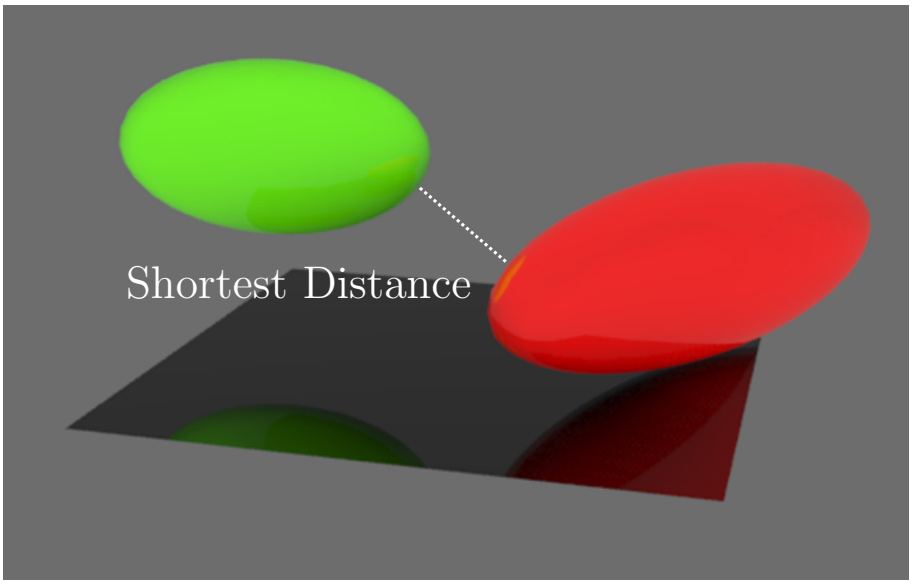

FIGURE 5.4: Cell overlap verification method.

$$\begin{bmatrix} x \\ y \\ z \end{bmatrix} = \begin{bmatrix} x_0 + a\cos\theta\sin\phi \\ y_0 + b\sin\theta\sin\phi \\ z_0 + c\cos\phi \end{bmatrix} \tag{5.17}$$

where a, b and c specify the major axes of the ellipsoid. After applying the three rotation matrices R_x, R_y, R_z to equation 5.17, we obtain an intricate matrix which is not presented in this thesis.

Using this matrix expression, it is possible to specify any point on an ellipsoid of arbitrary size and rotation with only two polar parameters θ and ϕ . Using this mathematical expression, a Matlab™ script was designed to take two inputs (θ and ϕ) and return the Cartesian coordinates x, y and z. Using this function a numerically solvable algorithm was developed to determine the minimum distance between any two random ellipsoids (figure 5.4).

The script was structured as follows. First, an angular interval was specified for searching across the ellipsoid through its two parameters θ and ϕ , such that $\theta \in [0, 2\pi)$ and $\phi \in [0, \pi)$. The smaller the step size, the more accurate the distance calculation, at the expense of processing time. Four matrices were then produced specifying every combination of θ_1, ϕ_1, for cell 1 and θ_2, ϕ_2 for cell 2. Once these matrices were processed through

the function described earlier, Cartesian points $[x_1, y_1, z_1]$ for cell 1 and $[x_2, y_2, z_2]$ for cell 2 were generated. These points were then processed to find the two nearest points. The distance between these two points allows for the determination of overlap. Careful considerations must be made when considering what step size to use in order to produce an accurate result while minimising processing time.

5.4 Importing Cell Coordinate System into Geant4

Once the ellipsoidal cell geometry coordinate system had been produced in Matlab™ the exported file containing the cell geometrical parameters was imported into Geant4. These parameters were used to construct the cell targets with which the simulated radiation beams would interact with. We assume that the thickness of the membrane is 10 nm and therefore once the Matlab output file has specified the properties of the membrane, the cytoplasm was constructed by building an ellipsoid 10 nm smaller in each axis than the membrane (i.e. two congruent ellipsoids). The reticulum, nucleus and nucleolus were of fixed size and were placed randomly within the cytoplasm.

Several difficulties were faced when attempting to parameterise the ellipsoids (replicate geometries). In the current version of Geant4, ellipsoids are not classed as constructed solid geometry (CSG). CSG solids define what geometries can be parameterised and as a result ellipsoids cannot be parameterised in the current version of Geant4. A new class was implemented in the current research called G4Cell. This class contained all the properties of a regular ellipsoid but enabled the geometry to be parameterised. Up until the publication date of this work, no reports of an ellipsoid being parameterised in such a way were found. Since the geometry of the cytoplasm within the cell geometry changes in each cell, the internal structure of the cell also had to be parameterised using the new class. This code is shown in Appendix A.

5.5 Geant4 Physics Models

For the purposes of microscopic simulations, ionisation events and radiation damage must be tracked on scales of less than 10 nm and less than 1 nm for the membrane and nucleus respectively. There are several physics lists available in Geant4 which suit this purpose: the Livermore, Penelope and Geant4-DNA models. These models are low energy models specifically designed for microdosimetric simulations. Each of these models has advantages and disadvantages.

Both the Penelope and Livermore models support photon and electron physics processes which include: photoelectric effect, Compton scattering, pair production and Rayleigh scattering for photons, and ionisation and bremsstrahlung processes for electrons in a variety of materials. The Geant4-DNA model supports electron, proton, alpha particle and several heavy ion physics processes at much lower energies but they are only supported in a liquid water medium. The purpose of this physics list is to study DNA damage only.

The Livermore physics model was chosen for simulation of photon and electron interactions as it provides physical processes on scales suitable for our needs but also supports a variety of organic media needed to accurately specify the composition of each component of the cell. Particles can be tracked to a minimum energy of 250 eV with the Livermore physics model. The Geant4-DNA physics list, which can track particles to lower energies still, may become suitable for our needs when further material cross sections are made available in future updates. [29]. While these physics models simulate the direct radiation effects with great accuracy, the indirect damages due to radiolytic species are not simulated in the current release of Geant4. In many cases (particularly photon irradiation) indirect damages are the most important damage leading to cell death. In chapter 10, the damage due to free radical formation was simulated directly using a second MC package, RITRACKS.

5.6 Model Verification using Geant4 Simulations

For the purposes of model testing we have imported approximately 65,000 cells (with co-ordinates generated by the Matlab™ script) into the Geant4 simulation defining a tumour with dimensions $1 \times 1 \times 1$ mm^3 in a water medium. This volume was chosen due to the time required to perform Geant4 simulations. To simulate a full 1 cm^3 cell volume in the future, we intend to distribute the radiation simulations over many CPU's and combine the results at the end of the simulations to decrease processing time. We used the Geant4 9.5 beta release of the Livermore physics list as a means of testing the cell geometry.

To verify that Geant4 would run without errors using parameterised volumes, a simulation of a monoenergetic 200 keV electron beam traversing a single cell as well as a tumour volume was performed. Analysis of simulation time was performed.

In order to be able to determine the significance of the results obtained, the variance in the number of ionisation events in each of the regions was evaluated. This was achieved by running 5 identical simulations for various quantities of primary 80 keV photons and calculating the standard deviation of the number of ionisation events for each number of primary particles. Based on the data obtained, the number of primary particles was selected that would give an overall statistical uncertainty of 2.5% in most cell regions.

Once the number of primary particles required had been determined, a series of simulations were run to determine the significance of using quasi-realistic chemical compositions in each cellular region compared with that of a simple water medium. Cells were composed of either: (a) a quasi-realistic chemical composition, (b) water of density 1 g/cm^3 or (c) water with the density scaled to match the density of a real organelle (between 1 and 1.1 g/cm^3). 8800 cells were placed in a $0.75 \times 0.75 \times 0.75$ mm^3 box at the centre of a 1.36 mm $\times$ 3 mm $\times$ 3 mm water box. A mono-energetic 80 keV photon source with a square field size 0.76 mm $\times$ 0.76 mm was used to irradiate the cells. The photon source was located 1 mm from the edge of the cells. These geometric properties were chosen to ensure that lateral and transverse electronic equilibrium was achieved. The Livermore physics list with a production cut-off value of 250 eV was used.

5.6.1 Tumour Model and Computational Time Optimisation

Following the overlap detection stage, approximately 200 million cells remained from the initial 10^9 cells in a tumour volume. The geometrical properties of the remaining cells were printed to file, ready to be imported into Geant4, where the interior components of the cells were populated. A distribution of 100,000 cells with diameters between 9 µm and 13 µm can be seen in figure 5.6. The final geometry consisted of approximately 200×10^6 cells which required approximately 15.5 Gb of RAM (∼13,000 cells per Mb).

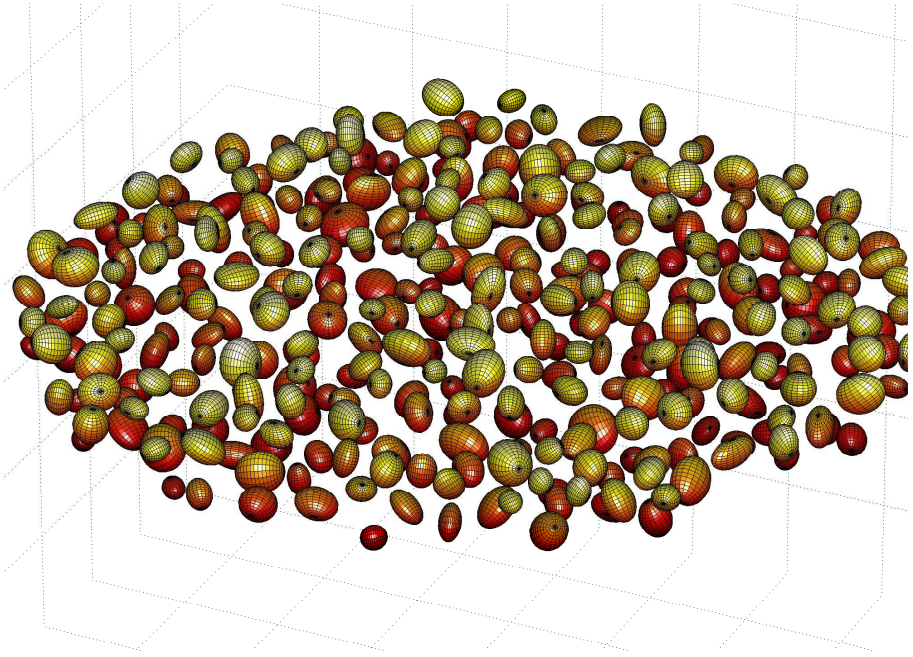

FIGURE 5.5: Enlarged visualisation showing the individual cells in a distribution.

The Matlab™ script described checked each cell against all remaining cells in the 1 cm^3 volume. The processing time with this approach was unreasonably large (>10 years). To reduce computation time, several techniques were employed. The first stage of optimisation involved "slicing" the tumour into multiple sections to reduce the number of checking operations for each cell. Since the processing time in each slice is proportional to the number of cells in each slice, the processing time was exponentially reduced with this technique. An attempt was made to find an optimal number of slices that resulted in an optimal processing time. An optimal solution arises when the time required to check the boundaries of the slices is approximately equal to half the time required to check the cells within each slice. However, it was found that for tumours on the order

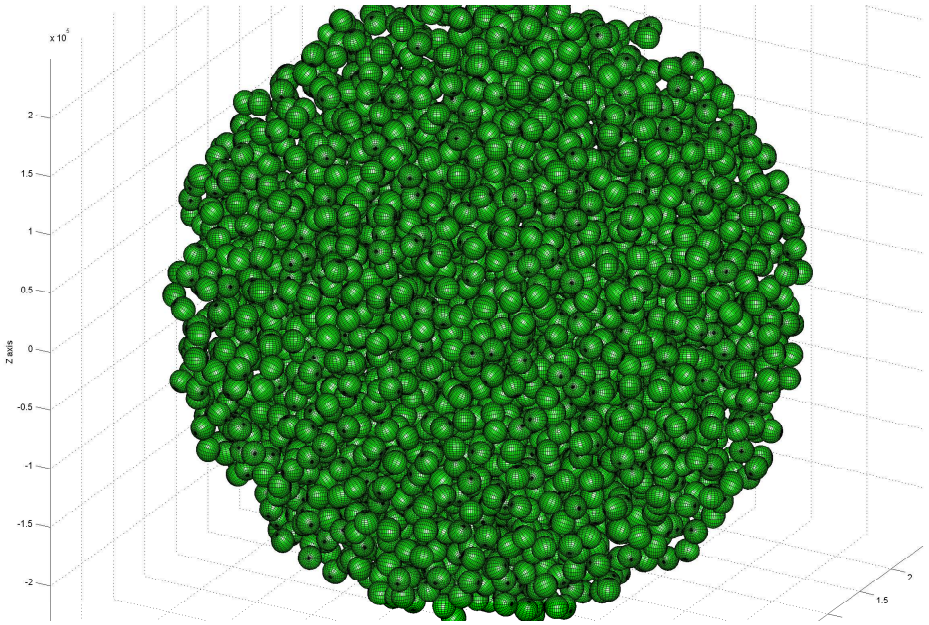

FIGURE 5.6: Tumour distribution containing $> 10^3$ cells.

of 1 cm^3 there appears to be no optimal number of slices to minimise processing time as the number of slices is limited first by the maximum number of slices permitted without producing banding artefacts. Therefore, we limited the slice thickness to no less than 10 times the maximum diameter of a cell within the slice, to avoid such artefacts. For larger tumours on the order of $10 \times 10 \times 10$ cm^3 there may be an optimal number of slices. Such a simulated tumour would require approximately 1.5 Tb to completely express the tumour, which is feasible in terms of storage capacity with current desktop PC's but not processing power. In order to generate larger tumours, a cluster of computers would be required.

The second optimisation process that was performed was the distribution of code onto multiple CPU cores. This enabled multiple cell slices to be processed in parallel. The PC which was used to run these simulations was an Intel i7, 3.3 GHz, 8 threads with 24 Gb RAM. Parallelising the code reduced overall processing time by a factor of six. During the first stage of the code, the program can be run on any number of CPU's as the different slices are independent of each other.

Once overlap checking within a slice has completed, the different slices must be "stitched" together by performing boundary checks for cells at the edge of each slice. This can also

be parallelised to some extent. Different slices can be distributed to multiple CPU cores. The dimensions of each voxel is 0.2 mm $\times$ 0.2 mm $\times$ 1 cm.

The final stage of the code involves stitching the z-slices together into a single file containing the complete tumour distribution. While this stage could also potentially be parallelised, it appears to be more computationally efficient to run this process on a single core.

The final optimisation technique used was the utilisation of NVidia™ graphics processing unit (GPU) CUDA cores for complex matrix operations. It has been demonstrated by NVidia™ that the utilisation of GPU cores for complex matrix operations can increase processing speed by up to 450% . The version of Matlab™ used was 2010b which included the parallel processing toolbox enabling many Matlab™ functions to be executed on NVidia™ GPU cores. The GPU being used for these simulations was an NVidia™ GTS 450 with 120 CUDA cores. The GPU was exclusively used for computing the large matrices associated with ellipsoid contact detection. This resulted in a decrease in total processing time of less than 5%. Since the GPU was used for such a small fraction of the total computation time only a small increase in processing speed was observed. However, Matlab™ 2011a now includes support for "while" and "for" loops to be executed on the GPU which could potentially decrease the processing time of this code by more than a factor of 100. Limited memory is a problem on the GPU, however, for users with an NVidia Tesla series of GPU, this method of optimisation would most likely decrease processing time significantly.

With these optimisation techniques implemented, the in-house developed Matlab™ code was able to grow semi-realistic cell distributions ($\sim 2 \times 10^8$ cells in 1 cm^3) in under 36 hours.

5.7 Results and Discussion

5.7.1 Cell Overlap Independence Verification Check

The second independent cell overlap check described in section 5.3 was performed on several small distributions ($\sim$ 3 mm^3 volume) and the results indicated that there were no overlapping cells. The secondary algorithm reported the smallest distance between all tested cells was 7 nm.

5.7.2 Model Verification using Geant4 Simulations

An example of a monoenergetic 200 keV electron beam interacting with a single cell is shown in figure 5.7. The individual cellular components are also shown. Analysis of simulation time indicates that for a 1 mm^3 tumour containing 63,000 cells with a secondary production cut-off of 250 eV (25 nm electron range) approximately 1.3 seconds per primary particle is required which is consistent with the results published in [29]. Both models use a parameterised geometry, however [29] models the damage to a single cell only whereas the model in this thesis can simulate radiation damage (i.e. ionisation events) in a macroscopic tumour containing many thousands of cells. A secondary range cut of 250 eV was chosen as this is the smallest cut-off which has been verified in the Livermore physics list.

In the second simulation, a mono-energetic 80 keV photon source with a 0.75 mm^2 square field size was used to irradiate the cells. The statistical uncertainty in the total number of ionisation events was calculated as a function of the number of primary particles. The variance decreases as N^{-1} where N is the number of primary particles. It was determined from five simulations that approximately 500,000 primary particles would give an overall statistical uncertainty in the deposited energy of 2.5% in most cell regions (the statistical uncertainty in the membrane was about 16% due to a small size/thickness of the membrane). This number of primary particles was used in the subsequent Geant4 simulations.

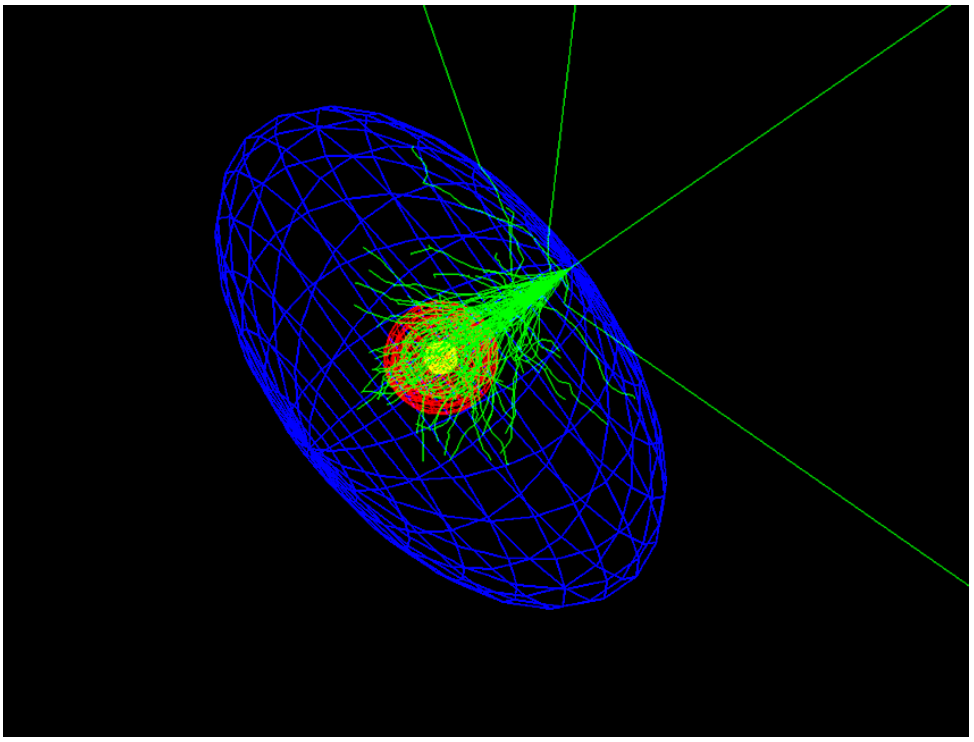

FIGURE 5.7: Enlarged Geant4 visualisation showing the particle trajectories originating from a monoenergetic 200 keV electron source within an individual cell - (green - electron trajectories).

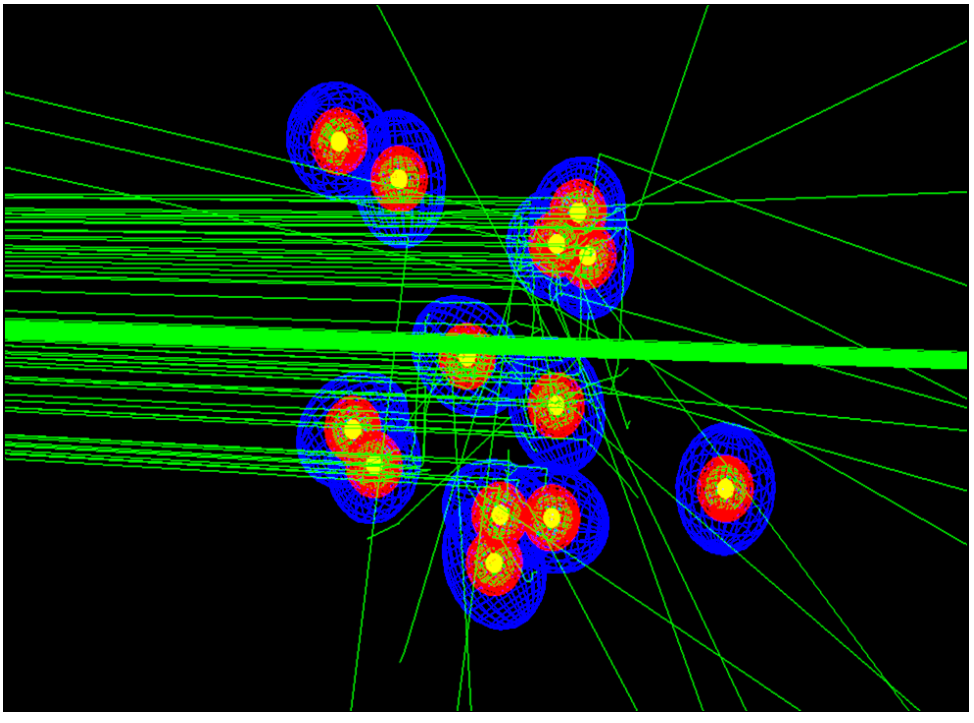

FIGURE 5.8: Interactions of 80 keV with a group of cells.

The results of simulations examining the significance of using quasi-realistic chemical compositions in each cellular region compared with that of a simple water medium are shown in figure 5.9. They show that there is a significant change in the number of ionisation events when realistic chemical materials and densities are used instead of a simple water medium. Using ANOVA analysis, a statistically significant change ($p<0.05$) in the number of ionisation events were observed in the nucleus, nucleolus and endoplasmic reticulum when using realistic materials in comparison with a liquid water medium only. The chemical compositions were obtained from [29] which reported that "they (molecular compositions) are sufficiently accurate to demonstrate the possibility of implementing realistic cellular models in a Monte Carlo simulation application." The current simulation results are summarised in table 5.3. As mentioned before, the statistical uncertainty for the number of ionisation events in the membrane was approximately 16% when using 500,000 primary particles.

The results indicate that the number of ionisation events depend on the cellular region as well as on the composition of this region. As a result, to predict the impact of radiation damage on associated biological processes (e.g. repair and death), the cellular components need to be modelled as realistically as possible.

In addition, it is desirable to reduce the cut-off energies for primary and secondary particles. This requires further development of physics models in Geant4; i.e. implementation of various chemical elements and compounds into the DNA model, or verification of validity of the Livermore model down to 10 eV cut-off energies.

In chapter 8, the ionisation track structure information is used to predict the likelihood of cell death based on ionisation clustering effects in the nucleus.

5.7.3 Re-Design and Optimisation of Cell Growth Model

After using the initial cell growth model for an extended period, it was discovered that this method has several limitations. Firstly, the complex matrix operations required to calculate cell overlap requires a relatively long time. Since these operations are performed

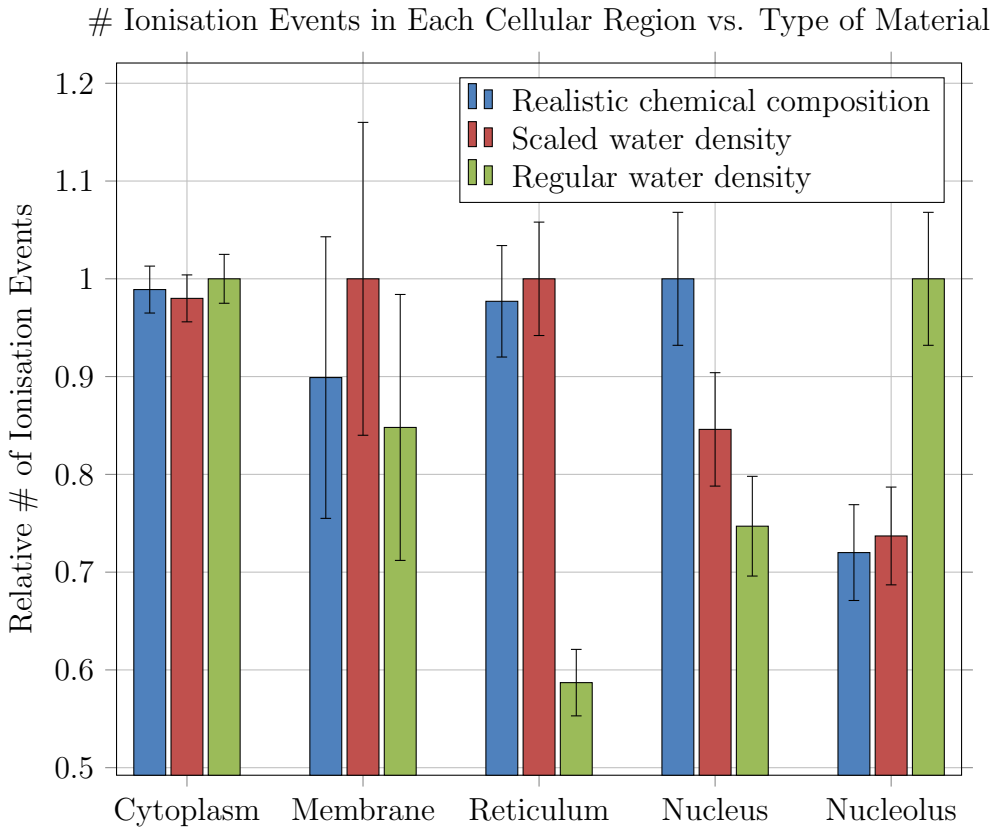

FIGURE 5.9: Relative number of ionisation events when the regions of the cell are composed of a realistic chemical composition (blue), water, but with realistic density (red), water: density = 1 g/cm^3 (green).

TABLE 5.3: The significance of using realistic chemical compositions and densities in each of the cell regions vs. a simple water medium (250 eV energy cut-off). Case 1: realistic chemical compositions, Case 2: scaled density water medium, Case 3: Regular water medium. NS: Not significant, S: significant.

Region of the Cell	Case 1 vs. Case 2	Case 1 vs. Case 3	Case 2 vs. Case 3
Membrane	NS	NS	NS
Cytoplasm	NS	NS	NS
Reticulum	NS	S	S
Nucleus	S	S	NS
Nucleolus	NS	S	S

at least 10^6 times in any given cell growth process, the total time to create a cell distribution with 10^9 cells ($\sim$ 1 cm^3) is computationally impractical. This method also has the inherent problem of deleting a large percentage of the initial cells in the distribution, resulting in a cell density which is less than observed clinically.

A new algorithm was developed to improve both computation time and the density of the cells in the grown tumour. This is an original algorithm developed in the current research (see appendix B for code).

We refer to this new algorithm as the "Marble"method due to its visual resemblance to a Marble. While this method is relatively simple in comparison to the initial cell growth algorithm, it produces a more densely packed cell distribution in much shorter times without the need for computer parallelisation. The new algorithm also has the advantage of mimicking real cell behaviours such as contact inhibition and cell growth which the first method did not. Since the code does not require parallelisation, there is no need for complex amalgamation of results into a single file. As a result, the probability for coding errors leading to inaccurate or faulty output data is substantially reduced.

The new code operates using the following steps. A single sphere is randomly placed within the specified tumour volume and is given a radius that is randomly chosen from a range of values specified for a given cell type. A second sphere of radius r_{min} is randomly placed within the same box. Collision with the first sphere is determined simply by checking if the separation between the two spheres is greater than the sum of their radii. If the second sphere does overlap with the first, the second sphere is deleted. If no collision is detected, the second sphere is allowed to grow in sub-micron increments. At each iteration of the growth stage, collision with the first sphere is calculated. At any time when the first and second spheres come into contact with each other, the second sphere is added to the distribution with the last radius in which the two spheres we not in contact. This property of the algorithm approximates the contact inhibition property of healthy cells which prevent cells from overlapping. A third sphere is placed randomly and is allowed to undergo the iterative growth process following the same set of conditions as stage 2. At each stage of cell growth, the collision with all neighbouring spheres is calculated. Growth is suspended if contact between any two spheres is detected. At

some point where the total volume of the cells in the box is approximately equal to the total volume of the box, spheres will frequently overlap with other spheres even before a growth phase is initiated. If the initial placement of a cell causes a collision, the cell is deleted and another attempt is made to add a cell at another location. This unique condition enables realistic biological cell densities of 10^9 cells per cm^3 to be achieved. At the beginning of the code, the total number of cells to be placed is calculated by dividing the total volume of the box by the minimum volume that a single sphere can occupy.

$$N = \frac{X_{box} Y_{box} Z_{box}}{\frac{4}{3}\pi r_{min}^3} \tag{5.18}$$

This is clearly an overestimate of the total number of cells that can be placed in the distribution of cells. This is a target value to be achieved. When the code cannot place further cells within a certain time limit, the sphere placement ceases. The ellipsoidal cells are formed by placing an ellipsoid within each of the placed spheres. Each ellipsoid is concentrically placed within the sphere with one axis of the same length as the diameter of the sphere. The two remaining axes have length randomised between r_{min} and r_{Sphere}. The ellipsoid is then randomly rotated in all three axes. This placement method ensures that no two ellipsoids overlap, the elliptical cells are randomised in size, position and rotation. Contact detection between two spheres requires substantially less processing time than determining contact between two ellipsoids. The cells are then written to a file using the same method as the previous algorithm. The cells can then be imported by Geant4.

Using this method, the percentage of volume filled in the box by cells increases to approximately 35% compared with 3-5% with the initial algorithm. The new density is consistent with the typical biological cell densities of 10^9 cells per cm^3. The new algorithm achieves much higher cell densities in approximately half the time with same initial target number of cells. For the remainder of this research, the optimised cell growth algorithm was used.

5.8 Conclusion

A fast and efficient algorithm has been developed for producing a randomised cell geometry which is composed of ellipsoidal cells of randomised sizes, positions and rotation angles. This code has been designed, tested and optimised to produce a virtual tumour volume containing up to 10,000 non-overlapping ellipsoidal cells in under an hour. This code has been verified by two distinct algorithms. The output of the Matlab™ code can be exported in many formats and as a result can be utilised in many Monte Carlo packages including Geant4.

This cell distribution has been successfully integrated into the particle tracking toolkit Geant4 where microdosimetric radiation simulations can be performed on the cellular targets. Using the currently available Livermore physics models we have been able to simulate radiation interactions within the tumour volume on scales of the order of 10 nm.

The significance of using realistic chemical materials for cellular components rather than a simple water medium has been investigated. It has been demonstrated that there is a statistically significant ($p<0.05$) change in the number of ionisation events when using realistic molecular compositions and densities in the different regions of the cell compared with using a simple liquid water medium to represent the cell.

The tumour growth model presented in this chapter is the first of a multi-stage radiobiological model. The tumour model developed in this chapter was established to test the functionality of the cell growth and import process only. In the next chapter, a more thorough investigation and development of a Geant4 physics list is described.

Chapter 6

Application of the Geant4 Cell Model – Investigation of the Effect of Gold Nanoparticles

In this chapter we use the code developed in chapter 5 to quantify the radio sensitisation of cells using gold nanoparticles. The effect of gold concentration, position within the cell and photon energy on the magnitude of the radiosensitisation was investigated.

6.1 Introduction to Gold Nanoparticles

The primary objective in radiotherapy is to maximize radiation exposure to the targeted tumour volume while sparing the healthy tissue surrounding it. For treatment delivered using linear accelerators this can be achieved by optimising the dose delivery method (e.g. Intensity modulated radiotherapy (IMRT)) or by increasing the radiosensitivity of the tumour being targeted.

Gold nanoparticles have been a topic of interest in medical research since the early 1950s. It has however only been in the last twenty years that the practical use of GNPs for imaging and radiotherapy has been demonstrated [59–67]. GNPs (figure 6.1 and 6.2) generally have an individual diameter between 1 nm and 1 µm and are suspended in an

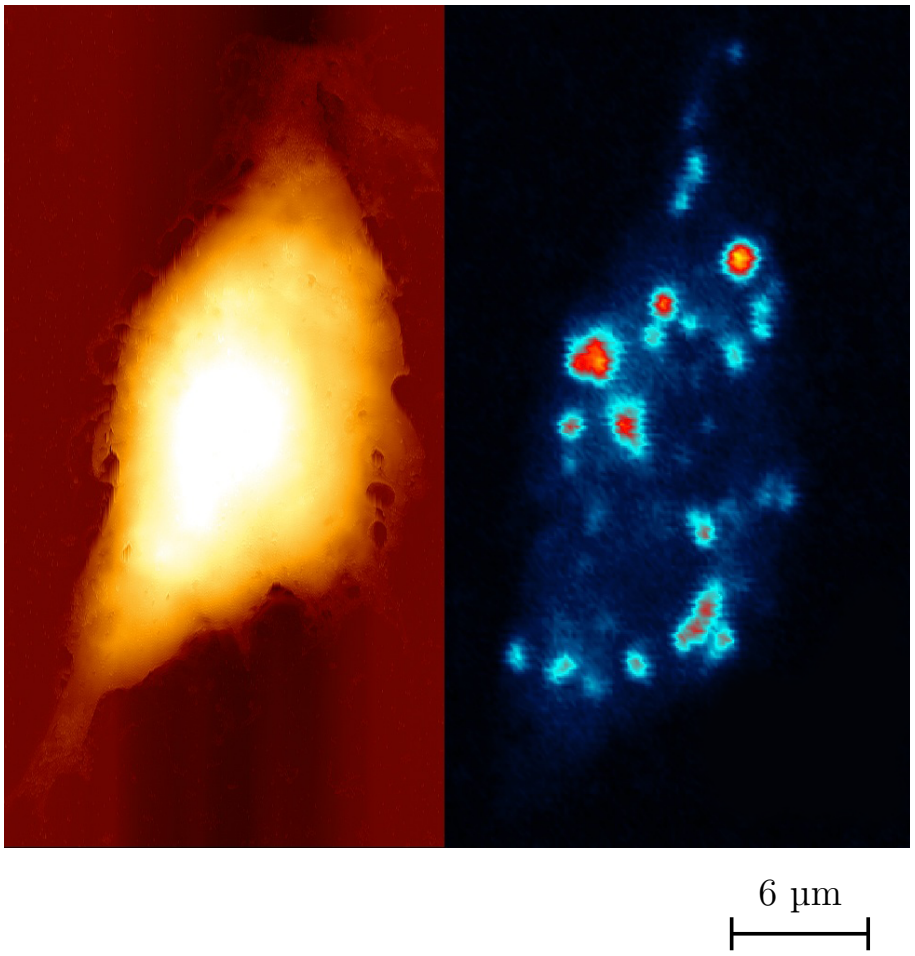

FIGURE 6.1: Left: Atomic force microscope image of an eukaryotic cell. Right: Confocal laser microscope image of the distribution of gold nanoparticles within the same cell. Image used with permission from Nadine Bohn of the University of Hamburg [69].

aqueous solution. The high atomic number of gold relative to tissue means that when gold is introduced into a tumour, it acts as a contrast agent in the case of imaging and it amplifies the biological damage in the case of external beam therapy or brachytherapy [68].

High Z materials have been shown to be most beneficial as radiosensitisers when irradiated with kilovoltage photon radiation due to the dominance of the photoelectric interactions at these energies [70]. The interaction cross sections for photoelectric processes is approximately proportional to Z^3 to $Z^{3.8}$ where Z is the atomic number of the material in which the photon is propagating. When the GNPs are delivered into the tumour volume, the increased effective atomic number results in a large increase in photoelectron

production which increases the local dose deposited within the tumour. This means that the amount of radiation dose required to achieve the same tumour control probability is reduced resulting in a greater normal tissue sparing effect. It has been reported that a secondary dose enhancement effect may result from the production of Auger electrons [71]. The low energy Auger electrons produced in the gold are able to travel beyond the extent of the GNP and cause ionisation damage to the cell region to which the gold is attached (typically cell membrane, cytoplasm or cell nucleus, depending on the size of the individual GNP).

Investigation of the effect of high Z materials on dose deposition began in the late 1940s. In 1949 Spiers suggested that the dose enhancement effect resulting from high Z material interfaces was the result of an increased production of photo-electrons. [72]. Many years later, iodine was discovered to behave as an x-ray contrast agent, increasing the contrast between anatomical structures due to its relatively high atomic number. As x-ray imaging is performed at kilovoltage energies, large differential absorption between materials of different atomic numbers produces excellent image contrast [3].

It was later suggested that iodine could also be used in radiotherapy as well as for imaging purposes. In 1980, Matsudaira et al. investigated the use of non-radioactive iodine on mouse lymphocytic leukaemia (L5178Y) cultured cells [70]. The dose enhancement effect of concentrated iodine was determined by calculating the cell survival fraction in the culture when exposed to iodine and in the control culture. The experiments were performed using both x-rays and gamma rays. When x-rays were used, an enhanced cell killing effect, increased frequency of micronuclei formation and an increased yield of DNA single strand breaks were observed. These effects were not observed when identical tests were performed using gamma rays. It was concluded that iodine contrast medium sensitises the cells by means of the photoelectric effect.

Modern GNP investigations began in the early 21st century. Herold et al. extended the research from high Z material interfaces to aqueous gold solutions [73]. Gold particles were implanted into tumor cells growing *in vivo* and were irradiated with low energy photons. In this study, three different cell types (CHO-K1, EMT-6 and DU-145) were irradiated with different kilovoltage photon energies: four energies between 100 and 240

kVp and 662 keV ^{137}Cs gamma rays. The GNPs were injected directly into the EMT-6 tumours growing in mice prior to irradiation. The tumour cell kill was assayed by an *in vivo* and *in vitro* technique. The GNPs had sizes ranging from 1.5 to 3 µm. These types of GNPs are now commonly referred to as microspheres. Microspheres preferentially attach to the outside of the cell membrane rather than clustering in the cytoplasm. A dose enhancement factor of 1.42 (based on cell survival curves) was recorded for 1% GNP solution with 200 kVp photons. A similar dose enhancement effect was recorded at the other energies except for the ^{137}Cs source. These results supported previous assumptions which predicted the dose enhancement effect is due primarily to an increased production of photo-electrons. The results also demonstrated different dose enhancement effect in different cell types. It was suggested that GNPs could be used in conjunction with interstitial brachytherapy using isotopes which emit low energy photons to significantly improve the therapeutic ratio.

While the dose enhancement effect of GNPs is derived from the increased production of photo-electrons when using kilovoltage photons, it has been reported that megavoltage photons may have a dose enhancement effect unrelated to photoelectrons. It has been reported that GNP are not entirely biologically inert. The GNPs may also cause oxidative stress and cell death post-irradiation. This suggests a possible biological mechanism of GNP radiosensitisation at clinical megavoltage photon energies [74].

In 2004, Hainfield [75] studied the effect of gold concentration on the dose enhancement of GNPs with a diameter of 1.9 nm (determined by electron microscopy) [75]. Small diameter nanoparticles were used to avoid high liver uptake which occurs with gold microspheres. This also resulted in endocytosis of the GNPs producing GNP clusters in the cytoplasm. Balb/C mice were injected with EMT-6 mammary carcinoma cells. Tumours were left to form over a period of 1 week with resulting sizes between 50 and 90 mm^3. GNPs were injected into the mice in a phosphate saline solution via the tail vein. The tumour region was then irradiated with 30 Gy using 250 kVp photon beam. A dramatic change in the rate of tumour growth was observed in mice receiving only radiation treatment and those receiving GNPs followed by radiation. One month after irradiation, mice that received only radiation treatment showed tumour growth up to five times the original size. Mice that received 1.36 g Au/kg GNPs showed no visible tumour one month post-irradiation.

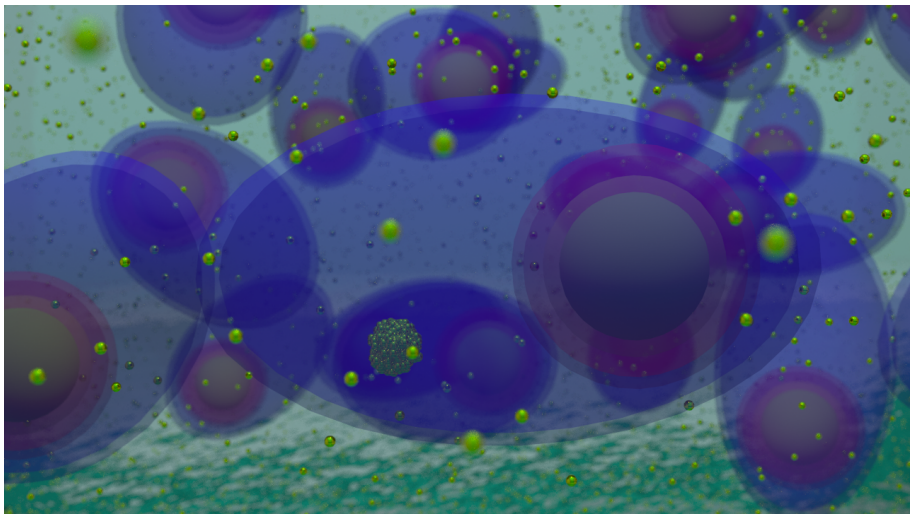

FIGURE 6.2: Illustration of a small number of cells suspended in a water medium which has been infused with a GNP solution (gold spheres). The GNPs are then absorbed into the cell through the biological process of endocytosis forming a cluster of GNPs in the cell (cell in foreground). Rendered in Autodesk 3DS Max.

The same year, Zhang published the results of a Monte Carlo simulation performed using the Geant4 [14] toolkit. This was the first simulation to model the structure of GNPs on a nanometre scale [76]. The simulation consisted of a macroscopic distribution of gold spheres (100 nm diameter) within a spherical water medium. The medium containing the GNPs was then irradiated with a modelled ^{192}Ir HDR source and the dose distribution was compared with that of a water medium without gold. While this model represented a significant improvement on the estimate of the physical dose increase due to GNPs, the model lacked the geometrical complexity of a real cell.

The use of GNPs to produce changes in physical dose distributions in radiotherapy has been investigated for many years. This research has brought targeted GNP therapy a step closer to clinical use. However, cellular mechanisms by which this dose enhancement effect occurs in cells is generally not understood. In order to gain the maximum benefit from GNPs in radiotherapy, the physical, chemical and biological processes involved in the irradiation of cells containing gold should be investigated in more detail.

To achieve this, the cell model developed in chapter 5 was used to simulate two GNP geometries and determine the physical DER in each case. This is the first computational model used to investigate radiosensitisation by GNPs using realistic cell geometry,

elemental composition and multiple cellular targets.

6.2 Method

6.2.1 Cell Modeling

The 3D randomised cell model developed in chapter 5 was used to model and simulate the interaction of kilovoltage photons with two gold cluster geometries within cells. Using the code developed in chapter 5, a tumour consisting of a non-overlapping cell distribution was grown. The cell distribution consisted of 850 individual randomised cells producing a cubic tumour with a side length of approximately 0.40 mm.

The tumour was then imported into Geant4 (version 4.9.5 patch 1). Each cell was placed at the position with orientation and size specified by the tumour growth code. Each of the cells was then populated by its internal cell geometries (cytoplasm, membrane, endoplasmic reticulum, nucleus and nucleolus). The radii values calculated by the Matlab™ code specify the outer radius for the membrane and cytoplasm. The regions within the cell were then scaled relative to the membrane radius. Each elliptical cell had a randomised semi-major axis length of between 9 and 13 µm. The membrane was 10 nm thick, the reticulum 5 µm, the nucleus 3 µm and the nucleolus 2 µm in radius. The approximate shape and dimensions of the cells and their structure can be seen in figure 6.3.

6.2.2 Simulation Scenarios

In this part of the project, the existing cell model was modified to include GNPs of various sizes and positions resulting from individualised delivery methods. The geometry of the first simulation case was based on [68] in which GNPs were delivered in an aqueous solution into the cells resulting in a GNP cluster of 400 nm radius forming in the cytoplasm (figure 6.4). In order to account for the randomised location of the GNPs in the cytoplasm, four different simulations were run where the gold cluster was placed at four randomised positions within the cells relative to the centre of the cell. Since the cells were of random

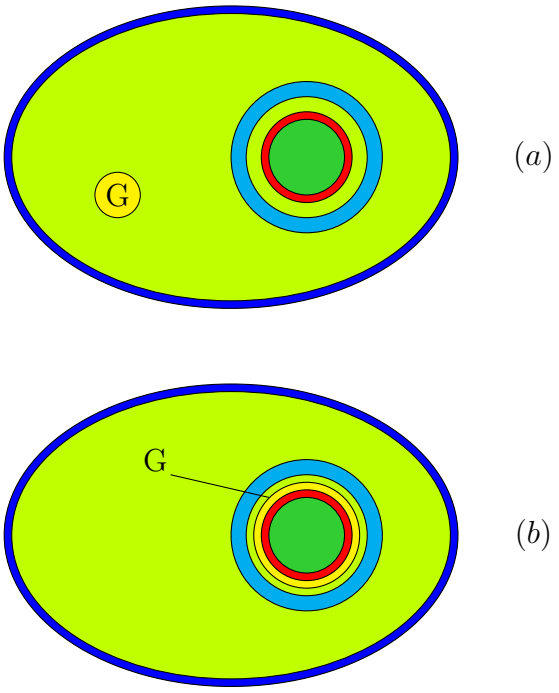

FIGURE 6.3: Illustration of cell cross-section with two types of simulation geometries. (a) 400 nm gold cluster located randomly in the cytoplasm and (b) A thin (300 nm) layer of gold (yellow) is attached to the nucleus. Membrane: blue, Cytoplasm: light green, Reticulum: cyan: Nucleus: red, Nucleolus: green. GNPs: yellow.

size and rotation relative to the particle source, the random nature of the gold cluster position was adequately approximated. The results from the four independent simulations were then concatenated before processing.

The geometry of the second simulation was based on [77] in which many gold clusters form within the cell with the majority of the clusters attaching to the nucleus. This geometry was approximated by adding a uniform 300 nm thick layer of gold around the nucleus. The two geometries are compared in figure 6.3. The parameters used in the control simulation, the 400 nm gold cluster and the 300 nm gold layer represent the extremes of possible gold geometries (from a single cluster in the cytoplasm to complete attachment to the nucleus) while still maintaining cell viability.

6.2.3 Physics List

In this chapter, the use of the Livermore and Geant4-DNA physics processes have been compared to investigate the dose deposition in all cellular regions. While the Livermore physics list is capable of simulating the dose distribution in cells down to energies of 250 eV, corresponding to an electron range cut of 25 nm for electrons, it is not capable of simulating microdosimetric track structures and therefore unable to predict DNA strand breaks. Using the Geant4-DNA processes in the nucleus and nucleolus regions of the cell the individual ionisation damages of the incident radiation to the DNA of the cell could be modelled.

The low energy physics processes in Geant4 from the Livermore and Penelope models are generally used when the production threshold of secondaries is required to be less than the 1 keV cut-off of the standard electromagnetic physics list. Monte Carlo packages such as EGS, FLUKA, Geant4 and MCNP all simulate dose distributions using a condensed history method of particle transport. These methods are sufficient for calculating the dose distributions on a macroscopic scale where the discrete energy losses are orders of magnitude larger than the electron binding energies (>1 keV). Low energy processes such as the Livermore or Penelope models are capable of simulating hard collisions in which secondary particles are generated down to 250 eV. The Geant4-DNA processes use analytical and semi-empirical cross sections which cover the energy range of 0.026 eV (thermalisation of electrons) to 10 keV for electrons.

In the first instance, only the Livermore physics list was used in the current work to irradiate the cells with a secondary energy cut-off of 250 eV. The results were then compared with those of a second physics list which used a combination of Livermore physics in addition to the Geant4-DNA physics processes in the nucleus and nucleolus. The use of the Geant4-DNA physics list is essential for nanodosimetry work as it is the only Geant4 physics list capable of simulating step-by-step radiation track structure on a nanometre scale. This is necessary for simulating the production of DNA double strand breaks.

The first physics list was implemented simply using a Geant4 modular physics list referencing the standard G4EmLivermorePhysics class. In the case of the DNA/Livermore combined physics list, a region (G4Region) was defined around the nucleus and nucleolus of each cell in order to apply different physical processes to different cell organelles. High precision ionisation/excitation track structure is very important in the nucleus and nucleolus due to the nature of cell death through DNA and RNA damage respectively. Conversely, cell death by damage to the cytoplasm, membrane and reticulum results from different physiochemical processes which do not depend strongly on the clustering of ionisation events. It was therefore decided to apply the Livermore physics model in the membrane, cytoplasm and reticulum in order to simulate the effect of organelle specific materials (water medium is the only supported material in the Geant4-DNA physics models). The Livermore processes were also applied to the GNP regions for two reasons. Firstly, the Geant4-DNA physics processes only support water material which means the particle interactions within the gold medium would not be physically realistic. Secondly, the track structure of electrons and photons within the gold medium is not of concern or of any relevance to the damage of the cells. What is important is the accurate simulation of the production and transport of secondary electrons from the GNPs into the cell structures. This can be achieved using the Livermore physics data.

The $0.4 \times 0.4 \times 0.4$ mm^3 tumour volume containing 850 cells (figure 6.5) was placed in a secondary water medium with appropriate dimensions to ensure both electronic equilibrium and to eliminate boundary errors (figures 6.7 and 6.8). This geometry was located in a $1 \times 1 \times 1$ cm^3 world volume. The cells were then irradiated by an 80 kVp photon source originating from a planar surface with dimensions 1.0 mm $\times$ 1.0 mm. It was determined by analysing the standard error of the output data that 10^6 primary particles were required to produce an uncertainty of 1% in the total dose deposited in the cytoplasm.

Processing time differed between physics lists. The Livermore only physics list simulation required approximately one day to complete while the DNA+Livermore physics list simulation required up to 5 days (with 24 Gb of available RAM and 4 instances of the code running on four 3.5 GHz processors). It is therefore important to choose simulation parameters which will result in the highest amount of cell damage in the shortest time.

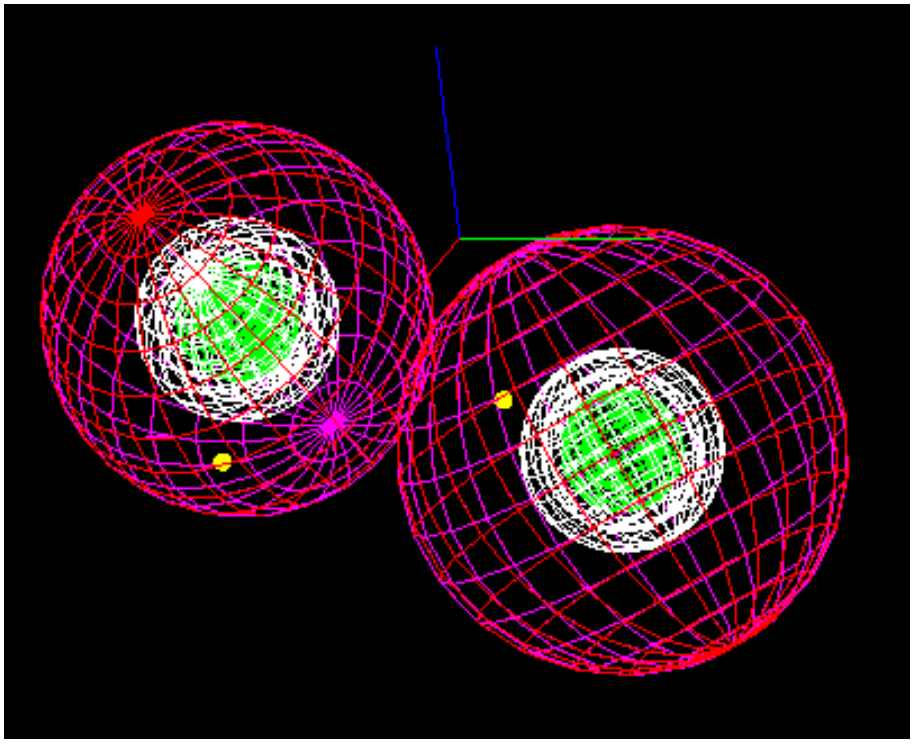

FIGURE 6.4: Visualisation from Geant4 showing two cells with biological structures and GNP clusters (yellow).

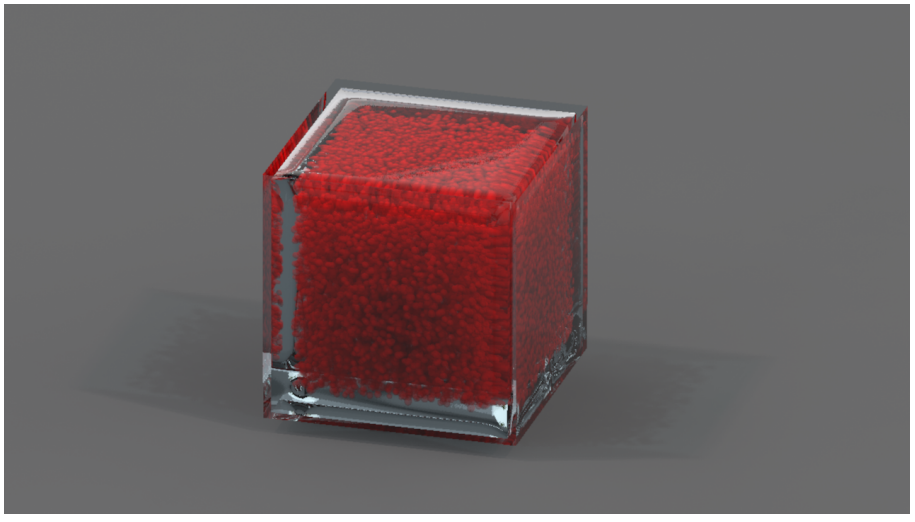

FIGURE 6.5: (a) Illustration of the geometrical irradiation set-up. The tumor containing 850 cells (red) are surrounded by a water suspension medium which is then irradiated by a 1 mm^2 80 kVp planar radiation field.

Since the target tumour volume is very small, 80 kVp radiation has a very small probability of interacting with the cells. As a result, it is necessary to fire high numbers of primary particles to produce enough statistics or to increase the interaction probability by "growing" more cells. In this work, we chose a smaller number of cells (850 cells) (simulation time is strongly dependent on the number of cells in the simulation) with a larger number of primary particles (10^6) to achieve the same standard error in the absorbed dose values. The variance in the absorbed dose measurements is inversely proportional to the number of primary particles N simulated in Geant4. By plotting the standard error in the mean (SEM) against the number of particles, the number of particles required to achieve sufficient precision in the dose deposited was predicted (figure 6.6).

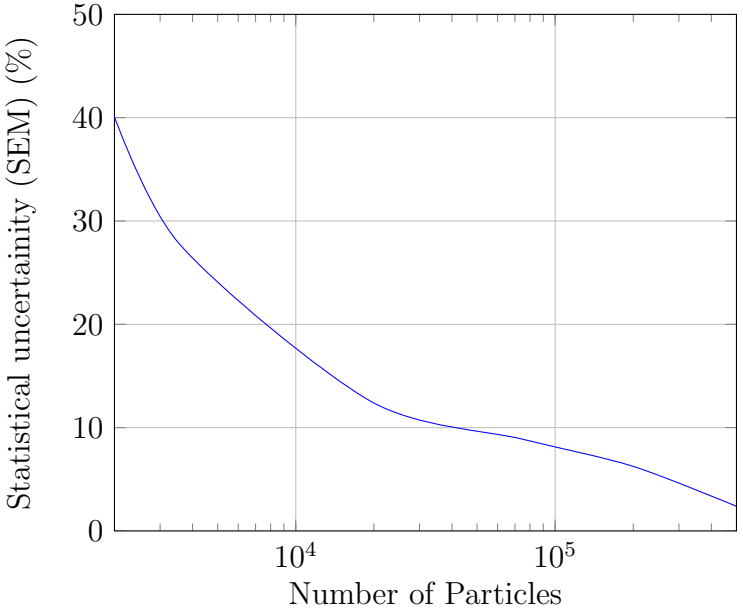

FIGURE 6.6: Simulation statistical uncertainity (SEM) vs. number of primary particles.

The output data from Geant4 was recorded using a modified "stepping action" class. As the primary particles are transported through the cell geometry a variety of output data is written to a text file for analysis at a later time. The data that is recorded includes: the cell in which an interaction occurs, the region of the cell where the interaction occurred, specific Cartesian coordinates of the interaction event, physical process of the interaction (e.g. ionisation, photoelectric) and the energy deposited per interaction. The energy deposit data is used to determine the dose deposited in each cell. The simulation output

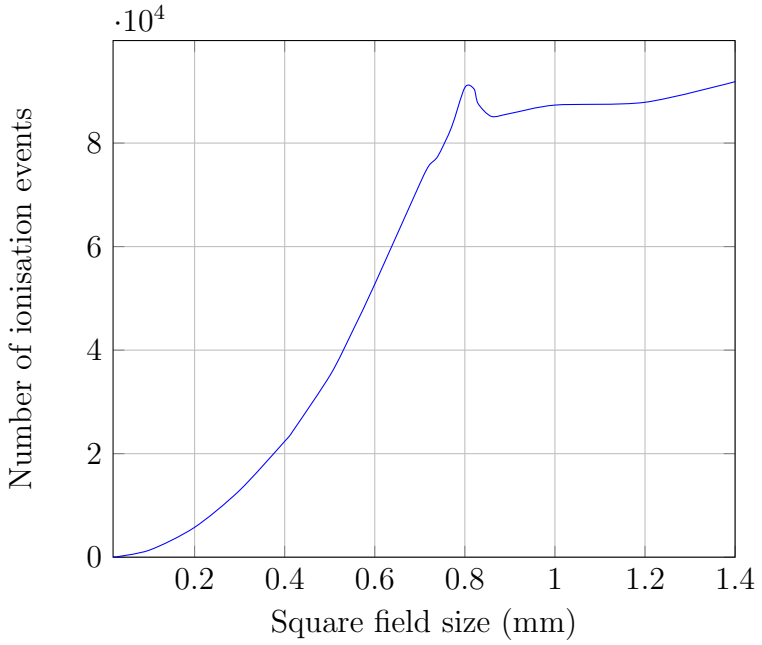

FIGURE 6.7: Number of ionisations recorded in target volume vs. size of radiation field.

data was analysed in order to determine the dose enhancement ratio (DER) of the two GNP geometries. In the current work, the DER is defined as the ratio of the absorbed dose deposited in the cells with and without the gold geometry for the same number of primary particles:

$$DER = \frac{D_{\text{With GNP}}}{D_{\text{Without GNP}}} \tag{6.1}$$

The absorbed dose deposited was calculated using a Matlab™ script and the statistical analysis was performed using the statistical analysis package "Graphpad Prism 5" (Graphpad, CA, USA). A 1 way ANOVA and Tukey-Kramer [78] multiple comparison test was used to determine the significance in the change in absorbed dose between the control and two GNP scenarios at a 95% confidence level.

6.2.4 Energy Dependence

The energy dependence of the GNP DER was calculated by simulating the dose deposited with two photon energy spectra. The dose distributions generated by the original 80 kVp

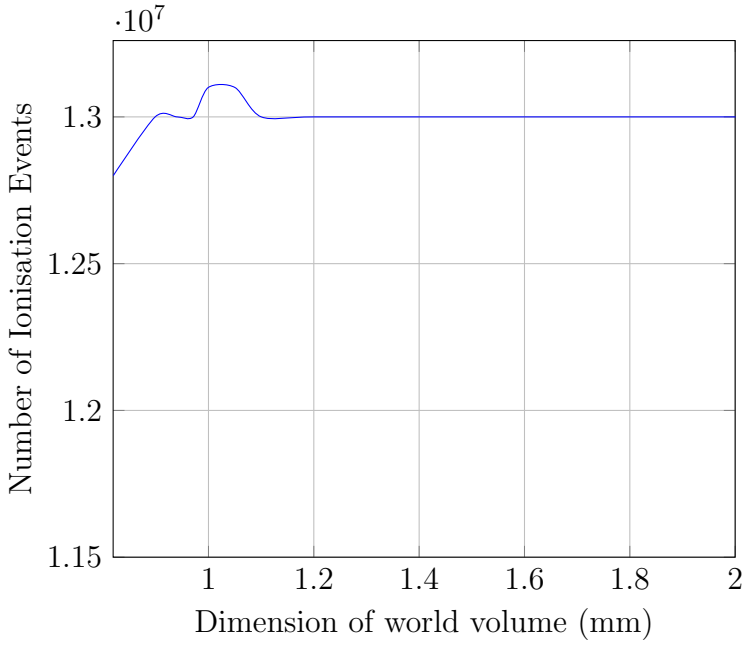

FIGURE 6.8: Number of ionisations recorded in target volume vs. size of world volume around the cells.

photon spectrum was compared with the results using a 6 MV photon spectrum produced by a Varian 6/100 linear accelerator (spectrum from beam modelling values at the Royal Adelaide Hospital). Identical simulation parameters were used in each case (number of cells, dimensions of water volume, number of primary particles). An identical build-up region of 1 mm was used in each case to enable direct comparison. The build-up region for both the 80 kVp and 6 MV beams were chosen to be identical to minimise the biasing effect of other variables on the calculated physical DER values (ratio of doses with and without the GNP for each energy spectrum).

6.2.5 Auger Electron Dose Contribution

To identify other possible causes of GNP cell radio sensitisation, the interactions of Auger electrons were modelled in Geant4.

The contributions from Auger electrons were calculated from two simulations. The Livermore physics list was used with identical parameters to the previously mentioned Geant4 simulations. The atomic de-excitation processes (including fluorescence, Auger

and PIXE) were activated in one simulation and not the other. While the total absorbed dose in the target volume remains the same, activation of Auger atomic de-excitation processes enables the Auger electrons to traverse outside the GNP and deposit their energy in the cell thus altering the dose distribution.

In order to confirm whether the Auger atomic de-excitation processes were functioning correctly in the simulation, we reduced the simulation geometry to a single 1 µm radius gold sphere surrounded by a $3 \times 3 \times 3$ µm^3 water medium. A scoring mesh was added to measure the dose distribution both in and around the gold sphere and water volume in order to identify the contribution from Auger electrons.

6.3 Results and Discussion

6.3.1 Challenges Overcome and Optimisation During Code Testing

The most crucial component of this section of work was the development of a physics list for Geant4 which utilised two independent physics models for specific regions of the cell geometry. The primary mechanism of radiation induced cell death is DNA double strand break damage caused by clustering of individual ionisation and photoelectric events on the DNA double helix. It was therefore imperative that ionisation track structures be modelled fully and accurately. This can only be achieved using the Geant4-DNA processes. In chapter 4, the importance of using realistic elemental compositions in each of the cell regions to obtain accurate results has been demonstrated. However, the Geant4-DNA processes only support a liquid water medium. Due to this limitation of Geant4, we were forced to use a water medium with a scaled density instead to represent the nucleus and nucleolus of the cell. Since double strand breaks are of no concern in the other regions of the cell (as there is no DNA to damage) we were able to implement realistic elemental compositions for these regions with appropriate densities. One of the most complicated tasks in the current work was merging the two physics processes into a single physics list.

The first issue encountered affected the tracking of delta electrons as they transitioned from the nucleus to cytoplasm. The specific fault occurred when a primary photon liberated a delta electron from the nucleus. This electron was tracked correctly with appropriate energy losses. However, when the electron transitioned into the cytoplasm, the electron appeared to have no available physical processes associated with it. This was indicated by the electron traversing the cytoplasm and membrane of the cell without interaction or energy loss. This problem occurred frequently in the simulations when the energy of the delta electron transitioned to the cytoplasm with energy below 250 eV. Since the lower bound for the Livermore physics cross sections is 250 eV, Geant4 was unable to determine how to track delta electrons in this circumstance. This problem was discovered to be the result of using a single set of energy cut-off values for the entire cell geometry. This problem was solved by defining a set of low energy cut-off values for the nucleus and nucleolus where the Geant4-DNA processes were in use, and a set of higher energy cut-off values for the remainder of the cell where the Livermore processes were active. Cut-off values of 1 nm and 1 µm were used for the nucleus/nucleolus and cytoplasm/membrane/reticulum regions respectively.

The second issue encountered was the inability to randomly place the gold spheres within the cytoplasm. When a random number generator was used to define the position parameter of the gold spheres, it was discovered that the position of the gold spheres changed with each iterative step of the particles. This would have clearly given inaccurate results. A work-around was developed to resolve this issue. Four simulations were run each with $\frac{1}{4}$ of the total number of primary particles. In each of the four simulations, the position of the gold was placed at four different positions within the cell. The random orientation of the cells coupled with the different positions of the gold within the cell, gave sufficiently randomised gold geometries.

The final problem encountered while running the gold nanoparticle simulations was the problem of simulation time management. Shortly after building a working physics list, it was discovered that particles were being tracked with high precision un-necessarily in the water medium in which the cells were located. The problem was isolated to the nucleus region definition. Since the nucleus is composed of water in the simulation where the high precision Geant4-DNA processes are activated, Geant4 mistakenly activated the high

precision model in the water medium surrounding the cells. In some cases, this resulted in simulation times of up to 18 hours per particle. A workaround was created by re-defining a water medium with the same properties of the nucleus material but a different name. Geant4 then interpreted the water medium around the cells as a second region independent of the nucleus and thus enabled the lower precision and quicker Livermore physics processes to be activated in this region. When low energy protons (<2 MeV) were simulated, the processing time decreased from 18 hours per particle to approximately 45 seconds per particle.

6.3.2 Absorbed Dose Measurements

In the first instance, the standard Livermore physics list was used for the Geant4 simulations. The dose deposited in each cell was analysed. Firstly, the total dose deposited in each of the cellular regions during the control simulation (no gold) and the gold cluster case (400 nm) was analysed. The results in figure 6.9 show no statistically significant ($p<0.05$) change in the absorbed dose in any of the cell regions. This is most likely due to small dimensions of the gold relative to the cell in this geometry and the lack of proximity to any of the neighbouring cell regions. The modelled 400 nm cluster may also experience high self-absorption of photo and Auger electrons resulting in lower absorbed doses in the surrounding medium.

In the second simulation geometry where the gold accumulates in clusters on the surface of the nucleus, a large increase in the energy deposited is observed in all regions of the cell except the membrane. Since the gold is located on the surface of the nucleus, this suggests that the gold particles produce a dose enhancement effect resulting from low energy photo-electrons propagating from the gold into the nucleus region of the cell. A statistically significant increase ($p<0.05$) in deposited energy is seen in all regions. This indicates that the additional photo-electrons produced by the gold cluster on the centralised nucleus propagate to all other regions of the cell and therefore increase the dose in these regions. The primary effect in this geometrical case is additional ionisation damage to the DNA of the cell thus producing a much larger physical and biological DER than the 400 nm cytoplasm cluster. This is also a result of the much larger surface area to

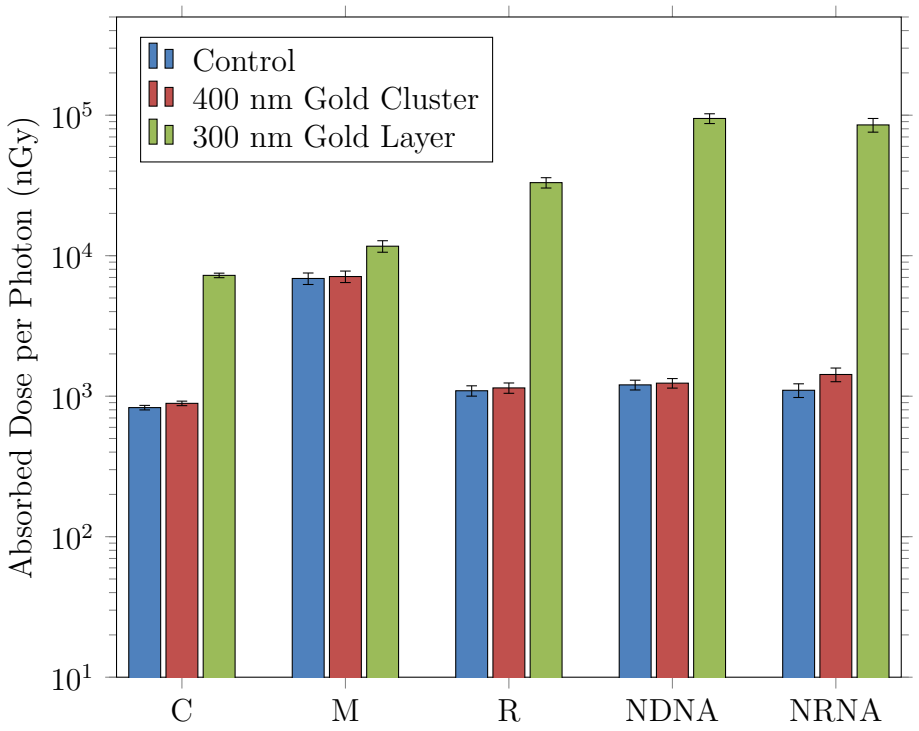

FIGURE 6.9: The total energy deposited per photon in the cytoplasm (C), membrane (M), endoplasmic reticulum (R), nucleus (NDNA) and nucleolus (NRNA) of the cells in the control (no gold) scenario, the 400 nm gold cluster and the 300 nm gold layer. Livermore only physics list.

volume ratio of the gold layer which results in reduced self-absorption of photoelectrons in the gold.

The results for the Livermore/DNA hybrid physics list are displayed in figure 6.10 and table 6.1. When the control and 400 nm randomised cluster simulation results are compared, we see a consistent result with the Livermore only physics list. Using both physics lists, we see no statistically significant change in the absorbed dose.

When the results of the control simulation with the 300 nm layered gold scenario are compared, a significant change in dose is observed in the nucleus and nucleolus. Since the gold is located adjacent to the nucleus, the majority of secondary electrons cannot traverse the cell to the membrane. Thus, we observe only a small dose enhancement effect in membrane. In the remaining cell regions of the cytoplasm and endoplasmic reticulum, an increase in the absorbed dose is seen when the gold geometry is changed to the 300 nm layer of gold representing the attachment of GNP clusters to the nucleus.

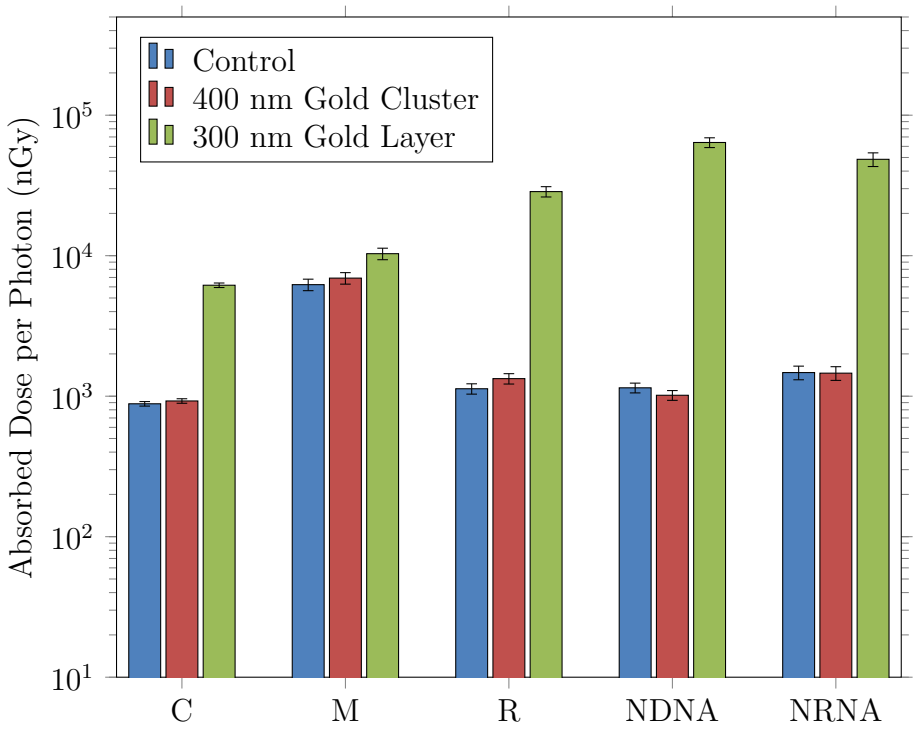

FIGURE 6.10: The total energy deposited per photon in the cytoplasm (C), membrane (M), endoplasmic reticulum (R), nucleus (NDNA) and nucleolus (NRNA) of the cells in the control (no gold) scenario, the 400 nm gold cluster and the 300 nm gold layer. Livermore/DNA hybrid physics list.

Small non-significant differences exist between the results when either the standalone Livermore physics list or Livermore/DNA physics list is used. We observe a large and consistent localised increase in the absorbed dose adjacent to the position of the layer of gold and smaller increases elsewhere in the cell. At kilo-voltage energies, the photons liberate low energy photo-electrons which deposit their energy within several microns of their point of liberation. The position of the membrane relative to the gold clusters protects it from the additional damages produced by the presence of the GNPs. Both the Livermore only and the Livermore/DNA hybrid physics lists produce very similar absorbed dose values in all regions of the cell. This means, that while the Geant4-DNA processes simulate the track structure of the electrons using a much more precise method (with a larger number of track steps), the overall deposited dose remains the same. These results indicate that the interaction cross sections for the Livermore and Geant4-DNA processes are consistent at these energies. Since the absorbed dose in the nucleus and nucleolus when using the Livermore physics processes is comparable to the dose deposited

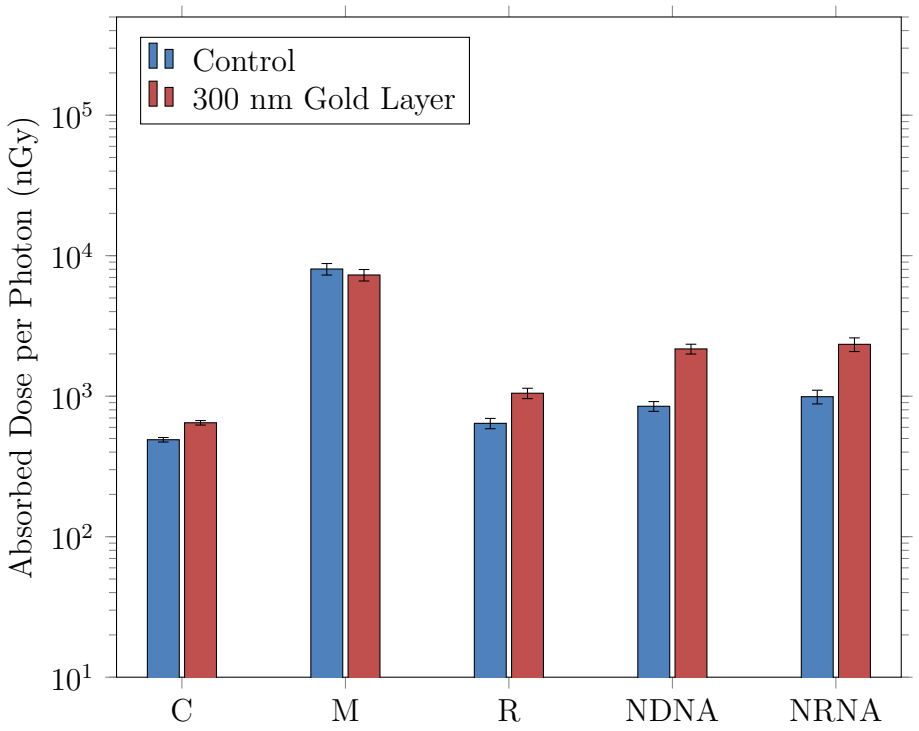

FIGURE 6.11: The dose deposited (mGy) per photon in all cells (by region) in the control simulation (no gold) and the GNP simulation (300 nm gold layer attached to nucleus) for 6 MV photon beam.

in these regions using the DNA physics list, the density scaled water media used to represent the elemental compositions of the nucleus and nucleolus are a good analogue for the realistic nucleus elemental composition used with the Livermore physics list. It was therefore expected that in chapter 8, where the cell survival fraction was calculated by simulating the formation of lesions formed by the clustering of ionisation events, the Geant4-DNA physics list produced accurate results.

6.3.3 Energy Dependence of GNP Dose Enhancement Effect

Figure 6.11 shows the dose deposited in all cells (grouped by cellular region) using two different energy spectra. The physical dose enhancement ratios for each spectrum are recorded in table 6.1. It is evident that the physical dose enhancement effect produced by GNPs is approximately an order of magnitude larger when and 80 kVp spectrum is used compared to a 6 MV energy spectrum.

TABLE 6.1: Dose enhancement ratios for 300 nm layer gold relative to control simulations ($D_{\text{with Au}}$ /$D_{\text{without Au}}$) ($\pm$ 2σ) for 80 kVp and 6 MV photon beams. Total is the sum of dose to all cell regions. Physics list used was the DNA/Livermore combined model.

	Cytoplasm	Membrane	Reticulum	Nucleus	Nucleolus	Total
80 kVp	6.98 ± 0.3	1.66 ± 0.2	25.3 ± 2.2	55.7 ± 0.8	32.9 ± 3.7	14.5 ± 1.4
6 MV	1.32 ± 0.05	0.91 ± 0.1	1.65 ± 0.2	2.56 ± 0.1	2.36 ± 0.3	1.23 ± 0.2

The largest DER values are seen in the nucleus and nucleolus region due to the proximity of the GNPs to these regions. These results justify the assumption that the primary dose enhancement effect of GNPs is the result of an increased photo-electric cross section produced by a localised increase in the atomic number generated by the GNP's.

6.3.4 Auger Electron Dose Contribution

Figures 6.12 and 6.13 show a two dimensional plot of the absorbed dose in and around a GNP of diameter 1 µm. Even as the spatial resolution of the dose distribution is increased, the contribution from the Auger electrons is not immediately apparent. A 1D line profile was generated by integrating the dose over the length of the GNP. Figure 6.14 shows the absorbed dose vs the distance from the centre of the gold sphere. It is evident in figure 6.14 that when Auger atomic de-excitation processes are activated, the absorbed dose inside the GNP decreases and the absorbed dose outside the GNP increases. This indicates that some Auger electrons have sufficient energy to propagate outside the nanoparticle and deposit their energy in the surrounding regions of the cell. Based on figure 6.14 it appears when 80 kVp photons are used, the maximum range that the Auger electrons can propagate outside the gold sphere is 500 nm. This indicates that the Auger electrons cannot influence the absorbed dose in other regions of the cell due to their distance from the GNP. Targeted Auger electron therapy with GNPs would therefore be most effective when the source of Auger electrons is located within the nucleus and attached to the DNA.

It can therefore be concluded that the primary dose enhancement effect of GNPs from 80 kVp photons originates from the Z^3 dependence of the photoelectric cross sections in gold leading to additional high energy photoelectrons being produced.

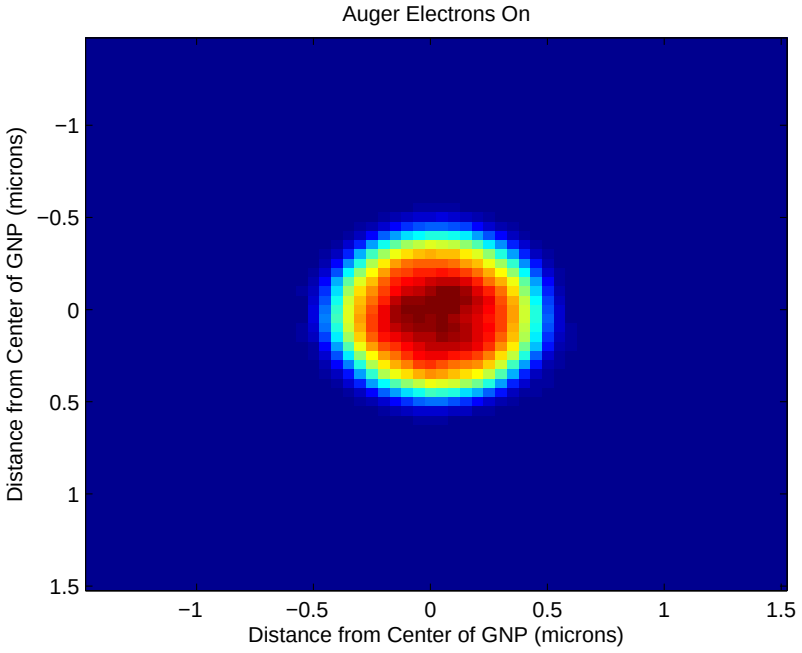

FIGURE 6.12: The dose distribution around a single 1 µm gold sphere immersed in a $3 \times 3 \times 3$ µm^3 water medium (Auger processes on). Radiation source is a planar 3×3 µm^2, 80 kVp photon source. 50 nm spatial resolution 2×10^7 particles.

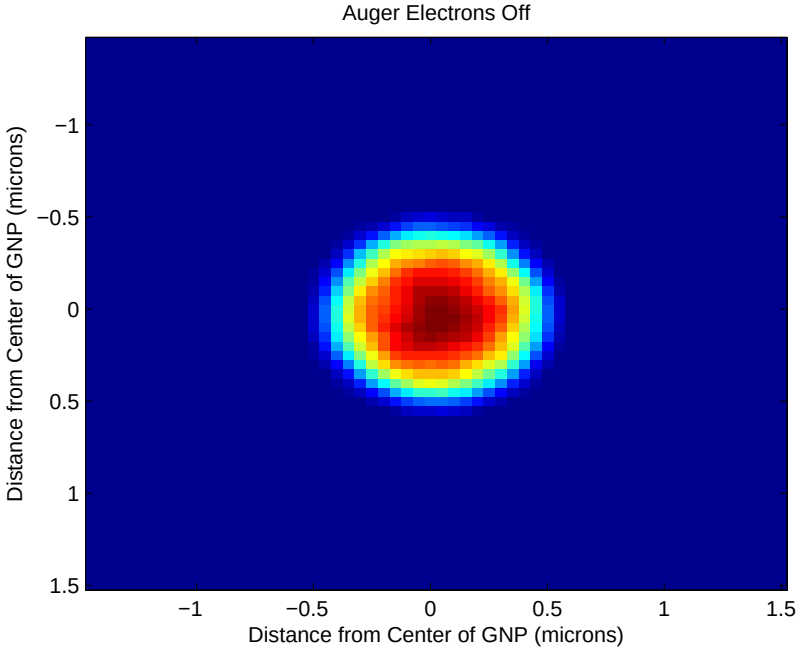

FIGURE 6.13: The dose distribution around a single 1 µm gold sphere immersed in a $3 \times 3 \times 3$ µm^3 water medium (Auger processes off). Radiation source is a planar 3×3 µm^2, 80 kVp photon source. 50 nm spatial resolution 2×10^7 particles.

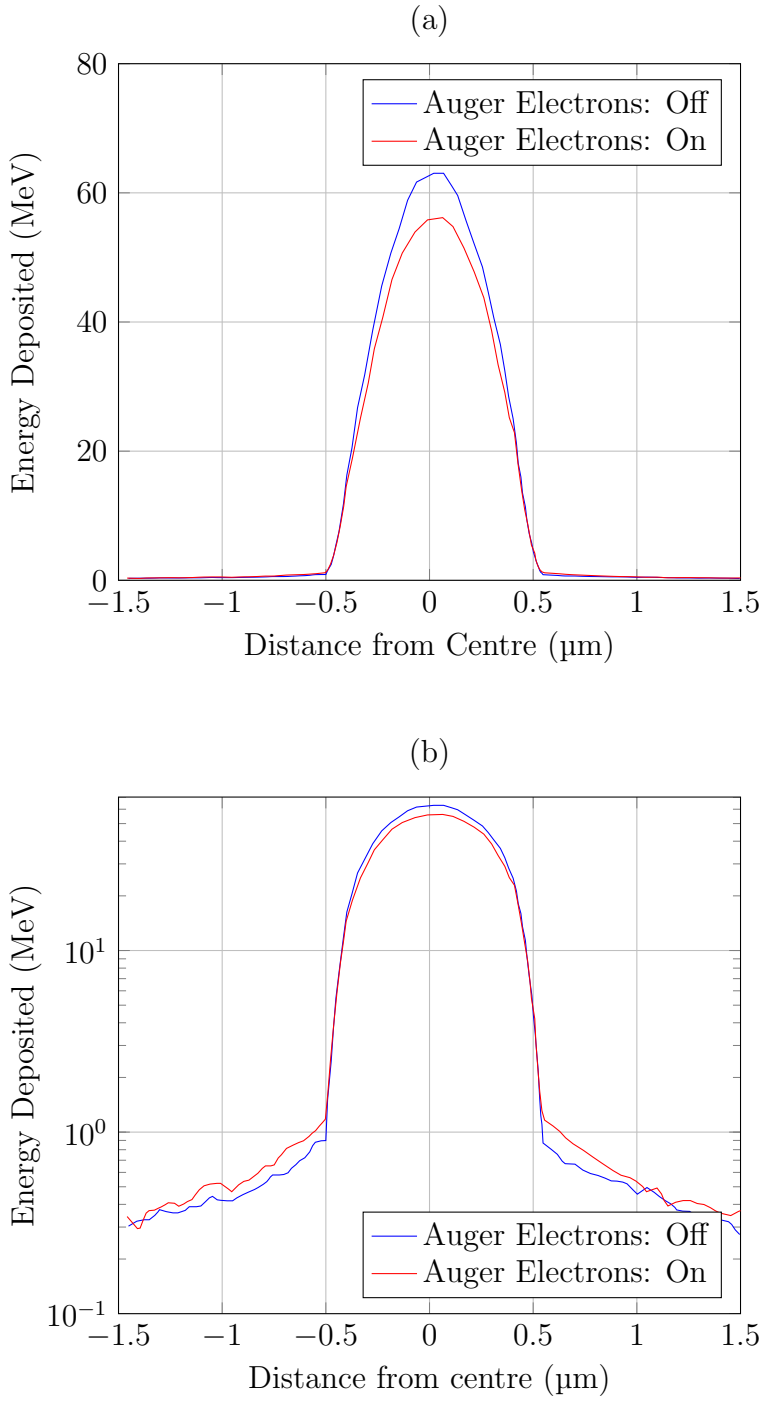

FIGURE 6.14: Line profile of absorbed dose averaged over the dimension of the gold sphere. Auger processes off (blue) and Auger processes on (red). Energy Deposited (MeV) vs distance across the gold sphere. (50 nm spatial resolution). (a) and (b) are the same graph shown on different scales to emphasise the reduction in dose at (a) the centre of the GNP and (b) the increase in dose outside the GNP .

6.3.5 Validity of Geant4 Models

The Geant4-DNA model was developed to be a microdosimetry model for simulating electron, proton, alpha particle and heavy ion track structure. While the quality of the model has been verified to energies as low as 1 keV [79], there is little experimental data to confirm the validity of the model below this energy. The accuracy of this model relies upon theoretical models such as the Emfietzoglou, Born [80] and Champion [81] models for excitation, ionisation and elastic processes respectively. The data produced by Geant4 using these models has not been fully experimentally verified. However, it has been demonstrated [79] that the ionisation stopping powers and cross sections for elastic scattering of electrons, match with experimental data to energies below 250 eV. While this may produce track structure results with limited accuracy, the total calculated dose deposited in each cell will be of acceptable statistical uncertainty.

There is very limited published data comparing the low energy models in Geant4 (including Livermore and Penelope) and the Geant4-DNA model for dose calculations. This is due to the Geant4-DNA model being primarily used for track structure simulations while the Livermore and Penelope models are more typically applied to integrated energy depositions. The low energy Livermore processes for photons and electron interactions are generally accepted to be valid down to energies of 250 eV [82] (although data is available to 100 eV with reduced accuracy). In this chapter, the dose deposition of photons (and delta electrons) in individual cells was calculated using a Livermore only and a combined Livermore/Geant4-DNA model. Each physics list produced very similar results. While this does not validate the Geant4-DNA processes down to 250 eV, it does provide evidence that the Geant4-DNA processes can be used to calculate dose distributions to energies as low as 250 eV. The physical models and their validity are discussed in greater detail in chapter 9.

6.4 Conclusions

In conclusion, a novel geometric cellular microdosimetry model has been developed which can be used to simulate a variety of radiation therapies. As new experimental data

becomes available, the accuracy of the Geant4 physics models can be verified and new models may be developed. Due to the modular structure of Geant4, these models can then be implemented into the existing cell model over time.

The two most common GNP clustering geometries (clustering of GNP in the cytoplasm and GNP clusters attaching to the cell nucleus) have been modelled using a randomised 3D cell irradiation model. It has been confirmed that these GNPs produce a localised dose enhancement effect most significantly in the nucleus (DER=55). The absorbed dose in the cell membrane is not strongly affected by the presence of GNP in the cell. This is due to the lack of proximity of the gold to this region and the maximum penetrative ability of secondary electrons at the selected energies of this work. It has been confirmed that the Livermore and Geant4-DNA processes produce statistically identical absorbed dose values in the nucleus and nucleolus of the cell when the realistic elemental composition used with the Livermore processes is substituted for a scaled water medium required by Geant4-DNA.

The energy dependence of the physical dose enhancement effect has been investigated with two distinct photon energy spectra: 80 kVp and 6 MV. The results of the simulation indicate that the dose enhancement effect is at least an order of magnitude larger at 80 kVp compared with 6 MV due to the dominance of the photoelectric processes at kilovoltage energies.

The contribution from Auger electrons to the dose enhancement effect of GNPs has been investigated. We have concluded that when 80 kVp photons are used as the radiation source, the Auger electrons produced in the gold medium do not have sufficient energy to traverse a sufficient distance to influence the absorbed dose in surrounding cell regions (maximum range 250-500 nm). We therefore conclude, when using 80 kVp photons, the primary dose enhancement effect originates from additional high energy photo-electrons liberated in the gold medium.

The possible inaccuracies in the data produced by Geant4-DNA processes have been discussed. Although the accuracy of the track structures simulated by this model are still in question, we are certain that the Geant4-DNA model is capable of simulating dose distributions in the individual cells of this model with a reasonable level of accuracy.

This is indicated by the high level of correlation between the results produced with the Livermore model and the Geant4-DNA model.

To directly compare the dose enhancement effect of GNPs with the available experimental results published in the literature, cell survival data rather than dose values will need to be calculated. A cell survival model has been developed based on [21] in chapter 8 which utilises the high precision track structure of the Geant4-DNA physics list to predict cell death based on DNA double strand breaks and damage to cell organelles.

The cell growth and irradiation model developed in this thesis has demonstrated its applicability for simulating novel radiation treatment modalities. Using this model, the potential of GNPs in enhancing radiotherapy treatments has been demonstrated. The largest dose enhancement effect in the cell occurs in the nucleus of the cell where the frequencies of double strand breaks are increased as a result. If GNPs are used clinically in radiotherapy, they have the potential to produce a greater normal tissue sparing effect as a smaller dose will be required to produce the same biological endpoint in the tumour.

Chapter 7

Gold Nanoparticle Imaging at the Australian Synchrotron Centre

As a parallel project to the development of the Geant4 cellular model, experiments were performed to image cells with implanted gold nanoparticles using synchrotron radiation at the Australian synchrotron centre (ASC) in order to identify and confirm the position of GNPs inside a cell.

7.1 Synchrotron Radiation

Synchrotron radiation is produced when ultra-relativistic electrons are deflected in their path by a magnetic field. The power of the radiation emitted is proportional to the square of the acceleration of the particle. Magnetic fields cannot be used to change the speed of an electron. In a synchrotron accelerator, bending magnets are used to curve the path of electrons. Undulators and wigglers are used to create sinusoidal oscillations of the electrons along their primary linear trajectories.

The radiation emitted from the electrons as they travel in a circular path is emitted in the direction of motion in the lab frame. The power of this radiation is increased by adding undulators and wiggler magnets. These magnets are designed to cause the electrons to

undergo rapid sinusoidal oscillations. These intense oscillations cause electromagnetic radiation to be produced in the direction of the electrons trajectory.

Wiggler magnets are designed to increase the intensity of the radiation. The intensity is proportional to the number of oscillations that the electron undergoes in the magnetic field. Undulator magnets produce less intense electron oscillations. These magnets are tuned to the transverse motion and linear trajectory of the electrons so that the electromagnetic waves undergo constructive interference. This enables the optimal wavelength of the EM radiation to be tuned by changing the gap between component magnets.

The radiation produced by a synchrotron has a characteristic linear polarisation (relative to the orbital plane) and generates a continuous electromagnetic spectrum which ranges from microwaves to x-rays [84]. The type of experiment will determine what part of the EM spectrum is used in a dedicated beamline. For example, infra-red radiation will be used by the infra-red microspectroscopy beamline whereas x-rays are used by several other beam lines including the x-ray fluorescence microscopy beamline. The remaining parts of the spectrum are filtered. The design of the synchrotron enables multiple beam lines and experiments to be run simultaneously without needing to shut down the primary storage ring where electrons are seeded.

7.2 Australian Synchrotron Centre Facility

In the Australian synchrotron, electrons are first produced by an electron gun by thermionic emission from a heated tungsten cathode [85]. An AC voltage signal is applied which means the electron generation is pulsed. The electrons are then accelerated to an energy of 90 keV. The electrons then move into a linear accelerator (figure 7.1). The electron beam is accelerated to an energy of 100 MeV by the linear accelerator. The electrons then move into the "booster" which is an electron synchrotron with a circumference of 130 metres which then accelerates the electrons from 100 MeV to 3 GeV. The magnetic field strength is 1.3 Tesla. The accelerated electrons are transferred to the storage ring which is capable of maintaining a 200 mA current with a beam lifetime of over 20 hours. The storage ring is 216 metres in circumference. The storage ring consists of 14 identical

sectors. Each sector consists of a 4.4 m straight section followed by an 11 m arc. Each arc consists of two dipole bending magnets where synchrotron radiation is produced. The total power requirements for the ASC is estimated at 4 MW with total energy at 25 GWh per year. The beam current is maintained at 200 mA by seeding the storage ring with electrons every 8 minutes. Although the beam life-time is about 25 hours, most experiments on the beamline require a pulsed constant output rather than a beam intensity that has continuous output but decreases exponentially with time over 25 hours.

The purpose of the experiment performed in the current work was to investigate the uptake and internal distribution of GNPs in EMT-6 breast cancer cells. The beamline that was used in the current work was the x-ray fluorescence micro probe (XFM) which utilises the x-rays produced by the synchrotron for imaging of fluorescent materials on micro and nanoscopic scales. The range of x-ray energies used is between 4 and 25 keV [85]. Once the radiation is produced at the bending magnet for the XFM beamline, it is filtered and focussed before reaching the sample and detector. There are two radiation shutters, the mono shutter and the sample shutter. The mono-shutter blocks all radiation prior to entering the beam line and the sample shutter blocks all radiation before entering the sample hutch. The radiation travels through a thermal absorber to block IR radiation, a double crystal mono-chromator and a multi-layer chromator which enables the x-ray energy to be precisely tuned to the desired monochromatic energy. The energy resolution is $\frac{\Delta E}{E} = 10^{-4}$. The beam then passes through a beam defining aperture which enables the particle flux to be precisely controlled so that the sample is not over or under exposed to the x-rays. Finally, the radiation is focused by a horizontal and vertical focusing mirror before reaching the detector and sample. Currently, there are two detectors used on the XFM beamline. The "Maia" detector is a fast, micrometre resolution fluorescence detector capable of measuring the fluorescence of materials with an atomic number larger than that of calcium. It was developed by the CSIRO and has only recently become commercially available. The second detector is called "Vortex" which is a slower yet higher resolution detector (100 nm) capable of detecting the fluorescence of materials with a much lower atomic number of 12 (Magnesium).

The primary use of the x-ray fluorescence micro-probe was to investigate the uptake and clustering of GNPs with a size of approximately 1 nm per particle inside the EMT6

TABLE 7.1: Properties of the XMF beamline.

Source	In-vacuum undulator, n = 90, 22 mm period
Energy Range	4.1 - 25 keV
Optimal Energy	5 - 12 keV
Beam Resolution	$\Delta E/E = 10^{-4}$

cells. The x-ray fluorescence micro probe is one of the beam lines at the Australian synchrotron centre. The synchrotron radiation produced is channelled into the micro-probe beam line where the x-rays are focused and made monochromatic by a double crystal monochromator. Only a small fraction of the original x-rays produced by the synchrotron reach the sample.

The micro-probe is capable of imaging the fluorescence of a sample medium with a resolution of 2 µm. Due to the limited resolution of the micro-probe detector, is it only capable of detecting the fluorescence of materials with an atomic number greater than 20 (Calcium). This makes it suitable for measuring the uptake of GNPs in mammalian cells.

When x-rays (of appropriate energy) are fired at a material, they are absorbed by the target material resulting in fluorescence (e.g. production of x-ray photons with an energy spectrum unique to each material in the sample [85]). By comparing a known spectrum for each elements with the energy spectrum for a given sample, the concentration of each element can be determined. The XFM beam-line is designed to scan a sample pixel by pixel and generate an energy spectrum for each of those pixels. The data file produced can either be displayed as an image file showing the distribution of each element in the sample or exported to a file containing the concentration of a given element (in ng/cm^2) in each pixel. The XFM beam line is capable of measuring the fluorescence of each pixel at a rate much faster than any other facility. It is therefore capable of imaging samples with sizes of the order of several centimetres with resolutions of 2 µm in under 3 hours. The "Maia" has a dwell time between 0.5 milliseconds and 50 milliseconds [85]. It is sensitive to photons above 3.3 keV. It is capable of observing the K-lines of elements heavier than calcium and L-lines of elements heavier than Sb (Z=51).

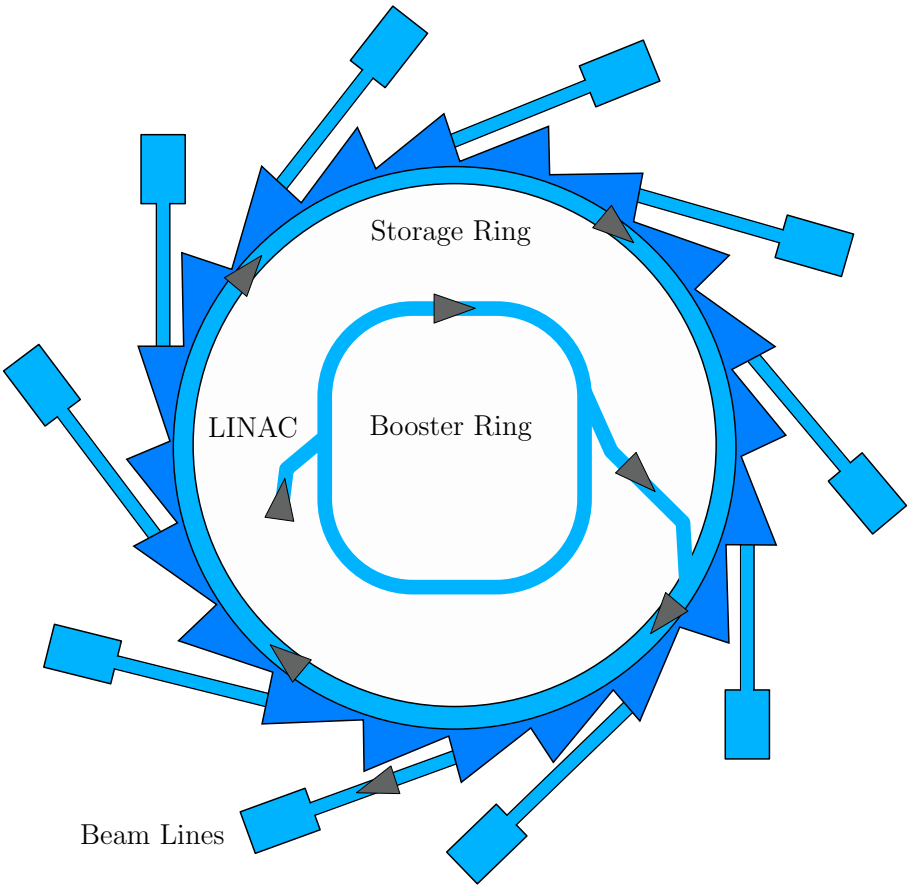

FIGURE 7.1: A structual diagram of the Australian Synchrotron Centre showing major components including: the linear accelerator (LINAC), the booster ring and the storage ring.

TABLE 7.2: Beam properties of the XMF beamline at 10 keV.

Focussing Method	No Focussing	KB Mirrors	Zone Plate
Spot Size	0.6 mm × 1 mm	5 µm	100 nm
Flux (photons/s)	10^{12}	4×10^{11}	10^{10}
Flux Density (photons/s/µm^2)	1.6×10^{6}	1.5×10^{10}	1.0×10^{12}

7.3 Methods

In the current work, EMT-6 mouse breast cancer cells were infused with GNPs with dimensions approximately 1 nm and irradiated them with a 6 MV photon beam from a Varian 6/100 linear accelerator [86]. A total of 12 samples were imaged using the XFM beamline. The samples were a combination of cells which were: infused with gold, iodine stained, anti-body stained and cells irradiated with the 6 MV photon beam. The average dimension of an EMT-6 cells was approximately 45 - 50 µm.

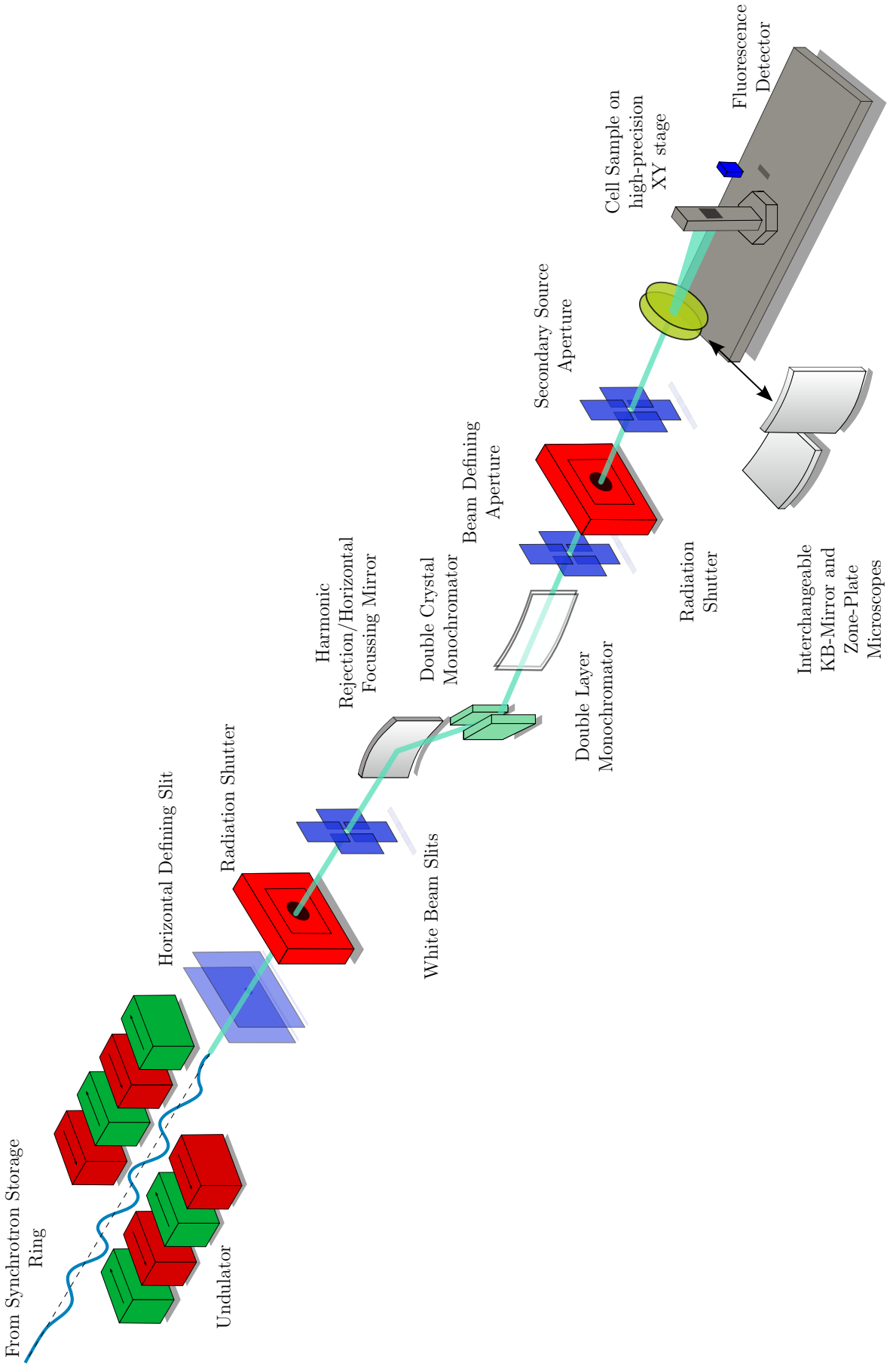

FIGURE 7.2: The various components of the XFM beamline at the Australian Synchrotron Centre.

The scan shown in figure 7.3 was acquired with the Maia detector over three hours. Each pixel has dimensions of 2 µm × 2 µm and the total area of the image is 3 mm × 1.5 mm.

7.4 Results

Clusters of GNPs were observed distributed throughout the sample (figure 7.3). Analysis of this sample showed a mean gold mass of between 0.76 – 1 picogram per cell (figure 7.4). Based on these values and assuming that the gold is concentrated in a single spherical volume, the geometry of the Geant4 simulation should consist of gold spheres with an average radius of 220 nm. These results are similar to the particle size used in the Geant4 simulations described in the previous chapter. While the GNPs are of the same order of magnitude, the size of the gold in the Geant4 simulations could potentially be decreased by 50%.

If the gold is distributed in multiple clusters around the nucleus, we can approximate this with a thin spherical shell of gold surrounding the nucleus. Based on the measured amount of gold and a nucleus radius of 3 µm, the thickness of the gold should approximately 0.46 nm (1/20 the thickness of the membrane). The assumption of a 3 µm radius for the cell nucleus was an assumption based on typical mammalian cell lines and may not be justified for the cell lines used in these experiments.

Since the Maia detector is not sensitive to phosphorous we were not able to correlate the position of the gold with the positions of the cells. In order to match the gold with the position of the cell a high powered optical microscope was used.

Once we had determined what region of the cell samples we wanted to image (using the XFM microprobe) we began using the nanoprobe detector to image the samples with much higher resolution. The detector used for these experiments was the Vortex detector. It has a dwell time between 0.2 and 2 seconds per pixel (much slower than the Maia detector). It is sensitive to photons with energies above 1.1 keV. It is capable of detecting the K, L and M lines of all elements heavier than Magnesium (Z=12). DNA is rich in phosphorous (Z=15) enabling excellent contrast to be obtained between the cell

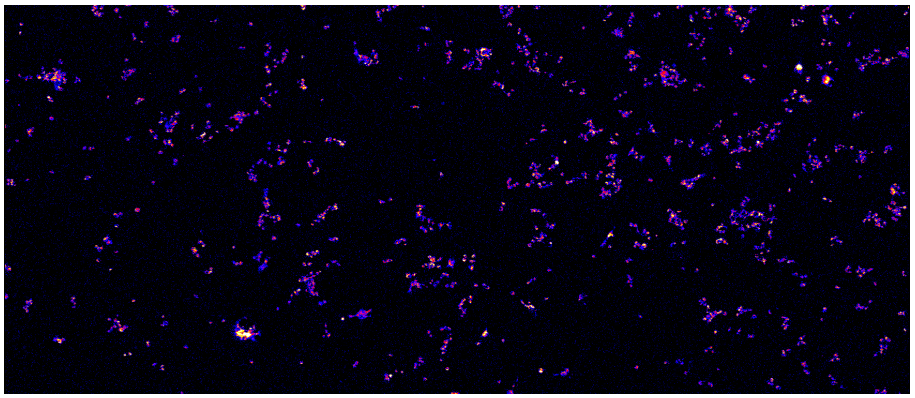

FIGURE 7.3: EMT6 cells containing GNPs, iodine stained, apaptosis stained and unirradiated. The cells were imaged using the Maia detector at the ASC. The intensity of the pixel in the image is proportional to the concentration of gold in the sample.

nucleus and the GNPs clustered around it. Based on the scans performed using the XFM nanoprobe, it appears that the GNPs cluster in multiple small clusters throughout the cytoplasm rather than binding to the nucleus. This is most likely the combination of the properties of the EMT-6 cell line and the delivery method used to infuse the cells with GNPs. The model in chapter 6 was based on human keratinocyte cells which may have different GNP distribution to EMT-6 cells.

We also used the XFM beam-line to image the lymph node of a mouse (figure 7.9). The lymph node was approximately 3 - 4 mm wide and was extracted from the mouse after receiving a GNP solution [86]. The GNPs from the tumour were transported to the lymph node through the lymph vessels where they were finally distributed inside the lymph node. Large quantities of gold, zinc and manganese were observed in different parts of the lymph node.

7.5 Conclusions

The distribution of GNPs within EMT-6 mice cells has been measured at the Australian Synchrotron Centre using the XFM beamline. It was determined that the mean amount of gold in each cell was approximately 1 picogram. This mass was of the same order of magnitude used in the Geant4 simulations of chapter 6. The scans performed using the

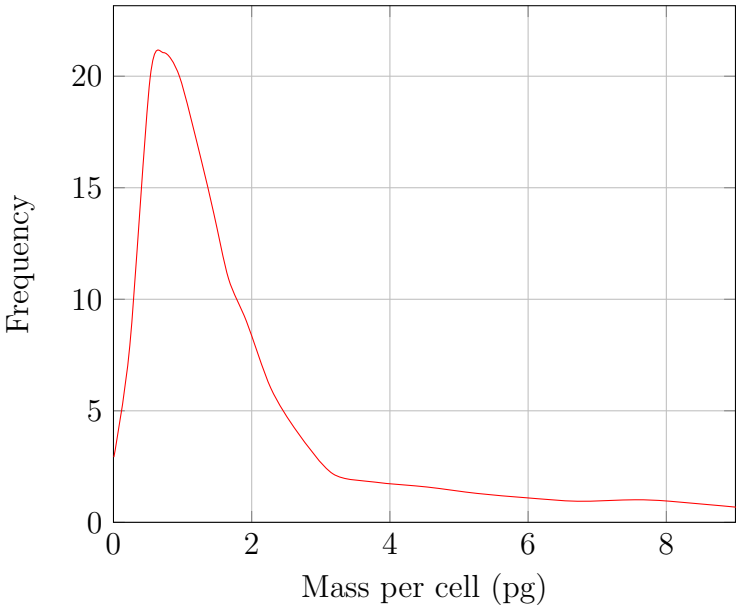

FIGURE 7.4: Mass of gold per cell (pg) vs frequency of cells [86].

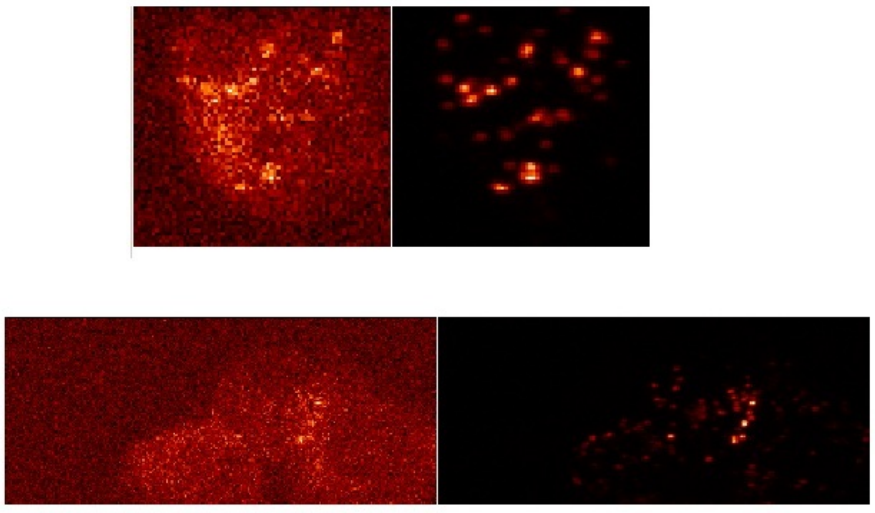

FIGURE 7.5: Cell cluster containing gold nanoparticles scanned with the nanoprobe.

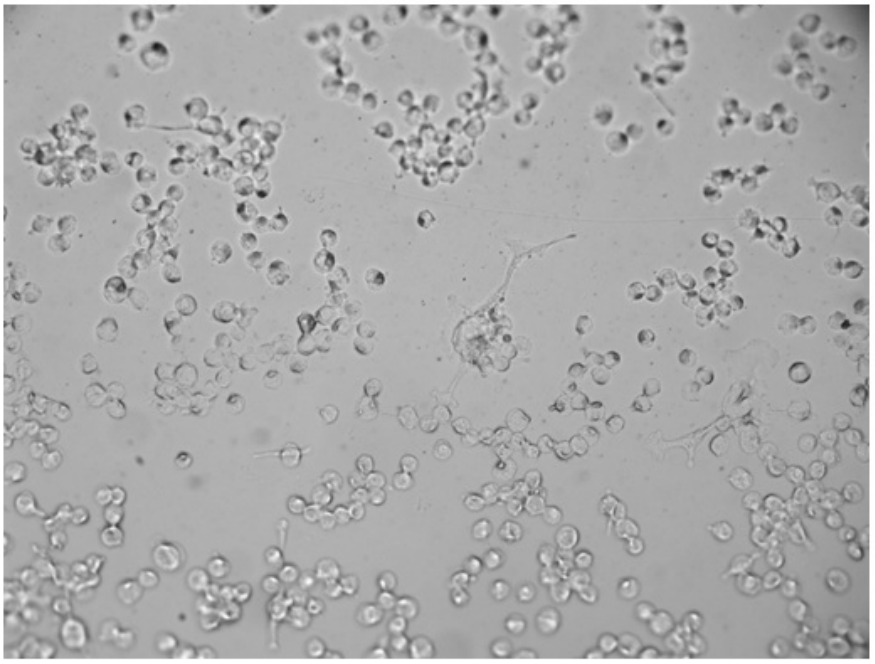

FIGURE 7.6: EMT6 cells at 20 x optical magnification.

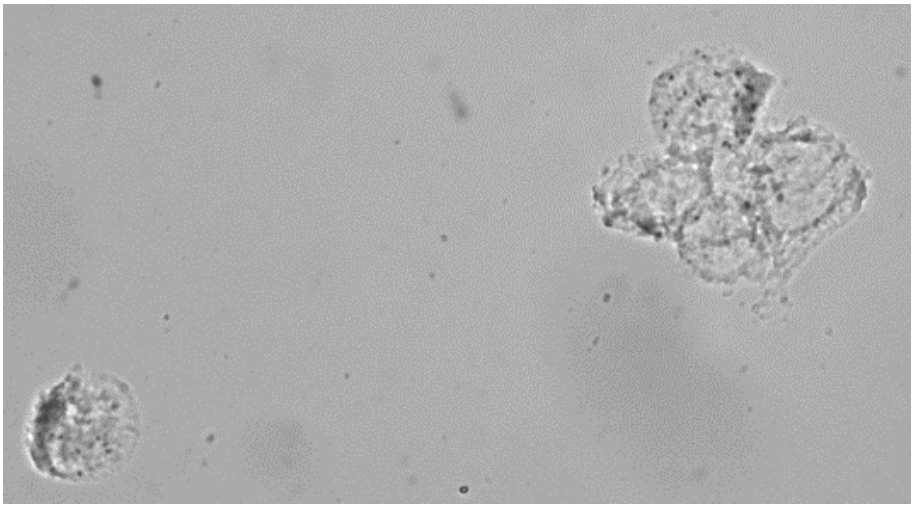

FIGURE 7.7: EMT6 cells targeted using the nanoprobe.

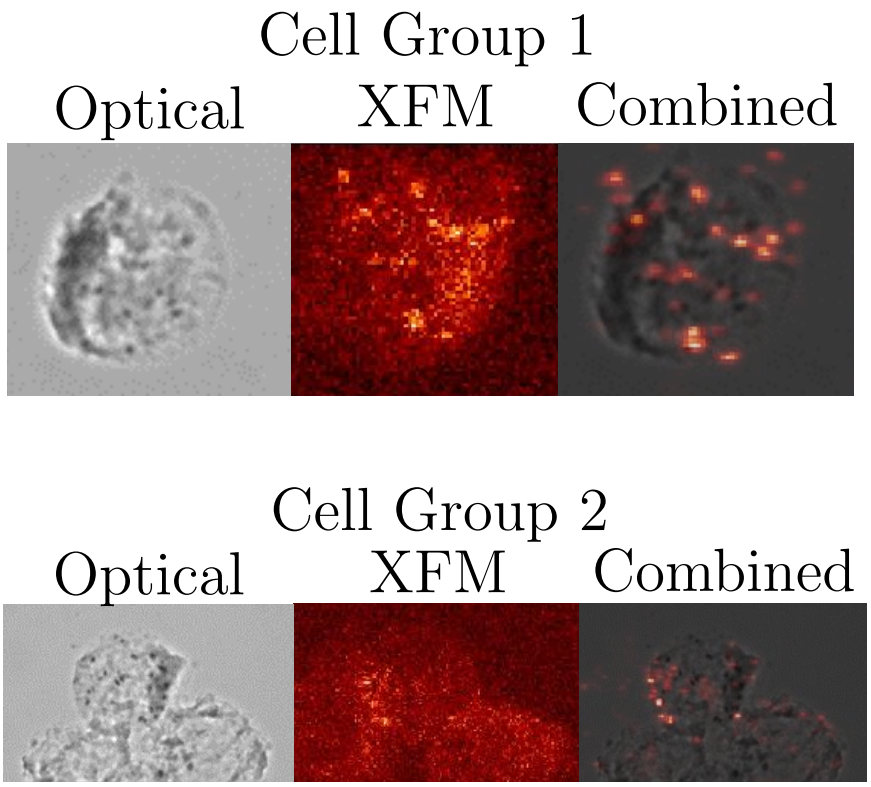

FIGURE 7.8: Overlay of optical and XFM images showing the distribution of GNPs in two different EMT6 cells.

high resolution nanoprobe revealed that the GNPs cluster in small (roughly spherical) volumes throughout the cytoplasm of the EMT-6 cells.

Based on these measurements, it was concluded that the concentration and distribution of gold used in the simulations of chapter 6 is approximately the same as what is observed clinically.

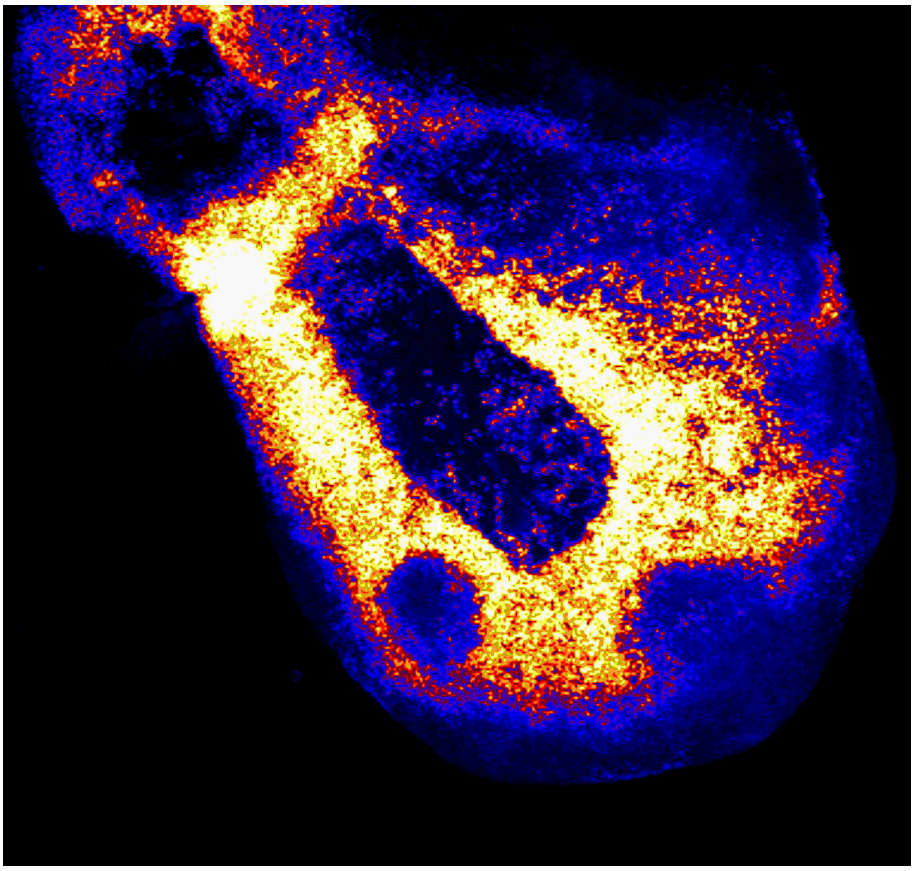

FIGURE 7.9: XFM image of a mouse lymph node containing gold nanoparticles using microprobe. Blue represents regions of low gold concentration and yellow/white represents regions of high gold concentration.

Chapter 8

Radiation Induced Cell Death Model

In this chapter the repair mechanisms of DNA DSBs in cells were modelled. The code developed in chapters 6 and 7 predicts the physical interactions of radiation but does not predict the biological outcome. The two lesion kinetic model was used in this chapter as the basis for the development of an extended stochastic cell survival model.

Cell kinetics form the basis of these radiobiological models and as such this topic will be reviewed.

8.1 Cell Kinetics

A cell that is able to proliferate indefinitely and form a large colony of cells from a single cell is said to be clonogenic. Most types of tumour cells have infinite replicative potential and can grow indefinitely in a cell culture. For cells growing in a culture, the loss of ability to replicate is called reproductive death. After a cell has been irradiated, cells may still maintain structural integrity and be able to produce proteins, synthesize new DNA and may even have the ability to undergo mitosis once or twice. However, if a cell has lost the ability to reproduce indefinitely, it is considered dead.

Sufficiently high doses of radiation (>100 Gy) cause the breakdown of all cellular functions. However, doses as low as 2 Gy may cause loss of reproductive ability [87].

DSB repair, cell death, cell cycle checkpoint arrest are mechanism by which the cell responds to radiation induced DNA damage [88]. The purpose of these processes is to prevent chromosome instability. In radiotherapy, the loss of reproductive ability of clonogenic cells following exposure to ionising radiation typically determines the outcome of the treatment [41].

Loss of proliferative potential of a cell can occur through multiple processes: quiescence, senescence, terminal differentiation and cell death (apoptosis, autophagy, necrosis).

In 1956, Puck [89] demonstrated that most clonogenic cells die through mitosis (mitotic catastrophe) after being exposed to ionisation radiation. The cell may not undergo apoptosis until several divisions have taken place. The number of divisions that take place depend on the radiation dose the cell received. Even after a dose of 2 Gy, the cell may undergo 2-3 cell divisions before apoptosis. The time scale for this process may be of the order of several days. Some cells may die by inter-phase death which is a more rapid process than mitotic apoptosis and occurs without cell division.

The key mechanisms of radiation induced cell death are: apoptosis, autophagy and necrosis [90]. These death pathways prevent the formation of potentially carcinogenic mutations. Apoptosis is an active cell death process where by the cell "decides" to commit suicide. During apoptosis, several processes occur: cell and nuclear shrinkage, nuclear fragmentation and formation of apoptotic bodies. The formation of apoptotic bodies is a process preventing the spread of toxic cellular contents of dying cells.

Autophagy is a cannibalistic mechanism that involves cell degradation of unnecessary or dysfunctional cellular components through the actions of lysosomes [91]. During this process, damaged or recyclable cellular components are isolated within autophagosomes, which are then fused with lysosomes and degraded or recycled. In the case of radiation exposure, this is a defensive reaction that leads to programmed cell death.

Cells that die due to necrosis do not follow the apoptotic signal transduction pathway. Necrosis can occur through various processes including nutrient deprivation and exposure to toxins. Radiation induced necrosis is a rapid process which involves the loss of the

structural integrity of the cell. Necrosis is associated with loss of membrane integrity, deregulated ion homeostasis and swelling of the cell.

Before apoptotic processes begin in a cell, the cell will often detect the radiation damage and arrest the cell cycle. Cells have checkpoints where the DNA sequence is checked for damages before proceeding to the next stage. This process is designed to ensure that chromosomes are replicated correctly and the genome maintains its integrity. Radiation of the cell causes the cells to arrest at these checkpoints. In the G_1 phase, cell cycle arrest is regulated by the p53 tumour suppressor protein [41]. The role of this protein is the conservation of the stability of the genome of the cell by preventing mutation. The p53 protein plays a vital role in the prevention of cancer by mediating apoptosis, maintaining genomic stability and the inhibition of angiogenesis. Actions of the p53 protein include: activation of DNA repair proteins when DNA damage is detected, arrest of the cell cycle between the G_1/S phases to allow time for DNA repair proteins to repair the damage and can also initiate apoptosis if the DNA damage cannot be repaired. The cell cycle can also be arrested during G_2 and M phases.

Radiation damage to DNA can be repaired by several processes:

1. **Recombination:** A nearby radical and the DNA radical can undergo an ionic reaction to regenerate the original DNA.

2. **Restitution:** Chemical restoration of the DNA without the assistance of an enzyme. This type of reaction is called reduction and is performed with the assistance of a reducing agent that reacts with the radicals. The most common intracellular reducing agent is called glutathione (GSH). It is a naturally occurring antioxidant synthesised in the body which prevents damage to important cellular components caused by reactive oxygen species including free radicals and peroxides. The sulfhydryl group on glutathione can donate a free hydrogen molecule to the DNA radical which restores the DNA and produces a stable sulphur radical.

3. **Repair:** There are several cellular enzymes that have the ability to recognise and repair DNA strand breaks. The time scale of repair is of the order of minutes to hours depending on the complexity of the DNA strand break.

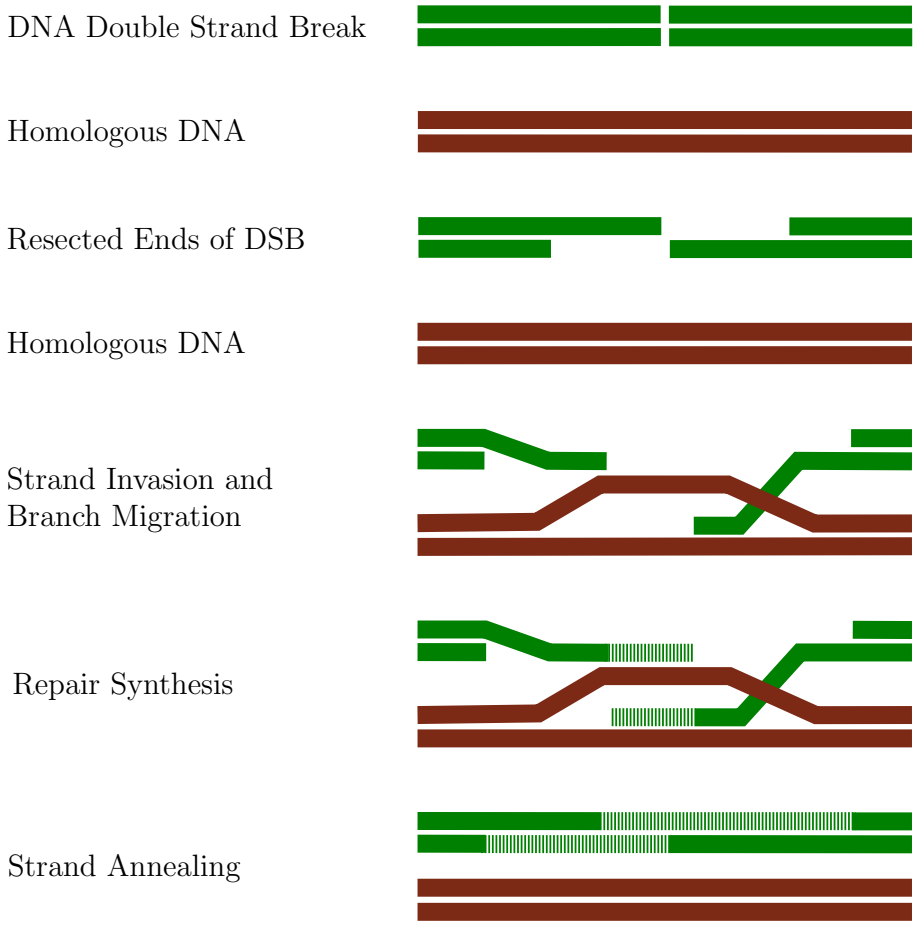

FIGURE 8.1: Homologous recombination.

There are several key mechanisms in which DNA strand breaks are repaired. These methods are base excision repair (BER), nucleotide excision repair (NER), DNA mismatch repair and DSB repair. DNA DSBs can be repaired by either homologous (figure 8.1) recombination or non-homologous end joining (figure 8.2).

Base excision repair is important for the repair of most single strand breaks and base damages [92]. The repair half-time for this process is approximately 5 minutes depending on cell type. Its primary function is the removal of damaged bases that could lead to mutations by misrepairing or lead to breaks in DNA during replication. BER is initiated by DNA glycosylases which recognises and removes specific damage or inappropriate bases leading to the formation of an abasic site (i.e. a section of DNA that does not contain a base). The single strand break is then repaired by synthesising and replacing a new nucleotide.

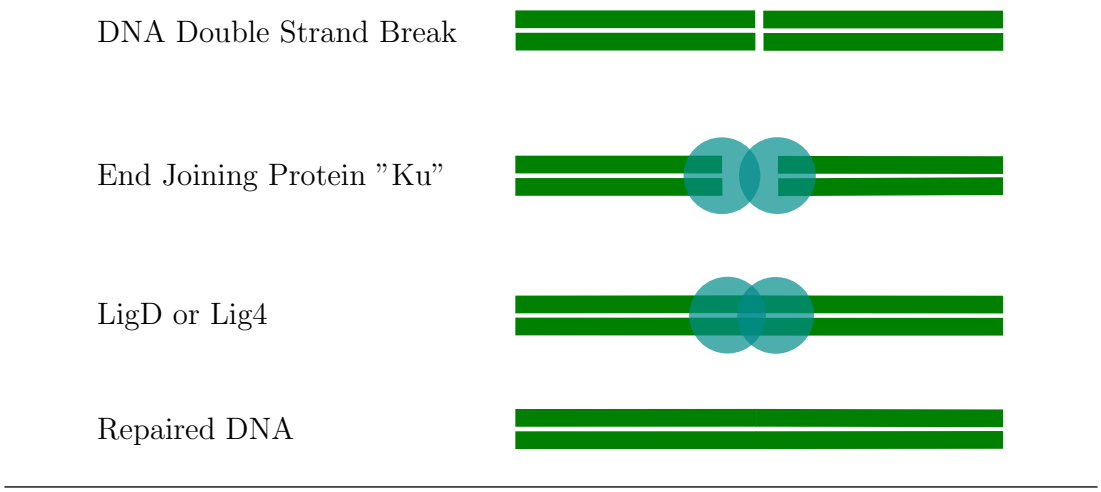

FIGURE 8.2: Non-homologous end joining.

DNA mismatch repair occurs when an incorrect nucleotide base is present in a particular sequence of the DNA [93]. In normal spiral DNA, bases form pairs between the two strands: adenine with thymine and cytosine with guanine. DNA mismatch repair is a system for recognising erroneous sequences of base pairs in the DNA. If a single base is missing or the wrong base is present in the DNA, the base simply needs to be replaced in accordance to the base present on the opposite strand. This process is typically very rapid and has a small probability of error.

Double strand breaks are repaired either by homologous recombination or non-homologous end joining processes.Homologous recombination occurs in cases where bases on opposite stands of DNA have been damaged or deleted and therefore DNA mismatch repair cannot occur [94]. Damages of this complexity require a similar or identical sequence of DNA which is used as a template for repair. If the cell is in the S or G_2 phase, the cell uses a sister chromatid as a template to repair the DNA. If the cell is in the M phase, it uses a second chromosome as a template. This process does not occur during G_1 phase.

The major mechanism of DSB repair is non-homologous end joining [94]. This process can be active in any stage of the cell cycle. This process differs from homologous recombination in that it does not require a homologous template. In this process, the broken ends of the DNA are ligated directly without the need for a template. This process is usually successful in repairing DNA DSBs. However, if the DNA has been exposed to a form of high LET radiation, multiple DSBs may form in close proximity. In this case,

there is a chance that other nearby damaged DNA molecules may be joined resulting in severe chromosomal rearrangements.

8.2 Summary of Two-Lesion Kinetic Model

The TLK model was designed to combine the biochemical repair processes of DNA DSBs and radiation induced cell death. It was suggested by Stewart [21] that a successful radiation induced cell death model should "be capable of predicting a wide range of exposure conditions using a single set of model parameters". The model assumes that more than one type of DSB exists. Another property of the TLK model is the ability of the DSBs to interact in a pair wise fashion to form irreversible lethal and non-lethal damages.

The TLK [21] model (as well as LPL and RMR models discussed in chapter 1) includes first order non-saturable repair processes meaning that the number of enzymes available for the repair of DNA is equal to or greater than the number of DSBs. It has been suggested [95] that the cellular repair processes associated with damage from 250 kV x-rays to V79 cells may saturate at doses as low as 2.4 cGy or as high as 30-90 Gy [96]. All three models assume that DNA repair is the result of biochemical enzymatic processes. The TLK model extends this assumption to suggest that the repair probability of DSBs depends on the severity of the lesion. In all three models, the specific biological repair processes are not included in the model but are instead hidden in a "lumped parameter" approach.

Stewart pointed out that as the complexity of a DNA repair model increases, the number of freely adjustable parameters inevitably increases. Such a model may unfortunately become a parameter tuning and curve fitting exercise that does not reflect the reality of DNA repair.

The radiobiological parameters used in the TLK model are λ, β, Y and η. The λ_1 and λ_2 are the repair probabilities of simple and complex DSBs by linear repair mechanisms.

These can be conveniently expressed in terms of simple and complex DSB repair half times τ_{DSB} (the time required for 50% of the lesions to be repaired).

$$\lambda_{DSB} = \frac{\ln(2)}{\tau_{DSB}} \tag{8.1}$$

The β_1 and β_2 parameters are the probabilities of incorrectly repairing simple and complex DSBs respectively. Y is the number of base pairs per cell and Σ_{DSB} is the expected number of DSBs initially created by the radiation per nucleotide per Gy. The η parameter is the rate of formation of lethal damages formed by pair wise interactions of DSB through end joining processes. Pairwise interaction of DSB occurs when two DSB breakages from distinct DNA helices interact (and attempt to repair incorrectly) to form lethal or non-lethal mutations.

These key parameters appear in the four first-order non-linear differential equations of the TLK model:

$$\frac{d\overline{L}_1(t)}{dt} = 2\dot{D}(t)Y\Sigma_1 - \lambda_1\overline{L}_1(t) - \eta\overline{L}_1(t)[\overline{L}_1(t) + \overline{L}_2(t)] \tag{8.2}$$

$$\frac{d\overline{L}_2(t)}{dt} = 2\dot{D}(t)Y\Sigma_2 - \lambda_2\overline{L}_2(t) - \eta\overline{L}_2(t)[\overline{L}_1(t) + \overline{L}_2(t)] \tag{8.3}$$

$\overline{L_1}$ and $\overline{L_2}$ are the expected numbers of simple and complex DSBs respectively at time t. They depend on factors such as the absorbed dose rate, binary misrepair probabilities and other biological parameters.

$\overline{L_f}$ and $\overline{L_m}$ are the average accumulated numbers of lethal lesions and non-lethal mutations respectively in the cell at time t. $\overline{L_f}$ and $\overline{L_m}$ depend on $\overline{L_1}$ and $\overline{L_2}$ at time t and therefore need to be solved numerically (in the general case):

$$\frac{d\overline{L}_f(t)}{dt} = \beta_1\lambda_1\overline{L}_1(t) + \beta_2\lambda_2\overline{L}_2(t) + 0.25 \times \eta[\overline{L}_1(t) + \overline{L}_2(t)]^2 \tag{8.4}$$

$$\frac{d\overline{L}_m(t)}{dt} = (1-\beta_1)\lambda_1\overline{L}_1(t) + (1-\beta_2)\lambda_2\overline{L}_2(t) + 0.75 \times \eta[\overline{L}_1(t) + \overline{L}_2(t)]^2 \tag{8.5}$$

In the TLK model, a simple DSB is considered to be a section of DNA between 10 and 20 base pairs in length containing a break in each strand of the DNA. A complex DSB is considered to be a simple DSB with additional elementary damages such as base damage, strand breaks or base deletion within the same section of DNA. This formalism has been used for the basis of the cell death model in the current work.

The TLK model was solved numerically in [21] using Gear's backward differential algorithm for an arbitrarily complex dose rate function $\dot{D}$. The biological parameters were calculated for the TLK model using a trial and error method which attempted to find a solution set of optimal parameters which fit experimental data for V79 cells. The quality of the fit was established by calculating a positively weighted sum of the error or "figure of merit" parameter. Optimal parameters for the TLK model were found and were consistent with experimental data.

The TLK model was calibrated and optimised in [22] using a set of experimental cell survival data for Chinese hamster (V79) cells for a single dose and split dose irradiations. After finding many local solutions to the parameter set, the TLK model was shown to be in good agreement with experimental data. Discrepancies between experimental and model predicted data was said to be the result of additional biological factors and processes not being included in the model.

The introduction of two types of DSB in the TLK model enabled a locally optimal set of simulation parameters to be found that was both consistent with biological parameters and accurately predicted cell survival data for V79 cells. Small discrepancies between experimental and model-predicted data suggest that there is still one or more missing biological repair processes not considered in the TLK model. It was suggested that enzymatic repair of DNA DSBs may saturate at high doses where the number of DSB in each cell is larger than the number of available enzymes to repair them. The importance of binary repair processes was expressed for high linear energy transfer (LET) radiation as there will be more spatially correlated DSB damages. Stewart also suggested that the

repair characteristics of the individual damages in a cell are most likely independent (or almost independent) of the particle LET. This means for example, that while low and high energy protons have different density ionisation tracks, the repair processes in the model should be equally valid for all LETs.

Utilising the analytical formulation of cell repair from TLK, its functionality will be extended to a cell by cell analysis in the current work. The model parameters presented in [21] have been used as a starting point for calibration of the model developed in the current work.

8.3 Methods

In the current work, the previously developed tumour growth and irradiation model of chapter 5 was extended to include a stochastic ionisation damage clustering and DNA lesion repair model.

8.3.1 Radiation Transport Simulation

In order to accurately predict the formation and distribution of DSBs in a cell, simulation of accurate radiation track structures is essential. The Geant4-DNA processes constitute a high precision model designed to track the individual interactions of a particle as it traverses a water medium. Using Geant4-DNA, the formation of DNA DSBs in the nucleus of the cell was modelled. To improve the efficiency of the simulations, damage to the remaining regions of the cell (cytoplasm, membrane, and endoplasmic reticulum) was simulated using the less computationally expensive low energy Livermore physics model as described in chapter 6. Since the cytoplasm, membrane and reticulum do not contain any DNA, the cell death mechanisms in these regions are very different. High precision track structure is therefore not necessary in these regions as there are no significant targets of nanoscopic scales. The Livermore physics processes enable the overall dose to other regions of the cell to be calculated. The probability of cell death due to damage to regions

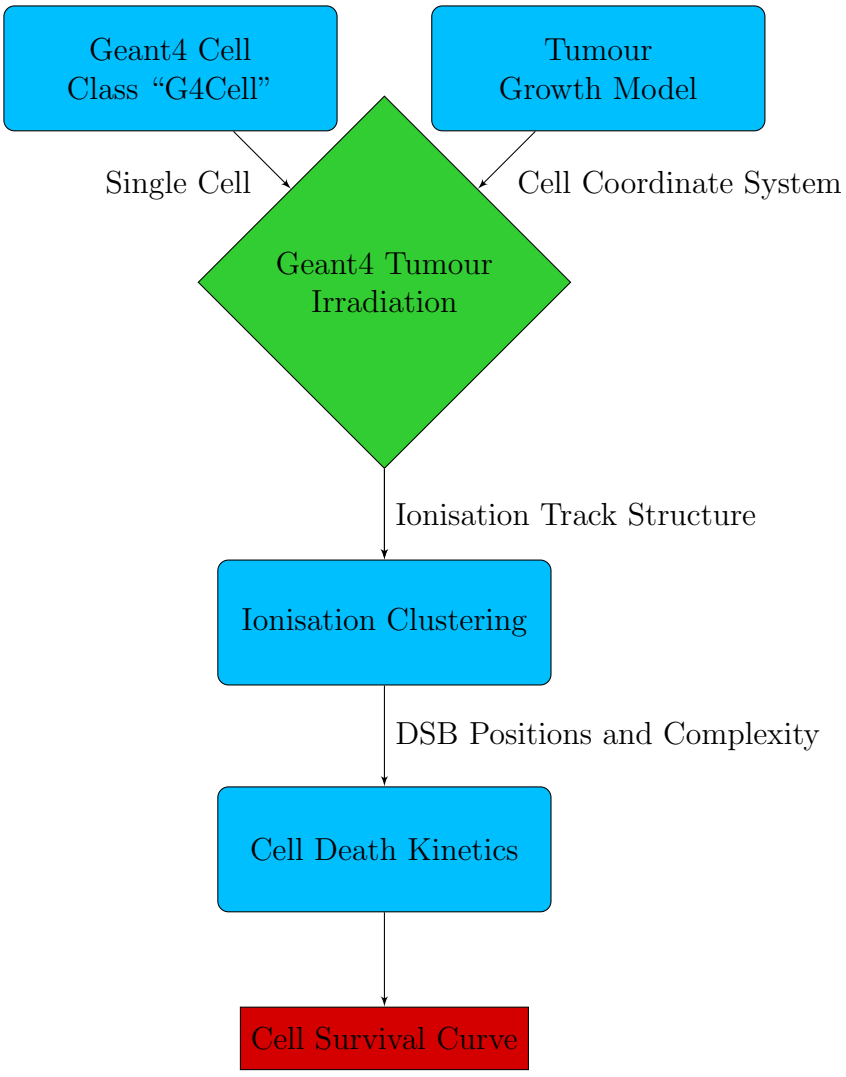

FIGURE 8.3: Diagram showing the structure of the integrated radiobiological model developed in the current work.

other than the nucleus will be considered to be proportional to the total dose deposited in these regions rather than the complexity of the ionisation track structure.

The radiation damage simulation developed using Geant4 in chapter 5 generates several output files during the simulation. These files contain large quantities of data including the position of every ionisation event produced in the nucleus and nucleolus, the energy deposited by every ionisation event and the cell number that was damaged. The data files produced for the nucleus and nucleolus are significantly larger than those produced in the cytoplasm as the position of every ionisation event is recorded.

8.3.2 Clustering Algorithm

The first stage in predicting the radiobiological processes was to design Matlab™ code to read in the damage from Geant4 and sort the damages into each cell. Each line of this data contains the cell number, the position of the ionisation event, the mass of the particular cell region and the energy deposited by the particle at each step. The Matlab™ code sorts the damage by cell and then places the damage in a $1 \times n$ cell array, where n is the number of cells in the tumour.

Once the data has been sorted and stored in Matlab™ the clustering of ionisation events into DSBs is performed. The definition of a DSB according to [21] is "two or more ionisation events located on the DNA double helix within a distance of 20 base pairs"(20 base pairs (bp) correspond to a distance of 6.8 Å). Using this definition for a DSB, an original ionisation clustering algorithm was developed in the current work to predict the formation of DSBs in the nucleus of the cell. Stewart allowed for the possibility of several types of DSB in the TLK model, containing a variable number of ionisation events in each cluster. Each type of DSB is believed to have independent enzymatic repair processes. In the current work, DSB clusters containing three or more ionisation events (complex DSB) are considered to have the same repair processes as a complex DSB.

The clustering algorithm was developed under the assumption that radiation deposits energy in discrete steps which form primary and secondary tracks of ionisation events. The density of the ionisation events in these tracks is proportional to the linear energy transfer of the radiation type.

The algorithm operates using the following steps (flowchart in figure 8.4 and code in appendix C):

1. Start at the beginning of an ionisation track.
2. Calculate if the next ionisation in the track is within 10 bp of the first.
3. If they are within 10 bp of each other, check to see if the third ionisation event in the track is within 10 bp of the first. If the first is located more than 10 bp from the third, the damage is treated as a simple DSB and recorded in the damage array.

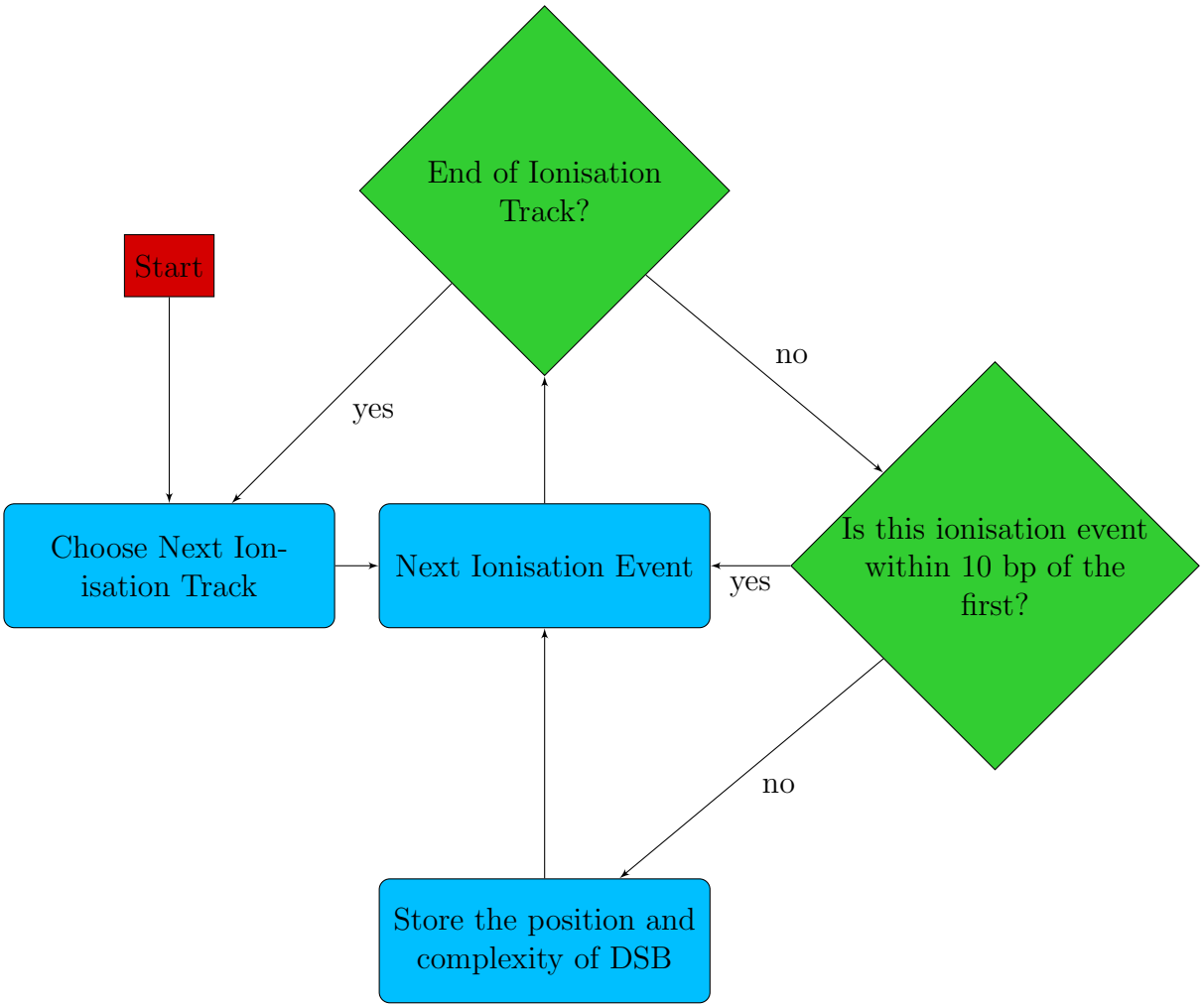

FIGURE 8.4: Diagram showing the structure of the ionisation clustering algorithm developed in the current work.

4. The code continues along the track, checking whether the ionisation events are separated by less than 10 bp and that the total diameter of the cluster is less than 10 bp.

5. Every time the distance exceeds 10 bp, the number of ionisations in that cluster is stored to a table and a new cluster starts.

6. This process is repeated for every ionisation event in the recorded tracks.

The limitation of this algorithm occurs in the case of the crossover of two particle tracks. If two particle tracks overlap, the ionisation events at the cross over point are clustered individually instead of forming a DSB of increased complexity. Closer inspection of the

track structure in each cell revealed that the crossover of two ionisation tracks in a single cell nucleus is a very rare occurrence for doses between $1 - 5$ Gy and as a result, the impact of this limitation is negligible. For the purposes of the current research, the assumptions made in the clustering algorithm are justified.

To account for the likelihood of an ionisation event in the nucleus interacting with DNA, the percentage of volume occupied by the DNA within the nucleus was required. Since the base pairs of the DNA in the nucleus are not modelled explicitly, a volumetric correction factor was added to calculate the probability that two or more ionisation events located in close proximity form a DNA DSB. With current computer technologies it would be computationally impractical to model each of the billions of base pairs that form the DNA double helix in each cell.

In many mathematical and computational models of the DNA double helix, DNA is assumed to be a cylinder of constant radius. Human (and most other mammal) genomes contain in the order of a billion base pairs. Each base is separated by 3.4 Å (0.34 nm). A genome sequence with a mean length of 4.682×10^9 bp for V79 cells is assumed in the current work (based on [21]).

The approximate radius of the DNA double helix is 1 nm. As a result, the volume of the DNA cylinder occupies approximately 5 μm^3.

V79 cells (a cell line used commonly in radiobiological research) have a nucleus diameter of 7 µm (also containing a 5 µm radius nucleolus which does not contain DNA). As a result the DNA occupies only 0.547 % of the total volume of the nucleus. In order to achieve accurate cell survival results, the spectrum of DSB values obtained using the clustering of ionisation method must be multiplied by the probability that a random cluster of 2 ionisation events within 20 bp will hit the DNA target. This probability is the fraction of volume occupied by the DNA in the nucleus (e.g. 5.47×10^{-3}). Since there is a great deal of uncertainty in the literature regarding the actual genome length of V79 cells, each cell in the model was allocated a random genome length from a Gaussian distribution with a mean of 3.3 Gbp and standard deviation 1.5 Gbp (based on values published in the literature [97]).

The damage clustering algorithm produces a damage spectrum for each cell containing the number of DSBs of each type. Once the DSB damage spectrum has been calculated for each cell, the likelihood of a particular cell surviving the radiation exposure can be calculated using a Monte Carlo implementation of the TLK model.

8.3.3 Cell Survival Algorithm

The TLK model described in [21] functions under the assumption that there are two types of enzymatic repair processes for the two types of DNA DSBs. Simple and complex DSBs are repaired using two independent methods each taking different amounts of time to repair. The probability of a given DSB being repaired depends on the DSB lesion repair half-time (i.e. the time required for half of the DSBs of a given type to repair). This half-time is cell line dependent but radiation type independent.

The formulation of the TLK model used in this chapter describes the kinetics of each cell within the tumour. The Geant4 model enables the damage to each individual cell in the tumour to be modelled and calculated. The differential equations 8.2 and 8.3 describe the repair rate of simple and complex DSBs as an average for the tumour. These equations are assumed to be equally valid in describing the rate of repair of DSBs in a single cell. These analytical formulas will be used to represent the repair kinetics of each of the individual cells in the tumor by making simple substitutions:

$$L_{1,i} \leftrightarrow \overline{L_1},\ L_{2,i} \leftrightarrow \overline{L_2},\ L_{f,i} \leftrightarrow \overline{L_f},\ L_{m,i} \leftrightarrow \overline{L_m}$$

$$\frac{dL_{1,i}(t)}{dt} = 2\dot{D}(t)Y\Sigma_1 - \lambda_1 L_{1,i}(t) - \eta L_{1,i}(t)[L_{1,i}(t) + L_{2,i}(t)] \tag{8.6}$$

$$\frac{dL_{2,i}(t)}{dt} = 2\dot{D}(t)Y\Sigma_2 - \lambda_2 L_{2,i}(t) - \eta L_{2,i}(t)[L_{1,i}(t) + L_{2,i}(t)] \tag{8.7}$$

These equations can be solved numerically using the Euler method for solving differential equations (providing a sufficiently small time interval Δt is chosen):

$$L'_{1,i} = \frac{dL_{1,i}}{dt} \tag{8.8}$$

$$L'_{1,i} \approx \frac{L_{1,i}(t+\Delta t) - L_{1,i}(t)}{\Delta t} \tag{8.9}$$

$$L_{1,i}(t+\Delta t) = L_{1,i}(t) + L'_{1,i}\Delta t \tag{8.10}$$

L_f and L_m depend on L_1 and L_2 at time t. Using the Euler method, the values of L_1 and L_2 at time t can be used to calculate L_f and L_m. For a sufficiently small time step Δt, the values of L_1, L_2, L_f and L_m can be solved by iterating through time from $t = 0$ to $t = T$ where T is the amount of time given to the cells to repair.

Using the Geant4 code developed previously, the boundary conditions for this model are:

$$L_{1,i}(0) = \text{Initial number of simple DSB after irradiation}$$
$$L_{2,i}(0) = \text{Initial number of complex DSB after irradiation}$$
$$L_{f,i}(0) = 0$$
$$L_{m,i}(0) = 0$$

This model has been implemented in Matlab™ and used to solve the equation for the accumulated number of lethal damages in each cell in the tumour.

The final step in generating a cell survival curve using the extended TLK model is to calculate the probability of survival for a cell with $L_{f,i}$ lethal damages. Assuming a Poisson distribution for the number of lethal lesions per cell, we can write the survival probability as [18]:

$$S_i = e^{-L_{f,i}(T)} \tag{8.11}$$

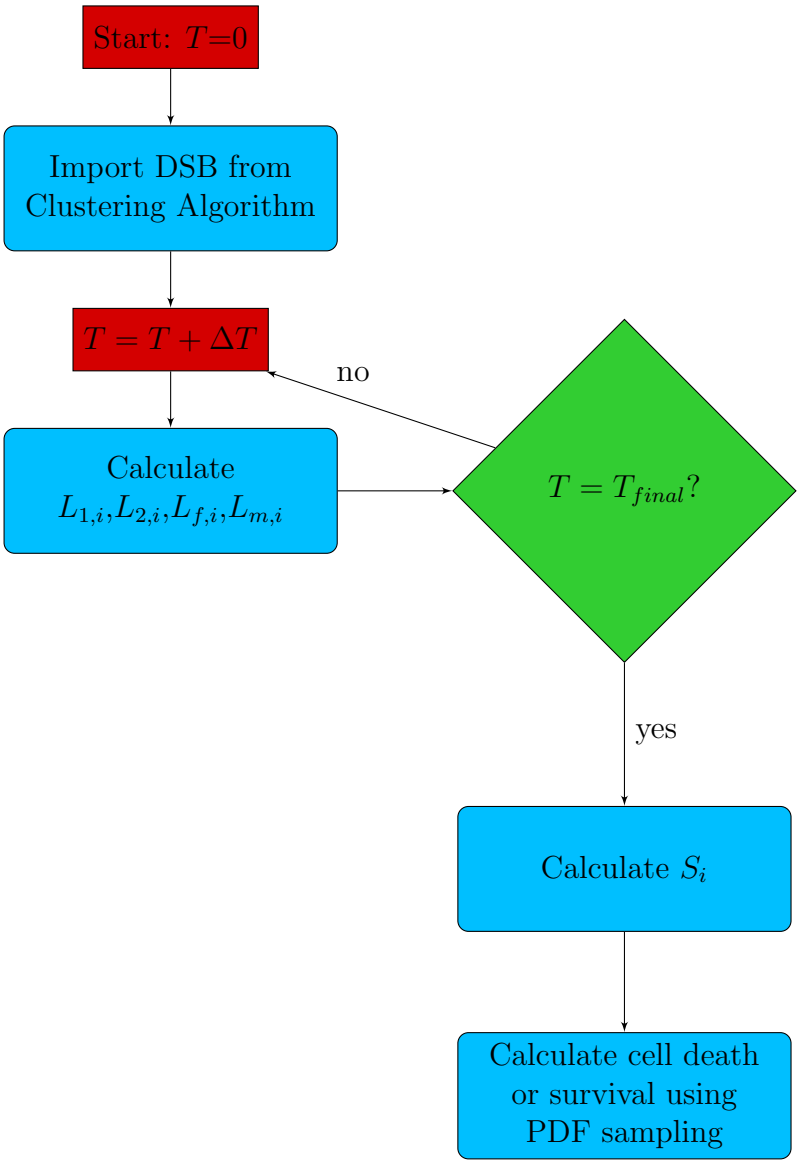

FIGURE 8.5: Diagram showing the structure of the cell death algorithm.

where T is the amount of time after irradiation that is given to cells to repair. For each cell in the tumour, S_i is calculated, (i.e. the probability that a given cell will survive after being irradiated in the Geant4 simulation). This code is listed in appendix D.

A pseudo-random number generator is used to determine whether a given cell survives by sampling the probability distribution. This process is repeated for each cell in the distribution and the total number of cells that survived is calculated (flowchart in figure 8.5).

8.3.4 Model Calibration

To calibrate the developed stochastic model, a suitable publication containing experimental data was identified. Since chemical damages induced by radiation have not been modelled in Geant4, it was likely that if x-ray radiation was used in the simulation, the results would over-estimate the cell survival fraction, as a large fraction of the damage caused by x-ray radiation is due to chemical interactions (chapter 10). It was decided that low energy proton radiation should be used for parameter calibration as the majority of biological damage from low energy proton radiation is due primarily to direct ionisation processes.

The irradiation stage of this code requires a significant amount of time to run and is highly dependent on the number of cells in the tumour. Since low energy proton radiation is a high LET form of radiation, the number of primary and secondary interactions that need to be tracked in Geant4 is much higher than that of x-ray radiation. Therefore the simulation time for proton radiation simulations is higher than that of x-ray radiation.

The publication that was chosen to calibrate the model was by Folkard et. al. 1989 [95]. This paper was chosen for several reasons. Firstly, the experimental set-up was described in great detail making it easier to replicate the conditions in Geant4. The geometry of the V79 cells including the size of the cell and its nucleus had been measured. The cell geometry that was used was a mono-layer of cells instead of a 3D volume which would decrease the amount of simulation time required. The energy spectra had also been measured at the cell layer which was replicated in the simulation. Finally, a clear cell survival curve for three low energy proton spectra were presented enabling experimental and computational results to be compared accurately.

In the experiment, low energy protons were produced by a Gray laboratory 4 MV Van de Graaff accelerator. The beam emerged from a 25 mm diameter by 50 µm thick polyimide window followed by a gold scattering foil. The physical V79 cell geometry used in our Geant4 simulations was identical to that reported in the publication (in terms of cell and nucleus size). The cells are depicted as an unattached cell with a mean diameter of 18 µm and a nucleus with mean diameter 15 µm. Data relating to the properties of the

TABLE 8.1: Summary of simulation cell parameters.

Cell Type	Value for V79
Mean Cell Radius	8.5 µm
Mean Nucleus Radius	7.0 µm
Mean Nucleolus Radius	5.0 µm
Simple DSB Repair Half-Time	4.0 minutes
Complex DSB Repair Half-Time	12.0 hours
Cell Cycle Time	15.0 hours
Tumour Geometry	918 cells (mono-layer) 0.6 mm × 0.6 mm

TABLE 8.2: Summary of simulation radiation parameters.

Radiation Property	Simulation Value
Radiation Type	Proton
Number of Particles	55,000 per Gy
Energy Spectra	Gaussian. Mean 0.76 MeV and 1.9 MeV, FWHM: 0.25 MeV
Source Type	Planar 0.7 × 0.7 mm^2, unidirectional

membrane, reticulum or nucleolus are not provided in [95]. The membrane was assumed to be 10 nm thick (chapter 5).

The energy spectra were measured at the position of the cells in [95]. After the 4 MV proton beam propagated through the apparatus and reached the cells, the energy spectra were Gaussian distributions with a mean energy of 0.76 MeV and 1.9 MeV and a full width at half-maximum of approximately 0.25 MeV. These spectra were modelled in the Geant4 simulations of the current work. The V79 cells were irradiated in air and the survival fraction at 1 Gy dose intervals were calculated after irradiation. A total dose of 5 Gy was delivered to the cells in 1 Gy intervals. A summary of all model parameters used in the current work are listed in tables 8.1, 8.2 and 8.3.

The uncertainties in the biological parameters such as linear and pairwise repair times were accounted for by randomly allocating parameter values from a Gaussian distribution to each cell. The mean and standard deviation for these distributions were calculated from the range of values provided in [21] for V79 cells. The uncertainty in the cell survival measurements were then calculated by running several simulations and calculating the mean and standard deviation of the results.

Table 8.3: Summary of clustering parameters.

Radiation Property	Simulation Value
Distance between DNA bases	3.4 Å (0.34 nm)
Radius of DNA Helix	10.0 Å (1 nm)

8.3.5 Parameter Sensitivity Analysis

The process of calculating a globally optimal parameter set for V79 cells began with an investigation of the effect of changing each parameter individually on the cell survival output. The models input parameters were changed individually between the extreme physically and biologically realistic values while keeping the others constant. A parameter sensitivity analysis was performed for the model parameters: λ_1, λ_2 (simple and complex DSB repair probabilities per unit time), β_1, β_2 (probability of simple and complex DSB being repaired incorrectly), η (binary interaction probability) and ξ (genome length). The changes observed in the simulated cell survival curve by a relative change to one of these parameters determined the order in which the parameters were optimised.

To verify the functionality of the model developed in this chapter, the simulation parameters were calibrated with the two sets of experimental measurements. The quality of the fit was determined by calculating the sum of the squared differences between the experimental and simulated cell survival data points. The parameter which altered the output value most significantly was varied first between a range of physical extrema. The optimal value for the first parameter was defined to be the value that minimised the residual function. Once the first parameter was optimised, the remaining parameters were optimised using the same method as the first.

8.4 Results

8.4.1 Clustering Algorithm

Figure 8.6 shows the results of the clustering algorithm when used to analyse the DNA damage of a cell exposed to three types of radiation: protons, alpha particles and carbon

ions. A single cell was exposed to a single ion with energy 10 MeV/amu. The ionisation damage was then exported from Geant4 and imported into the clustering algorithm developed in the current work. The results indicate that the complexity of the DNA damages increases with increasing ion atomic number. Protons (of this energy) are capable of producing complex double strand breaks (CDSBs) containing at most 3 ionisation damages. Carbon ions of the same energy per nucleon are capable of producing lesions containing 6 or more ionisation events which are significantly more difficult to repair. This mechanism is responsible for the higher relative biological effectiveness seen for heavy ions compared to low LET radiation.

The time required to calculate the damage spectrum is strongly dependant on the total number of ionisation events. To calculate the damage spectrum of a single 10 MeV/amu carbon ion, the processing time is approximately 15 seconds. For a proton, the processing time is less than half a second.

8.4.2 Model Calibration

The parameters implemented in the current work were calibrated to fit the cell survival data after irradiation with two different proton energies. The cell survival curves for each subset of parameters in the physically and biologically plausible range of values were calculated (using a sufficiently small step size). Each cell survival curve was compared with the experimental values and a globally optimised set of parameters was deduced. The set of optimal parameters for V79 cells in the current model were determined to be: $\lambda_1 = 10 \pm 0.5$ SDSB/hour/cell (4.15 minute repair half time), $\lambda_2 = 0.0565 \pm 0.0001$ SDSB/hour/cell (12 hour repair half time), $\eta = 0.00005 \pm 5 \times 10^{-7}$, $\beta_1 = 0$ (simple DSBs almost always repair correctly) and $\beta_2 = 0.00090 \pm 0.0001$ (9 in every 10,000 CDSB repair incorrectly).

Cell survival curves produced by the developed cell death model are seen in figure 8.7. The figure shows the percentage of cells that survived the low energy proton radiation exposure as a function of the radiation dose received by the cells. The experimental results are presented in the same figure for comparison. There is a large amount of uncertainty in

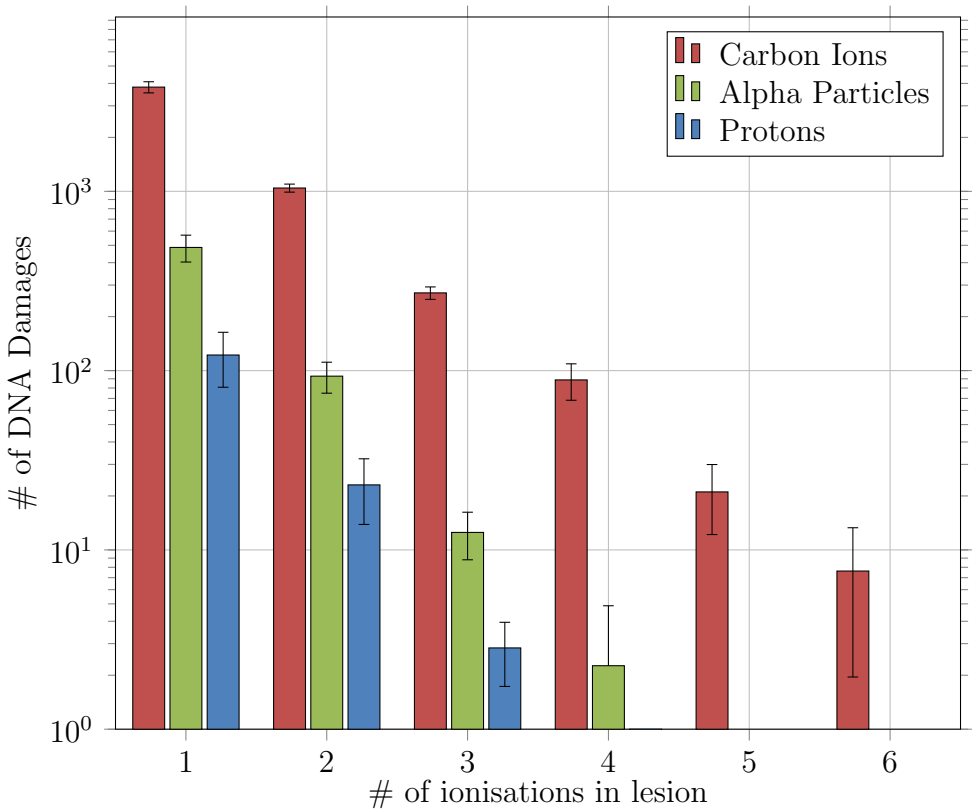

FIGURE 8.6: Number of recorded DNA damages of increasing complexity in a cell exposed to proton, alpha particles and carbon ions of energy 10 MeV/amu. Calculated using the ionisation clustering algorithm.

the parameters used to generate the data in figure 8.7. The largest of these is the amount of volume occupied by the DNA in the cell whose value varies by as much as a factor of 2. Other significant sources of uncertainty include the repair probabilities for simple and complex DSB which may also vary by as much as a factor of 3. Despite these initial uncertainties, the simulation results show excellent agreement with the experimental data. The effect of these uncertainties on the quality of the model calibration was investigated by performing a parameter sensitivity analysis.

8.4.3 Parameter Sensitivity Analysis

From figures 8.8 - 8.13 it is apparent that the parameters that affect the cell survival curves most significantly are β_2, η and ξ. The genome length ξ has the largest degree of uncertainty of all the parameters used in this model. To integrate this uncertainty

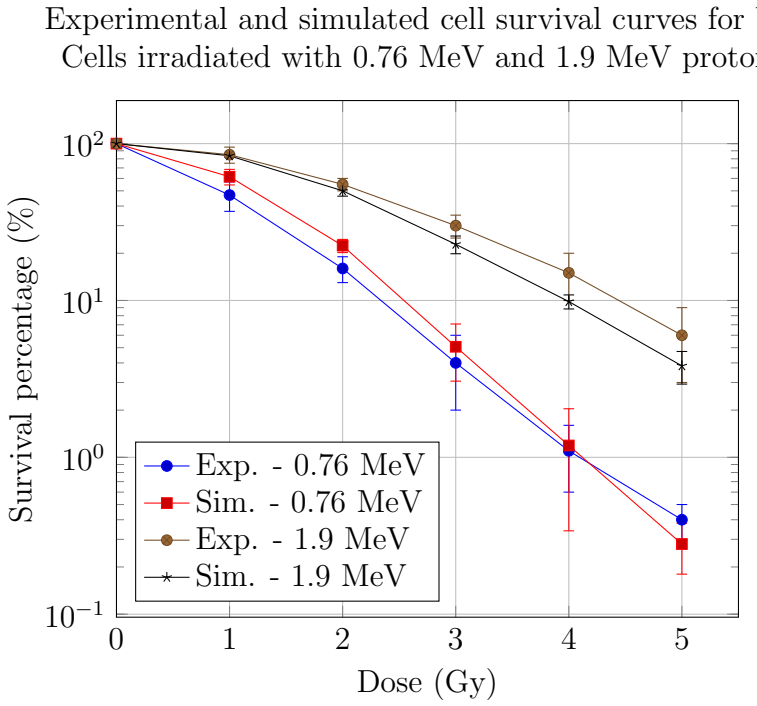

FIGURE 8.7: A comparison of simulated cell survival curves (generated in the current work) vs. experimental values [96] for V79 cells irradiated with 0.76 MeV and 1.9 MeV proton radiation.

into the model, each cell was allocated a random genome length in the range published in the literature. The average genome length used in the model was 3.7 Gbp. The η parameter which accounts for the binary recombination interaction of DSBs is a very difficult parameter to determine experimentally. In the current work, the initial value for η was set to the value determined in [21] and then optimised to fit the data. Similarly, the initial values for the λ and β parameters were taken from [21] and then optimised in the current work. The large degree of uncertainty in the initial model parameters is reflected in figure 8.7 by the size of the error bars. As more precise values for the model parameters are obtained, the accuracy of the values predicted by the simulation will improve.

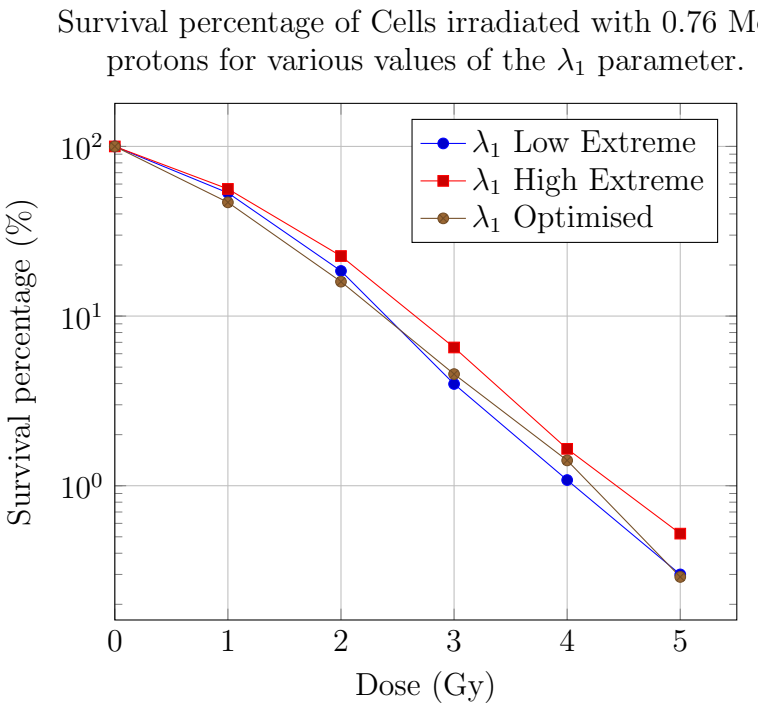

FIGURE 8.8: Parameter sensitivity analysis for the λ_1 parameter (probability of SDSB repair per unit time).

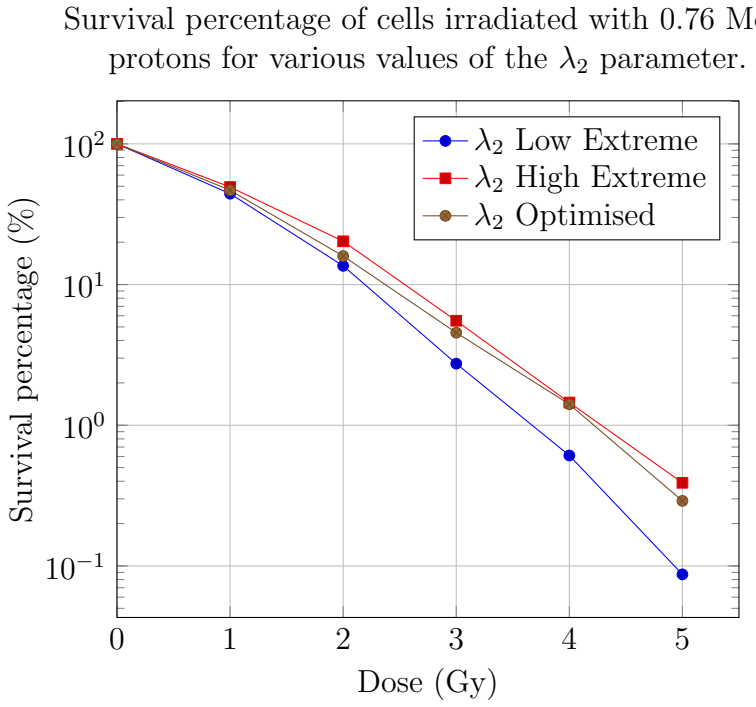

FIGURE 8.9: Parameter sensitivity analysis for the λ_2 parameter (probability of CDSB repair per unit time).

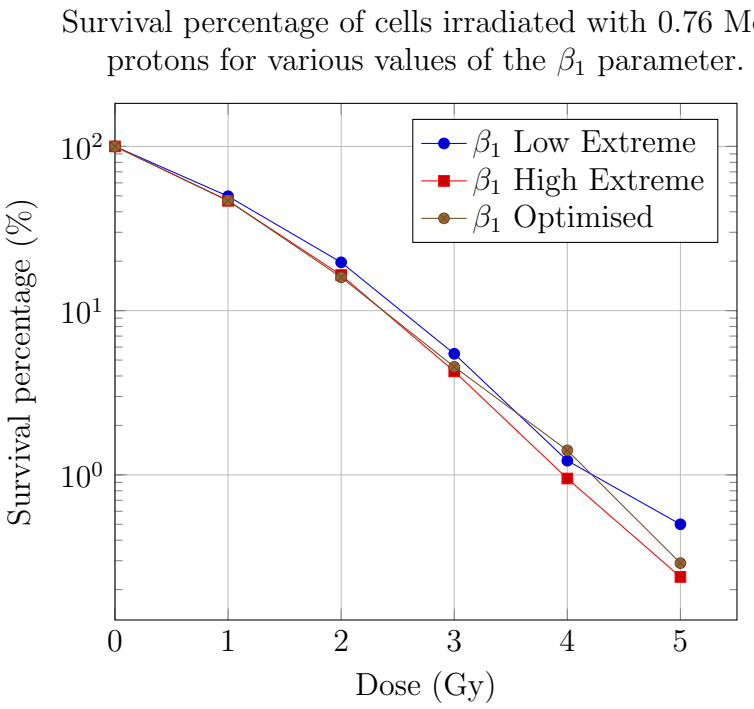

FIGURE 8.10: Parameter sensitivity analysis for the β_1 parameter (probability of incorrectly repairing a SDSB given that it was repaired).

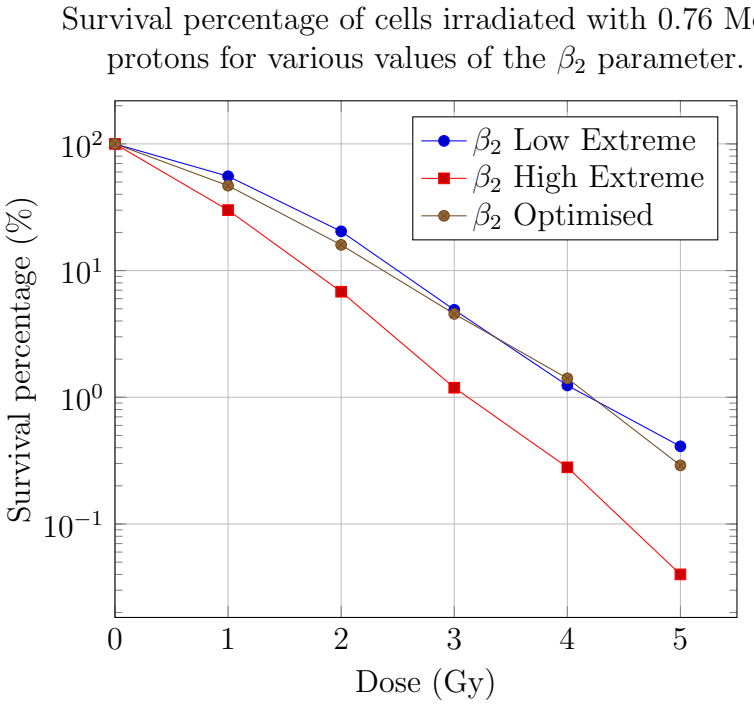

FIGURE 8.11: Parameter sensitivity analysis for the β_2 parameter (probability of incorrectly repairing a CDSB given that it was repaired).

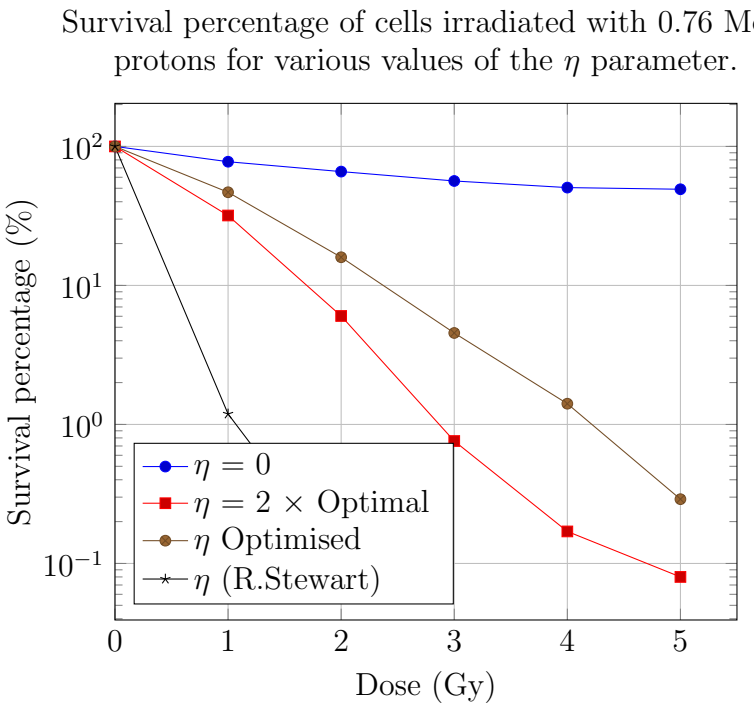

FIGURE 8.12: Parameter sensitivity analysis for the η parameter (probability of binary misrepair).

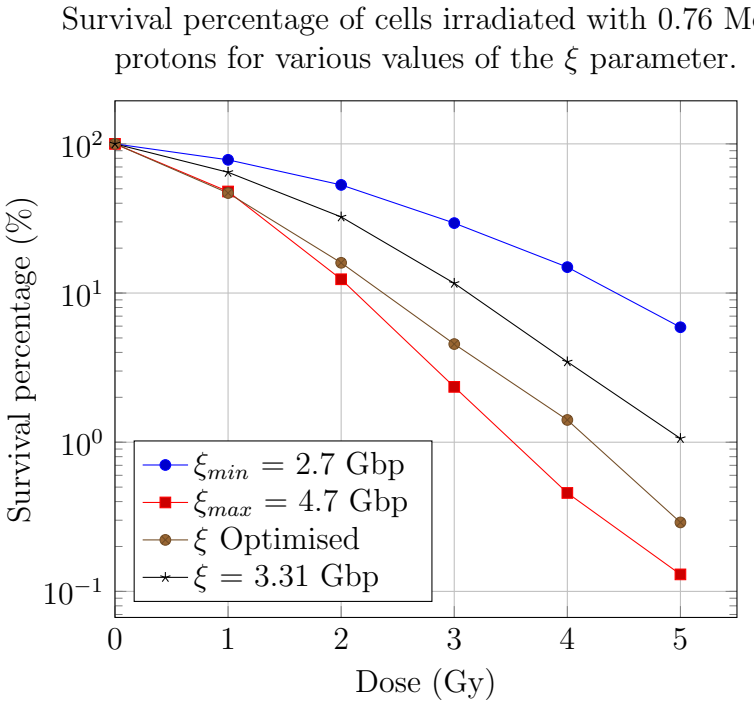

FIGURE 8.13: Parameter sensitivity analysis for the ξ parameter (genome size of CHO V79 cells).

8.5 Discussion and Future Work

A stochastic Monte Carlo cell death model based on the two lesion kinetic model has been developed in the current work. The Geant4 MC toolkit was used to simulate the ionisation track structure of protons and then export this data to a file for analysis. A clustering algorithm was developed to group spatially correlated ionisation events from Geant4 into DNA damages. These DNA damages were then repaired according to the TLK model.

The model has been calibrated for low energy (< 2 MeV) proton irradiation of V79 cells. Predicted values for cell survival of V79 cells for doses of proton radiation between 1-5 Gy show good agreement (less than 10% difference in cell survival) in this preliminary model. Discrepancies between simulation and experimental values may be caused by issues with the radiation transport calculation e.g. the Geant4 cross sections at very low energies or the clustering analysis e.g. lack of detail in the inter-track clustering model. However, discrepancies are more likely due to a lack of the biological processes of radiation induced cell death being modelled. The largest difference between simulated and experimental data occurs when 0.76 MeV protons are used at low doses (high LET, low dose region). This may be the result of damages by chemical species not being modelled in this investigation.

In chapter 10, this model was improved by incorporating a mainstream clustering algorithm (k-means) to more accurately and efficiently predict DSB clusters and more accurately model the inter- and intra-track clustering of ionisation events. Other possibilities include incorporating bystander effect models to predict low dose radiation effects, incorporating cell damage by chemical species into the model as data becomes available and studying the contribution of other irradiated organelles such as the cytoplasm and membrane.

Chapter 9

Investigation of the Validity of Geant4 Cross Sections

Until this point, the accuracy of the Geant4 physical models and cross sectional data and its impact on the uncertainty of the simulation results has not been considered. In this chapter, this was evaluated by comparing Geant4 and experimental cross section data. This data was also compared with a second MC package called RITRACKS which was also used to investigate the impact of chemical damages on cell survival (chapter 10). A brief introduction of the structure and capabilities of RITRACKS is presented followed by a review of the physical models used in both Geant4 and RITRACKS.

9.1 Introduction to RITRACKS

RITRACKS [98] is a Monte Carlo particle tracking software designed to simulate the interactions of cosmic radiation in a space environment. It was developed by Ianik Plante of the NASA Johnson Space Centre in 2011. It is capable of simulating all the interactions of cosmic radiation and electrons in liquid water.

One advantage of RITRACKS over Geant4, is its ability to simulate the production of radiolytic species originating from the primary ion radiation. The user friendly nature of RITRACKS (figures 9.1 - 9.4) compared with Geant4 makes it limited in its ability to

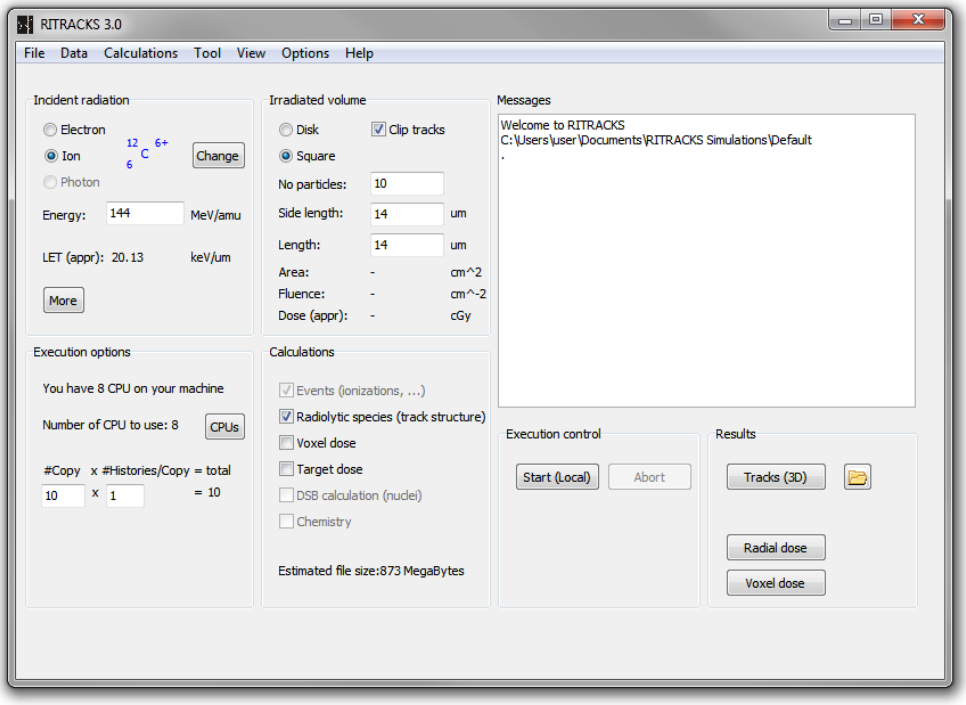

FIGURE 9.1: The RITRACKS graphical user interface (GUI).

be customised. As a result, RITRACKS currently only supports cubical and cylindrical water volumes (with adjustable dimensions).

9.2 RITRACKS Physics Models

9.2.1 Electron Ionisation

Ionisation cross sections for electrons are calculated in RITRACKS using two distinct models covering two different energy ranges. The Rudd model [99] is used for electron energies between 1 eV and 50 keV and Seltzer's model [100, 101] for energies over 50 keV.

Rudd [99] derived a semi-empirical equation for the differential cross section for electron ionisation based on the Mott equation. The Pauli principle states that the secondary electrons in ionisation interactions are indistinguishable from the primary electrons which leads to:

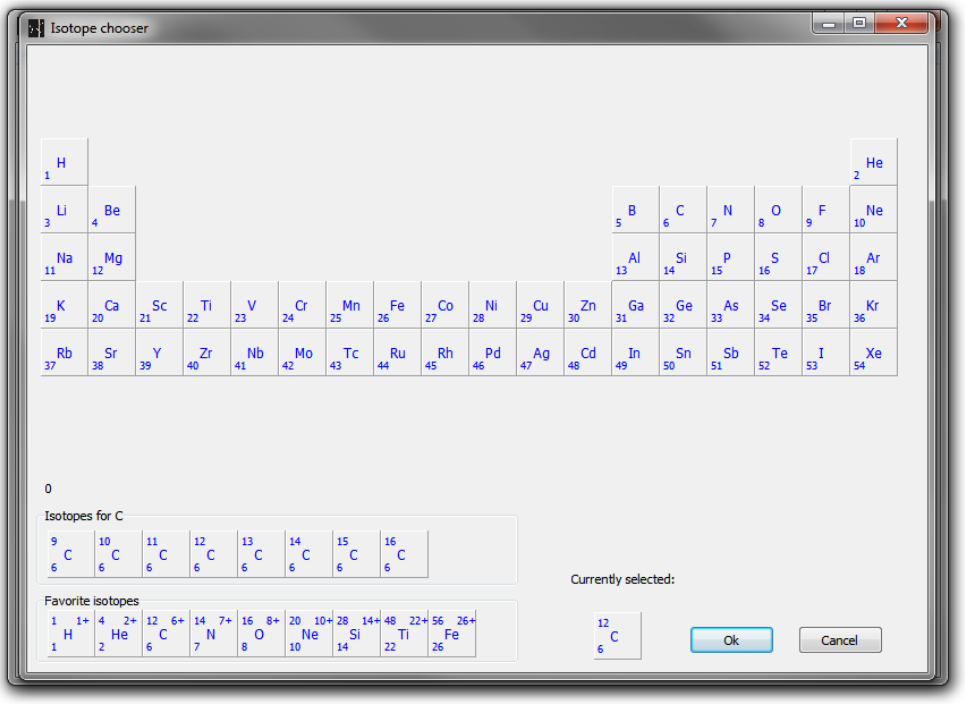

FIGURE 9.2: RITRACKS ion selector.

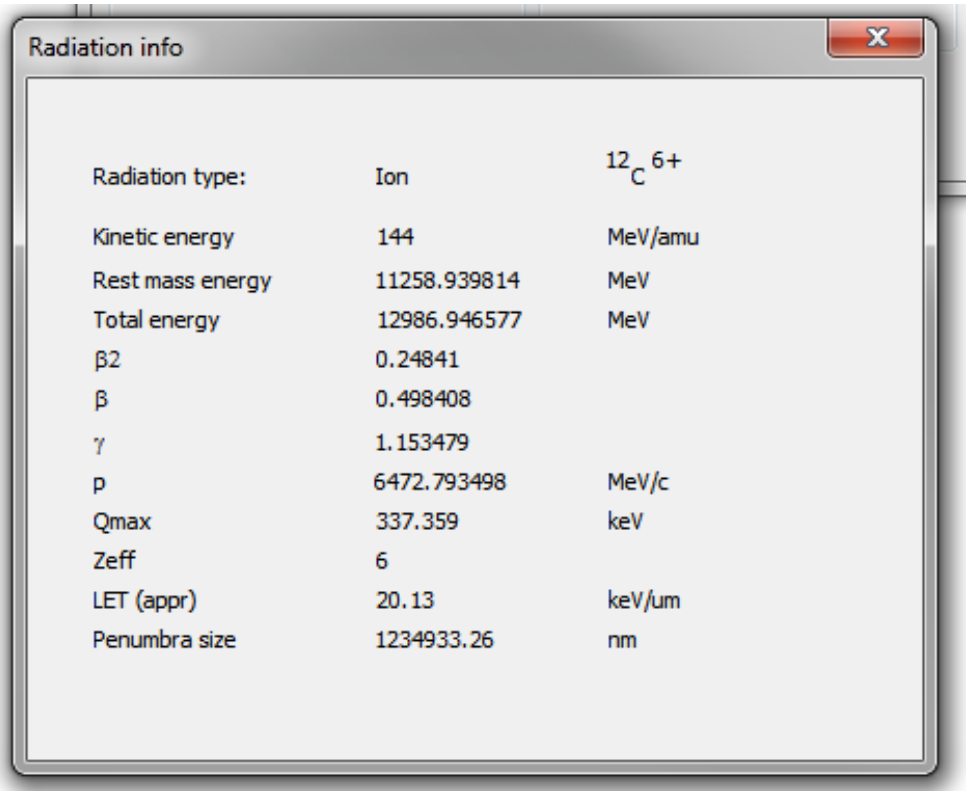

FIGURE 9.3: RITRACKS information window.

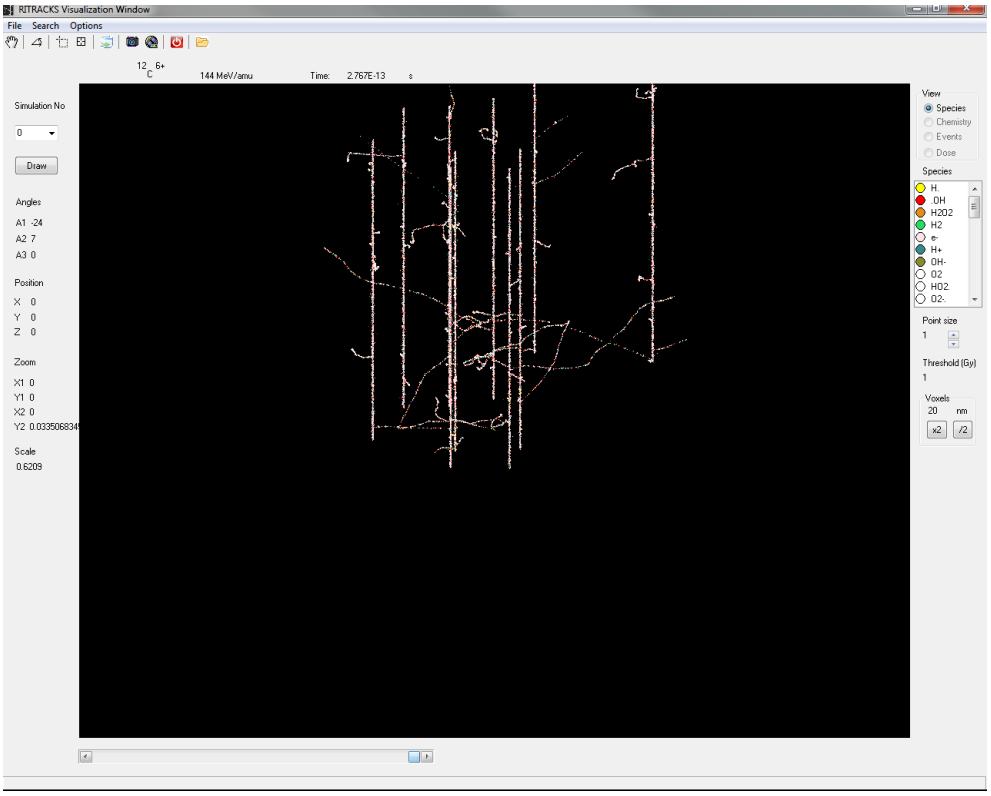

FIGURE 9.4: RITRACKS particle track visualisation.

$$\frac{d\sigma^{i}_{ion}}{d\omega} = \frac{d\sigma^{i(1)}_{ion}}{d\omega} + \frac{d\sigma^{i(2)}_{ion}}{d\omega} \tag{9.1}$$

$$\frac{d\sigma^{i}_{ion}(1)}{d\omega} = \frac{S_i}{I_i} F_1(t) \left[\frac{1}{(1+\omega)^3} + \frac{1}{(t-\omega)^3} - \frac{1}{(1+\omega)^{3/2}(t-\omega)^{3/2}} \right] \tag{9.2}$$

$$\frac{d\sigma^{i}_{ion}(2)}{d\omega} = \frac{S_i}{I_i} F_2(t) \left[\frac{1}{(1+\omega)^2} + \frac{1}{(t-\omega)^2} - \frac{1}{(1+\omega)(t-\omega)} \right] \tag{9.3}$$

Where $t = T/I_i$ and $\omega = W/I_i$, T is the energy of the primary electron, W is the energy of the ejected electron, I_i is the binding energy of the electron in the i^{th} molecular orbital, $S_i = 4\pi a_o^2 N_i (\mathfrak{R}/I_i)^2$, a_0 is the Bohr radius, $\mathfrak{R}$ is the Rydberg constant and N_i is the number of electrons in the orbital [102]:

$$F_1(t) = A_1 \frac{\ln(t)}{t + B_1} \tag{9.4}$$

TABLE 9.1: Semi-empirical parameters used for Rudd's ionisation model in [102].

Parameter	Liquid	Inner Shells
A_1	0.94	1.31
A_2	1.13	0.37
B_1	2.30	0.00
B_2	22.0	0.00

$$F_2(t) = A_2 \frac{\ln(t)}{t + B_2} \tag{9.5}$$

Where A_1, A_2, B_1, B_2 are constants determined through fitting of experimental data.

Above 50 keV, RITRACKS uses Seltzer's formula for the differential cross section of electron ionisation [100, 101]. This formula is used to calculate the cross section for the i^{th} orbital of the water molecule for a secondary electron with energy W and an incident electron with kinetic energy T. It is the sum of the close collision and distant collision contributions:

$$\frac{d\sigma^i_{ion}}{dW} = \frac{d\sigma^i_c}{dW} + \frac{d\sigma^i_d}{dW} \tag{9.6}$$

$$\frac{d\sigma^i_c}{dW} = \left[\frac{1}{E^2} + \frac{1}{(T-W)^2} + \frac{1}{T^2}\left(\frac{\tau}{\tau+1}\right)^2 - \frac{2\tau+1}{(\tau+1)^2}\frac{1}{E(T-W)} + G_i\right] \times \frac{2\pi r_e^2 mc^2 N_i}{\beta^2}\frac{T}{T+B_i+U_i} \tag{9.7}$$

$$G_i = \frac{8U_i}{3\pi}\left[\frac{1}{E^3} + \frac{1}{(T-W)^3}\right]\left[\tan^{-1}\sqrt{y} + \frac{\sqrt{y}(y-1)}{(y+1)^2}\right] \tag{9.8}$$

The distal collision term is expressed as:

$$\frac{d\sigma^i_d}{dW} = N_i I(E)\sigma^i_{PE}(E) \tag{9.9}$$

TABLE 9.2: Semi-empirical parameters used for Seltzer's ionisation model in [102]. N_i is the number of electrons per orbital, B_i is the ionisation energy of the orbital, U_i is the mean kinetic energy of the target electron in the orbital and $\langle r \rangle_i$ is the expected value of the radius of the i^{th} orbital of the water molecule [102]. Orbital digrams shown in figure 9.5.

i	Orbital	N_i	B_i (eV)	U_i (eV)	$\langle r \rangle_i$
1	$^1b_1$	2	11.50	30	0.833
2	$^3a_1$	2	11.75	40	0.867
3	$^1b_2$	2	13.51	50	0.901
4	$^2a_1$	2	16.0	60	0.906
5	$^1a_1$	2	539.7	700	0.129

Where $\sigma^i_{PE}(E)$ is the photoelectric cross section for the i^{th} molecular orbital of water for a photon with incident energy $E = W + B_i$, τ is the kinetic energy of the electron in units of electron rest mass, U_i is the mean kinetic energy of the target electron in the orbital, B_i is the binding energy and $y = W/U_i$.

9.2.2 Electron Excitation

The electron excitation differential cross section in water is calculated in RITRACKS using two different models. The two models cover the energy range from < 100 eV and > 100 eV respectively. The cross sections in the higher energy range are calculated using the model of Kutcher and Green [104]:

$$\frac{d\sigma^i_{ex}}{dW} = \rho(W) W f_i(W) \ln\left[\frac{4T}{Q_{min}}\right] \tag{9.10}$$

Where T is the energy of the incident electron, $\rho(W)$ is the differential cross section for charged particles on free electrons at rest, Q_{min} is the minimum energy that is transferred in an interaction [102]:

$$Q_{min} = 2T\left(1 - \frac{1}{2}\frac{W}{T} - \sqrt{1 - \frac{W}{T}}\right) \tag{9.11}$$

$$\rho(W) = \frac{e^4}{8\pi\epsilon_0^2 m \upsilon^2 W^2} = \frac{4\pi a_o^2}{T}\left(\frac{\mathfrak{R}}{W}\right)^2 \tag{9.12}$$

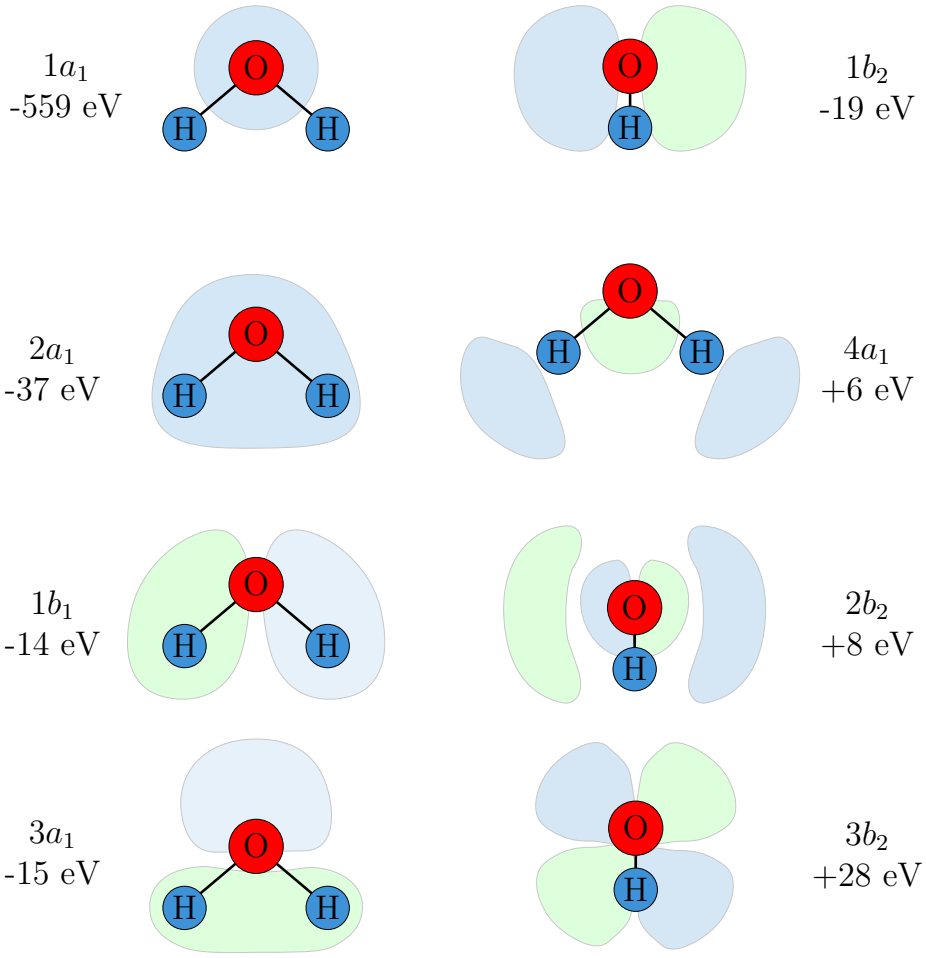

FIGURE 9.5: The five occupied and lowest three unocupied molecular obitals of an isolated water molecule. Calculated using the restricted Hartree-Fock wave function [103].

Where a_0 is the Bohr radius, ϵ_0 is the vacuum permittivity, $\mathfrak{R}$ is the Rydberg constant.

In the energy range where the electron energy is close to the excitation energy of the molecule the above model is not valid. For electrons of energy less than 100 eV, Kaplan and Sukhonosov [105] and Cobut [106] developed the following model for calculating the electron excitation differential cross section:

$$\frac{d\sigma^i_{ex}}{dW} = \rho(W) W f_i(W) \ln\left[\frac{\alpha(t)T}{W}\right] \tag{9.13}$$

where $\alpha(t) = 4 - 3\exp[-(W - W_{0,i})/\alpha_i]$, $\alpha_i = 4E_{min}/\ln(2)$, $E_{min} = 7.34$ eV is the minimum energy transfer by excitation.

9.2.3 Proton Ionisation

The ionisation differential cross section for protons and heavy ions are calculated in RITRACKS using a semi-empirical equation. The equation was proposed by Rudd [99] for the differential cross section of each molecular orbital of liquid water by protons (equation 9.14).

A relativistic correction has been applied to the semi-empirical cross sections for proton ionisation and excitation in water molecules to extend the cross sections to 10 GeV/amu. The non-relativistic formula is:

$$\frac{d\sigma_{ion}^{i}}{d\omega} = \frac{S_i}{I_i} \frac{F_1(\upsilon) + \omega F_2(\upsilon)}{I_i(1+w)^3(1+\exp(\alpha(\omega-\omega_{c_i})/\upsilon)} \tag{9.14}$$

where i is the index of the orbital, I_i is the binding energy of the electron in the target, $\omega = W/I_i$, W is the energy of the secondary electron and E_p is the energy of the incident proton. F_1 and F_2 consist of a series of values fitted from experimental data. The molecular orbits considered in the model are the ${}^1b_1$, ${}^3a_1$, ${}^1b_2$, ${}^2a_1$ and ${}^1a_1$. $T = E_p(m/M_p)$ is the kinetic energy of an electron of mass m which would have the same velocity as a proton of mass M_p and $\upsilon = \sqrt{T/I_i}$ is a scaled velocity of the incident particle.

This semi-empirical model is valid only in the classical energy range. In [107], the classical model was extended to the relativistic energy range by making the substitution:

$$\upsilon^2 = \frac{mc^2}{2I_i}\left[1 - \frac{1}{(1+T/mc^2)^2}\right] \tag{9.15}$$

For track structure simulations of protons and heavy ions, the first order plane wave Born approximation is used. To obtain the interaction cross sections for heavy ions, the cross section for protons (of the same velocity υ as the heavy ion) are scaled by the square of the charge Z of the ion [107, 108]:

$$\frac{d\sigma_{ion}(\upsilon)}{dW} = Z^2 \frac{d\sigma_{proton}(\upsilon)}{dW} \tag{9.16}$$

Equation 9.17 can be used to calculate the kinetic energy of an ion which has the same velocity as a proton with kinetic energy τ. This formulation is true for both relativistic non-relativistic ions:

$$E_{ion} = \frac{M}{M_p}\tau \tag{9.17}$$

In some cases, heavy ions at low energies may have a reduced effective charge due to the attachment of electrons. In order to accurately calculate the cross sections for both ionisation and excitation in a water medium, the "reduced"charge must be calculated. Booth and Grant [109] derived an equation for the effective charge of an ion:

$$\frac{Z^*}{Z} = 1 - \exp(-1.316x + 0.112x^2 - 0.0650x^3) \tag{9.18}$$

$$\text{where } x = 100\beta Z^{-2/3}.$$

This correction term becomes significant at approximately 0.2 MeV for protons [107].

9.3 Geant4-DNA Physics Models

Geant4 implements many of the same models as RITRACKS for calculating the differential cross sections of protons, electrons, alpha particles and heavy ions. All possible physical interactions are taken into account such as: ionisation, excitation, charge transfer and elastic scattering [110].

Similarly to RITRACKS, Geant4 calculates inelastic cross sections using the plane wave first Born approximation [80, 111]. At very low energies, the cross sections for electrons has to be corrected. For protons and alpha particles in water, the theoretical predictive models were replaced by semi-empirical models. While the proton cross sections are available for energies between 100 eV and 100 MeV, the cross sections have not been verified experimentally below 1 keV. Electron interactions can be simulated from thermalisation

energy (0.025 eV) to relativistic energies of 1 MeV. Alpha particle interactions can be simulated in the range of 1 keV - 400 MeV.

The Born double differential inverse mean free path is given by [110]:

$$\frac{d^2\sigma(T,E,q)}{dE.dq} = \frac{1}{\pi\alpha_0 Tq} Im[-1/\epsilon(E,q)]\theta[q-q_-(E,\tau)]\theta[q_+(E,\tau)-q]\theta[\tau-E] \tag{9.19}$$

The first Born approximation relates the energy and momentum transfers to the energy loss function Im$[-1/\epsilon(E,q)]$.

Where α_0 is the Bohr radius, τ is the particle kinetic energy, $T = (m/M)\tau$ is the kinetic energy of an electron travelling with the same velocity of the considered particle, m is the electron mass, M is the particle mass, θ is the heavy side step function and $\epsilon = \epsilon_1 + i\epsilon_2$ is the complex dielectric response function of the material in which the particle is propagating and [110]:

$$q_\pm = \sqrt{2M}(\sqrt{\tau} \pm \sqrt{\tau - E}) \tag{9.20}$$

When the speed of the incident particle approaches the speed of the electrons orbiting the water molecule in the medium ($<$ 1 keV for electrons and $<$ 300 keV for protons) the first Born approximation is no longer valid. Proton ionisation cross sections were corrected using the Rudd ionisation model and Miller and Green model for excitation processes [110]. Electron cross sections were corrected using a Coulomb field correction proposed in ICRU 37 [112].

Electrons with energy below 8 eV do not have sufficient energy to ionise a water molecule. However, these electrons still have sufficient energy to undergo vibrational and rotational excitations of the water medium until the electron finally reaches thermalisation. At the current time, there are no theoretical models which accurately describe this process. For Geant4-DNA, experimental cross sections for ice targets published by [113] are utilised

for electron excitation by performing a phase-scaling correction. This correction enabled the cross sections to be used for a liquid water medium [110].

Alpha particle (and other heavy ion) cross sections are calculated in Geant4-DNA using the same method implemented in RITRACKS (scaling proton cross sections by the squared charge of the ion). Similarly, cross sections for ions with bound electrons (at low energies) are corrected using the same method as RITRACKS (Z_* method)

In Geant4-DNA, the inelastic (ionisation) cross sections are calculated using five ionisation and five excitation states for water. Both RITRACKS and Geant4 consider particle interactions in a water medium only due to limited amounts of experimental data for verification and semi-empirical model development. However, water is considered to be the primary component of cells and therefore both these models are thought to replicate the physical interactions in cells with reasonable accuracy.

Ionisation cross sections are calculated in Geant4-DNA using the Rudd ionisation model and excitations calculated using the Miller and Green model [114]. Differential cross sections for carbon ions are calculated in Geant4-DNA using an "in house" model. The energy range covered by this model is 1 MeV/amu - 10 GeV/amu.

9.4 Methods

In this section, the published cross sections for Geant4-DNA are compared with published experimental data and RITRACKS models in order to estimate the energy range for protons and electrons in which we can confidently assume that our simulation predictions are accurate.

The physical interactions of significant interest in this thesis are: proton ionisations, electron ionisations and electron excitation processes. These processes dominate the energy loss mechanisms of protons and contribute most significantly to the biological damage of cells.

A literature review was performed to obtain several independent experimental and analytical data sets for the interaction cross sections of protons and electrons. This data was compared with the cross sections published for Geant4-DNA and RITRACKS.

The ionisation tracks of protons and electrons in water using Geant4 and RITRACKS were then compared. A small cubic water volume with dimensions 7 µm × 7 µm × 7 µm was used as a target for radiation interactions in both simulation tool kits. A single proton was fired at the water volume and the total number of primary and secondary ionisation events in the water volume was recorded (figure 9.6). The simulation was run multiple times and the values averaged in order to obtain the statistical uncertainty. The energy of the incident proton was then varied between 10^{-2} and 10^{2} MeV and the total number of ionisations were recorded. This simple simulation utilises all the proton and electron cross sections and models characterised earlier. If the models and cross sections are the same, then the predicted number of ionisation events using both toolkits should be statistically identical.

In chapter 8, the biological implications of exposure of V79 cells to proton radiation was predicted using Geant4-DNA. One of the key assumptions in making said predictions was the equivalence of water and the intra-nuclear composition of cells. A recent publication by the Geant4-DNA collaboration [81] presented an update to the existing Geant4-DNA model by including cross sections for adenine, a primary constituent of DNA. The effect of utilising chemically realistic materials for the composition of DNA on the ionisation track structure of protons was also investigated. The ionisation cross sections for protons in water and adenine were compared.

9.5 Results

In figure 9.7, the total interaction cross section for proton ionisation interactions is shown in the energy range of 1 keV to 10 MeV. The calculated cross sections for Geant4-DNA and RITRACKS are compared with experimental data collected since the mid 1980s. As expected, there is excellent agreement between Geant4-DNA and RITRACKS predictions as each tool kit uses similar implementations of the same model (the Rudd ionisation

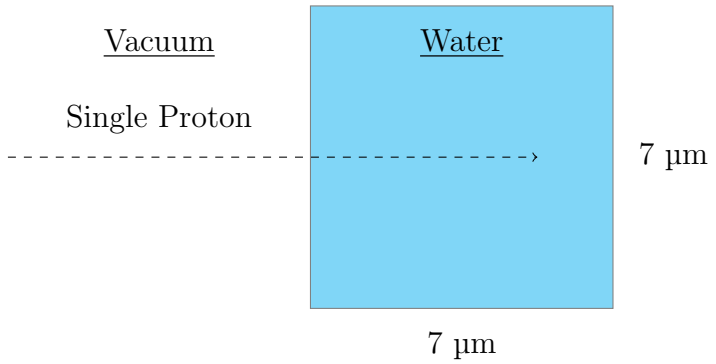

FIGURE 9.6: The simulation geometry used to compare the physics models in Geant4-DNA and RITRACKS.

model). There is also excellent agreement between computational and experimental data for energies above 1 keV.

Figure 9.8 compares the total ionisation cross section for electron ionisation between energies of 10 eV and 10 keV. There is still excellent agreement between the two toolkits above energies of 1 keV. However, the models used to predict electron interactions differ between the two toolkits resulting in a significant difference in cross sections at very low energies (factor of 200 difference at 13 eV). It appears that Geant4-DNA predicted data is generally in better agreement with experimental data over the entire applicable energy range.

Electronic excitation processes in Geant4-DNA and RITRACKS are different implementations of the same model (the Green formula [108]). The two different simulations (RITRACKS and Geant4-DNA) produce significantly different interaction cross sections for all energies (an order of magnitude difference). In addition to the experimental data in figure 9.9, the predicted data from two additional Monte Carlo codes (PARTRAC and NOREC) are plotted on the same axes. While it appears that all four Monte Carlo codes use the same model (indicated by the identical shape of the curve) each semi-empirical model has been calibrated using a different set of parameters.

Figure 9.10 shows the total number of ionisation events produced by the passage of a single proton vs. the energy of the incident proton. There is reasonable agreement between RITRACKS and Geant4 for proton energies above 0.25 MeV. Below 0.25 MeV,

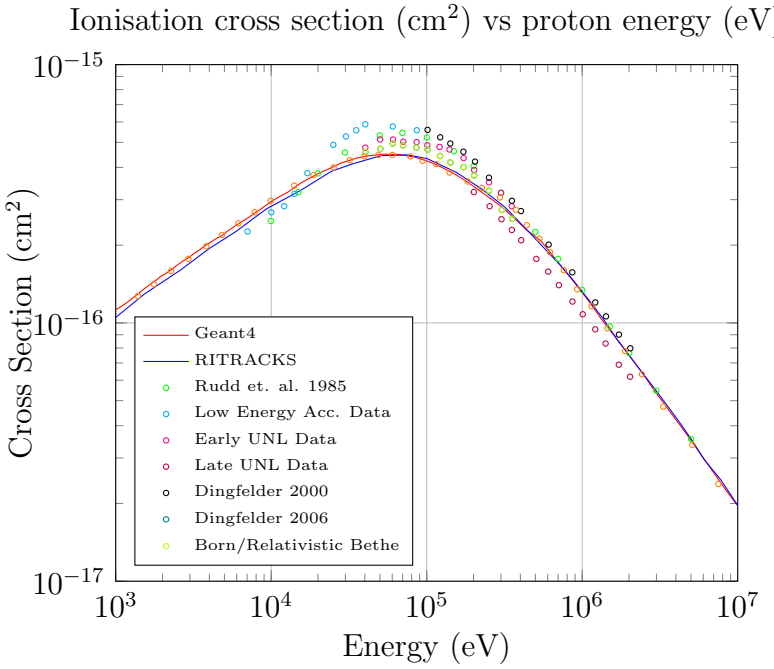

FIGURE 9.7: Total ionisation cross section for protons in the energy range of 1 keV to 10 MeV.

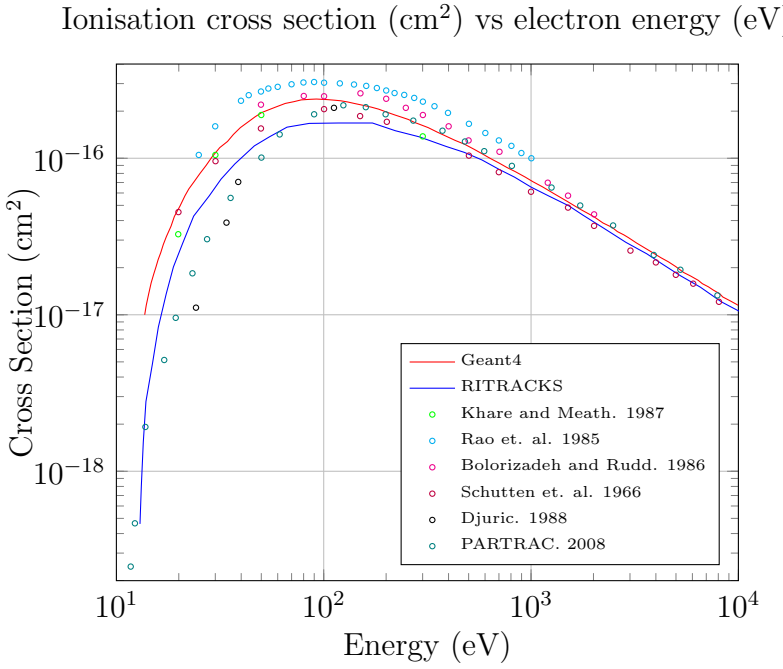

FIGURE 9.8: Total ionisation cross section for electrons in the energy range of 10 eV to 10 keV.

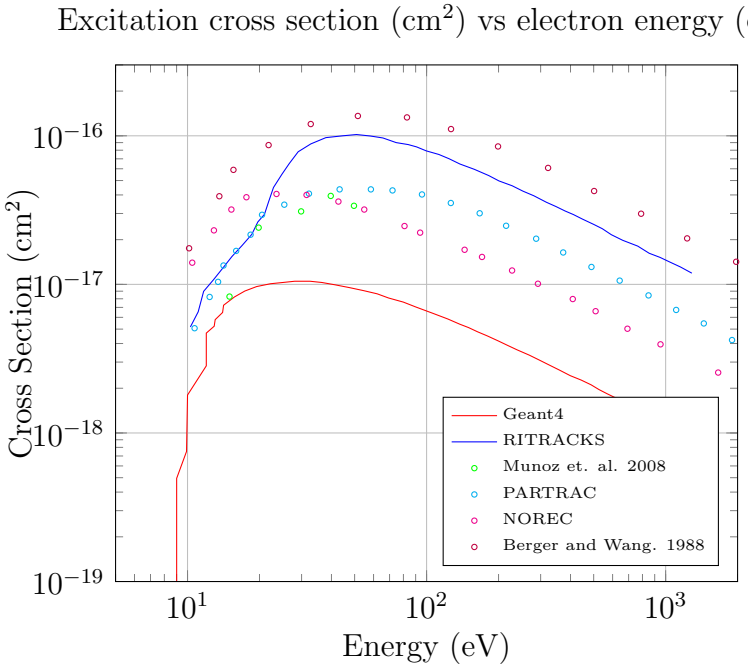

FIGURE 9.9: Total excitation cross section for electrons in the energy range of 1 eV to 1 keV.

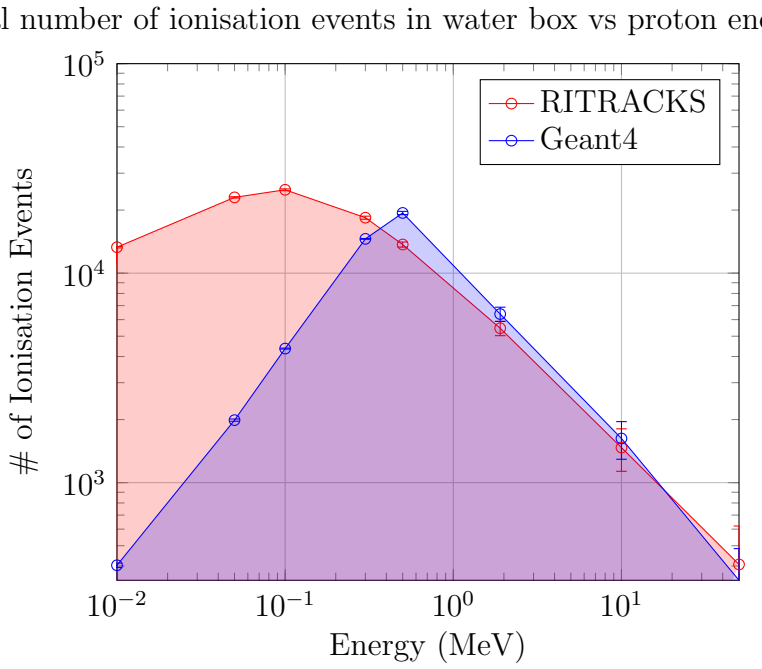

FIGURE 9.10: Total number of ionisation events recorded in a 7 µm × 7 µm × 7 µm water box from the passage of a single proton using Geant4 and RITRACKS.

there is a large discrepancy between the total number of ionisation events recorded using each simulation toolkit. Although cross sections for ionisation are larger in Geant4-DNA, the excitation processes dominate at low energies. The current version of RITRACKS (v3.2) has been modified to limit incident protons to energies above 0.1 MeV.

9.6 Proton Ionisation in a Realistic DNA Material vs. Water

Figure 9.11 compares the interaction cross sections for a simple water medium and adenine in the energy range of 1 keV to 1 MeV. At very low energies ($\sim$ 1 keV) there is a difference of a factor of five in the total cross section for water and adenine. This significantly higher cross section would result in an increased probability of DSBs in DNA when exposed to low energy protons. However, in the previous chapter it was demonstrated that less than 1% of the total volume of the nucleus of a cell is composed of DNA. To correct for this in the clustering algorithm, a scaling factor was applied to the number of clustered ionisation events to calculate the correct number of DNA DSBs. DNA is composed of four different nucleobases: adenine, guanine, thymine and cytosine. If we assume roughly equal fractions of each base in DNA, then each comprises less than 0.25% by volume in the nucleus. To more accurately calculate the cross section in the nucleus, the cross sections of water and ATGC would have to be scaled by their fractional composition (i.e. 99% water, 1% realistic DNA). The track structure of a proton in the cell nucleus is therefore not likely to differ significantly from a proton in water.

Future models implementing a complete DNA geometry should however include realistic base pair materials in order to improve the accuracy of the predicted DNA DSB damage.

9.7 Discussion and Conclusion

A comparison between the physics models for proton and electron interactions used in RITRACKS and Geant4-DNA has been performed. Proton and heavy ion interaction

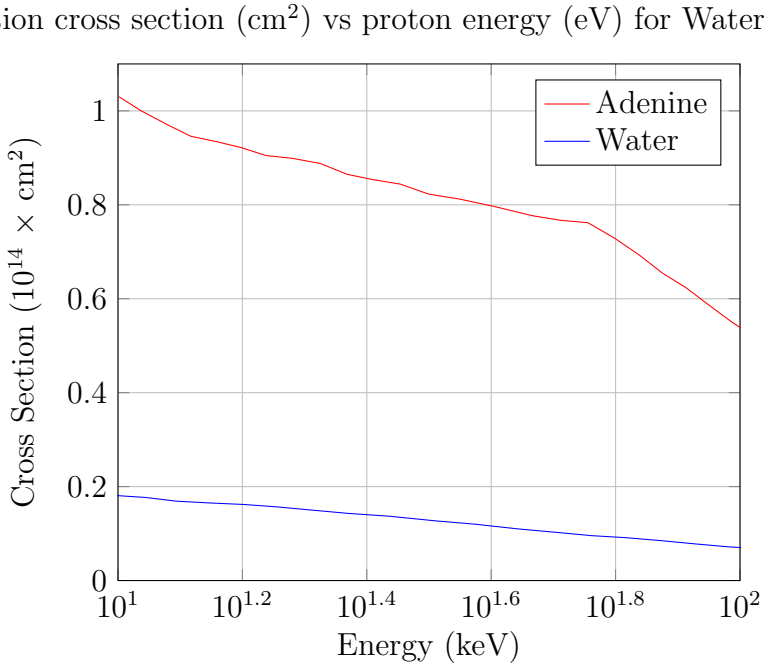

FIGURE 9.11: Total ionisation cross section for protons in the energy range of 1 keV to 1 MeV for adenine and water [81].

cross sections are implemented with the same semi-empirical models in both Geant4 and RITRACKS. This is reflected by the agreement in the data predicted using Geant4 and RITRACKS.

A preliminary investigation has been performed to compare the predicted interaction cross sections of the two Monte Carlo toolkits Geant4-DNA and RITRACKS. In the energy range above 1 keV, there is excellent agreement between all Monte Carlo packages and experimental data. Below 1 keV, there are several mathematical models which attempt to predict the interaction cross section for excitation and ionisation processes. Both RITRACKS and Geant4 use semi-empirical models to predict these cross sections. The accuracy of the predictions made by these models depends on accurate experimental measurements. Below 1 keV, it is very difficult to perform accurate measurements of the required parameters and as a result there are very large discrepancies in the simulated data. With the current Monte Carlo models, any predictions made in this energy range should be considered with caution.

It has been demonstrated that in the energy range applicable to the work performed in

this thesis (0.5 MeV - 10 MeV), there is excellent agreement between theoretical, semi-empirical and simulated data. Therefore, the accuracy of the predictions made in chapter 8 pertaining to cellular survival after low energy proton radiation can be considered to be high (less than 7% uncertainty in this energy range).

More research is required to acquire accurate experimental data (i.e. cross sections) for particle interactions in the low energy range ($<$ 500 keV for protons) so that more accurate semi-empirical models can be developed.

Chapter 10

Prediction of Indirect Radiation Damage

It has been well established (through clinical evidence and studies [115]) that approximately 80% of x-ray induced biological damage is the result of indirect DNA damage. Since Geant4 is presently incapable of simulating the physio-chemical interactions associated with indirect DNA damage, in this chapter the MC software RITRACKS was used to investigate these processes. In chapter 8, the biological damage of low energy proton radiation was investigated using Geant4. Using RITRACKS, the DNA damage resulting from the direct and indirect DNA damage of heavy ions was investigated.

10.1 Indirect DNA Damage

Radiation damage of organic matter is a multi-stage process occurring on different time scales. Throughout the previous chapters of this thesis, the process of radiation damage has been treated as a series of physical interactions only. In reality, radiation damage occurs through a complex series of physical, chemical and biological processes. In typical x-ray radiotherapy treatments, the primary cause of radiation induced cell death in both healthy and tumour cells is chemical damage.

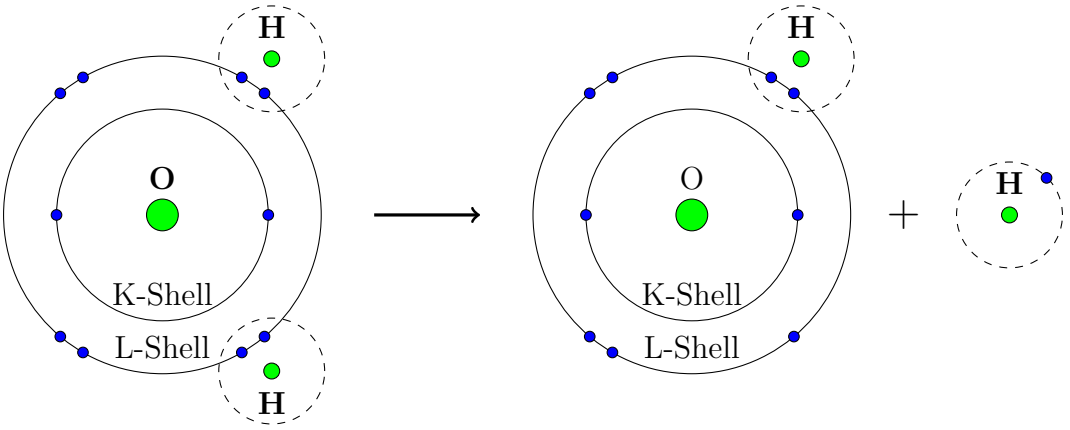

FIGURE 10.1: Radical formation.

The first stage of radiation induced cell damage is the physical interactions of a particle of ionising radiation within the cell medium. The initial event is the transfer of energy (typically between 7 and 100 eV) from the ionising particle to the medium in the form of multiple ionisations or excitation of molecules. Transfer of energy to the biological medium usually involves ionisation of a water molecule but can also involve direct ionisation of other molecules such as DNA. As the ionising particle traverses the medium, it ionises and excites the medium and creates multiple chemical species in the local vicinity of the particle track (figure 10.1 and 10.2). Direct ionisation of water produces a radical ion and a free sub-excitation electron (energy less than 7.4 eV) [116].

$$H_2O \xrightarrow{\text{rad}} H_2O^+ + e^- \tag{10.1}$$

Energy transfer can produce a water molecule in an excited state.

$$H_2O \xrightarrow{\text{rad}} H_2O^* \tag{10.2}$$

The time scale for the creation of these species is on the order of 10^{-16} seconds. Successive ionisation and excitation processes by the ionising particle occur on time scales of the order of 10^{-15} seconds. Within 10^{-14} seconds after exposure, electronically excited species have dissociated and energy has been transferred to vibrational modes (thermal). At approximately the same time, reactions between the three initial species and molecules

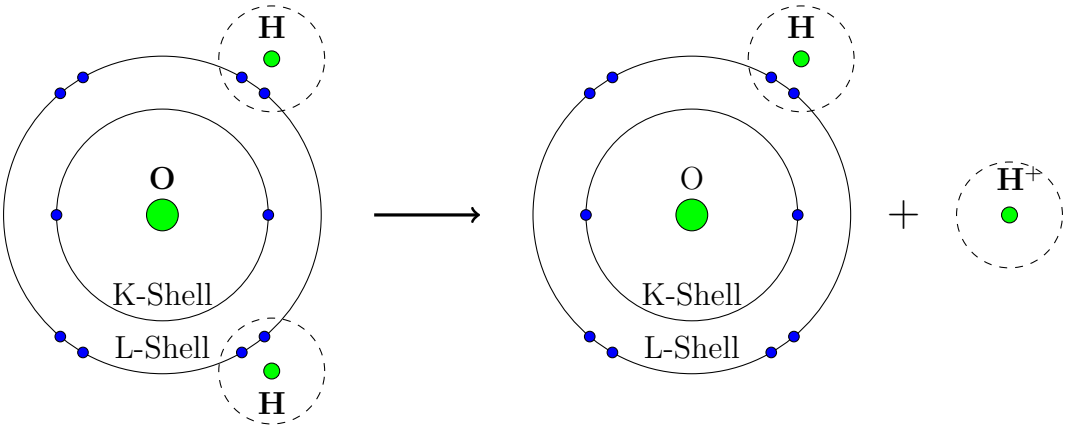

FIGURE 10.2: Ion formation.

within the medium begin to occur. These reactions produce chemical radicals which further damage the DNA within the cells (figure 10.3). Radicals refer to an atom or molecule that contains an unpaired electron. Radicals are highly chemically reactive. The radicals produced in such reactions begin to diffuse throughout the cell on time scales of approximately 10^{-12} seconds. The most highly reactive radicals are captured by other molecules within 10^{-5} seconds. The free electrons produced in the initial reactions are captured by nearby water molecules through dipolar interactions becoming solvated and is referred to as an aqueous electron or a solvated electron. A solvated electron is a free electron in a solution. The radical ion of water can dissociate to produce a hydroxyl radical and a hydrogen ion [116]:

$$H_2O^+ \rightarrow H^+ + OH \tag{10.3}$$

A solvated electron can react with the free hydrogen atom to form a new radical:

$$e^- + H^+ \rightarrow H \tag{10.4}$$

The excited water molecule can dissipate excess energy through molecular bond breakage to produce hydroxyl and hydrogen radicals. It requires approximately 5 eV to break the O-H bond in the water molecule:

$$H_2O^* \rightarrow OH + H \tag{10.5}$$

Thus, the three initial species H_2O^*, H_2O^+ and e^- undergo a physiochemical reaction to form the chemically reactive species HO, H and e_{aq}. OH is a powerful oxidising agent which is highly chemically reactive. Oxidation is the process where electrons are transferred to the oxidising agent which becomes reduced. Once the physiochemical interactions between the ionising particles and the water molecules have been completed (after 10^{-12}) seconds, the chemical species are still located in close proximity to the original excited and ionised water molecules. These species now undergo dispersion processes and migrate randomly around their initial positions. Various pairs of radicals and ions may move close enough to react with each other. Several possible reactions that may take place include:

$$OH^{\cdot} + OH^{\cdot} \rightarrow H_2O_2 \tag{10.6}$$

$$OH^{\cdot} + e^-_{aq} \rightarrow OH^- \tag{10.7}$$

Most of these reactions progress towards a state where chemically reactive radical species are removed from the system. After approximately 10^{-6} seconds all of the reactive species have diffused far enough away from the reaction site that further reactions are unlikely. If the measured diffusion constant for a given species is D, then on average, it will move a small distance s in a time t such that [116]:

$$\frac{s^2}{6t} = D \tag{10.8}$$

The reaction radius R (table 10.1) is a measure of the reactivity of the individual species. If a reactive species diffuses closer to the target than its reactive radius then it will react.

The diffusion formula and the recombination reactions described above allow Monte Carlo simulations of the production, dispersion and reaction of radical species to be performed.

TABLE 10.1: Reaction radius [117].

Species	D (10^{-5} cm^2 s^{-1})	R (Å)
OH	2	2.4
e^-_{aq}	5	2.1
H_3O^+	8	0.30
H	8	0.42

TABLE 10.2: G values (number per 100 eV) for various species at 10^{-7} seconds for protons of several energies and alpha particles of the same velocities (table 13.4 in [117].)

	Protons				Alpha Particles			
Species	1 MeV	2 MeV	5 MeV	10 MeV	4 MeV	8 MeV	20 MeV	40 MeV
OH	1.05	1.44	2.00	2.49	0.35	0.66	1.15	1.54
H_3O^+	3.53	3.70	3.90	4.11	3.29	3.41	3.55	3.70
e_{aq}	0.19	0.40	0.83	1.19	0.02	0.08	0.25	0.46
H	1.37	1.53	1.66	1.81	0.79	1.03	1.33	1.57
H_2	1.22	1.13	1.02	0.93	1.41	1.32	1.19	1.10
H_2O_2	1.48	1.37	1.27	1.18	1.64	1.54	1.41	1.33
Fe^{3+}	8.69	9.97	12.01	13.86	6.07	7.06	8.72	10.31

Using Monte Carlo simulations, the total number of various chemical species can be integrated with time. It is common to calculate the number of a particular species produced per 100 eV of energy lost by ionising radiation and its secondaries when it comes to rest in water. This value is called the G value [116]. By 10^{-6} seconds, the chemical interactions have essentially ceased. By this time, the G value has obtained a static equilibrium value (table 10.2).

The linear energy transfer of the alpha particle is four times as high as that of a proton. The linear energy transfer of a particle decreases with increasing energy, as a result the initial density of reactants is lower and therefore more survive without recombining. The alpha particle LET is higher and therefore the density of the ionisation track is higher. As a result the G value is lower because the recombination rate of radicals is higher (more radicals are in close proximity to each other, i.e. within the reactive radius). All types of directly ionising radiation (electrons, protons and alpha particles) all produce the same species in the track region (10^{-15} s). These physiochemical species are H_2O^*, H_2O^+, e^-. The chemical and biological differences (which occur on longer time scales) due to different types of radiation are the results of differences in the spatial distribution

of ionisation events along the track.

Radiation can also interact with the DNA of a cell directly rather than the medium surrounding it. While the physical interactions of ionising radiation with water and DNA remain the same, the types of radical species that can be produced are quite different. The biological radicals that are produced undergo similar reactions to those of water radicals. Due to the geometry and position of the DNA target within a cell, radiation can damage DNA through two different processes: direct and indirect action. Direct damage is the result of energy deposition directly to the DNA molecule. The damage response is approximately linear to the energy deposited. Radiation can also indirectly damage the DNA by ionising the medium around the molecule. Since these radicals must travel (diffuse) towards the DNA target, the damage response can be difficult to predict. Chemical scavengers can be used to preferentially interact with the radicals instead of the DNA. These molecules act as antioxidants which inhibit the oxidation of other molecules which would otherwise lead to the production of free radicals. Scavengers (such as Amifostine) have the ability to block the indirect effects of radiation. Historical measurements with scavengers specific to reactive species have shown that the hydroxyl radical ($OH^{\cdot}$) is primarily responsible for radiation damage to DNA. For high LET radiation, direct radiation damage is the predominant mechanism of radiation induced DNA damage. In the case of x-rays, the indirect damage to the DNA accounts for approximately 75% of the total DNA damage.

Damage fixation of DNA strand breaks is an important concept in radiobiology. Molecular oxygen O_2 is a powerful oxidising agent. When radiation interacts with a DNA molecule it produces DNA radicals:

$$\text{DNA}^{\cdot} + O_2 \rightarrow \text{DNA-O-O (DNA hydroperoxy radical)} \tag{10.9}$$

$$\text{DNA-O-O}^{\cdot} + H_1 \rightarrow \text{DNA-O-OH (DNA hydroperoxide)} \tag{10.10}$$

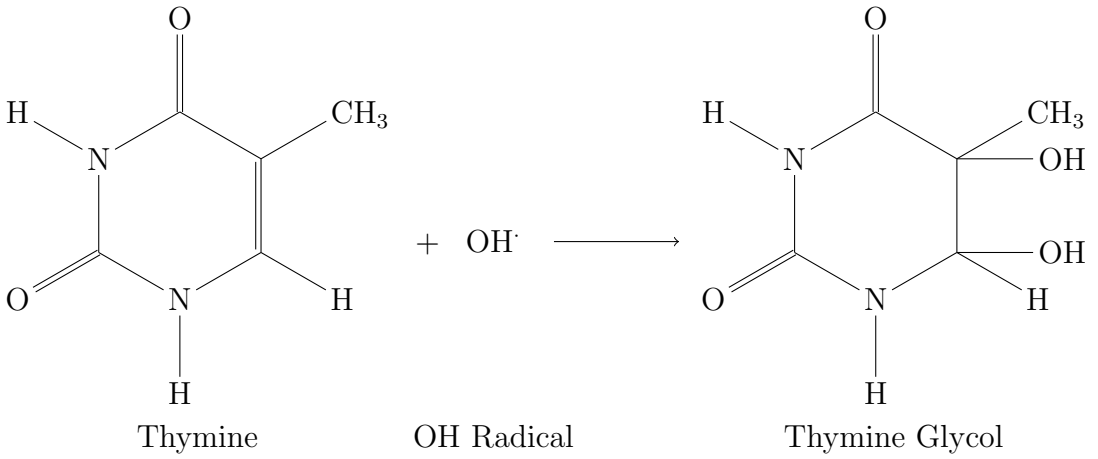

FIGURE 10.3: The chemical reaction between an OH radical (produced by ionising radiation) and thymine (one of the bases of DNA). This is an example of indirect DNA damage.

If oxygen then reacts with the DNA radicals before it has had sufficient time to repair, the damage becomes more difficult if not impossible to repair. If the damage has undergone oxygen fixation it cannot be repaired by chemical restitution processes. It was previously discussed in chapter 8, that in the absence of indirect radiation damages, clustered ionisation damage is the primary cause of radiation induced DNA damage and cell death. Clustered DNA damage is more difficult, if not impossible for cells to repair and is thought to be the underlying reason why high LET particles such alpha particles are more damaging to cells than low LET radiation such as photons and electrons.

In previous chapters it has been demonstrated that Geant4 can be used to simulate the direct ionisation damage of radiation to cells and use this information to predict the fraction of cells that will survive. However, Geant4 does not currently include a physics list capable of predicting the formation or tracking of radiolytic species (under development). Geant4 is therefore likely to underestimate the radiation damage to the cells.

The Monte Carlo track structure code RITRACKS simulates the interactions of ionising radiation with water using the following steps:

1. Simulate the traversal and interactions of the primary particle with the medium

TABLE 10.3: Indirect action from radiation of different LET and energy [115].

Radiation	E (MeV/amu)	LET (keV/µm)	Indirect Action (%)
X-Rays	–	9.4	76 ± 5
Carbon Ions	144	20	65 ± 2
Iron Ions	416	200	50 ± 21
Iron Ions	29	1298	39 ± 4
Iron Ions	16	2106	32 ± 2

(including ionisation, excitation, vibrational excitation and charge exchange processes).

2. Generation of secondary electrons liberated from the medium by the primary radiation. Simulation of the traversal and interactions of the secondary electrons.

3. Generation of radiolytic species.

4. Diffusion of chemically reactive species using a random walk (condensed history transport).

5. Recombination events of any pairs of radicals that travel within the "reactive" radius of each other.

The contributions from indirect DNA damage have been measured by [115] and [119]. Experimentally, this contribution is measured by measuring cell survival with the addition of an OH radical scavenger. After irradiation, the radiolytic species will react chemically with the DNA causing DSB. The addition of an OH radical scavenger results in the radiolytic species binding preferentially to the scavenger rather than the DNA. This decreases the contribution from indirect damage to the cell. In [115], the OH radical scavenger dimethylsulfoxide (DMSO) was used to suppress the indirect radiation action. The survival fraction of the cells post-irradiation was measured for increasing concentrations of DMSO. Their results were then extrapolated in the limit where the concentration of DMSO approaches infinity (i.e. the indirect radiation action was completely suppressed). From these results, the total contribution from indirect radiation damage was estimated for several types of radiation including; x-rays, carbon ions and iron ions (table 10.3).

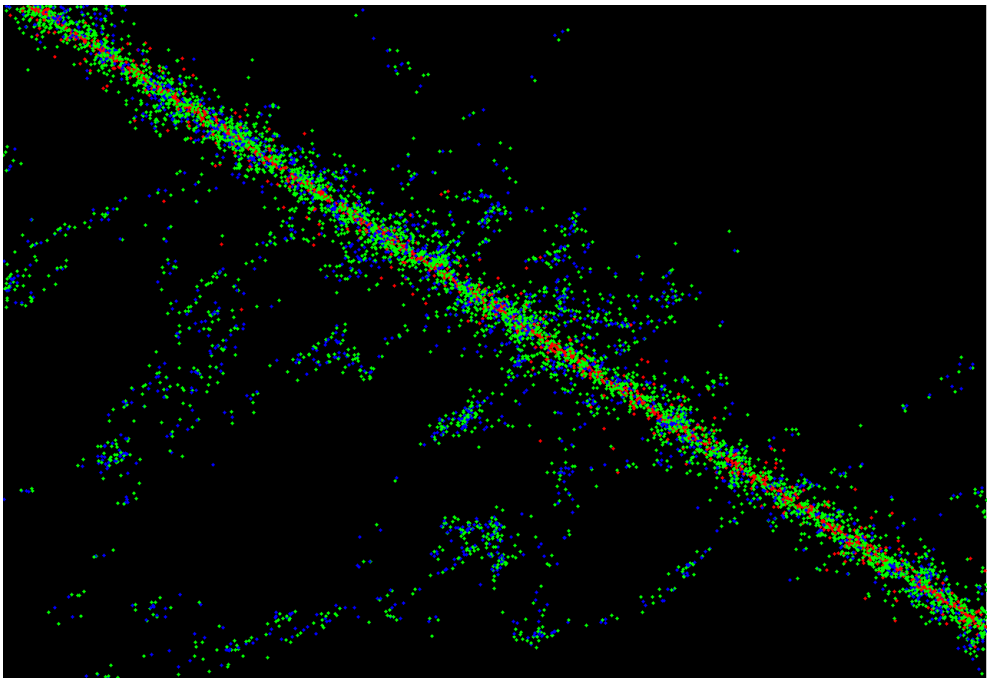

FIGURE 10.4: The ionisation track structure of a low energy proton - Red: Primary proton ionisations, Green: Secondary electron ionisations, Blue: OH radical species.

10.2 Objectives

In this chapter, a preliminary investigation was performed to measure the contributions from indirect DNA damage on the survival of V79 cells after irradiation by heavy ion radiation. Since RITRACKS has the capability of simulating the production of radiolytic species, it was used to perform this investigation. In the previous chapter it was shown that the physical cross sections were in excellent agreement above energies of 100 keV. Using RITRACKS, we have attempted to verify the data published in [115] for the contributions from indirect DNA damage for carbon and iron ions at clinical energies (16 - 416 MeV/amu).

10.3 Methods

RITRACKS does not have the capability of importing a customised geometry for irradiation (chapter 5). At the present time, RITRACKS can simulate track structure in

two different geometries; a cylindrical and cubic water volume with adjustable dimensions. To approximate the cellular geometry developed previously in Geant4, a cubic water volume was used with dimensions approximately equal to those of V79 cells. As previously discussed (in chapter 8) the nucleus of the cell contains a sub-region called the nucleolus which does not contain any DNA targets. RITRACKS does not permit a secondary volume representing the nucleolus to be created. To overcome this limitation, the analysis stage of the code filters out all data points which lie within the region where the nucleolus would be located.

An improved version of the original ionisation clustering algorithm (developed in chapter 8) has been developed for analysis in this chapter. The Matlab™ statistics toolbox contains several hierarchical clustering algorithms which were used in the development of the improved clustering algorithm. RITRACKS, similarly to Geant4 exports the position and energy deposited by each ionisation event produced by the primary and secondary particles (i.e. proton and secondary electron radiation). Previously, the ionisation events (simulated by Geant4) were spatially clustered into DNA DSBs in order to predict the survival probability of each cell in the tumour. The same method was performed using RITRACKS. In addition, the radiolytic species predicted by RITRACKS were clustered to produce additional DSB.

The clustering method included in Matlab™ has several advantages over the custom algorithm developed in chapter 8. The clustering algorithm is almost entirely vectorised meaning that there are very few 'for' or 'while' loops in the code. This greatly improves the speed at which the ionisation events are clustered. Secondly, intertrack ionisation events can combine to form more complex DSB rather than form multiple smaller DSBs (which is not physically correct and was a limitation of the previous algorithm). The major disadvantage of this algorithm is the memory requirements. As a result this method can only be used for simple track structure geometries. In order to cluster the ionisation events into spatially correlated groups, a distance matrix needs to be computed. This operation converts a ($n \times 3$ matrix) into a ($n \times n$ matrix) where each element is the Euclidean distance between each of the n ionisation events.

If the rows of the matrix A represent the Cartesian coordinates of the ionisation events:

$$A_{i,j} = X_j(i) \tag{10.11}$$

where j = 1,2 or 3 and i = 1....n where n is the number of recorded ionisation events.

Then the distance matrix M is given by:

$$M_{i,j} = \sqrt{(X_1(i) - X_1(j))^2 + (X_2(i) - X_2(j))^2 + (X_3(i) - X_3(j))^2} \tag{10.12}$$

In a typical radiation track structure simulation, a single proton will produce at least 10^4 ionisation events in a cell. In addition, the position of each radiolytic species will need to be recorded. The value of n is typically of the order of 10^4 to 10^6 for a single cell. Therefore $M_{i,j}$ will have dimensions in excess of $10^4 \times 10^4 = 10^8$ elements. Each element uses double precision variables to store the position of each ionisation and the distance between ionisations. The memory requirements are therefore extremely large. To perform such calculations, a 64 bit operating system with a 64 bit version of Matlab™ was used. The 32 bit version has inherent memory limitations which prevents matrices of the required dimensions from being created. The maximum array size permitted by our computer system using Matlab™ 64 bit was 81 Gb which is more than sufficient to hold matrices of the required size. The functions included in Matlab™ also include a 'savememory' option which reduces the memory required to perform the clustering operation by calculating distances between ionisations one at a time rather than calculating $M_{i,j}$. This process, while consuming less memory is significantly slower than calculating the distance matrix.

The "cluserdata" function included in the Matlab™ statistics toolbox was used to cluster ionisation events separated by less than the DNA segment length (defined to be 3.4 nm in chapter 8). Ionisation events and radiolytic species are clustered into DSB by defining ionisation 'centroids'. The centroid is the unweighted 'centre of mass' of the ionisation events. This serves as the geometric mean position of a group of ionisation events. Ionisation clusters are defined to be a group containing at least two ionisations such that all ionisations are located within 3.4 nm of the position of the centroid.

While ionising radiation produces many different radiolytic species, most of which are capable of causing indirect damage to DNA, experimental data [115] has shown that it is primarily the OH radical that causes the majority of indirect DNA damage. For the purposes of this chapter, we have considered that only OH radicals contribute to the indirect DNA damage and excluded all other radiolytic species.

When OH radicals are formed by ionising radiation, they may either react with the DNA molecule to produce indirect DNA damage or harmlessly react with other nearby radicals to produce less reactive species. A complete radiochemical model should consider the proximity of each radical and calculate the number of OH radicals that react only with DNA. Radiolytic chemistry is a subject of great complexity and beyond the scope of this research. For the purposes of this chapter, we have assumed that 15% of the OH radicals will react with DNA molecules and the remaining radicals will chemically react harmlessly with each other. This assumption was based on the results of [120]. Razskazovskiy [121] reported a similar efficiency for direct ionisation events. Given that a direct ionisation is in proximity to the DNA molecule, there is a 30% probability that a single strand break will be produced [122].

These assumptions were implemented into our code by randomly sampling 15% of the OH radicals that were formed by the ionising radiation and deleting the remaining 85% before clustering. A similar procedure was used for ionisation events (30% sampling).

However, in chapter 8, it was determined that DNA occupies less than 1% of the volume of nucleus. A volumetric correction factor was derived to account for the probability that a ionisation cluster was located in proximity to the DNA molecule. The same factor was used in the current work (5.47×10^{-3}) to scale the total number of DNA DSB.

A 3 µm × 3 µm × 3 µm water volume was irradiated in RITRACKS by single carbon and iron ions with energies listed in [115] (table 10.3). These ions were chosen due to the availability of the experimental data for comparison in [115]. The position of every ion ionisation, electron ionisation and OH radical was exported for clustering. To obtain a mean and standard deviation for the measured contributions, multiple simulations with identical geometry but different random number seeds were used. Each element of

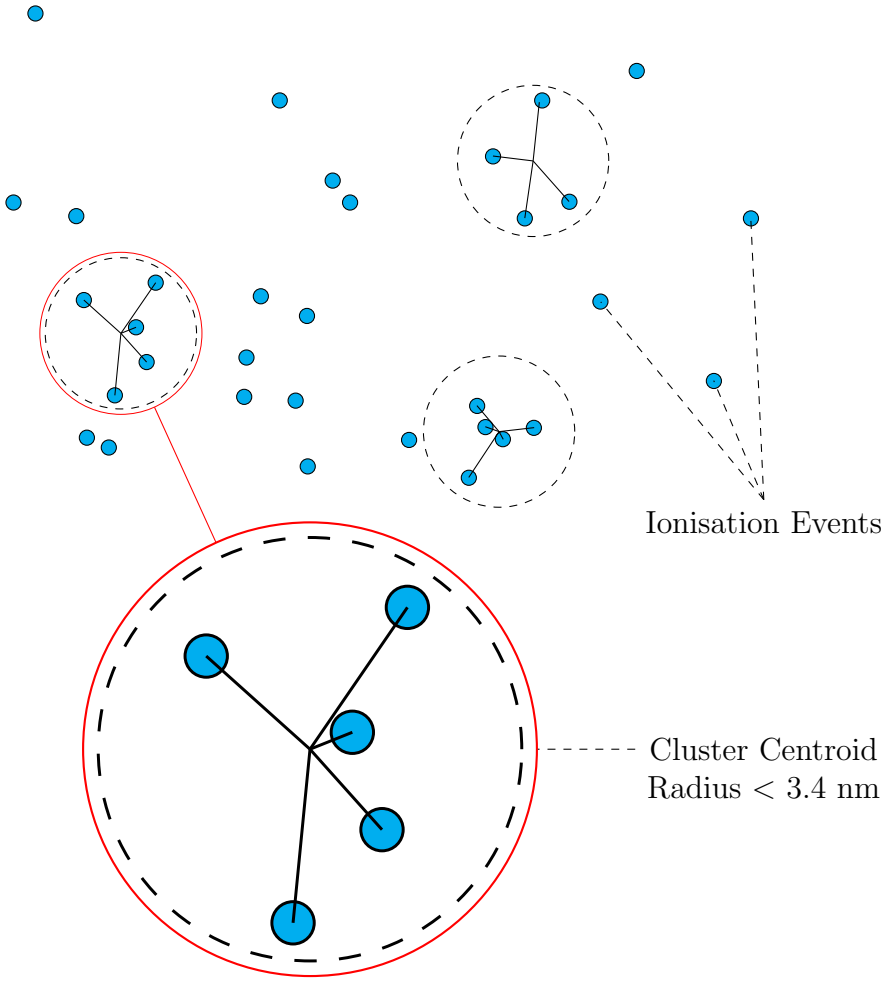

FIGURE 10.5: Illustration showing the mechanism of the hierarchal clustering algorithm which groups sptially correlated ionisation events into DSB. The requirements for a cluster of ionisation events to be classified as a DSB is at least 2 ionisation events within 3.4 nm of the centre of the cluster centroid (unweighted centre of mass).

the DNA DSB spectrum was averaged over all simulations and the standard deviation calculated.

Using the aforementioned clustering algorithm, the number of simple and complex double strand breaks was calculated with and without the contributions of OH radicals to estimate the effect of the indirect DNA damage.

TABLE 10.4: Indirect action contribution (%) - Simulated and experimental results averaged over 10 simulations.

Radiation	E (MeV/amu)	LET (keV/µm)	Exp. (%)	Sim. (%)
Carbon Ions	144	20	65 ± 2	61 ± 23
Iron Ions	416	200	50 ± 21	53 ± 10
Iron Ions	29	1298	39 ± 4	35 ± 3
Iron Ions	16	2106	32 ± 2	37 ± 5

10.4 Results

Table 10.4 and figure 10.6 compare the predictions made by RITRACKS and experimental values from [115] for the contribution from indirect ionisation damage to radiation induced cell death. There is large amount of uncertainty in both the experimental and simulated values. The uncertainty in the simulated data is the result of the relatively small number of ionisations produced at low LETs. As a result the sample size is smaller and therefore higher uncertainty at low LET. Due to the processing time required to cluster the ionisation events, only a small number of simulations were performed (n=10). An ANOVA analysis was performed on the two sets of data. The first variables that were tested for equality were the mean indirect contributions of experimental vs. simulated data. At a 95% confidence, there was no difference between the values predicted by RITRACKS and the experimental values published in [115].

The effect of particle LET on indirect DNA damage was tested at a 95% confidence level. There was a extremely significant effect of LET on indirect DNA damage ($p<0.0001$).

10.5 Conclusion

The work in this chapter has been performed to demonstrate the applicability of the damage clustering and cell death algorithm to indirect radiation damage. It has been demonstrated that the contribution from indirect DNA damage is significant ($> 30\%$) for particle LETs as large as 2100 keV/µm and increases with decreasing LET. The contribution of indirect DNA damage appears to decrease exponentially with increasing LET.

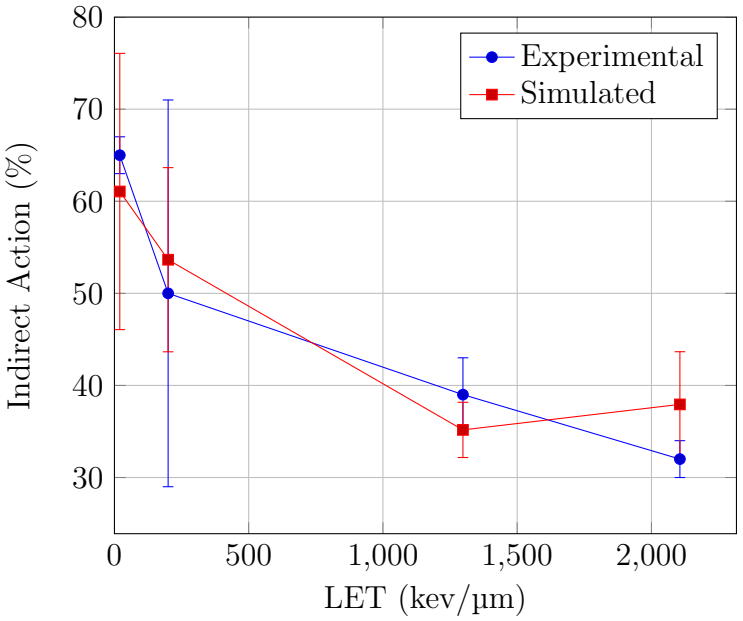

FIGURE 10.6: Contribution from indirect DNA damage for radiation of increasing LET. Comparison of experimental and simulated values.

In chapter 8, it was assumed that protons damaged cells primarily through direct ionisation processes. The results of this chapter suggest that the assumption was incorrect. The correlation between experimental and simulated data in chapter 8 indicates that the contribution from indirect damages (not simulated) has been integrated into the model during the calibration process. While this is not likely to impact radiobiological predictions under most clinical settings, under rare circumstances the model will give inaccurate results. For example, if the effect of free radical scavengers (e.g. Amifostine) were to be investigated in the cell model, the direct and indirect damages would first need to be separated. At the current time, Geant4 is not capable of performing this task.

With the release of Geant4 version 10.0 (2014), it will be possible to simulate the contribution of free radical species to DNA damage in future work.

Chapter 11

Conclusions and Future Work

11.1 Conclusion

The primary focus of the current work has been to develop a computational model to study the effects of radiation at a microscopic and nanoscopic level. The key reason for this was to overcome the inherent limitations of macroscopic models (such as LQ) which hide many of the fundamental physical, chemical and biological interactions in a lumped parameter mathematical model. This prevents the model from accurately predicting the behaviour of systems which have a diverse range of microscopic parameters. For example, a specific cell line has known alpha and beta values for use in the linear quadratic model. The LQ model has been shown to accurately predict the cell survival for that cell line. If a microscopic change was made to the system of cells (such as introduction of gold nanoparticles) the LQ model would no longer give accurate results. Typically this would be corrected by specifying new alpha/beta values or post multiplying the LQ model with a correction term. In the field of contemporary radiobiology, this is considered a parameter fitting exercise [21] and does not provide a method of explaining the mechanisms of the system.

Consequently, the primary objectives of this work was to develop a model capable of predicting macroscopic outcomes to radiobiological experiments (the same reason for LQ) but produce these results by modelling the physical, biological and chemical interactions

on a more fundamental (molecular) level. This has resulted in a robust software toolkit capable of modelling a wide range of experimental conditions. This model has the ability to investigate the effectiveness of novel cancer treatment therapies before experimental (cellular assays, animal studies and clinical trials) need to be performed. Experimental studies can often be cost and time prohibitive and often require ethical approval before proceeding.

The key achievements in the development of the model are:

1. Development of an application for growing a tumour composed of individual cells which can be exported to another software application for additional simulations. For the purposes of the current work, the tumour volume was imported into the Monte Carlo toolkit Geant4 for modelling radiation interactions. The growth characteristics of the cells and tumour were modelled using a custom quasi-realistic algorithm which includes biological processes such cell "contact inhibition". The cell growth algorithm went through several optimisation processes throughout this thesis. Three separate algorithms were developed over the course of several years to improve performance, biological realism and for testing. A simple graphical user interface was developed (see appendix B) for this software.

2. The second major achievement of this work was to develop an efficient method of importing the very complex cellular geometry (from chapter 3) into Geant4 for irradiation. At the time this work was performed, geometry of this complexity had never been utilised to our knowledge inside a Monte Carlo particle tracking toolkit before. This required the development of a C++ class inside Geant4 (called Membrane Parameterisation) which imported the coordinate system of the cells from the previous algorithm into Geant4 and populated each cell with a randomised organelle system and realistic elemental composition.

3. The first two stages were then tested by applying the code to study the characteristics of a novel radiotherapy technique called gold nanoparticle radiotherapy. The distribution of gold within each cell was modelled on nanometre scales and the resultant physical interactions of x-rays in this geometry was investigated. It

was concluded that gold nanoparticle therapy may have clear advantages for use in superficial cancer treatments due to effectiveness at low x-ray energies. It was also demonstrated that gold nanoparticles could potentially be used with high energy photons but with reduced efficiency.

4. The physical interactions modelled in the previous sections do not (on their own) predict the biological behaviour of the tumour after exposure to radiation and therefore cannot predict macroscopic behaviour of tumours. A new module for the software was therefore developed to predict biological response of the cells to irradiation. The first stage of this process was to determine the amount and location of ionisation events in individual cells. The widely adopted view of radiation induced cell death is that multiple localised damages to the DNA double helix inside the nucleus of a given cell results in double strand breaks which must be repaired otherwise the cell becomes reproductively dead. This process was modelled by first clustering the physical ionisation events from Geant4 into localised DNA DSBs. The relative position and complexity of the DSBs were calculated and stored for each irradiated cell. The biological response to this damage was then predicted by improving upon the mathematical model "TLK". This model was improved in several key areas: (a) adapting the model to study the radiation effects on individual cells rather than the average over an entire tumour, (b) predicting the radiation damage using a stochastic Monte Carlo method rather than a linear mathematical equation and (c) adding a spatial and temporal component to the model to more accurately represent the repair processes within each cell.

5. The quality of the predictions made in chapters 5-8 was then assessed by comparing the physical cross sections and corresponding Geant4 models with published experimental measurements. The Geant4 cross sections were shown to be in good agreement with experimental data above energies of 1 keV for protons. As a result, the results predicted in chapters 6-8 are likely to be accurate. The data was also compared with a new Monte Carlo software package called RITRACKS. Simulated proton track structure was statistically identical to Geant4 for energies above 0.5 MeV.

6. Finally, a preliminary investigation was performed to study the contributions from indirect radiation damage to DNA using RITRACKS. Preliminary results showed (based on modelling assumptions) that at least 50% of radiation damage from common forms of ionising radiation (x-rays, electrons, protons) is the result of indirect (chemical) damage.

The key results obtained using this model are outlined below:

1. It was determined that the chemical composition used for the different organelles of the cells in radiobiological modelling has significant effects on the predicted outcome. A statistical analysis was performed to determine whether a water medium was a suitable analogue for the composition of a cell organelle. The results indicated that there was no statistically significant change in the damage to the membrane or cytoplasm when a water medium was used instead of a realistic chemical composition. In the nucleus, it was determined that the importance of using a realistic elemental composition is the result of the effective atomic number rather than density. The nucleus (containing DNA) is composed of several elements with atomic numbers significantly higher than oxygen. As a result the interaction cross section for photons in the nucleus is significantly reduced when a water medium is used instead of DNA. This effect was investigated in chapter 9 by comparing the cross section of interactions of proton radiation in a water medium and in a medium composed of adenine, a primary component of DNA. In the nucleolus, it was determined that it is more important to use a realistic mass density rather than realistic effective atomic number for the composition. In the development of the cell death model, this consideration was included by using a scaled density water medium as the composition of the nucleolus. However, future models which explicitly model the structure of DNA should use a realistic DNA composition to accurately predict the number of DNA DSBs.

2. During our investigation of cell radio sensitisation by gold nanoparticles, it was determined that predicted dose deposited generated using the Livermore and DNA physics list in Geant4 give statistically identical results in terms of integral dose

deposited. Since the Livermore physics models have been extensively verified in the literature this gave us confidence that the Geant4-DNA models could be used in future microdosimetric track structure simulations.

3. The analysis of gold nano particle radiosensitisation revealed a strong dependence on the energy of the photons used to irradiate the cells. Gold nanoparticles were not as effective in radio sensitising cells at megavoltage energies compared with superficial energy x-rays (80 kV). This was determined to be the result of the strong $Z^{3.8}$ dependence on the interaction cross section for photo electric interactions at low photon energies. The addition of gold nanoparticles to the cells resulted in a large increase in the effective atomic number in the cells resulting in more photon interactions and as a result, more biological damage.

4. The size and relative position of the gold nanoparticles was also determined to be a key consideration when radio sensitising a cell. Typical methods of delivering GNPs into a cell result in gold clustering inside the cytoplasm of the cell or attaching to the nucleus. According to our calculations, the former results in minimal radio sensitisation of the cell due to the absence of any radiosensitive targets in cytoplasmic region. When the gold nanoparticles cluster on the cell nucleus, the short range electrons produced by x-ray radiation have the ability to penetrate the nucleus and increase the damage to the DNA. The key results obtained from this investigation were that the radiosensitisation by gold nanoparticles depends on three main factors: the energy of the ionising radiation, the concentration of the gold in the cell and the delivery method (which determines the spatial distribution of the gold within the cell).

5. The contribution to the radio sensitisation effect by Auger electrons was investigated. The Auger cascade processes were activated and de-activated inside Geant4 and the differences in damage were observed. It was determined that Auger electrons potentially result in a spatial redistribution of the radiation damage rather than a change in magnitude of the damage. Energy that would otherwise be absorbed in the gold medium is able to be transported outside the GNP and damage the surrounding biological medium. This effect is significantly more pronounced

when the gold nanoparticle is in contact with the nucleus because the Auger electrons have a very short range.

6. The results of the gold nanoparticle study were qualitatively verified by performing measurements at the Australian Synchrotron Centre on the XFM beamline. The major conclusion from the experimental work was the confirmation of the quantity of gold used in the previous computational study. The spatial distribution of gold was determined to be multiple small clustered gold particles distributed within the cytoplasm of the cell.

7. After integrating the cell growth, irradiation and damage repair models together, the cell survival curves for V79 cells following irradiation by protons of 0.76 MeV and 1.9 MeV were predicted and were in good agreement with experimental data. This demonstrated that our model has the ability to predict macroscopic radiobiological parameters by simulating physical processes on nanometre scales.

8. The Geant4 physical models were compared against experimental measurements and the independent Monte Carlo package RITRACKS. For proton radiation, both Geant4 and RITRACKS have been shown to be in good agreement with experimental measurements. Electron ionisation models are in good agreement above 100 eV however there is a clear discrepancy between results predicted for electron excitation processes. There is no widely adopted theoretical or semi-empirical model describing charge particle excitation processes in the literature.

9. Using RITRACKS, the clustering and cell death model were shown to be capable of predicting radiobiological outcomes resulting from indirect DNA damage. The contribution to DNA damage from indirect processes was calculated to be greater than 30% for heavy ion radiation.

11.2 Future Work

The capabilities of this new software package have been extensively demonstrated throughout this thesis. These capabilities are still limited and require further development. Some

improvements to be implemented in the future include:

- Including a temporal component to the cell growth and irradiation stage.
- A more realistic model of the growth characteristics of the tumour (more realistic spatial properties of the cell).
- Implementing a more robust mathematical model to describe the repair characteristics of the DNA DSB. The TLK model while easy to implement in the current work still required several approximations (over simplifications) which were included using a lumped parameter approach. The model developed by [24] made fewer approximations in its development and as a result may provide more accurate predictions.
- Optimisation of the Geant4 irradiation stage. While the work performed as part of this thesis made it feasible to simulate radiation interactions in a large group of cells, it is still time prohibitive.
- Implementation of radiolytic damage into Geant4 as the models become available.

Appendix A

Membrane Parameterisation Code

This C++ code is used to import the tumour coordinate system from Matlab™ into a Geant4 simulation. The cell is placed with coordinates, dimensions and rotations specified by the input file. The cell organelles are then placed within the membrane of the cell.

```
include "MembraneParameterisation.hh"

#include "G4VPhysicalVolume.hh"
#include "G4ThreeVector.hh"
#include "G4LogicalVolume.hh"

#if 1
#include "G4Ellipsoid.hh"
#include "G4Sphere.hh"
#else
#include "G4Sphere.hh"
#endif
//====================================

CellParams::CellParams():
                m_fp(NULL),
                m_readPosition(0)
{
}

CellParams::~CellParams()
```

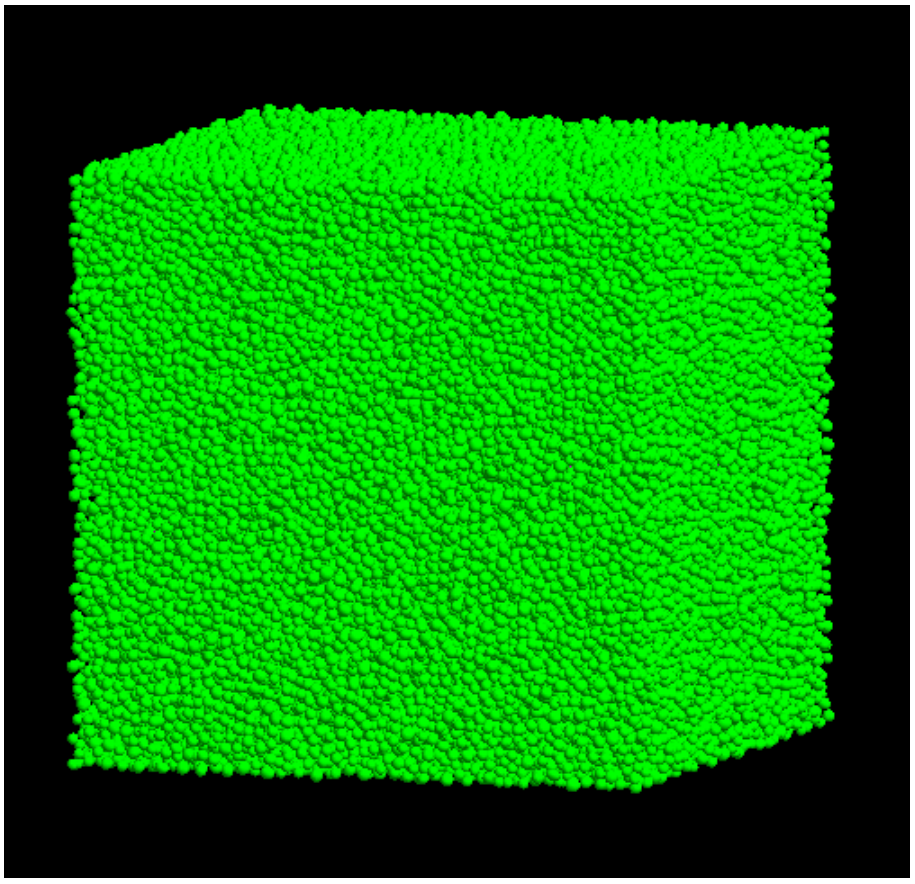

FIGURE A.1: Visualisation showing a tumour grown in Maltab™ being imported into Geant4 ready to be irradiated.

```
{
        if(m_fp != NULL)
        {
        fclose(m_fp);
        m_fp = NULL;
        }
}

G4int CellParams::initParams(char *fname, G4int &num)
{
        G4int rtn = false;
        G4int numcells;

        m_fp = fopen(fname,"rt");
        if(m_fp != NULL)
        {
    fscanf(m_fp, "%d\n",&numcells);
                num = numcells;
                m_readPosition = 0; // line number read //in the csv file
                rtn = true;
```

```
        }
        return rtn;
}

void CellParams::read_stuff(G4int copyNo, CellParam_t *cell)
{
        G4double x,y,z; //Cell Positions
        G4double a,b,c; //Cell Dimensions
        G4double alpha,beta,gamma; //Cell Rotations
        G4int numcells; //Number of Cells
    G4int recordlength;


        if(m_fp != NULL)
        {
                        fseek ( m_fp, 0, SEEK_SET );

                //Reads in Number of Cells from Matlab
                fscanf(m_fp, "%d %d\n",&numcells,...
                &recordlength);
                if(copyNo >= numcells)
                {
                        printf("copy number (%d) GE numcells...
                        \n", copyNo);









                }




                if(!feof(m_fp))
                {

                fscanf(m_fp, "%lf,%lf,%lf...
                ,%lf,%lf,%lf,%lf,%lf,%lf\n",
                &x, &y, &z,             //Reads in Cell Positions
                &a, &b, &c,                     //Reads in Cell Sizes
                &alpha, &beta, &gamma); //Reads in Cell Rotations

                        cell->x = x; //Allocates Spatial Coordinates to Cell
                        cell->y = y; //Allocates Spatial Coordinates to Cell
                        cell->z = z; //Allocates Spatial Coordinates to Cell
```

```
                        cell->a = a; //Allocates Cell Size
                        cell->b = b; //Allocates Cell Size
                        cell->c = c; //Allocates Cell Size


                        cell->alpha = alpha; //Allocates Cell Rotation
                        cell->beta = beta;   //Allocates Cell Rotation
                        cell->gamma = gamma; //Allocates Cell Rotation

                        m_readPosition++; //Look for next cell

                }
        }
        else
        {
                printf("file not open");
                //If the file cannot be read, throw an exception

                G4Exception("MembraneParameterisation construction: could not open file");
        }

}

G4int MembraneParameterisation::getNumCells()
{
        return fNoCells;
}

MembraneParameterisation::MembraneParameterisation...
(G4int&NoCells, char *fname)
{
        G4int numCells;

   fNoCells =  0;
   NoCells = 0;


   rotD3_Cyto = new G4RotationMatrix(); //Generates a cell rotation matrix
   rotD3 = new G4RotationMatrix();



   strncpy(fParamName,fname,PARAM_FILENAME_SIZE-1);
   fParamName[PARAM_FILENAME_SIZE-1] = 0x0;

        parms = new CellParams;

   if (parms->initParams(fname, numCells) == false)
```

```
   {
           printf("could not open file %s\n", fname);

   }

   fNoCells = numCells;
   NoCells = numCells;
}

//=============================================

MembraneParameterisation::~MembraneParameterisation()
{


  //printf("Deleting The rotation matricies and parms\n");
    delete rotD3_Cyto;
        delete rotD3;
        delete parms;

}

//=============================================

void MembraneParameterisation::ComputeTransformation
(const G4int copyNo, G4VPhysicalVolume* physVol) const
{
  CellParam_t mycell ;

#ifdef MIKESVERBOSE
#endif

  parms->read_stuff(copyNo, &mycell);



        rotD3->rotateX(mycell.alpha*rad); //Rotates cell by specified value
        rotD3->rotateY(mycell.beta*rad);  //Rotates cell by specified value
        rotD3->rotateZ(mycell.gamma*rad); //Rotates cell by specified value



  G4ThreeVector origin(mycell.x*nm, //Position of Cell
                                          mycell.y*nm, //Position of Cell
                                          mycell.z*nm); //Position of Cell

  physVol->SetRotation(rotD3);
  physVol->SetTranslation(origin);
```

```
}

//============================================

void MembraneParameterisation::ComputeDimensions
#if 1
(MikesG4Ellipsoid& cell, const G4int copyNo,...
 const G4VPhysicalVolume* physVol ) const
#else
(G4Sphere& cell, const G4int copyNo, const...
 G4VPhysicalVolume*) const
#endif
{

  //This section is for getting handles to the cell organelles
  //and specifying their size, rotation and position relative to
  //the cell membrane

  printf("Getting the logical volumes of the daughters\n");

  CellParam_t mycell;
  G4LogicalVolume* LogicalVolume = physVol->...
  GetLogicalVolume();


  G4VPhysicalVolume* cytoplasmPV = LogicalVolume->...
  GetDaughter(0);
  G4LogicalVolume*   cytoplasmLV = cytoplasmPV->...
  GetLogicalVolume();

  G4VPhysicalVolume* GoldPV = cytoplasmLV->...
  GetDaughter(0);
  G4VPhysicalVolume* RenticulumPV = cytoplasmLV->...
  GetDaughter(1);
  G4VPhysicalVolume* NucleolusPV = cytoplasmLV->...
  GetDaughter(2);

  G4LogicalVolume*   GoldLV = GoldPV->...
  GetLogicalVolume();
  G4LogicalVolume*   ReticulumnLV = RenticulumPV->...
  GetLogicalVolume();
  G4LogicalVolume*   NucleolusLV = NucleolusPV->...
  GetLogicalVolume();


 G4VPhysicalVolume* NucleusPV = NucleolusLV->...
 GetDaughter(0);
```

```
 G4LogicalVolume* NucleusLV=NucleusPV->...
 GetLogicalVolume();

  G4Sphere* GoldS=(G4Sphere*)GoldLV->GetSolid();
  G4Sphere* ReticulumS=(G4Sphere*)ReticulumnLV->GetSolid();
  G4Sphere* NucleolusS=(G4Sphere*)NucleolusLV->GetSolid();
  G4Sphere* NucleusS=(G4Sphere*)NucleusLV->GetSolid();


 MikesG4Ellipsoid* cytoplasmS = (MikesG4Ellipsoid*)...
 cytoplasmLV->GetSolid();



#ifdef MIKESVERBOSE
  printf("MembraneParameterisation:...
  ComputeDimensions %d\n",copyNo);
#endif

  parms->read_stuff(copyNo, &mycell);


  G4double xlength = mycell.a*nm;
  G4double ylength = mycell.b*nm;
  G4double zlength = mycell.c*nm;

  cell.SetSemiAxis (xlength, ylength, zlength);
  cell.SetZCuts (-zlength, zlength);


  //Membrane Thickness in nm
  G4int nuc_cyto_dist = 10;

  printf("Overiding the cytoplasm dimensions\n");

  cytoplasmS->SetSemiAxis ((mycell.a-nuc_cyto_dist)...
  *nm, (mycell.b-nuc_cyto_dist)*nm, (mycell.c-nuc_cyto_dist)*nm);
  cytoplasmS->SetZCuts((-mycell.c+nuc_cyto_dist)*nm,...
  (mycell.c-nuc_cyto_dist)*nm);

   //Specifies Gold Nano-Particle Dimensions

   GoldS->SetOuterRadius(0.4*um);
   GoldS->SetInnerRadius(0.0*um);


   //Specifies Reticulum Dimensions
   ReticulumS->SetOuterRadius(5*um);
```

```
   ReticulumS->SetInnerRadius(4*um);


   //Specifies Nucleolus Dimensions
   NucleolusS->SetInnerRadius(0*um);
   NucleolusS->SetOuterRadius(3*um);

   //Specifies Nucleus Dimensions
   NucleusS->SetInnerRadius(0*um);
   NucleusS->SetOuterRadius(2*um);



   G4ThreeVector origin_cytoplasm(0*nm,
                                          0*nm,
                                          0*nm);

   //Where to place the gold nano-particle in the cell
   G4ThreeVector origin_gold(2*um,7*um,3*um);

 //printf("Rotating the cytoplasm by 0 degrees\n");
        rotD3_Cyto->rotateX(0*deg);
        rotD3_Cyto->rotateY(0*deg);
        rotD3_Cyto->rotateZ(0*deg);



 printf("Rotating each of the daughter volumes\n");

cytoplasmPV->SetRotation(rotD3_Cyto);
cytoplasmPV->SetTranslation(origin_cytoplasm);


GoldPV->SetRotation(rotD3_Cyto);
GoldPV->SetTranslation(origin_gold);



RenticulumPV->SetRotation(rotD3_Cyto);
RenticulumPV->SetTranslation(origin_cytoplasm);

NucleolusPV->SetRotation(rotD3_Cyto);
NucleolusPV->SetTranslation(origin_cytoplasm);

NucleusPV->SetRotation(rotD3_Cyto);
NucleusPV->SetTranslation(origin_cytoplasm);
  //printf("%f   %f\n",minaxis, cytoplasmS->GetOuterRadius() );
```

Appendix B

Cell Growth Code

This Matlab™ code grows a tumour composed of individual randomised cells. Using the graphical user interface (GUI), the user specifies the upper and lower limits for the cell size and the dimensions of the tumour.

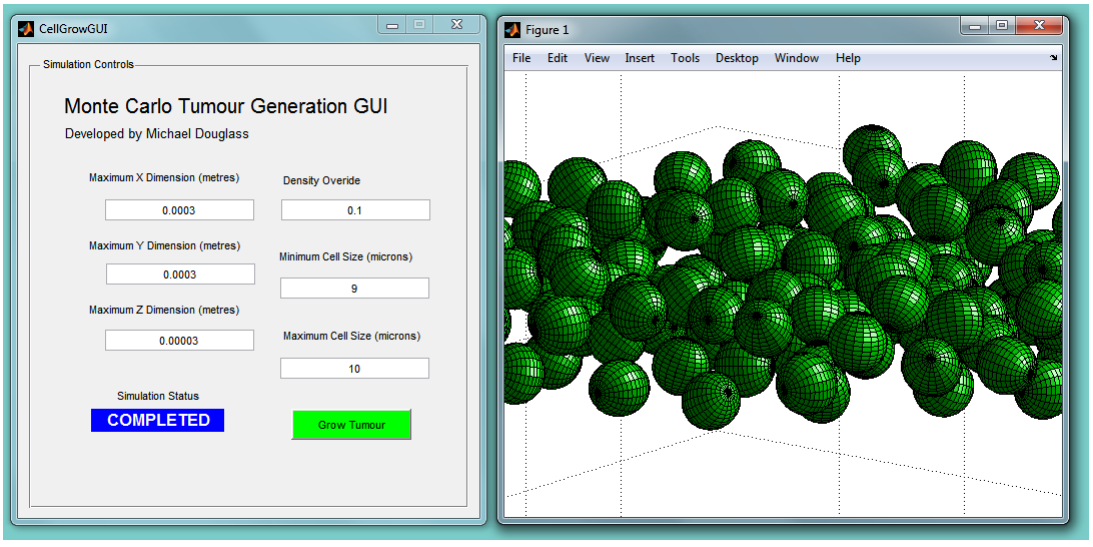

FIGURE B.1: Demonstration of the cell growth graphical user interface.

```
%Second Generation Cell Growing Code
clear
clc

%Ensures enough precision
format long
```

```
%Set maximum dimension limits for the tumour

%=======================================
X_Maximum = 0.3; %mm
Y_Maximum = 0.3; %mm
Z_Maximum = 0.00001; %mm
%=======================================

%Mono-Layer, 1=Yes, 2=No
MonoLayer = 1;

%Set Maximum and Minimum Cell Size
%=======================================
Cell_Min_Size = 11.5; %micrometers
Cell_Max_Size = 14; %micrometers
%=======================================

%How Many Growth Phases
%=======================================
Number_of_Steps_Size = 30;
%=======================================


if MonoLayer ==1

    disp('MonoLayer')

    %Calculates the number of cells to grow if the tumour is a single layer

    Number_Of_Cells = round((4*X_Maximum*Y_Maximum)...
    /(pi*Cell_Min_Size^2));
    Target = round((4*X_Maximum*Y_Maximum)/...
    (pi*Cell_Max_Size^2));


%Calculates the number of cells to grow if the tumour is not a monolayer

else if MonoLayer ==0;

        disp('3D Volume')

%Upper Limit on the Number of Cells that need to be created
        Number_Of_Cells = round((X_Maximum*Y_Maximum...
        *Z_Maximum*2^3)
            (4/3*pi*Cell_Min_Size^3));
Lower Limit on the Number of Cells that need to be created - to display the user
        Target = round((X_Maximum*Y_Maximum...
        *Z_Maximum*2^3)
            (4/3*pi*Cell_Max_Size^3));

    end

end

%Number of allowed tries to place a cell with no success
Number_of_False_Tries_Remaining = Number_Of_Cells*10;


%Initialises cell values to zero
X = 0;
Y = 0;
Z = 0;
R = 0;

%Puts the first cell in the distribution.
X(1) = -1*X_Maximum + (2*X_Maximum).*rand(1);
Y(1) = -1*Y_Maximum + (2*Y_Maximum).*rand(1);
Z(1) = -1*Z_Maximum + (2*Z_Maximum).*rand(1);
R(1) = Cell_Min_Size + (Cell_Max_Size-Cell_Min_Size)...
       *rand(1);
```

```
%Cell Counter
Cell_Num = 2;

%Next Cell
Number_Of_Cells_Left_to_Place = Number_Of_Cells - 1;

IterationsCounter = 1;

%Keeps placing cells until there are no more left to place
while (Number_Of_Cells_Left_to_Place>0)

    clc
%Displays to user the number of cells placed and the target amount
    fprintf('Target # of Cells = %d\n',Target);
    fprintf('Number of Cells Placed = %d\n',length(X));

%Randomly Places the next cell
    Temp_X = -1*X_Maximum + (2*X_Maximum).*rand(1);
    Temp_Y = -1*Y_Maximum + (2*Y_Maximum).*rand(1);
    Temp_Z = -1*Z_Maximum + (2*Z_Maximum).*rand(1);

%Cell growth minimum size
    Temp_R = Cell_Min_Size;

%Upper limit for cell growth
    Finish_R = Temp_R + (Cell_Max_Size-Cell_Min_Size)...
               *rand(1);

%Checks if cell is overlapping during growth cycle using Eigenvalue method
  Number_Of_cells_Overlapping = CheckOverlap(X,Y,Z,R,Temp_X,Temp_Y,Temp_Z,Temp_R);


    %Keeps trying to place cells until it finds a space
    if (Number_Of_cells_Overlapping>0)

        %Reduces the cut-off limit of placing cells by 1
        Number_of_False_Tries_Remaining = ...
            Number_of_False_Tries_Remaining - 1;

        if (Number_of_False_Tries_Remaining==0)
            %Stops the code if it has placed a cell
            %unsuccesfully for many tries
            break
        else
            continue

        end



    elseif (Number_Of_cells_Overlapping==0)
        %Incement Cell Counter Placed by 1

        %The cell continues to grow

        StopSize = randi(Number_of_Steps_Size+1);

        %Grows the cell
        for i = 1:StopSize

            %New cell radius
            Temp_R = Temp_R + (Cell_Max_Size-Cell_Min_Size)
                Number_of_Steps_Size;

            Number_Of_cells_Overlapping =...
                CheckOverlap(X,Y,Z,R,Temp_X,Temp_Y,...
                             Temp_Z,Temp_R);

            if (Number_Of_cells_Overlapping == 0)
```

```
                %If the cell has grown to its maximum
                %it places the cell
                if i==StopSize;

                    X(Cell_Num) = Temp_X;
                    Y(Cell_Num) = Temp_Y;
                    Z(Cell_Num) = Temp_Z;
                    R(Cell_Num) = Temp_R;

                    %Incements the cell number if placed
                    %succesfully
                    Cell_Num = Cell_Num + 1;
                    %If it has successfully placed a
                    %cell, reset the number
                    %of false tries
                    Number_of_False_Tries_Remaining...
                    = Number_Of_Cells*10;

                    break

                else

                    continue

                end
            elseif (Number_Of_cells_Overlapping > 0)

                %If the cell growth leads to an
                %intersection with another cell,
                %place the previously un-overlapped cell size
                X(Cell_Num) = Temp_X;
                Y(Cell_Num) = Temp_Y;
                Z(Cell_Num) = Temp_Z;
                R(Cell_Num) = Temp_R - (Cell_Max_Size- ...
                              Cell_Min_Size)
                    Number_of_Steps_Size;

                %Incements the cell number if placed
                $succesfully
                Cell_Num = Cell_Num + 1;

                Number_of_False_Tries_Remaining = ...
                             Number_Of_Cells*10;

                break


            end

        end

    %Displays an error if the code gives a strange result

    else if (Number_Of_cells_Overlapping<0)

            disp('Error: Number of Cells overlapping is < 0');



        end

    end


    %Once this is done, randomise the size of the
    %ellipsoid within the sphere, rotations, and
    %size. This could be done using ParFor.
    Number_Of_Cells_Left_to_Place = ...
    Number_Of_Cells_Left_to_Place - 1;
    IterationsCounter = IterationsCounter + 1;
```

```
end


%Transposes the Position and Size Vectors for Processing
X = X';
Y = Y';
Z = Z';
R = R';

%Sends the data to be randomised as ellispoids
%and print it to a file
Geant4CellData(X,Y,Z,R,Cell_Min_Size,Cell_Max_Size);
```

Appendix C

Damage Clustering Code

This Matlab™ code imports the output file from Geant4 and groups spatially correlated ionisation events into DSBs of varying complexity.

```
%%%%%%%%%%%%%%%%%%%%%%%%%%%%%%%%%%%%
clear
clc
format long
%%%%%%%%%%%%%%%%%%%%%%%%%%%%%%%%%%%%
%matlabpool open
FiletoRead = 'OuterCenter.txt';
%CriticalRadius = 3.4; %nm
NumIonisationsInCluster = 2; %This is the number of ionisations in a cluster
%Required to be consisered a fatal cluster

A = ReadInAndSort(FiletoRead);

%Sorts all of the damages by grouping damages into cell arrays
Damage = SortDamagesByCell(A);


%data containing the cell properties of position, size and rotation
CellPosition = csvread('cells.csv');

%Removes the Header Line
CellPosition(1,:) = [];
%Keeps only the positions of the cells and not size or rotation
CellPosition = CellPosition(:,[1 2 3]);


%Specify the Radius of the Nucleus
RadiusOfNucleus = 7000; %nm

%The Distance the ionisations must be to produce a cluster
CriticalRadius = 3.4; %nm

%Voxel Size = Radius of Cluster
DX = CriticalRadius;

%Number of Voxels in Each Axis of the Nucleus
NumberofVoxels = RadiusOfNucleus*2/CriticalRadius;

Start = -RadiusOfNucleus;
```

```
Spectrum{length(Damage)}=0;



for i = 1:length(Damage)


    %If No damages a present in the current cell nucleus, move to next cell
    if length(Damage{i})==0;

        Spectrum{i}=0;
        continue

    end

    %Stores the current damages in a temporary variable.
    TempCellStore = Damage{i};
    X = TempCellStore(:,1)-CellPosition(i+1,1);
    Y = TempCellStore(:,2)-CellPosition(i+1,2);
    Z = TempCellStore(:,3)-CellPosition(i+1,3);

    %Converts nm to microns
    %X = X * 10^-3;
    %Y = Y * 10^-3;
    %Z = Z * 10^-3;

    Spectrum_Temp = 0;



    Spectrum_Temp(100000)=0;

    %Cycles through all the Voxels in the 3D Matrix
    for j = 1:NumberofVoxels

        clc
       fprintf('Completed %2.9f%% of Current Cell\n', j/NumberofVoxels*100);
       fprintf('Completed %2.1f%% of All Cells\n', i/ length(CellPosition)*100);



       for k = 1: NumberofVoxels

          for l = 1: NumberofVoxels



              %Loop across a cubic matrix (3D) and sum up all the damages
              %in those voxels
              TempX = Start + DX*l;
              TempY = Start + DX*k;
              TempZ = Start + DX*j;


              count = length(X((X>=TempX)&(X<=(TempX+DX))&(Y>=TempY)&...
              (Y>=TempY)&(Y<=(TempY+DX))&(Z>=TempZ)&(Z<=(TempZ+DX))));
              %DamageMatrix(j,k,l) = count;

              %If there are not enough damages to form a cluster, do not
              %add them to the spectrum of damages
              if (count<NumIonisationsInCluster)

                  continue

              end

              %Add Data to Spectrum Matrix
              Spectrum_Temp(count) = Spectrum_Temp(count) + 1;


          end
```

```
        end


    end

    %Removes all of the un-necessary zeros at the end of the spectrum
    Spectrum_Temp = Spectrum_Temp(1:max(find(Spectrum_Temp)));
    if isempty(Spectrum_Temp)

        Spectrum{i}=0;

        continue
    end

    %Adds the temporary spectrum to the spectrum cell data
    Spectrum{i}= Spectrum_Temp;


    clear Spectrum_Temp;

end

%matlabpool close
%Read in Membrane and Cytoplasm Doses
```

Appendix D

Cell Death Code

This code predicts whether a particular cell in the tumour will survive or die based on the complexity of the radiation damage produced in the Geant4 simulation.

```
%====================================
%====================================
CELL GROWTH IRRADIATION REPAIR DEATH
%====================================
%====================================

%Picks a random starting seed based on CPU clock time.
randomvariable = clock;


%===========
%PARAMATERS
%===========

%Time Resolution
delta_t = 10/60; %ten minutes

%Minimum Number of Ionisations to Form a DSB
NumIonisationsInCluster = 2;

%Time allowed for Repair after Irradiation
TimeAfterIrradiation = 6; %hours

%Creates an empty surival matrix
Survival(length(Spectrum))=0;

%Cells are all alive to start
Survival(:)=1;


    %How random numbers are defined in code
    %=======================================
    %random number = a + (b-a)*rand;
    %random number = normrnd(mu,sigma);
    %=======================================


    %================================================
    %Calibrated for V79 Cells - Based on Robert Stewart
    %================================================
    Cell_Cycle_Time = 15; %hours - Time for V79 Cells to complete 1 cell cycle
    lamda1 =normrnd(10,0.5); %Repair rate of simple DSB
    lamda2 =normrnd(0.0565,0.0001111); % Repair Rate of Complex DSB
```

```
    gamma =0.25; %Correction Factor proposed by (Stewart, 2001)
    eta =normrnd(0.00005,0.0000005); %Interaction Coefficient for Binary Interactions
    beta1 = 0; %Probability of Incorrectly Repairing a Simple DSB
    beta2 = 0.00090; %Probability of Incorrectly Repairing a Complex DSB
    %================================================


    MaxSearch = length(Spectrum{1});

    %Starting Time
    T = 0;

    %Starting Damages Calculated from Geant4 Data
    L1 = Spectrum{1}(2);
    L2 = sum(Spectrum{1}(3:MaxSearch));

    %Initially there are no lethal lesions or mutations
    Lm = 0;
    Lf = 0;

    Survival(1)=1;

    %Iterate until Repair Time has been Reached
    while (T<TimeAfterIrradiation)

        %If there is a fractional amount of damage, round down

        if L1<1.0

            L1=0;

        %If there are damages, reduce the number of damages by value in TLK
        else

            L1 = L1 - (lamda1*L1-eta*L1*(L1+L2))*delta_t;

        end


        %If there is a fractional amount of damage, round down
        if L2<1.0

            L2=0;


        %If there are damages, reduce the number of damages by value in TLK

        else

            L2 = L2 - (lamda2*L2-eta*L2*(L1+L2))*delta_t;

        end

                %Calculate the number of Lethal lesions and non-lethal mutations
        Lf = Lf + (beta1*lamda1*L1+beta2*lamda2*L2+...
             gamma*eta*(L1+L2)^2)*delta_t;
        Lm = Lm+ ((1-beta1)*lamda1*L1+(1-beta2)...
            *lamda2*L2+(1-gamma)*eta*(L1+L2)^2)*delta_t;

                %Increment the Time Step
        T = T + delta_t;

    end
        %Calculate cell survival probability according to Poisson Statistics
        S = exp(-1*Lf);


        %Use a random number generator to determine if cell survives
        MC_Random_Number = rand(1);

        if (MC_Random_Number<S)
```

```
            Survival(1) = 1;

        else
            Survival(1) = 0;


        end
```

Appendix E

Revised Clustering Code

This is the improved clustering code developed using the K-Means clustering algorithm. While this method is quicker than the previous method (appendix C), the memory requirements are much larger.

```
clear
clc

format long

Outer_Dim = 14; %um
Inner_Dim = 10; %um

Volume_of_DNA = 5; %um3
Volume_of_Nucleus = Outer_Dim^3-Inner_Dim^3;

%Fraction by Volume of DNA in the Cell Nucleus
Fraction_DNA_Volume = Volume_of_DNA/Volume_of_Nucleus;


Outer_Dim=Outer_Dim * 10000;
Inner_Dim=Inner_Dim * 10000;

%Maximum Radius of DNA Segment (10bp = 3.4 nm)
clusterradius = 3.4;
%Number of files from RITRACKS to read
Number_of_Files = 19;

%What fraction of the OH Radicals react with the DNA
OHReactionEfficiency = 0.15;
%What fraction of the Ionisations react with the DNA
IonisationEfficiency = 0.30;



for m =1:Number_of_Files


    IonFile = ['C:\Users\user\Documents\RITRACKS ...
        Simulations\Default\Tracks\Track', num2str(m)...
        , '\IonEvents.dat'];

    Read(IonFile);
    Ion = data;
```

```
    ElectronFile = ['C:\Users\user\Documents\RITRACKS ...
        Simulations\Default\Tracks\Track', num2str(m), ...
        '\ElEvents.dat'];

    Read(ElectronFile);
    Electron = data;

    ChemistryFile = ['C:\Users\user\Documents\RITRACKS ...
        Simulations\Default\Tracks\Track', num2str(m), ...
        '\pospc.dat'];

    Read(ChemistryFile);
    Chemical = data;


%Sorts data into ionisation and OH radical damge only

Ion = Ion(Ion(:,4)<5,:);
Electron = Electron(Electron(:,4)<5,:);
Chemical = Chemical(Chemical(:,4)==2,:);

Ion = [Ion;Electron];

Ion = Ion(:,[1,2,3]);

%Removes DNA Damage from Nucleolus

TRUTH = (Ion(:,2)<(Outer_Dim/2+Inner_Dim/2));
TRUTH = TRUTH.*(Ion(:,2)>(Outer_Dim/2-Inner_Dim/2));
TRUTH = TRUTH.*(Ion(:,1)<(Inner_Dim/2));
TRUTH = TRUTH.*(Ion(:,1)>(-Inner_Dim/2));
TRUTH = TRUTH.*(Ion(:,3)<(Inner_Dim/2));
TRUTH = TRUTH.*(Ion(:,3)>(-Inner_Dim/2));

Ion = Ion(TRUTH == 0,:);

TRUTH = (Chemical(:,2)<(Outer_Dim/2+Inner_Dim/2));
TRUTH = TRUTH.*(Chemical(:,2)>(Outer_Dim/2-Inner_Dim/2));
TRUTH = TRUTH.*(Chemical(:,1)<(Inner_Dim/2));
TRUTH = TRUTH.*(Chemical(:,1)>(-Inner_Dim/2));
TRUTH = TRUTH.*(Chemical(:,3)<(Inner_Dim/2));
TRUTH = TRUTH.*(Chemical(:,3)>(-Inner_Dim/2));

Chemical = Chemical(TRUTH == 0,:);


%Throws away some of the ionisation and chemical damages
%depending on their reaction efficiency

EfficiencySelection = randperm(length(Ion));

Numbertokeep = round(IonisationEfficiency*length(Ion));

Ion = Ion(EfficiencySelection(1:Numbertokeep),:);

Chemical = Chemical(:,[1,2,3]);

EfficiencySelection = randperm(length(Chemical));

Numbertokeep = round(OHReactionEfficiency*length(Chemical));

Chemical = Chemical(EfficiencySelection(1:Numbertokeep),:);

Chemical = [Chemical; Ion];

%Clusters the Ionisation Damage

X = [Ion(:,1),Ion(:,2),Ion(:,3)];
c  = clusterdata(X,'criterion','distance','cutoff'...
     ,clusterradius,...
    'distance','euclidean','linkage','centroid',...
```

```
    'savememory','on');


Ionisations = GroupSpectrum(c);
Ionisations = round([Ionisations zeros(1,5)].*...
              Fraction_DNA_Volume);

I_Damage(m,1) = Ionisations(1);
I_Damage(m,2) = Ionisations(2);
I_Damage(m,3) =sum(Ionisations)-Ionisations(1)-...
               Ionisations(2);



%Clusters the Ionisation + Chemical Damage

X = [Chemical(:,1),Chemical(:,2),Chemical(:,3)];
c  = clusterdata(X,'criterion','distance','cutoff',...
     clusterradius, ...
    'distance','euclidean','linkage','centroid',...
    'savememory','on');

Chemicals = GroupSpectrum(c);
Chemicals = round([Chemicals zeros(1,5)].*...
            Fraction_DNA_Volume);

C_Damage(m,1) = Chemicals(1);
C_Damage(m,2) = Chemicals(2);
C_Damage(m,3) = sum(Chemicals)-Chemicals(1)-Chemicals(2);


I{m} = Ionisations;
C{m} = Chemicals;


clear data, colheaders, textdata;

end
I_Damage_SD = [std(I_Damage(:,1)) std(I_Damage(:,2))...
               std(I_Damage(:,3))];
I_Damage = [mean(I_Damage(:,1)) mean(I_Damage(:,2))...
            mean(I_Damage(:,3))];

C_Damage_SD = [std(C_Damage(:,1)) std(C_Damage(:,2))...
               std(C_Damage(:,3))];
C_Damage = [mean(C_Damage(:,1)) mean(C_Damage(:,2))...
            mean(C_Damage(:,3))];

ExportFile = [I_Damage; I_Damage_SD; C_Damage; C_Damage_SD];

Av(1) = 100-(I_Damage(2) + I_Damage(3))/...
        (C_Damage(2)+C_Damage(3))*100;
Av(2) = 100-(I_Damage(2)+I_Damage_SD(2)...
        + I_Damage(3)+I_Damage_SD(3))/...
        (C_Damage(2)-C_Damage_SD(2)+C_Damage(3)...
        -C_Damage_SD(3))*100;
Av(3) = 100-(I_Damage(2)-I_Damage_SD(2) +...
        I_Damage(3)-I_Damage_SD(3))/...
        (C_Damage(2)+C_Damage_SD(2)+C_Damage(3)...
        +C_Damage_SD(3))*100;


%Writes DSB Values to a File for Processing
csvwrite('export.csv',ExportFile)

mean(Av)
std(Av)

%============================================================
%Can calculate cell survival probabilities if needed
%============================================================
```

```
for i =1:length(I)

Spectrum{1} = I{i};
CellDeath
IonisationDeath(i) = S*100;

Spectrum{1} = C{i};
CellDeath
ChemicalDeath(i) = S*100;

C{i} = [C{i} zeros(1,10-length(C{i}))];
I{i} = [I{i} zeros(1,10-length(I{i}))];

end

IonisationDeath = [mean(IonisationDeath) std(IonisationDeath)]
ChemicalDeath = [mean(ChemicalDeath) std(ChemicalDeath)]

%=============================================================
```

Appendix F

Presentation Renderings

These figures were rendered using Autodesk™ 3DS Max for conference presentations.

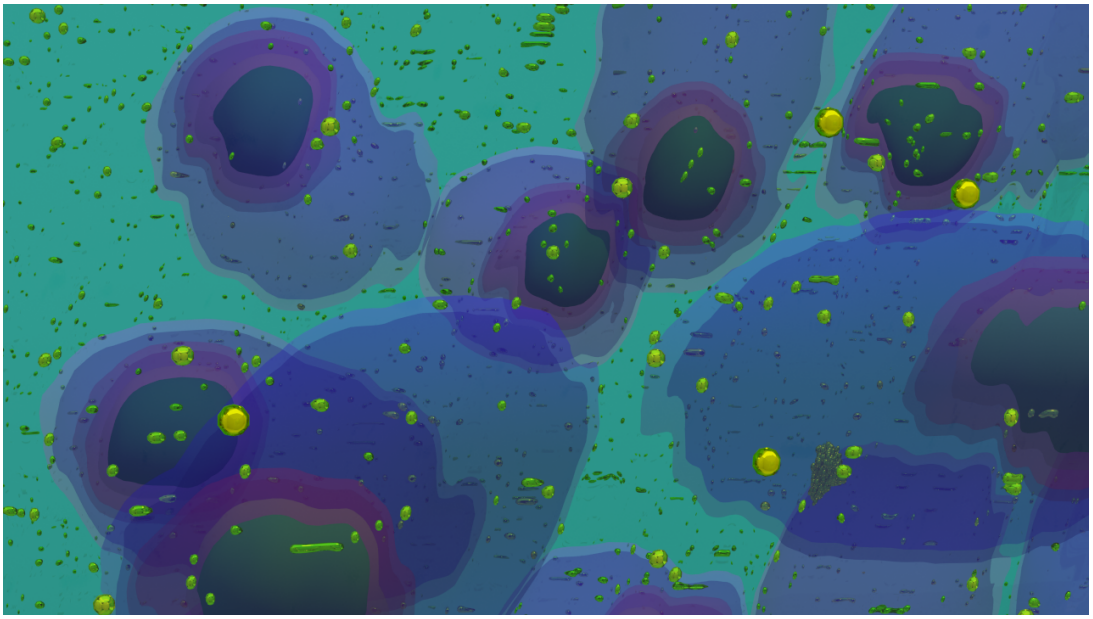

FIGURE F.1: Rendering of gold nanoparticles in cells.

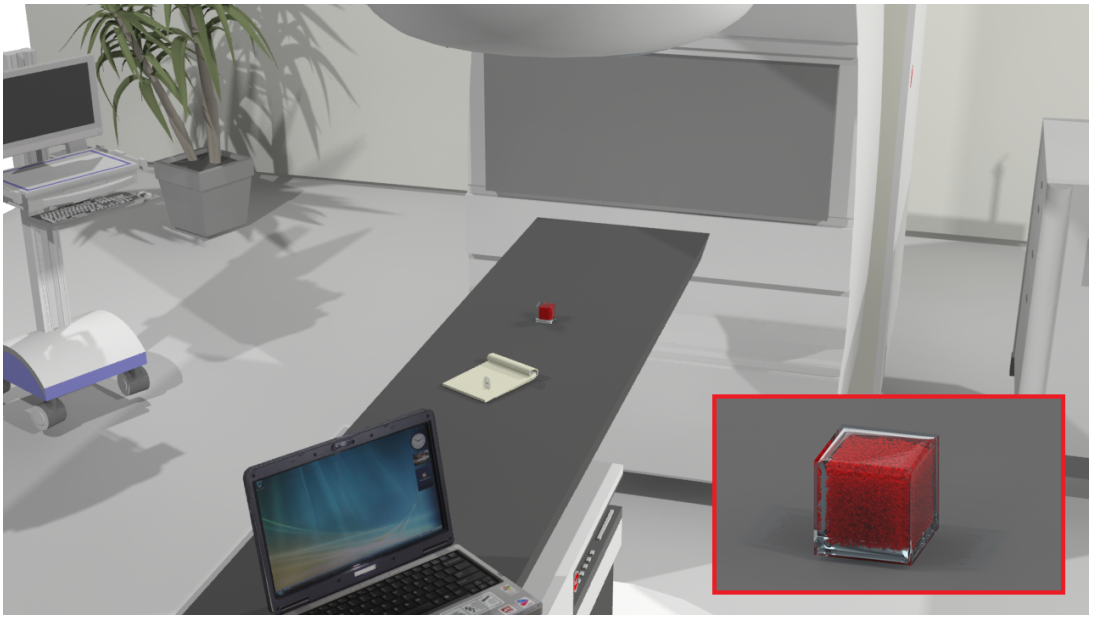

FIGURE F.2: Rendering of irradiation setup.

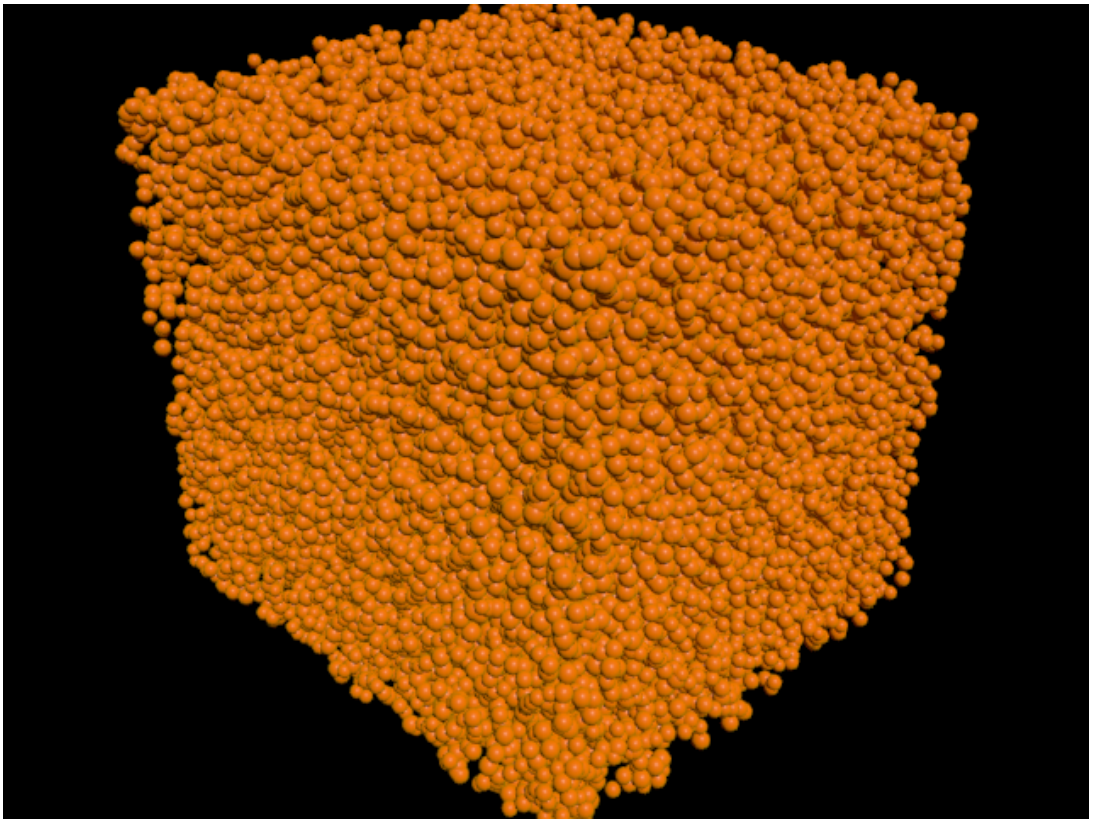

FIGURE F.3: Cells imported into Autodesk 3DS Max.

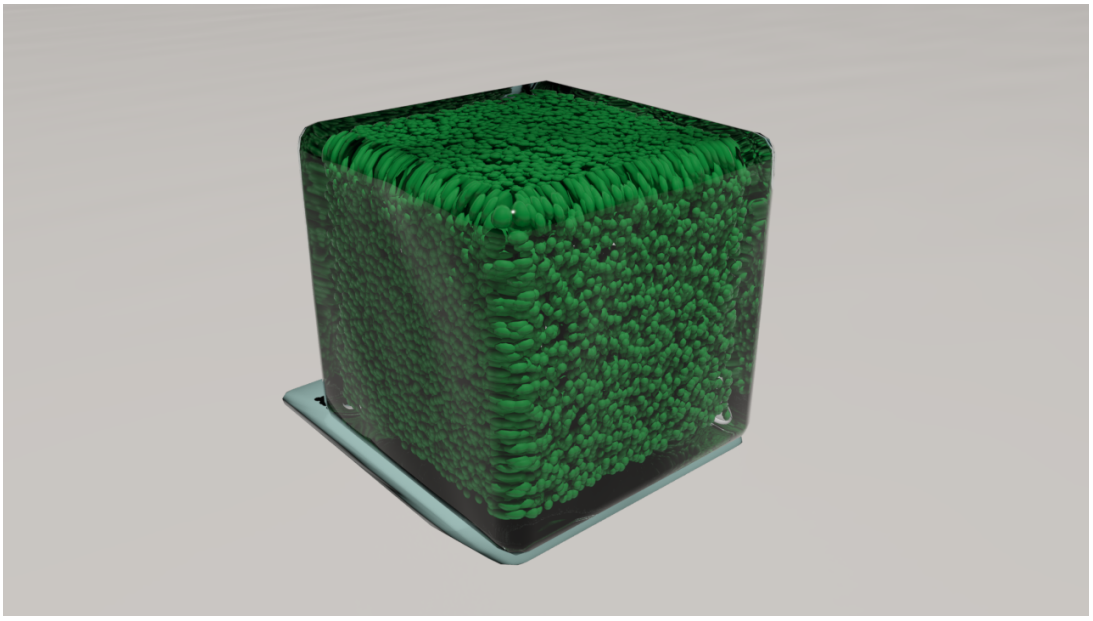

FIGURE F.4: Cells imported into Autodesk 3DS Max.

Bibliography

[1] Howlader N., Noone A.M., Krapcho M., Garshell J., Neyman N., Altekruse S.F., and Kosary C.L. Seer cancer statistics review, 1975 - 2010. *Bethesda*, 2013.

[2] Kevles B.H. *Naked to the Bone: Medical Imaging in the Twentieth Century*. Rutgers University Press, 1996.

[3] Johns H.E. and Cunningham J.R. *The Physics of Radiology, Fourth Edition*. Charles C Thomas Publications Ltd., 1983.

[4] Sheets N.C. Intensity modulated radiation therapy, proton therapy, or conformal radiation therapy and the morbidity and disease control in localized prostate cancer. *Journal of the American Medical Association*, 307, 2012.

[5] Moran J.M., Demosey M., Eisbruch A., and Benedick A. Safety considerations for IMRT: Executive summary. *Practical Radiation Oncology*, 1:190–195, 2011.

[6] Nguyen P.L., Trofimov A., and Zietman A.L. Proton beam vs intensity modulated radiation therapy. which is best for treating prostate cancer? *Oncology*, 22:748–754, 2008.

[7] Kandula S., Zhu X., Garden A.S., and Gillin M. Spot scanning beam proton therapy vs. intensity modulated radiation therapy for ipsilateral head and neck malignancies: a treatment planning comparison. *Medical Dosimetry*, 38:390–394, 2013.

[8] Lundkvist J., Ekman M., and Ericsson S.R. Proton therapy of cancer: Potential clinical advantages and cost-effectiveness. *Acta Oncologica*, 44:850–861, 2005.

[9] Haberer T.H., Debus J., Eickhoff H., and Jakel O. The heidelberg ion therapy center. *Radiotherapy and Oncology*, 73:186–190, 2004.

[10] Feng M. and Eisbruch A. Future issues in highly conformal radiotherapy for head and neck cancer. *Journal of Clinical Oncology*, 25:1009–1013, 2007.

[11] Allen B.J. Clinical trials of targeted alpha therapy for cancer. *Reviews on Recent Clinical Trials*, 3:185–191, 2008.

[12] Nagesha D.K., Tada D.B., Stambaugh C.K.K., Gultepe E., Jost E., Levy C.O., Cormack R., Makrigiorgos G.M., and Sridhar S. Radiosensitizer-eluting nanocoatings on gold fiducials for biological in-situ image guided radiotherapy - bis-igrt. *Physics in Medicine and Biology*, 55:6039–6052, 2010.

[13] Lea D.E. Actions of radiations on living cells. *Cambride University Press*, 1956.

[14] Agostinelli S. Geant4 – a simulation toolkit. *Nucl. Instrum. Methods Phys.*, 506: 250–303, 2003.

[15] Chadwick K.H. and Leenhouts H.P. A molecular theory of cell survival. *Physics in medicine and biology*, 18:78–87, 1973.

[16] Tobias C.A. The repair-misrepair model in radiobiology: Comparison with other models. *Physics in medicine and biology*, 8:77–95, 1985.

[17] Sontag W. Comparison of six different models describing survival of mammalian cells after irradiation. *Radiation Environtal Biophysics*, 8:185–201, 1990.

[18] Curtis S.B. Lethal and potentially lethal lesions induced by radiation - a unified repair model. *Radiation Research*, 8:252–270, 1986.

[19] Bender M.A. and Gooch P.C. The kinetics of x-ray survival of mammalian cells in vitro. *International Journal of Radiation Biology*, 5:133–145, 1962.

[20] Fertil B., Reydellet I., and Deschayanne P. A benchmark of cell survival models using survival curves for human cells after completion of repair of potentially lethal damage. *Radiation Research*, 138:61–69, 1994.

[21] Stewart R.D. Two-lesion kinetic model of dsb rejoining and cell killing. *Radiation Research*, 152:101–104, 2001.

[22] Semenenko V.A. and Stewart R.D. A fast monte carlo algorithm to simulate the spectrum of DNA damages formed by ionizing radiation. *Radiation Research*, 161: 451–457, 2004.

[23] Ostashevsky J.Y. A model relating cell survival to DNA fragment loss and unrepaired double strand breaks. *Radiation Research*, 118:437–466, 1989.

[24] Hawkins R.B. A microdosimetric-kinetic model for the effect of non-poisson distribution of lethal lesions on the variation of rbe with let. *Radiation Research*, 160: 61–69, 2003.

[25] Düchting W and Vogelsaenger T. Recent progress in modelling and simulation of three-dimensional tumor growth and treatment. *Biosystems*, 18:79–91, 1985.

[26] Friedland W., Dingfelder M., Kundrát P., and Jacob P. Track structures, DNA targets and radiation effects in the biophysical monte carlo simulation code partrac. *Mutation Research/Fundamental and Molecular Mechanisms of Mutagenesis*, 711: 28–40, 2011.

[27] Scholz M., Matsufuji N., and Kanai T. Test of the local effect model using clinical data: tumour control probability for lung tumours after treatment with carbon ion beams. *Radiation Protection Dosimetry*, 122:478–479, 2006.

[28] Partridge M. Radiobiological modelling in radiation oncology. *Clinical Oncology*, 20:269, 2008.

[29] Incerti S. Monte carlo dosimetry for targeted irradiation of individual cells using a microbeam facility. *Radiation Protection Dosimetry*, 133:2–11, 2009.

[30] Harriss-Phillips W.M., Bezak E., and Yeoh E.K. Monte carlo radiotherapy simulations of accelerated repopulation and reoxygenation for hypoxic head and neck cancer. *The British Journal of Radiology*, 84:903–918, 2011.

[31] Lliakis G. The role of DNA double strand breaks in ionizing radiation-induced killing of eukaryotic cells. *BioEssays*, 13:641–648, 1991.

[32] Tucker S.L., Howard D., and M.G. Taylor. How well is the probability of tumour cure after fractionated irradiation described by poisson statistics. *Radiation Research*, 124:273–282, 1990.

[33] Rothkamm K., Kruger I., Thompson L.H., and Lobrich M. Pathways of DNA double strand break repair during the mammalian cell cycle. *Molecular and Cellular Biology*, 23:5706–5715, 2003.

[34] Dikomey E. and Lorenzen J. Saturated and unsaturated repair of DNA strand breaks in cho cells after x-irradiation with doses ranging from 3 to 90 gy. *International Journal of Radiation Biology*, 64:659–667, 1993.

[35] Prise K.M., Schettino G., Folkard M., and Keld K.D. New insights on cell death from radiation exposure. *The Lancet Oncology*, 6:520–528, 2005.

[36] Warters R.L., Hofer K.G., Harris C.R., and Smith J.M. Radionuclide toxicity in cultured mammalian cells: elucidation of the primary site of radiation damage. *Current Topics in Radiation Research*, 12:389–407, 1978.

[37] Haimovitz-Friedman A., Kan C., Ehleiter D., Persaud R., McLoughlin M., Fuks Z., and Kolesnick R. Ionizing radiation acts on cellular membranes to generate ceramide and initate apoptosis. *The Journal of Experimental Medicine*, 180:525–535, 1994.

[38] Mishra K.P. Cell membrane oxidative damage induced by gamma radiation and apoptotic sensitivity. *Journal of Environmental Pathology, Toxicology and Oncology*, 23:6, 2004.

[39] Richter C., Park J. W., and Ames B. N. Normal oxidative damage to mitochondrial and nuclear DNA is extensive. *Proceedings of the National Academy of Sciences of the United States of America*, 85:6465, 1988.

[40] Taneja N., Tjalkens R., Philbert M.A., and Rehemtulla A. Irradiation of motochondria initiates apoptosis in a cell free system. *Oncogene*, 20:167–177, 2001.

[41] Bezak E. Marcu L. and Allen B. *Biomedical Physics in Radiotherapy for Cancer*. CSIRO Publishing, 2012.

[42] Fowler J. F. The linear quadratic formula and progress in fractionated radiotherapy. *British Journal of Radiology*, 62:679–694, 1989.

[43] Lambert J. H. On the measure and gradations of light colors and shade. *Augusta Vindelicorum*, page 391, 1760.

[44] Beer. Determination of the absorption of red light in colored liquids. *Annalen der Physik und Chemie*, 86:78–88, 1852.

[45] Compton A. H. A quantum theory of the scattering of x-rays by light elements. *Physical Review*, 21:483–502, 1923.

[46] Klein O. and Nishina Y. Uber die streuung von strahlung durch freie elektronen nach der neuen relativistischen quantendynamik von dirac. *Zeitschrift fur Physik*, 52:853–868, 1929.

[47] Tsai Y.S. Pair production and bremsstrahlung of charged leptons. *Reviews of Modern Physics*, 46:815–851, 1974.

[48] Migdal A.B. Bremsstrahlung and pair production in condensed media at high energies. *Physical Review*, 103:1811–1820, 1956.

[49] Dirac P.A.M. The quantum theory of the electron. *Proceedings of the Royal Society of London. Series A*, 117:610–624, 1928.

[50] Khan F.M. *The Physics of Radiation Therapy, 4th Edition*. Lippincott Williams and Wilkins, 2009.

[51] Brada M., Johannesma M.P., and Ruysscher D.D. Proton therapy in clinical practice: Current clinical evidence. *Journal of Clinical Oncology*, 25:965, 2007.

[52] Douglass M. and Bezak E. Physical modelling of proton and heavy ion radiation using geant4. *Proceedings from the Heavy Ion Accelerator Symposium on Fundamental and Applied Science 2012*, 35, 2012.

[53] Buffon G. Essai d'arithmetique morale. *Histoire Naturelle, Generale er Particuliere*, 4:46–123, 1777.

[54] Berger M.J. Monte carlo calculation of the penetration and diffusion of fast charged particles. *Methods in Computational Physics*, 1:81, 1963.

[55] Kawrakow I. The monte carlo simulation of radiation transport. *AAPM Conference Presentation*, 1999.

[56] Fippel M. *Monte Carlo Techniques in Radiation Therapy*. CRC Press, 2013.

[57] Eyges L. Multiple scattering with energy loss. *Phys. Review*, 74:1534–1535, 1948.

[58] Alfano S. and Greer M. Determining if two solid ellipsoids intersect. *Journal of Guidance and Control Dynamics*, 26:106–110, 2003.

[59] McMahon S. Energy dependence of gold nanoparticle radiosensitization in plasmid DNA. *J. Phys. Chem.*, 115:20160–20167, 2011.

[60] Mesbahi A. A review on gold nano particles radiosensitization effect in radiation therapy of cancer. *Rep. Pract. Oncol. Radiother.*, 15:176–180, 2010.

[61] Lechtman E. Implications on clinical scenario of gold nano particle radiosensitisation in regards to photon energy, nano-particle size, concentration and location. *Phys. Med. Biol*, 56:4631, 2011.

[62] Butterworth K. Physical basis and biological mechanisms of gold nano particle radiosensitization. *Nanoscale*, 4:4830–4838, 2012.

[63] Zheng Y. Radiosensitization of DNA by gold nanoparticles irradiated with high energy electrons. *Radiat. Res.*, 169:481–482, 2008.

[64] McMahon S. Comment on "implications on clinical scenario of gold nanoparticle radiosensitization in regards to photon energy, nanoparticle size, concentration and location. *Phys. Med. Biol.*, 57:287, 2012.

[65] Suneill J. Cell-specific radiosensitization by gold nano-particles at megavoltage radiation energies. *Int. J. Radiat. Oncol.*, 79:531–539, 2010.

[66] Smith L. Nanoparticles in cancer imaging and therapy. *J. Nanomater.*, 2012.

[67] Castillo M. Effects of radiotherapy on mandibular reconstruction plates. *Am. J. Surg.*, 156:261–263, 1988.

[68] Zhang S. Quantifying tumor-selective radiation dose enhancements using gold nanoparticles: A monte carlo study. *Biomed. Microdevices*, 11:925–933, 2009.

[69] Bohn N., Flessau S., and Chillian B. Characterization of bio functionalized semiconductor nanocrystals or gold nanoparticles, January 2014. URL `www.chemie.uni-hamburg.de/pc/mews/research/Bio-Nano.html`.

[70] Matsudaira H. Iodine contrast medium sensitizes cultured mammalian cells to x-rays but not to gamma rays. *Radiat. Res.*, 84:144–148, 1980.

[71] Garnica-Garza H.M. Microdosimetry of x-ray irradiated gold nanoparticles. *Radiat. Prot. Dosim.*, 648, 2012.

[72] Spiers F. The influence of energy absorption and electron range on dosage in irradiated bone. *Br. J. Radiol.*, 22:521–533, 1949.

[73] Herold D.M. Gold microspheres: A selective technique for producing biologically effective dose enhancement. *Int. J. Radiat.*, 76:1357–1364, 2000.

[74] Jain S. Cell-specific radiosensitization by gold nanoparticles at megavoltage radiation energies. *Int. J. Radiat. Oncol., Biol.*, 79:531–539, 2011.

[75] Hainfield J. The use of gold nano particles to enhance radiotherapy in mice. *Int. J. Radiat. Oncol., Biol.*, 49:309–315, 2004.

[76] Rahman W.N. Enhancement of radiation effects by gold nano particles for superficial radiation therapy. *Nanomedicine*, 5:136–142, 2009.

[77] Liu C. Enhanced x-ray irradiation-induced cancer cell damage by gold nano particles treated by a new synthesis method of polyethylene glycol modification. *Radiat. Prot. Dosim.*, 19:2–11, 2008.

[78] Miller R.G. *Beyond Anova: Basics Of Applied Statistics*. Chapman Hall/CRC, 2001.

[79] Liu C. Comparison of geant4 very low energy cross section models with experimental data in water. *Radiat. Prot. Dosim.*, 37:4692, 2010.

[80] Landau L.D. and Lifshitz E.M. Electrodynamics of continuous media, 2nd edition. *Pergamon Press*, 1960.

[81] Champion C., Incerti S., Tran H.N., Karamitros M., Shin J.I., Lee S.B., Lekadir H., Bernal M., Francis Z., Ivanchenko V., Fojón O.A., Hanssen J., and Rivarola R.D. Proton transport in water and DNA components: A geant4 monte carlo simulation. *Nuclear Instruments and Methods in Physics Research B*, 306:165–168, 2013.

[82] Cirrone G.A.P. Validation of the geant4 electromagnetic photon cross-sections for elements and compounds. *Nucl. Instrum. Methods Phys. Res. A*, 618:315–322, 2010.

[83] Larmor J. On a dynamical theory of the electric and luminiferous medium. *Philosophical Transactions of the Royal Society*, 190:205–300, 1897.

[84] Bordovitsyn V.A. Synchrotron radiation in astrophysics. *Synchrotron Radiation Theory and Its Development*, 1999.

[85] Paterson D., de Jonge M.D., Howard D.L., Lewis W. McKinlay J., Starritt A., Kusel M., Ryan C.G., Kirkham R., Moorhead G., and Siddons D.P. X-ray fluorescence microscopy beamline at the australian synchrotron. *AIP Conf. Proc.*, 1365:219–222, 2011.

[86] I.M. Kempson, E. Smith, M. Douglass, B. Thierry, T.Q. Liu, D. Howard, M. DeJonge, and E. Bezak. Applications of large area xrf mapping of metals in biology at the australian synchrotron. *X-ray Fluorescence Newsletter*, pages 12–15, 2012.

[87] Vavrova J., Marekova M., and Vokurkova D. Radiation induced apoptosis and cell cycle progression in tp53 deficient human leukemia cell line hl-60. *Neoplasma*, 48(1): 26–33, 2001.

[88] Mladenov E., Magin S., Soni A., and Lliakis G. DNA double strand break repair as a determinant of cellular radiosensitivity to killing and target in radiation therapy. *Front Oncology*, 3:113, 2013.

[89] Puck T.T. and Marcus P.I. Action of x-rays on mammalian cells. *J Exp Med.*, 103: 653–666, 1956.

[90] Elmore S. Apoptosis: A review of programmed cell death. *Toxicologic Pathology*, 35:653–666, 2007.

[91] Kilonsky D. *Methods in Enzymology Volume 452. Autophagy in Mammalian Systems Part B*. Academic Press, 2009.

[92] Hickson I.D. *Base Excision Repair of DNA Damage*. Springer, 1997.

[93] Alberts B. *Essential Cell Biology. Volume 2*. Garland Science, 1998.

[94] Hall E.J. and Giaccia A.J. *Radiobiology for the Radiologist*. Lippincott Williams and Wilkins, 2006.

[95] Reddy N.M, Mayer P.J, and Lange C.S. The saturated repair kinetics of chinese hamster v79 cells suggest a damage accumulation - interaction model of cell killing. *Radiation Research*, 121(3):304–311, 1990.

[96] Folkard M. The irradiation of v79 mammalian cells by protons with energies below 2 mev. part i: Experimental arrangement and measurements of cell survival. *Journal of Radiation Biology*, 56(3):221–237, 1989.

[97] Bachmann K. Genome size in mammals. *Journal of Radiation Biology*, 37(1):85–93, 1972.

[98] Plante I. and Cucinotta F.A. Monte-carlo simulation of ionizing radiation tracks. *Applications of Monte Carlo Methods in Biology, Medicine and Other Fields of Science*, 2011.

[99] Rudd M.E. Cross sections for production of secondary electrons by charged particles. *Radiat. Prot. Dosim.*, 31:17–22, 1990.

[100] Nikjoo H., Uehara S., Emfietzoglou D., and Brahme A. Heavy charged particles in radiation biology and biophysics. *New journal of physics*, 10, 2008.

[101] Uehara S., Nikjoo H., and Goodhead D. T. Cross sections for water vapour for the monte carlo electron track structure code from 10 ev to the mev region, physics in medicine and biology. *Physics in medicine and biology*, 38:1841–58, 1993.

[102] Plante I. and Cucinoitta F.A. Cross sections for the interaction of 1 ev - 100 mev electrons in liquid water and application to monte carlo simulation of hze radiation tracks. *New Journal of Physics*, 11, 2009.

[103] Ning C.G., Hajgato B., Huang Y.R., Zhang S.F., and Luo K. High resolution electron momentum spectroscopy of the valence orbitals of water. *Chem. Phys.*, 343:19–30, 2008.

[104] Kutcher G.J. and Green A.E.S. A model for energy deposition in liquid water. *Radiation Research*, 67:408–25, 1976.

[105] Kaplan I.G. and Sukhonosov W.Y. Simulation of the passage of fast electrons and the early stage of water radiolysis by monte carlo method. *Radiation Research*, 127, 1991.

[106] Cobut V. Simulation monte carlo du transport d'electrons non relativistes dans l'eau liquide pure et de l'evolution du milieu irradie: rendements des especes creees de 10^{-15} a 10^{-7} seconds. *PhD Thesis University of Sherbrooke, Canada*, pages 408–25, 1993.

[107] Plante I. and Cucinoitta F.A. Ionization and excitation cross sections for the interaction of hze particles in liquid water and application to monte carlo simulation of radiation tracks. *New Journal of Physics*, 10, 2008.

[108] Dingfelder M., Inokuti M., and Paretzke H.G. Inelastic collision cross section of liquid water for interactions of energetic protons. *Rad. Phys. Chemis.*, 59:255–75, 2000.

[109] Booth W. and Grant I.S. Energy loss of oxygen and chlorine ions in solid. *Nuclear Physics*, 63:481–95, 1965.

[110] Francis Z., Incerti S., Karamitros M., Tran H.N., and Villagrasa C. Stopping power and ranges of electrons, protons and alpha particles in liquid water using the geant4-DNA package. *Nuclear instruments and Methods in physics Research B*, pages 2307–2311, 2011.

[111] Bethe H. Zur theorie des durchgangs schneller korpuskularstrahlen durch materie. *Ann. Physics (Leipzig)*, 5:325–400, 1930.

[112] ICRU. ICRU report 37. *International Comission on radiation units and measurements*, 1984.

[113] Michaud M., Wen A., and Sanche L. Cross sections for low-energy (1–100 ev) electron elastic and inelastic scattering in amorphous ice. *Radiation Research*, pages 3–22, 2003.

[114] Dingfelder M., Hantke D., Inokuti M., and Paretkze H.G. Electron inelastic scattering cross sections in liquid water. *Radiation Physics and Chemistry*, 53:1–18, 1998.

[115] Hirayama R., Ito A., Tomita M., Tsukada T., Yatagai F., Noguchi M., Matsumoto Y., Kase Y., Ando K., Okayasu R., and Furusawa Y. Contributions of direct and indirect actions in cell killing by high-let radiations. *Radiation Research*, 171(2): 212–218, 2009.

[116] Coderre J. Principles of radiation interactions, 22.55j. *MIT Lecture Notes*, 2004.

[117] Turner J.E. Atoms, radiation and radiation protection, 2nd edition. *Wiley-Interscience*, 99, 1995.

[118] Sinha R.P. and Häder D.P. UV induced DNA damage and repair: a review. *Photochem. Photobiol. Sci.*, 1:225–236, 2002.

[119] Friedland W., Bernhardt P., Jacob P., Paretzke H. G., and Dingfelder M. Simulation of DNA damage after proton and low let radiation. *Radiation Protection Dosimetry*, 99:99–102, 2002.

[120] Scholes G., Ward J.F., and Weiss J. Mechanism of radiation induced degradation of nucleic acids. *J. Mol. Biol.*, 379:99–102, 1960.

[121] Razskazovskiy Y., Debije M.G., and Bernhard W. Strand breaks produced by x-irradiated crystalline DNA: influence of base sequence. *Radiation Research*, 159(5): 663–669, 2003.

[122] Ward. J.F. DNA damage as the cause of ionizing radiation induced gene activation. *Radiation Research*, 138:85–88, 1994.